



The
University
Of
Sheffield.

The molecular architecture of the Gram-positive bacterial cell wall and how it is disrupted by antibiotics

Laila Pasquina Lemonche

A thesis submitted for the degree of
Doctor of Philosophy

The University of Sheffield
Faculty of Science
Department of Physics and Astronomy

August 2020

Acknowledgements

There are not enough pages in this thesis to express how thankful I am to so many people that have helped me on the personal level and the scientific front. This has been an amazing collective experience that has shaped me during the past four years.

I would like to start by thanking my first supervisor Professor Jamie K Hobbs. You have given me the opportunity to discover the wonderful world of bacteria and to push myself to learn more about the AFM to hopefully one day become an expert in this technique. Thank you for given me the freedom to explore my own experiments and to have such long and interesting conversations of science and life. I consider you a mentor more than a supervisor and I hope we can continue to collaborate in the future.

I would like to thank enormously my second supervisor Professor Simon J Foster for bearing with me with all the questions about microbiology I constantly made in our meetings. Thank you for guiding me through this unfamiliar field and helping me feel more like a biophysicist than I felt four years ago.

To all the members past and present of the Hobbs group who have always support me through this journey and for finding time to chat about my project. Specially I would like to mention Jonny, Sandip, Raveen, Vinny and Xinyue for being some of my best friends and helping me get through the good and bad times. I would like to thank Nic for all the incalculable knowledge you have taught me about AFMs, I aspire to be like you one day.

To all the members past and present of the Foster lab, who have open their doors to a physicist with no prior knowledge of how to work with bacteria. You have been a massive support system for science and coffee times. Especially, I would like to thank Bob, Bartek, Oliver, Kasia and Josh for always sparing some time to answer my multiple questions and for having interesting science discussions at every chance we got. I would like to thank Mina and Mariana for always having supportive and therapeutic chats.

To Lucia, for being my best friend, for always supporting me in all my decisions and listen to all my problems, for all the hugs and Spanish conversations, for all the microbiology help and for being the person I would always want to explain my new results first. This friendship will last a lifetime and I feel lucky to be part of your life now.

To all the members of the Florey Institute student cohort and the Imagine: Imaging life student cohort. For all the amazing experiences of outreach and science communications we have shared together and the opportunity to plan two symposiums on our own. I would like to especially thank Yin for always make me smile and share her positivity.

I would like to thank the Florey Institute for the funding to undertake this project and provide me enough financial help to move to the UK and live independently without any trouble during these years. Thank you to the people who have proofread my thesis: Professor Jamie K Hobbs, Dr Andrew Parnell, Dr James Jennings and Dr Samuel Nuñez. It has been a challenge and I could not have done it without your help.

On a more personal note, I would like to thank all the amazing friends I have made during these years in the UK or the ones who followed me from Spain. First, Anna and Sergio for an incredible time living in Coventry with Sam, I enjoyed those weekends that we were all there together. Then, my dear friends Iago and Rafa that followed the same path as me and we all came to do PhDs here after the Master. It was great visiting you and seeing how our lives progress parallelly. My friends in Sheffield James and Mon for great times and although we were always busy we would make time for coffee and catch up. Finally, to Bea for always supporting me since day one, and for those very effective study afternoons that help with my writing period and would remind us from our undergrad time together. Thanks for opening your home when I felt lonely and for being there.

Every time I would go back to my hometown, I had my biggest supporters and best friends, Elena and Esther. Thanks for always being there and for never losing contact despite the distance. Thanks to Roger and Javi for always finding time to meet me when I was there and to all my friends who always cheer me up when I needed it. To my family for always believing in me and love me unconditionally, especially to my parents Enric and Enriqueta and my brother Jordi without whom I would not have studied physics in the first place.

Finally, it is difficult to find the right words to describe how thankful I am to my husband, best friend and partner in life Samuel Nuñez. Without you this thesis would not be like it is. You have inspired me to perform better experiments, you have believed in me and gave me confidence when I was at my lowest, you always shared the same joy I had when the results were good. I feel fortunate to have shared the past 5 years and a half with you and I feel the luckiest person on Earth knowing you will always be by my side in the future journeys ahead.

Abstract

Peptidoglycan is the main component of the bacterial cell wall. It is crucial for cell survival because it acts as a barrier between the internal contents of the cell and the outer environment; maintaining cellular integrity and shape. Despite its chemical structure being defined in great detail, its organisation in the cell at molecular level is still unknown. In this thesis, Atomic Force microscopy combined with quantitative image analysis were used to decipher the peptidoglycan molecular architecture in different bacterial strains and environments.

First, in Chapter 3 a novel approach to study peptidoglycan using sacculi in liquid environment is presented and the structure of the external peptidoglycan for *Staphylococcus aureus* is explored in detail: the nascent areas are formed of concentric rings and the mature regions form a randomly oriented fibrous mesh. Then, in Chapter 4, the structure of the internal peptidoglycan surface of *Staphylococcus aureus* is directly imaged for the first time, consisting on a dense mesh with pores of ~ 6 nm. In contrast, the external mesh contains many pores larger than 30 nm in diameter. The septal plate architecture is presented as a complex structure formed by oriented rings on the external septal wall while disordered mesh on the internal surface. Next, in Chapter 5 a comprehensive comparison between different mutant strains is performed. Mutants lacking either hydrolysis or peptidoglycan synthesis enzymes result in significant differences in cell wall architecture. This is the first step towards molecular phenotypes. Another Gram-positive bacteria species, rod-shaped *Bacillus subtilis* is studied in Chapter 6 using the methodologies developed during previous chapters. The internal surface is highly ordered along the short circumferential axis. However, the septal plate presents a striking open mesh structure. Finally, the addition of different antibiotics causes critical big holes that perforate through the cell wall not observed on healthy *Staphylococcus aureus* cells. This answers the 80 years old question of how antibiotics work, which is key to defeat the antimicrobial resistance crisis.

Declaration

This thesis is submitted to The University of Sheffield in support of my application for the degree of Doctor of Philosophy. I, the author, confirm that the thesis is my own work. *I am aware of the University's Guidance on the Use of Unfair Means (www.sheffield.ac.uk/ssid/unfair-means)*. *This work has not been previously been presented for an award at this, or any other, university.*

The work presented herein has been conducted by myself, except the following:

- The *S. aureus* live cells images from *Figures 3.1, 3.10, 3.12, 3.23, 3.26*, and *B. subtilis* live cells images from *Figures 6.12, 6.14* provided by Dr. Jonathan Burns (University of Sheffield)
- The TEM image in *Figure 5.2* provided by Lucia Lafage (University of Sheffield)
- Dr Joshua Sutton (University of Sheffield) purified the peptidoglycan material from mutants *pbp3* and *pbp4* used to obtain images for *sections 5.4* and *5.5*.
- The *B. subtilis* internal sacculi images from *Figure 6.4 g-h* and external surface from *Figure 6.12 b* provided by Dr Sandip Kumar (University of Oxford)
- The *B. subtilis* internal sacculi images from *Figure 6.4 c-f* provided by Dr Robert Turner (University of Sheffield)
- The specified *B. subtilis* septa images from *Figure 6.9* provided by Dr Raveen Tank (University of Sheffield)
- The theoretical background used to explain *section 4.3* was provided by Dr Buddhapriya Chakrabarti (University of Sheffield)
- The 3D half bacteria schematics for *Figures 3.26, 4.12, 4.21* and *6.30* were provided by Dr Robert Turner (University of Sheffield)
- The results from *section 7.1.3* were produced by Dr Milena L Von Und Zur Muhlen (University of Sheffield)

Most of the work described in *Chapters 3, 4, 5* and *6* has been published in:

L. Pasquina-Lemonche, J. Burns, R. Turner, S. Kumar, R. Tank, N. Mullin, J. Wilson, B. Chakrabarti, P. Bullough, S. Foster and J. Hobbs, "The architecture of the Gram-positive bacterial cell wall," *Nature*, vol. 582, no. 7811, pp. 294–297, 2020.

List of Figures

Figure 1.1 – Antibiotic timeline and death rate caused by AMR and other diseases	20
Figure 1.2 – Different levels of complexity of peptidoglycan structure	23
Figure 1.3– Chemical structure of the Peptidoglycan subunit from <i>S. aureus</i>	25
Figure 1.4– Representation of different cross-link positions on peptidoglycan	26
Figure 1.5 - Chemical structure of Wall Teichoic Acids from <i>S. aureus</i> .	27
Figure 1.6 – Models of peptidoglycan molecular architecture from NMR data	29
Figure 1.7 – Scaffold versus layered models for peptidoglycan organisation on the cell	30
Figure 1.8 – Peptidoglycan synthesis in <i>S. aureus</i>	32
Figure 1.9 – Different parts of the cell wall highlighting the setum	35
Figure 1.10 – Septum formation stages on <i>S. aureus</i>	36
Figure 1.11 – Structural inheritance of division planes in <i>S. aureus</i>	37
Figure 1.12 – Scheme of the main components of an AFM set-up	41
Figure 1.13 – Forces interacting between AFM tip and the surface	46
Figure 1.14 - Scheme explaining the working principle of contact mode AFM	47
Figure 1.15 – Scheme explaining the working principle of IC-AFM and a tuning graph	49
Figure 1.16 – Pulse-force and PeakForce modes schematics	51
Figure 1.17 – Force curves and amplitude curves at different electrolyte concentrations	56
Figure 1.18 – AFM height images of Staphylococcus aureus live cells	58
Figure 1.19 – Peptidoglycan architecture from sacculi for different bacterial species	62
Figure 3.1 – High resolution images of <i>S. aureus</i> live cells with AFM	93
Figure 3.2 – Schematics of the workflow from sample preparation to imaging sacculi	95
Figure 3.3 – AFM images of sacculi in dried environment from published work	96
Figure 3.4 – AFM images of sacculi in dried environment from this study	96
Figure 3.5 - First attempt at imaging sacculi on PLL coated glass in liquid environment	98
Figure 3.6 – Optimizing <i>S. aureus</i> sacculi concentration in PLL coated glass	100
Figure 3.7 – Sacculi attachment comparison between PLL and Cell-Tak	101
Figure 3.8 – Optimization of incubation time for sacculi stock B	102
Figure 3.9 – AFM images of nascent peptidoglycan sacculi in liquid using IC-AFM	103
Figure 3.10 - Quantitative comparison between living cells and sacculi images	104
Figure 3.11 - AFM images of nascent peptidoglycan sacculi in liquid using PeakForce	106
Figure 3.12- Periodic features between and along the glycan strands in nascent PG	108
Figure 3.13 – Mature PG hydrated sacculi using IC-AFM in liquid environment	110
Figure 3.14 – Mature PG hydrated sacculi using PeakForce in liquid environment	111
Figure 3.15 – Glass grid correlation method: set-up and results	113

Figure 3.16 - Mesh to knobble correlation of mature PG in liquid and dry environments _____	114
Figure 3.17 – Methodology to measure thickness of sacculi and the impact of force _____	117
Figure 3.18 – Thickness measurements of <i>S. aureus</i> sacculi in liquid and air environments __	117
Figure 3.19 – Manual profiling analysis to calculate depth of pores on mature PG _____	119
Figure 3.20 – Manual profiling analysis to measure width of fibres on mature PG _____	120
Figure 3.21- Histogram of fibre width comparing <i>S. aureus</i> live cells and sacculi _____	120
Figure 3.22 – Workflow to analyse mature PG using two-dimensional sectioning _____	122
Figure 3.23 – Comparison of pore depth between <i>S. aureus</i> live cells and sacculi _____	123
Figure 3.24 – 3D representation with Avizo of mature PG images from different views _____	124
Figure 3.25 – Pore depth analysis in 3D comparing <i>S. aureus</i> live cells and sacculi _____	125
Figure 3.26 – Scheme of external PG structure of <i>S. aureus</i> with all different structures _____	128
Figure 4.1 – AFM images of internal PG surface of sacculus partially broken in liquid _____	134
Figure 4.2 – Images of internal PG from sacculi fragments with different conformations _____	135
Figure 4.3– Sacculi fragments with a piecrust like feature with different orientations _____	136
Figure 4.4 – Manual analysis to compare the pore size between external and internal PG _____	138
Figure 4.5 – Workflow for the semi-automated analysis of pore size _____	139
Figure 4.6 – Different outcomes of analysis depending on raw data treatment _____	141
Figure 4.7 – Manual check after performing the automated analysis to discard errors _____	142
Figure 4.8 – Histogram of pore area from external live cells, external and internal sacculi _____	143
Figure 4.9 – Steps to produce the cumulative fraction of total area versus area graph _____	145
Figure 4.10 – Cumulative fraction of total area graphs for all <i>S. aureus</i> data sets _____	146
Figure 4.11 – 3D schematics of different stages of <i>S. aureus</i> cell division _____	150
Figure 4.12 – Summary of growth curve experiment conditions and results _____	151
Figure 4.13 – AFM images in air of sacculi purified at different cell cycle stages _____	152
Figure 4.14 – AFM images in liquid of an unfinished septum with high resolution _____	154
Figure 4.15 – Cumulative fraction of total area comparing internal septa and internal PG _____	155
Figure 4.16 – AFM images of external septal wall from different sacculi in liquid _____	156
Figure 4.17 – Workflow to apply the glycan strand orientation analysis _____	158
Figure 4.18 – Glycan strand orientation results for different PG structures of <i>S. aureus</i> _____	158
Figure 4.19 – 3D scheme representing the CW from external to internal and septa _____	161
Figure 5.1 – AFM images of tarO live cells trapped in silicon grids _____	165
Figure 5.2 – Chemical fixated TEM and AFM of ItaS cells and sacculi respectively _____	168
Figure 5.3 – AFM images of sagB sacculi in liquid environment _____	170
Figure 5.4 – Cumulative fraction of total area comparing WT and sagB external PG _____	172
Figure 5.5 – Wide field images used to measure the sacculi thickness of sagB _____	173
Figure 5.6 – Comparison of sagB thickness and WT in liquid and air environments _____	174

Figure 5.7 – AFM images of pbp3 in liquid at high resolution _____	176
Figure 5.8 – AFM images of pbp4 in liquid at high resolution and comparison to WT _____	179
Figure 5.9 – Two perpendicular planes of concentric rings in a pbp4 sacculus _____	180
Figure 6.1 – AFM images of <i>B. subtilis</i> sacculi in dried environment from published work ____	186
Figure 6.2 – AFM images of <i>B. subtilis</i> sacculi in dried environment from this study _____	187
Figure 6.3 – AFM images of <i>B. subtilis</i> sacculi in liquid environment _____	189
Figure 6.4 – AFM images of <i>B. subtilis</i> internal PG structure with orientation analysis _____	191
Figure 6.5 – Series of AFM phase images from <i>B. subtilis</i> septa from published work _____	192
Figure 6.6 – <i>B. subtilis</i> septa correlation between air and liquid environments _____	193
Figure 6.7 – <i>B. subtilis</i> septa in liquid at high resolution and other sacculi fragments _____	194
Figure 6.8 – Workflow to apply the pore analysis for <i>B. subtilis</i> septa _____	196
Figure 6.9 – Six septa images used for the analysis of the pores _____	198
Figure 6.10– Resultant graph from <i>B. subtilis</i> septa pore analysis _____	199
Figure 6.11 – Thickness measurements of <i>B. subtilis</i> sacculi in liquid and air environments __	200
Figure 6.12 – AFM images of mature external surface of <i>B. subtilis</i> live cells _____	203
Figure 6.13 – Manual measurement of fibre width for two <i>B. subtilis</i> images and results ____	204
Figure 6.14– Comparison of pore depth between <i>S. aureus</i> and <i>B. subtilis</i> live cells _____	206
Figure 6.15 – Workflow of how the code in Appendix 2 works to produce pore analysis _____	207
Figure 6.16 – HCFA curves and number of pores graphs for <i>B. subtilis</i> and <i>S. aureus</i> _____	208
Figure 6.17 – Comparison between <i>B. subtilis</i> and <i>S. aureus</i> using automated analysis _____	209
Figure 6.18 – AFM images of nascent external surface of <i>B. subtilis</i> live cells _____	210
Figure 6.19 – AFM images of nascent external of <i>B. subtilis</i> live cells at high resolution _____	211
Figure 6.20 – Summary of SDS killing curve experiment conditions and OD graph _____	213
Figure 6.21 – CFU per ml graphs after SDS killing curve in two environments _____	214
Figure 6.22 – Dynamics of 2.5 % SDS treatment to live <i>B. subtilis</i> cells using AFM _____	215
Figure 6.23 – 3D comparison of shape of the pores before and after 2.5 % SDS addition ____	216
Figure 6.24– Dynamics of 5 % SDS treatment to live <i>B. subtilis</i> cells using AFM _____	217
Figure 6.25– Wide field images showing four targeted cells to measure their dimensions ____	219
Figure 6.26 – Published work on mreBCD <i>B. subtilis</i> mutants and their role in PG synthesis _	222
Figure 6.27– AFM images of Δ mreB mutant sacculi in liquid with high resolution _____	224
Figure 6.28 – AFM images of Δ rsgI mutant sacculi in liquid with high resolution _____	226
Figure 6.29 – Glycan orientation analysis comparing Δ mreB, Δ rsgI and <i>B. subtilis</i> WT _____	227
Figure 6.30 – Molecular PG architecture model for <i>S. aureus</i> and <i>B. subtilis</i> _____	230
Figure 7.1 – Chemical structures of D-Ala-D-Ala, Penicillin and Methicillin _____	234
Figure 7.2 – Vancomycin chemical structure _____	236
Figure 7.3 – Methicillin and Vancomycin killin curves with 10x MIC of <i>S. aureus</i> _____	238

Figure 7.4 – SIM images of <i>S. aureus</i> treated with 10xMIC Methicillin and Vancomycin _____	240
Figure 7.5 –Quantification of PG incorporation after 10xMIC of Methicillin and Vancomycin	242
Figure 7.6 – Schematics of sacculi preparation after antibiotic treatment _____	244
Figure 7.7 – AFM images of sacculi in liquid and analysis of WT M30 _____	245
Figure 7.8 – Schematics of the perforation holes analysis present in antibiotic samples _____	246
Figure 7.9 – HCFA curves for internal pores and holes for WT M30 compared to WT _____	248
Figure 7.10 – HCFA curves for different WT M30 images and number of pores graphs _____	249
Figure 7.11 – AFM images of sacculi in liquid and analysis of WT M60 _____	250
Figure 7.10 – Internal and external pores analysis for WT M60 compared to WT _____	252
Figure 7.13 - AFM images of sacculi in liquid and analysis of WT M120 _____	253
Figure 7.14 – Internal and external pores analysis for WT M120 compared to WT _____	255
Figure 7.15 - AFM images of sacculi in liquid and analysis of WT V30 _____	256
Figure 7.16 – Internal and external pores analysis for WT V30 compared to WT _____	258
Figure 7.17 - AFM images of sacculi in liquid and analysis of WT V60 _____	259
Figure 7.18 – Internal and external pores analysis for WT V60 compared to WT _____	261
Figure 7.19 - AFM images of sacculi in liquid and analysis of WT V120 _____	262
Figure 7.20 – Internal and external pores analysis for WT V120 compared to WT _____	264
Figure 7.21 – Internal PG images for all samples and quantitative analysis _____	265
Figure 7.22 – Summary of quantitative analysis of external PG parameters for all samples _____	266
Figure 7.23 – Quantitative analysis of perforating holes for all samples _____	267
Figure 7.24 – Thickness of sacculi fragments in air for all samples _____	268
Figure 7.25 – Model of death mechanism caused by CW antibiotics _____	270

List of Tables

Table 1.1 – Types of hydrolases with their name and functions in <i>S. aureus</i> _____	34
Table 2.1 – Bacterial strains used in sections and chapters of this thesis _____	73
Table 2.2 – AFM probes with their names and physical characteristics _____	77
Table 2.3 – Sacculi batches prepared independently from different strains _____	77
Table 2.4 – Sacculi dilutions and their optical dispersity values _____	78
Table 3.1 – Experimental conditions used in Figure 3.1 _____	94
Table 3.2- Experimental conditions used in Figure 3.4 _____	97
Table 3.3 – Summary of stablished PG structures and unknown structures _____	97
Table 3.4 - Experimental conditions used in Figure 3.5 _____	99
Table 3.5 – Sacculi dilutions 1-6 with their OD concentration _____	99
Table 3.6 – Experimental conditions used in Figure 3.8 _____	102
Table 3.7 - Experimental conditions used in Figure 3.9 _____	103
Table 3.8 - Experimental conditions used in Figure 3.11 _____	105
Table 3.9 - Experimental conditions used in Figure 3.12 _____	107
Table 3.10 – Experimental conditions used in Figure 3.14 _____	112
Table 3.11 - Experimental conditions used in Figure 3.16 _____	114
Table 3.12– Complete summary of PG structures identified using AFM in different samples _	115
Table 3.13 - Experimental conditions used in Figure 3.18 _____	118
Table 3.14 – Summary of the results obtained from the manual analysis of mature PG _____	121
Table 3.15 – Summary of results presented in Figure 3.23 _____	123
Table 4.1 – Experimental conditions used in Figure 4.2 _____	135
Table 4.2 – Summary of the results extracted from the Histograms in Figure 4.8 _____	144
Table 4.3 - Summary of the results extracted from the graphs in Figure 4.10 _____	146
Table 4.4 – Different sacculi samples at specific time points and ODs for <i>S. aureus</i> _____	152
Table 4.5 - Experimental conditions used in Figure 4.14. _____	154
Table 5.1 – Experimental conditions used in Figure 5.1 _____	166
Table 5.2 – Experimental conditions used in Figure 5.2 _____	168
Table 5.3 – Experimental conditions used in Figure 5.3, 5.5 and 5.6 _____	170
Table 5.4 – Mean values and their standard deviation from Figure 5.6 c _____	175
Table 5.5 – Experimental conditions used in Figure 5.7 _____	176
Table 6.1 – Experimental conditions used in Figure 6.2 and Figure 6.3 _____	188
Table 6.2 – Experimental conditions used in Figure 6.12 _____	204
Table 6.3 – Fibre width median and standard deviation from Figure 6.13 _____	205
Table 6.4 – Dimensions of <i>B. subtilis</i> cells before and after 2h treatment with 5% SDS _____	219

Table 6.5 – Experimental conditions used in Figure 6.27 _____	224
Table 7.1 – Nomenclature of samples at different time points antibiotic treatment _____	239
Table 7.2 – Experimental conditions used in Figure 7.7 _____	246
Table 7.3 – Experimental conditions used in Figure 7.15 _____	257
Table 7.4 – Results from quantitative analysis of all samples studied in chapter 7 _____	269

Table of Contents

Acknowledgements	1
Abstract	3
Declaration	5
List of Figures	7
List of Tables	11
Chapter 1 Introduction	19
1.1 The antimicrobial resistance problem	19
1.2 Staphylococcus aureus	21
1.2.1 Clinical background	22
1.3 The cell wall architecture and function	23
1.3.1 Cell wall chemical structure	24
1.3.1.1 Wall teichoic acids	26
1.3.1.2 Lipo Teichoic acids	27
1.3.2 Peptidoglycan architecture (scaffold vs layered)	28
1.3.3 Cell wall Synthesis, hydrolysis and cell division	31
1.3.3.1 Synthesis	31
1.3.3.2 Hydrolysis	33
1.3.3.3 Cell division	34
1.3.4 Cell wall function and target for main antibiotics	37
1.4 Atomic Force Microscopy	39
1.4.1 Atomic force microscopy working principle	40
1.4.2 Surface interactions	42
1.4.2.1 Origin of short-range and long-range forces	42
1.4.2.1.1 Van der Waals interaction	43
1.4.2.1.2 The double-layer force	44
1.4.2.2 The ideal tip-sample interaction	44
1.4.3 Atomic force microscopy modes of operation	46
1.4.3.1 Contact mode	46
1.4.3.2 Intermittent contact - Tapping™ mode	48
1.4.3.3 Alternative imaging modes and PeakForce	50
1.4.4 High resolution imaging	52
1.4.4.1.1 Screening of electric double-layer	55
1.4.5 Study of bacteria using Atomic force microscopy	57
1.4.5.1 Living bacteria	57
1.4.5.2 Sacculi samples	60
1.5 Project aims	63
1.6 Bibliography	65
Chapter 2 Materials and Methods	73
2.1 Materials	73
2.1.1 Bacterial strains	73
2.1.2 Antibiotics	73
2.1.3 Buffers and solutions required for cell wall purification	74
2.1.3.1 Tris buffer	74
2.1.3.2 Sodium dodecyl sulfate	74
2.1.3.3 Pronase solution	74
2.1.4 Buffers for atomic force microscopy experiment	74
2.1.4.1 Imaging buffer for sacculi	74
2.1.4.2 Buffers for surface coatings	75
2.1.5 Substrates for atomic force microscopy experiments	75
2.1.5.1 Mica discs	75

2.1.5.2	Glass coverslips	75
2.1.5.3	Silicon grids	75
2.1.5.4	Complementary materials for substrate preparation	76
2.1.6	Surface Coatings for Atomic force microscopy experiments	76
2.1.6.1	Poly-L-Lysin (PLL)	76
2.1.6.2	Cell-Tak™ tissue adhesive	76
2.1.7	Atomic force microscopy probes	77
2.1.8	Sacculi dilutions and batches	77
2.2	Microbiology protocols	78
2.2.1	Cell growth conditions and growth/killing curves	78
2.2.1.1	Optical Density	78
2.2.1.2	Growth conditions for <i>S. aureus</i>	78
2.2.1.3	Growth conditions for <i>B. subtilis</i>	78
2.2.1.4	Growth conditions for <i>S. aureus</i> mutant strains	79
2.2.1.5	Growth conditions for <i>B. subtilis</i> mutant strains	79
2.2.1.6	Growth curves	80
2.2.1.7	Killing curves with SDS	80
2.2.2	Cell Wall purification protocols	81
2.2.2.1	Cell Wall purification protocol for <i>S. aureus</i>	81
2.2.2.2	With and without wall teichoic acids (stocks A and B)	82
2.2.2.3	Improvements from established protocol	83
2.2.2.4	Cell Wall purification protocol for <i>B. subtilis</i>	83
2.2.2.5	Cell Wall purification for antibiotic treated cells	84
2.3	Atomic Force Microscopy protocols	84
2.3.1	Substrate preparation	84
2.3.1.1	Mica discs	85
2.3.1.2	High precision glass coverslip and glass etched grids	85
2.3.1.3	Silicon grids	85
2.3.2	Surface mounting and buffer for imaging of purified cell wall	86
2.3.2.1	Sacculi dilution and tip sonicating	86
2.3.2.2	PLL coated surfaces for mounting sacculi in liquid	86
2.3.2.2.1	PLL coated glass	86
2.3.2.2.2	PLL coated mica	87
2.3.2.3	Cell-Tak™ coated surfaces for mounting sacculi in liquid	87
2.3.2.3.1	Cell-Tak™ coated glass	87
2.3.2.3.2	Cell-Tak™ coated mica	87
2.3.2.4	Surface mounting in ambient conditions of purified cell wall	88
2.3.2.5	Air to liquid correlation methods	88
2.3.3	Surface mounting to image live cells	89
2.3.3.1	<i>S. aureus</i> SH1000 live cells in silicon grids	89
2.3.3.2	<i>S. aureus</i> SH1000 <i>tarO</i> live cells in silicon grids	89
2.3.3.3	<i>B. subtilis</i> live cells in Cell Tak coated mica	89
2.3.3.3.1	Imaging <i>B. subtilis</i> live cells with SDS treatment	90
2.3.4	Achieve the highest resolution possible with Atomic force microscopy	90
2.3.4.1	Sacculi in liquid	90
2.3.4.2	Living cells	91
2.4	References	91
Chapter 3	The external peptidoglycan architecture of <i>Staphylococcus aureus</i>	93
3.1	The external cell wall architecture of living bacteria	93
3.2	Purified peptidoglycan in ambient conditions	94
3.3	Optimization process of sacculi adhesion in liquid conditions	98
3.3.1	Poly-L-Lysine coated glass	98
3.3.2	Optimized sacculi concentration	99
3.3.3	Sacculi attach to Cell-Tak™ coated Glass	100
3.3.4	Sacculi attach to Cell-Tak™ coated Mica	101
3.3.5	Sample incubation optimization	102
3.4	Nascent purified peptidoglycan in liquid environment	103
3.4.1	Molecular resolution of nascent peptidoglycan	103

3.4.2	Periodicity along glycan strands	107
3.5	Mature purified peptidoglycan in liquid environment	109
3.5.1	Hydrated mature sacculi in tapping mode	109
3.5.2	Hydrated mature sacculi in PeakForce mode	110
3.5.3	Comparison of mature peptidoglycan in different environments	112
3.5.3.1	Optimization of correlating methods	112
3.5.3.1.1	Gridded glass coverslip	112
3.5.3.1.2	Marks on Mica	113
3.5.3.2	Mesh to Knobbles correlation	114
3.5.3.3	Hydrogel behaviour	116
3.5.4	Different approaches of analysis of mature peptidoglycan	118
3.5.4.1	Manual profiles measuring depth of pores and width of fibres	118
3.5.4.2	Two-dimensional sectioning (depth maps)	121
3.5.4.3	From AFM image to 3D representation using Avizo	124
3.6	Discussion	126
3.7	References	129
Chapter 4	<i>The internal peptidoglycan architecture of Staphylococcus aureus</i>	133
4.1	Molecular resolution of internal cell wall	133
4.1.1	Imaging the internal cell wall under liquid conditions	133
4.2	Quantitative analysis of pores across the cell wall	137
4.2.1	Optimisation to analyse pore size	137
4.2.1.1	Manual measuring of individual pores for each image	137
4.2.1.2	Semi-automated method with final manual check	138
4.2.2	Quantitative comparison of internal and external cell wall	142
4.3	Theoretical approach to turgor pressure equilibrium	147
4.4	The septum structure	149
4.4.1	Optimization of sample preparation to obtain more septa on AFM	150
4.4.2	The septal plate architecture inside out	153
4.4.2.1	Internal septal wall structure	153
4.4.2.2	External septal wall structure	156
4.4.3	Glycan strands orientation analysis	157
4.5	Discussion	159
4.6	References	162
Chapter 5	<i>Staphylococcus aureus mutants</i>	165
5.1	Removal of WTA (SH1000 <i>tarO</i>)	165
5.2	Removal of LTA (SH1000 <i>ItaS</i>)	166
5.3	Removal of SagB hydrolase (SH1000 <i>sagB</i>)	169
5.3.1	Sacculi images of SH1000 <i>sagB</i> in liquid	170
5.3.2	Pore morphology comparison between <i>sagB</i> mutant and WT	171
5.3.3	Hydrogel behaviour of <i>sagB</i> mutant	172
5.4	Removal of non-essential synthase PBP3 (SH1000 <i>pbp3</i>)	175
5.5	Removal of non-essential synthase PBP4 (SH1000 <i>pbp4</i>)	177
5.6	Discussion	181
5.7	References	183
Chapter 6	<i>Bacillus subtilis</i>	185
6.1	<i>Bacillus subtilis</i> wild type sacculi	185
6.1.1	Atomic force microscopy images in air	186
6.1.2	Atomic force microscopy images in liquid	188
6.1.3	The Septum	192
6.1.3.1	Air to Liquid structural correlation	192

6.1.3.2	Septa pores morphology (back-filling)	195
6.1.4	Hydrogel behaviour	200
6.2	<i>Bacillus subtilis</i> wild type living cells	201
6.2.1	External mature cell wall	201
6.2.1.1	Fibre width measurements	204
6.2.1.2	Improved quantitative characterization of pores	205
6.2.2	External nascent cell wall	210
6.2.3	SDS treatment of <i>Bacillus subtilis</i>	212
6.2.3.1	Killing dynamics of SDS at population level	212
6.2.3.2	Dynamics of 2.5% SDS under Atomic force microscopy	214
6.2.3.3	Dynamics of 5% SDS under Atomic force microscopy	217
6.3	<i>Bacillus subtilis</i> mutants	220
6.3.1	The MreB filaments	220
6.3.1.1	The role of MreB complex in cell morphology	221
6.3.1.2	Molecular structure of strain lacking MreB (Δ mreB strain)	223
6.3.2	The rsgI mutant (background strain for Δ mreB)	225
6.3.3	Internal strand orientation is shape dependant	226
6.4	Discussion	228
6.5	References	231
Chapter 7	<i>Antibiotic effect on Staphylococcus aureus</i>	233
7.1	Methicillin versus Vancomycin	233
7.1.1	β -lactam antibiotics	233
7.1.1.1	Methicillin	235
7.1.2	Glycopeptide antibiotics	235
7.1.2.1	Vancomycin	235
7.1.3	Methicillin and Vancomycin effect at population level	236
7.1.3.1	Growing and killing assays	236
7.1.3.2	Cell volume variability	239
7.1.3.3	Di-peptide and ^{14}C -GlcNAc incorporation	241
7.2	<i>Staphylococcus aureus</i> sacculi treated with Methicillin	243
7.2.1	Methicillin effect in sacculi after 30 min treatment	245
7.2.2	Methicillin effect in sacculi after 60 min treatment	250
7.2.3	Methicillin effect in sacculi after 120 min treatment	253
7.3	<i>Staphylococcus aureus</i> sacculi treated with Vancomycin	256
7.3.1	Vancomycin effect in sacculi after 30 min treatment	256
7.3.2	Vancomycin effect in sacculi after 60 min treatment	259
7.3.3	Vancomycin effect in sacculi after 120 min treatment	262
7.4	Quantitative comparison between healthy and Methicillin/Vancomycin treated cells	265
7.5	Model of action of cell wall antibiotics	269
7.6	Discussion	271
7.7	References	275
Chapter 8	<i>Conclusions and future work</i>	277
Appendix 1	<i>– MATLAB code for analysing Bacillus subtilis septa pores</i>	285
Appendix 2	<i>– FIJI code for analysing mature mesh pores</i>	285
Appendix 3	<i>– Comparison between S. aureus sacculi and live cells</i>	286
Abbreviations list		287

*This thesis is dedicated to Samuel, for
being my unconditional partner in this journey and my rock*

*“I would rather have questions that can’t be answered than
answers that can’t be questioned “*

- Richard P. Feynman -

Chapter 1 Introduction

1.1 The antimicrobial resistance problem

Antibiotics were first discovered in the late 19th century. Since then, these molecules have been considered a “magic bullet” that specifically killed microorganisms leaving the host organism unharmed. The most famous discovery in this field was in 1920 when Alexander Fleming realized that a microorganism (*i.e. Penicillium notatum*) produced an antibiotic compound, later called penicillin.[1], [2] This antimicrobial compound kills bacteria such as *Staphylococcus aureus* (*S. aureus*), preventing infections from being fatal. Penicillin was first applied during World War II, successfully saving many lives. Nowadays, it is still the most widely used antibiotic worldwide. In the second half of the 20th century, particularly the 1950s, novel and powerful antibiotics such as streptomycin, tetracycline, and chloramphenicol were discovered. However this sustained period of antibiotic discovery lasted until the late 1990s. [1], [2] Since then a hiatus has occurred, as during the last 30 years only two new classes of antibiotics have been discovered, with the lipoglycopeptide being the last class discovered in 2009. To date, the last new antibiotic compound discovered was Dalbavancin in 2014 which belongs to the lipoglycopeptide class. Since 2015,[3] the research focus has shifted to develop combined treatments of commonly used antibiotics (such as ceftazidime) with β -lactamase inhibitor enzymes such as Avibactam [4] which when paired increase the efficacy of the treatment.

The lack of new discoveries means that our drug resources to defeat bacterial infections are limited to the existing classes of antibiotics. If microbial infections were a disease with no variation over time then the existing antibiotics would cure these infections. Unfortunately, this is not the case. Since the first antibiotics were discovered, a progressively increasing resistance to antimicrobial substances has been observed (see *Figure 1.1 a*).[1] A microorganism species becomes resistant to a specific antimicrobial agent when colonies are able to grow despite exposure to the antimicrobial. [2], [5], [6] The evolved (*i.e. mutated*) bacterial strains capable of surviving under a particular drug treatment, can grow rapidly and spread due to the lack of competition from other non-resistant strains. Over the past two decades, antimicrobial resistance (AMR) has

increasingly become a major public health crisis.[7], [8] The main reason is that the overuse of antimicrobials has become widespread in human patients and also animals.[9] It has been common practice to add antimicrobials to animal food supplies in the absence of any infection, to increase their growth rate.[10] Consequently, the rate at which resistance is developing and spreading has increased. The result of this situation is the emergence of ‘superbugs’ such as Methicillin-resistant *Staphylococcus aureus* (MRSA)[11] which is responsible for hundreds of deaths in the UK every year and many more worldwide.[12], [13] Another example is the extremely drug resistant *Tuberculosis* (TB) strain, which is almost impossible to treat with existing antibiotic drugs. Some *Salmonella* strains show resistance to crucial fluoroquinolone antibiotics (DT104), and recently in 2015, resistant strains to the antibiotic of last resort, Colistin, have begun emerging.[5]

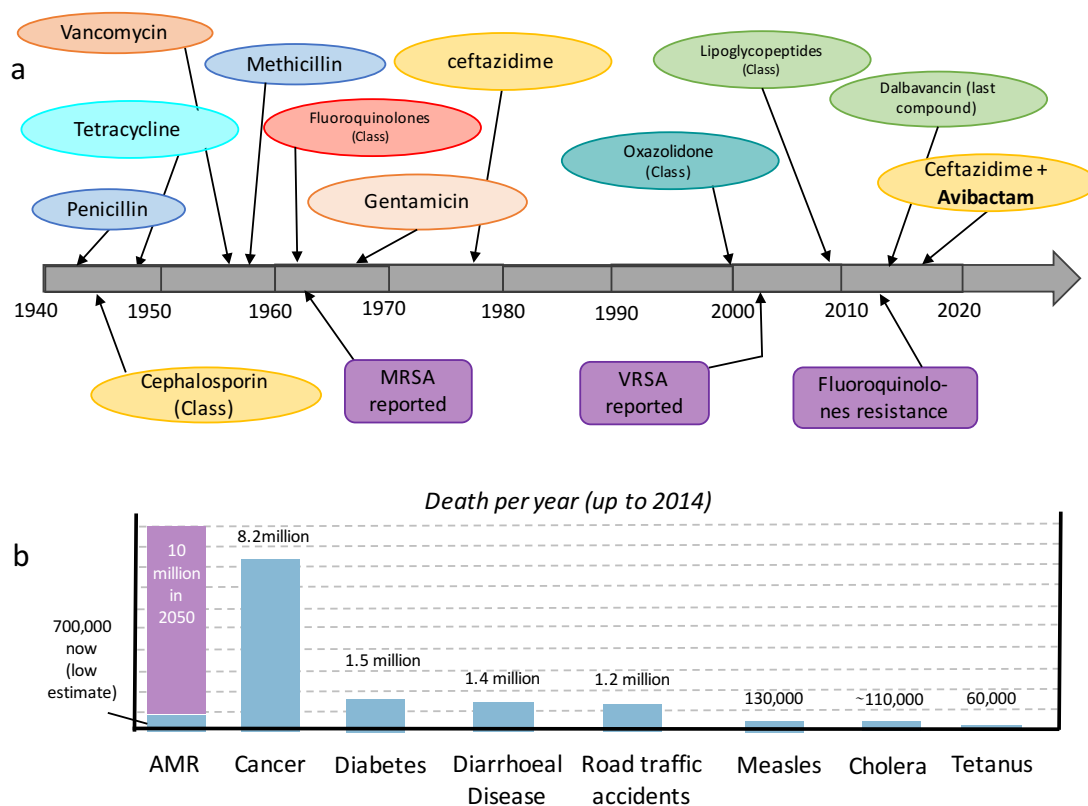


Figure 1.1 – a) Timeline of crucial antibiotic classes and compounds discoveries alongside the emergence of resistant strains; b) deaths attributable to AMR and other disease every year (up to 2014 in blue) prediction of deaths by AMR in 2050, inspired by [5].

According to the O’Neill review on antimicrobial resistance (data up to 2014), [5] about 700,000 people die every year from AMR strains of common microbial infections, such as *Escherichia coli* (*E. coli*), TB and malaria. In this review,[5] it was estimated that unless

action is taken, the number of deaths caused by AMR could rise to 10 million each year by 2050, surpassing even the rate of deaths by Cancer (see *Figure 1.1 b*). The absence of effective treatments against AMR has triggered a global action plan from the World Health Organisation focused both on the protection of current antimicrobials and research on this phenomenon. [7]

A key action to tackle the above problem would be to perform research focused on the development of new antimicrobial drugs or alternative treatments. One of the most common approaches in pharmaceutical industries is the mass screening of potential antimicrobials, most recently this has been assisted by artificial intelligence technology.[14] However there is still a lack of fundamental knowledge on the mechanism of action of current antibiotics, which have been identified because of their efficacy of killing bacteria. However, there is not a clear understanding about the underlying biological mechanism by which they ultimately kill bacteria. This thesis aims to deepen the mechanistic insight of antimicrobial activity on a non-resistant strain of *Staphylococcus aureus*.

1.2 *Staphylococcus aureus*

Bacterial cells can be classified in two major groups: Gram-positive and Gram-negative species.[1] This classification divides bacteria according to their cell envelope characteristics. The cell envelope of most bacteria is composed of the cell wall and the cell membranes. Gram-positive bacteria have a thick cell wall (CW) made of a complex three-dimensional network of peptidoglycan surrounding the most exterior part of the cell. Underneath the CW there is a lipid bilayer that encloses the cytoplasm inside.[1] By contrast, Gram-negative bacteria have two cell membranes and a thin layer of peptidoglycan in between. The Gram stain (invented by Hans Christian Gram) is a method that uses crystal violet to dye the CW. [15], [16] After dyeing the bacteria, there is an alcohol rinse which removes almost all the stain from Gram-negative bacteria while Gram-positive bacteria keep their purple colour from the crystal violet. This is because Gram-positive bacteria have a thicker CW than Gram-negative. Then, a pink counter stain is added (safranin or fuchsine) which mostly stains the Gram-negative with a pale pink colour. This method, has been used since 1884 to qualitatively classify bacterial species in these two groups. [17], [18]

S. aureus is a spherical shaped Gram-positive bacteria species from the *Staphylococcus* genus which is part of the *Bacilli* class. [1] In this thesis only Gram-positive bacteria will be studied, and the main focus of the work will be *S. aureus*. However another Gram-positive bacterial species will be studied in *Chapter 6*, the rod-shaped *Bacillus subtilis* (*B. subtilis*).

1.2.1 Clinical background

S. aureus is usually a commensal organism (non-pathogenic) but on some occasions can colonize the host causing infections. This type of bacteria are described as opportunistic bacteria. These non-pathogenic cells can be naturally found inside the nostrils, on the skin and intestinal tracts of humans and other animals. [1] The colonization process is complex and poorly understood. However, it has been shown that *S. aureus* can evade immune response from the host organism and has the ability to adhere to host cells or prostatic material and cause infections as dangerous as septicaemia. The worst possible scenario is when *S. aureus* forms biofilms or invades endothelial cells (*e.g.* endocarditis). [19] Other potential complications of *S. aureus* infections include: septic arthritis, septicaemia, prosthetic and catheter infections, invasive skin infections and necrotic pneumonia, tissue destruction, metastatic infections, food poisoning, toxic shocks and impetigo.[20] Only a small proportion of *S. aureus* infections lead to host death. The Office of National Statistics of England and Wales reported less than 500 deaths featuring the term *S. aureus* in the death certificate in 1993, with only 12% of those caused by MRSA.[21] However, in 2006 this number had raised to 2000 and almost 80% of the deaths were caused by MRSA strains. Since then, the number of deaths has reduced substantially. However, the last record in 2012 showed that 52% of the 557 deaths involving *S. aureus* were caused by an MRSA strain. [21]

MRSA strains are resistant to Methicillin and in some cases to other β -lactam derivatives such as Penicillin, Benzylpenicillin and Oxacillin.[22] These β -lactam antibiotics inhibit the synthesis of peptidoglycan which is the main component of the CW; the disruption of cell wall synthesis machinery ultimately leads to cell death.[1] However, as the CW components, its organization on the cell, its synthesis and function is not yet well understood [23], a countermeasure against MRSA is difficult to find. Therefore, this

project focuses on better understanding of certain aspects of the CW of Gram-positive bacteria to reduce the knowledge gap necessary to cure MRSA infections.[12], [13]

1.3 The cell wall architecture and function

Peptidoglycan (PG), is the main component of the cell wall for all species of bacteria. It is a macro-biopolymer surrounding the internal cytoplasmic membrane.[23] Its crucial functions range from: acting as a barrier between the internal contents of the cell and the outer environment;[24] maintaining cellular integrity and shape; withstanding osmotic pressure from inside the cell (*i.e.* turgor pressure ~ 25 atm) and for some species, local changes in the PG architecture controls the cell division cycle. [25] As mentioned above, PG is the target of a range of antibiotics such as β -lactams and glycopeptides. [7] Now that AMR is rising to critical levels, having a deeper understanding of PG is essential. So far, our understanding of PG ranges from the atomic chemical structure to the cellular level.[26]–[30] However, there is a gap of knowledge in the middle, which is the three-dimensional arrangement of the molecules forming this biopolymer and how they orient with respect to other components on the cell.

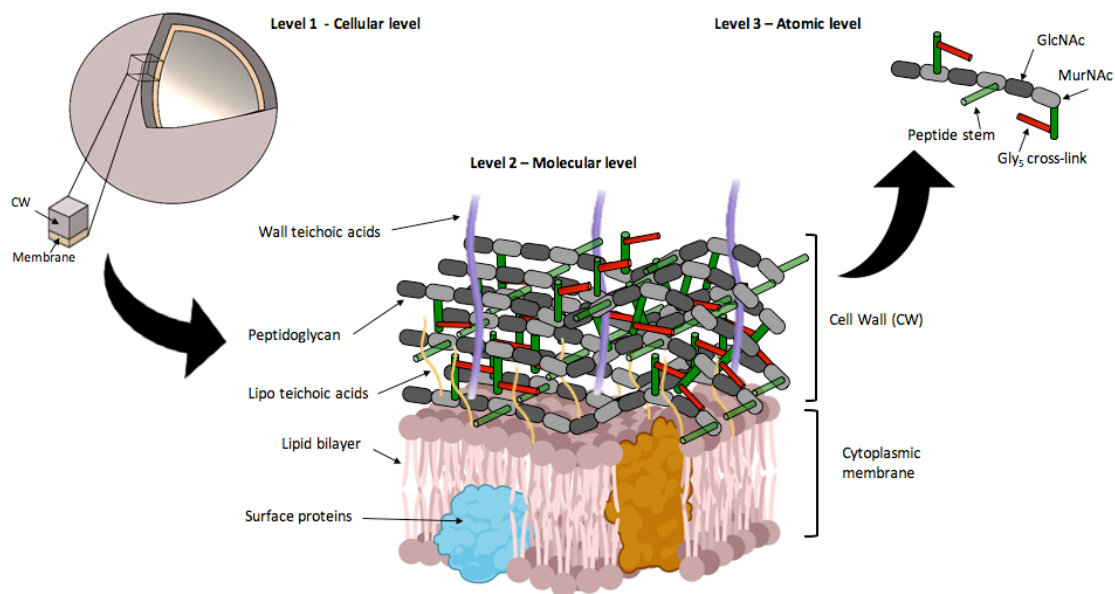


Figure 1.2 – Different levels of complexity of the PG cell wall - Level 1: cellular level of complexity; Level 2: Molecular level; Level 3: atomic level of complexity

Figure 1.2 shows a schematic of the different levels of complexity at which PG can be studied. There is currently experimental data supporting the cellular and atomic level but there is a lack of literature supporting the representation of the level in between, the molecular architecture. In all textbooks and illustrations about this topic, the

molecular architecture of PG in three-dimensions (3D) has always been based only on assumptions.[23] In this project, this level of complexity will be tackled, and solid experimental data will be provided to try to build a more realistic model of the bacterial cell wall.

1.3.1 Cell wall chemical structure

The chemical structure of peptidoglycan and teichoic acids vary among different species. Firstly, the Peptidoglycan chemical structure will be explained in detail before the other components of the cell wall, the Teichoic acids, are addressed.

PG is a biopolymer and its forming unit are the focus of all the structural chemical studies. The PG-repeat unit of *S. aureus* consists of a disaccharide backbone cross-linked by short peptides (stems).[24] The glycan backbone (glycan chain) is composed of repeating units of the disaccharide N-acetyl-glucosamine (NAG) and N-acetyl-muramic acid (NAM), with their residues linked by β -1 \rightarrow 4 bonds and together they are named (GlcNAc-MurNac). Each NAM has its D-lactoyl residue substituted by the peptide stem whose composition varies with each species of bacteria. [23] In this case the peptide stem is formed by the following amino-acids: L-Ala, D-iso Gln, L-Lys, D-Ala and D-Ala.[25] However, there is another layer of complexity. The PG network would not be able to withstand the turgor pressure without a certain percentage of these subunits cross-linked via a penta-glycine bridge (Gly)₅. Cross-links can be formed between the L-Lys from one peptide stem and the fourth amino-acid of another peptide stem (D-Ala), see *Figure 1.3*. The main experimental techniques used to determine this information are reverse-phase-high pressure liquid chromatography (HPLC) [26] and mass spectrometry.[31]

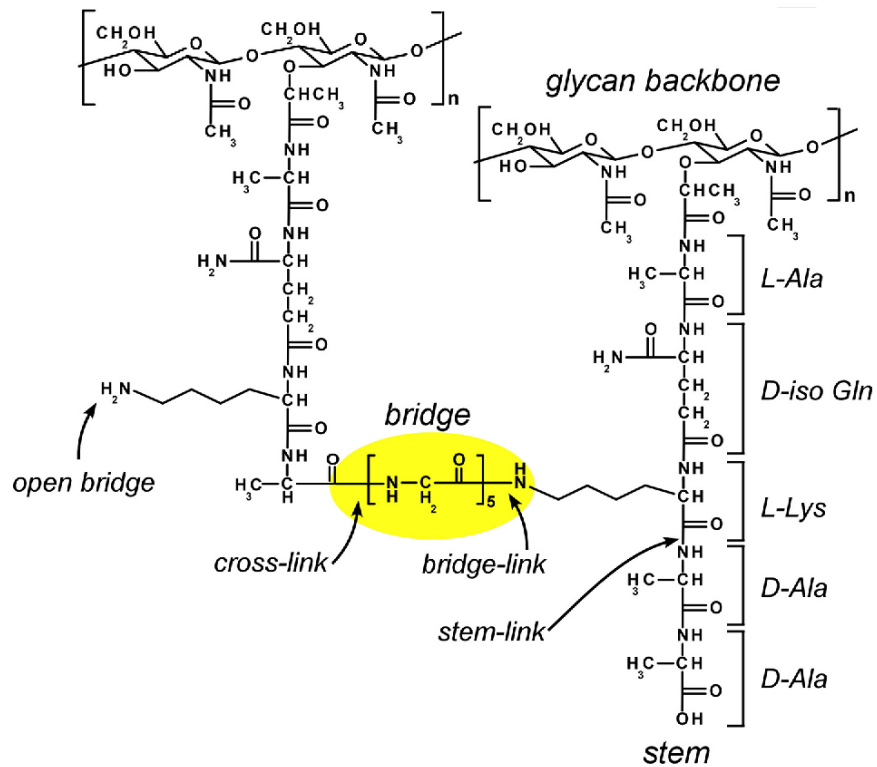


Figure 1.3– Chemical structure of the Peptidoglycan subunit from *S. aureus* with a cross-link between the 3rd and the 4th amino-acid of two peptide stems. Reproduced with permission from [27]

Another structural variation that can be found even within the same cell is the position of the cross-link bridge. The most dominant scenario is usually when the bridge is formed between the residue of the third amino-acid on one peptide stem and the carboxyl group of the fourth amino-acid (D-Ala) in the other peptide stem (see *Figure 1.4 a*). However, there is a less common scenario, in which the bridge is formed between the second amino-acid of one peptide stem and the D-Ala at position 4 of another. This later scenario would cause the two neighbouring glycan chains to be closer ($d' < d$) than in the first case (see *Figure 1.4 b*). These cross-linking reactions are catalysed by the transpeptidase domain of penicillin-binding proteins (see *section 1.3.3*). [26]

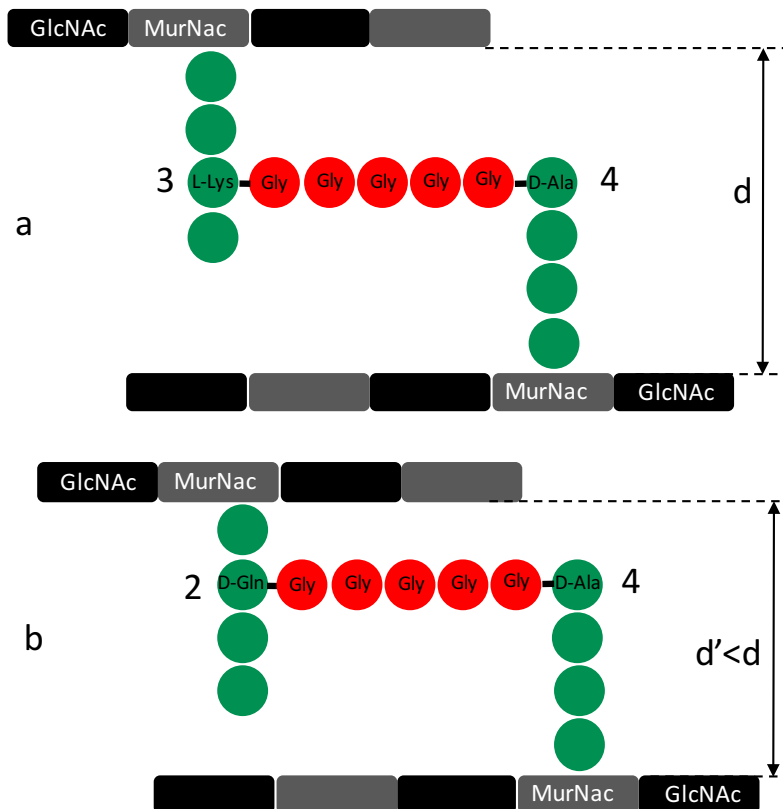


Figure 1.4– Representation of Peptidoglycan structure with: a) crosslink between amino-acid 3(L-Lys) and 4 (D-Ala); b) crosslink between amino-acid 2 (D-iso Gln) and 4 (D-Ala).

In conclusion, not only is there a huge variability of cross-linking between species (*E. coli* 20%, while *S. aureus* has 80%) but even within one individual bacterial cell there is an enormous variability from one glycan backbone to another. Therefore, the possibilities by which these building blocks could assemble in three-dimensions are almost endless.[25]

1.3.1.1 Wall teichoic acids

The second major component of the CW after PG is the Wall Teichoic Acids (WTA). The term teichoic acids (TA) was first mentioned in 1960,[32] and its name originates from the Greek word *teichos*, which means 'wall'. Later, all the molecules considered to be part of the TA group were differentiated into two subgroups according to their location in the CW. Here, the WTA are the focus. They are not attached to the lipid membrane, only anchored to the peptidoglycan where they extend further into the extracellular environment.[33]

The chemical structure of WTA is composed of two main sections: the linkage unit which is covalently anchored to the peptidoglycan and the anionic glycopolymer chain. The

linkage unit binds to the PG at the C6 hydroxyl of the NAM from the glycan backbone. The glycopolymer consists of approximately 40-repeat units of ribitol-phosphate (Rbo-P) with variable radicals depending on the bacterial species.[34] The WTA structure for *S. aureus* is shown in *Figure 1.5*.

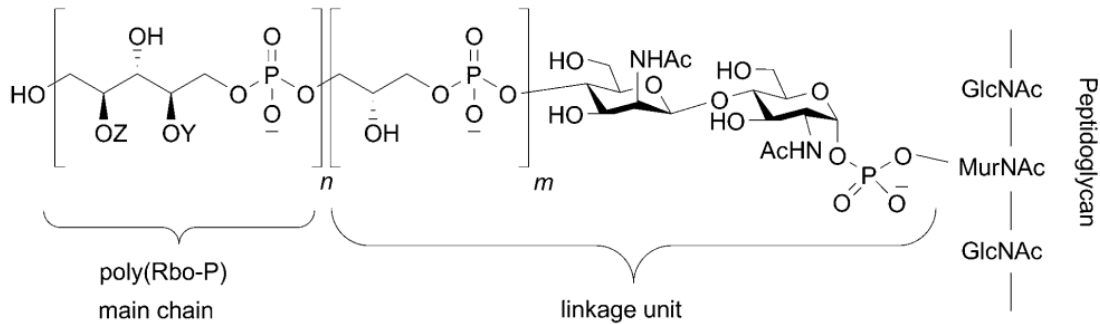


Figure 1.5 - Chemical structure of Wall Teichoic Acids from S. aureus. Reproduced with permission from [5]

Figure 1.5 shows the peptidoglycan backbone on the right, then the linkage unit and the main chain of WTA towards the left. The repeating units are $n \sim 40$ and $m \sim 2$; the residues in *S. aureus* vary between $Y = \alpha$ or β GlcNAc and $Z =$ D-ala or H. It is believed that each cell has a distribution of these residues.[35] This might be relevant because altering these residues could alter the WTA function and location, however it is still unknown. [34]

Despite the well-established chemical structure, the architecture of WTA and how they organize within the CW is unknown. There are only a few studies about the localization of these molecules across the different parts of the cell, for example a lectin named Con A has been used as a label for WTA.[36] The main challenge to achieve an accurate localization is the lack of specificity of this biopolymer and its high resemblance to PG and the other type of TA, the lipo teichoic acids (LTA). [33]

The role of WTA in the cell is not fully understood. There are speculations about its importance in controlling cell division, defining the nanomechanical properties of the CW and playing a role in infections during the pathogen-host interaction. [34]

1.3.1.2 Lipo teichoic acids

The lipo teichoic acids (LTA) acquired their name because they are anchored to the lipid membrane of the cell. Then, they extend up to the internal surface of the PG covering

the periplasmic space. In Gram-positive bacteria this is sometimes referred to as the inner cell wall zone. [33], [37]

Since their discovery, [38] it has been hypothesized that they play a crucial role in preventing the periplasmic space from collapsing onto the membrane.[37] Moreover, LTA play an important role in bacterial growth and physiology. It has recently been proposed to use LTA as vaccine candidates and LTA synthesis enzymes as novel antimicrobial targets.[33]

1.3.2 Peptidoglycan architecture (scaffold vs layered)

Although the chemical structure of the CW is well known, its physical structure is not. As mentioned above, the focus of this work will be on the PG macromolecule architecture. Huge controversy revolves around how PG assembles within the CW into a three-dimensional (3D) structure in Gram-positive bacteria. Studying the PG molecular architecture is challenging because PG is an insoluble, complex and heterogeneous supra-molecule incompatible with the conventional structural approaches.[27]

Despite the difficulties in this field, breakthroughs in structural understanding of PG have been underpinned by advances in experimentations such as HPLC,[26] nuclear magnetic resonance (NMR)[27] and direct imaging techniques.[25] The technique of solid-state NMR gives the unique ability to provide an average of the PG 3D architecture at angstrom resolution for bacteria, such as Gram-positive *S. aureus*.[28] The outcome of this NMR experiment was to quantify the distance between anomeric carbons from the glycan chains (GlcNAc-MurNac) to Gly forming the cross-linking bridge. This distance had been calculated to be larger than 10 Å on average. However, it was shown to be 5 Å, meaning the carbon and Gly responsible for the NMR signal must correspond to different PG-repeat units (see yellow areas in *Figure 1.6 a*). The lattice structure of PG-chains was also corroborated by other NMR experiments, this time using intact *S. aureus* cells.[39] On this occasion, they measured the distance between the first and fourth amino-acids (D-[1-¹³C] Ala and L-[¹⁵N] Ala). Results showed a separation of only 4.4 Å instead of the theoretical 8.8 Å, again supporting the lattice model previously published (see blue areas in *Figure 1.6 a*).[39]

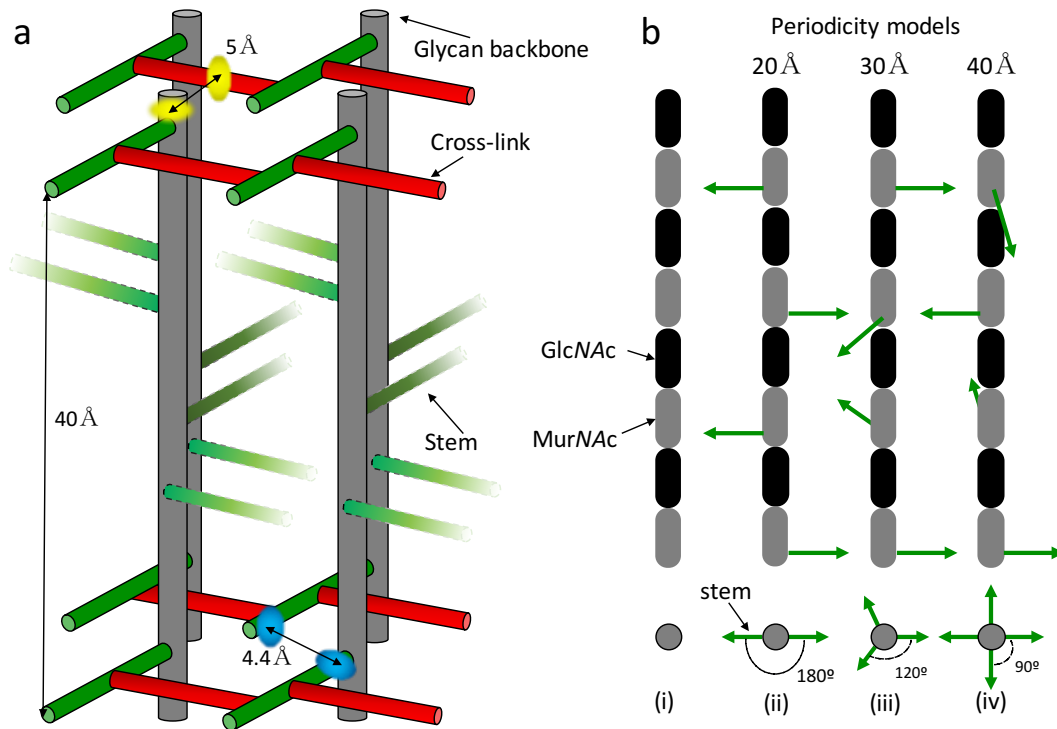


Figure 1.6 – a) Peptidoglycan architecture of helical 4-fold axial symmetry with parallel PG stems and four neighbouring backbones (grey); b) Schematic representation of different backbone conformations, the configurations represent different degrees of rotation from the previous stem with (i) no stem, (ii) 180°, (iii) 120° and (iv) 90° rotation. Inspired by [27]

The spacings determined from the NMR experiments can only be explained if the PG glycan backbone in *S. aureus* is formed by a parallel-stem architecture, of 90° helical twist with a periodicity of 40 Å (see case iv in Figure 1.6 b).[27] By contrast, other experiments measured a periodicity between the PG-bridges of 30 Å (see case iii in Figure 1.6 b), which suggests an alternative three-dimensional PG-lattice named tertiary architecture.[28], [40] However, the consensus is that PG glycan chains in *S. aureus* are highly ordered and densely packed with neighbouring glycan chains.[27]

A more controversial aspect related to the structure of the PG is the orientation and distribution of the glycan strands with respect the lipid membrane.[24] From assumptions based on chemical composition of PG two theoretical models have been proposed: the layered and scaffold models.[25] In the classical layered model PG chains are synthesized parallel to the membrane (see section 1.3.3.1), [24] whereas in the most recent scaffold model PG chains are aligned perpendicular to the membrane (Figure 1.7). [41], [42]

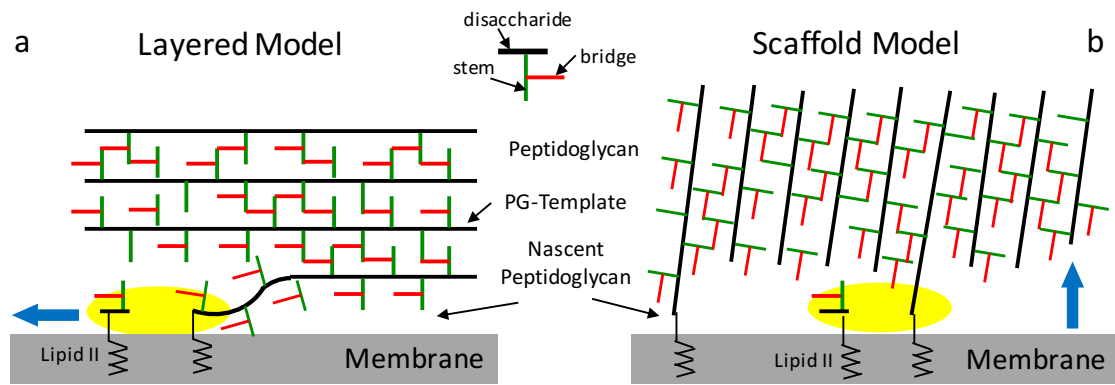


Figure 1.7 – Left) The layered model with glycan chains orientated parallel to the membrane. Right) The scaffold model with glycan chains orientated perpendicular to the membrane. Inspired by [27]

The most intuitive approach to decide which model is valid is to correlate the thickness of the cell wall with the average length of the glycan chains. In order to measure the glycan chain length (GCL), the most widely accepted technique in the literature is by HPLC. This technique separates different polysaccharides species of different sizes, which contain a certain number of disaccharide units (DU).[26] HPLC averages the values from the purified PG of a cell population. For the Gram-negative *E. coli*, the average GCL ranges between 18 and 60 DU.[31] If the PG is organised according to the scaffold model, this would lead to a CW exceeding 25 nm. This hypothetical CW thickness has been shown to be wrong, thanks to thickness measurements using cryo-transmission electron microscopy (cryo-TEM)[43] and Atomic Force Microscopy (AFM)[44], where *E. coli* CW was between 3 nm and 7 nm thick. By contrast, in *S. aureus*, shorter strands were found with an average GCL of 6 DU.[31] *S. aureus* has a CW thickness between 20 and 40 nm, as measured by cryo-TEM [45] and AFM [46], which could favour the scaffold model. Moreover, due to the short glycan chains and a high level of cross-linking (80%) the CW would be structurally resistant to mechanical stress caused by the turgor pressure.[27] In the case of the Gram-positive rod shape bacteria *B. subtilis*, the glycan strands were too long to be resolved by HPLC (due to limitations of the technique). Therefore, AFM was used to analyse isolated strands, which gave a value of GCL up to 5000 DU (corresponding to approximately 5 μm).[47] Similarly to *E. coli*, due to this high DU number, the scaffold model does not support the existence of a thinner CW for *B. subtilis* of 10-20 nm (measured by cryo-TEM[48] and AFM[49]).

To elucidate some further quantitative data on this controversy, other studies[50], [51] used solid-state NMR (REDOR) to determine the orientation of newly synthesized glycan chains in *S. aureus*. The authors prepared protoplast, by removing all the older PG material to study the biosynthesis of new PG material. [51] Measuring the signal from ^{13}C on the glycan backbone, most of it was located near the membrane, meaning the biosynthesis of new PG was parallel to the membrane. In conclusion, these results supported the layered model. [27]

Despite all experimental results supporting or refuting the theoretical models, there is a common weakness for both models, which is the requirement for a high degree of order and periodicity.[52] All models suggest that PG structure is composed of ordered and identical arrays of glycan strands, peptide stems and cross-links (PG-bridges).[24] However, the evidence provided by direct imaging methods such as scanning electron microscopy (SEM) and AFM show the opposite: the PG architecture in *S. aureus* is heterogeneous throughout the cell-cycle with two main architectures: mature mesh and nascent rings.[46], [53] Therefore, there is a need for a more heterogeneous model rather than the current static homogeneous models.

Peptidoglycan chemistry and architecture encloses a huge diversity among species and mutations. For this reason, it is crucial to be aware of the dangers of over-generalizing a unique model for all the species.[23] Building a new model for Gram-positive bacteria that unifies all the available data is key for a greater understanding of PG structure and its biosynthesis pathways.

1.3.3 Cell wall synthesis, hydrolysis and cell division

The most important function of CW, is the viability of the cell. If the CW is damaged or has defects it can lead to cell death. For this reason, understanding the enzymes involved in CW synthesis and remodelling is very important.

1.3.3.1 Synthesis

The antibiotics used in this thesis (see *chapter 7*), target the PG synthesis. Although LTA and WTA synthesis mechanisms are also important, they are not the target of this study, so only the PG synthesis will be the focus. The PG synthesis is summarized in the *Figure*

1.8. The four main stages of peptidoglycan synthesis are: precursor synthesis, assembly of the lipid II, flipping of lipid II across the membrane and PG polymerisation. [54]

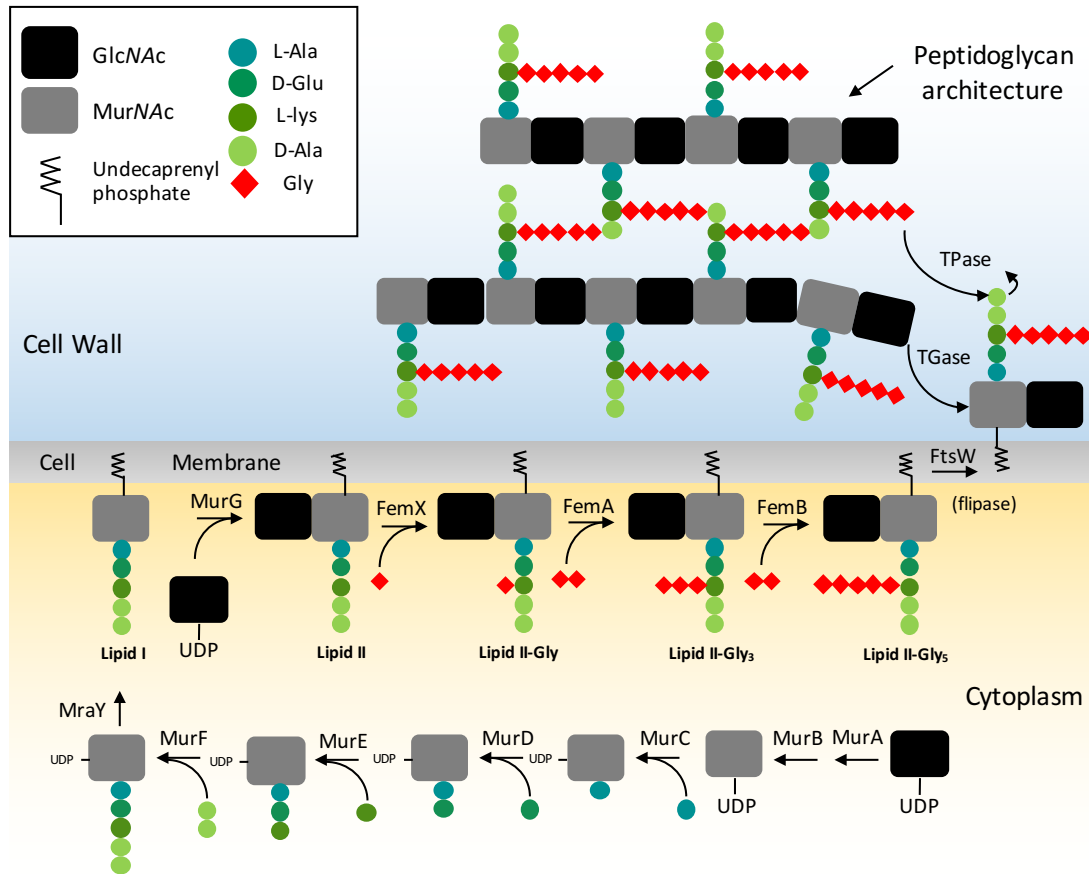


Figure 1.8 – Peptidoglycan synthesis in *S. aureus* from UDP, to lipid II precursor, to the assembly of the CW by transglycosylase (TGase) and transpeptidase (TPase) enzymes. Inspired by [54]

The precursor synthesis stage happens at the cytoplasm. MurNAc, one of the main sugars forming the glycan chains of the PG, is assembled with the first amino-acid of the peptide stem, a reaction that is catalysed by Mur ligases. Other ligases attach the rest of the amino-acids to the peptide stem. The final two D-Ala units are added together as a dipeptide, catalysed by MurF. [55] Next the intermediate moiety uridine diphosphate (UDP)-MurNac-peptide stem is transferred onto a carrier called undecaprenyl phosphate (Und-P) which is anchored to the membrane. [54] The final product is called lipid II. At this stage lipid II is located at the internal side of the lipid membrane, then it needs to be flipped to be able to continue the process of PG synthesis.[54] An enzyme called flipase is required for this step, however there is no specific enzyme known to perform this. FtsW [56] or MurJ [57] are two putative candidates to be flipases, but more studies are required in this area to provide solid evidence. Once the lipid II, which is a

hydrophilic moiety, has crossed the highly hydrophobic lipid membrane, the polymerisation of glycan strands starts. [58] This is by associating the MurNac from one lipid II to the GlucNac group of another lipid II, leaving an Und-P free to be recycled again, this transglycosylation reaction is catalysed by transglycosylases. [59] Other enzymes cross-link the neighbouring stem peptides by covalently bonding for example, the residue of the 4th amino-acid to the residue of the 3rd amino-acid via the pentaglycine bridge. This reaction is called transpeptidation and is catalysed by transpeptidases. [55]

In *S. aureus*, Penicillin Binding Proteins (PBPs) are the main synthesis machinery which carry out the peptidoglycan polymerisation. PBP2 is a bifunctional enzyme acting as a transglycosylase and a transpeptidase. Other enzymes of the same family are PBP1 and PBP 3 which are only transpeptidases. Finally, PBP4 is able to recognize the C-terminal of stem peptides (D-Ala-D-Ala), it is bifunctional with both DD-carboxypeptidase and transpeptidase activity. [32], [60], [61] The activity relevant to PG biosynthesis is its ability to catalyse the cross-linking between two peptide stems (see non-essential mutants of *pbp3* and *pbp4* in *Chapter 5*). This family of proteins gained their name because β -lactam antibiotics are PBP substrate analogues by mimicking the D-Ala-D-Ala dipeptide. These antibiotics inhibit PBPs functionality by acylating their active domain. PBP1 and PBP2 are essential for the cell, if either of them cannot function properly the cell dies There are also several enzymes acting only as transglycosylases aside from the PBPs family: Mgt, SgtA and FtsW. [62][63]

1.3.3.2 Hydrolysis

PG hydrolysis plays a role in important processes such as cellular division, cell growth and sporulation in some species such as *B. subtilis*. [64] It has been shown that strains lacking one or more hydrolases are not viable. [65]

All the main bonds described above (see *section 1.3.3.1*) can be cleaved by a specific type of hydrolase. There are four types presented in *Table 1.1*.

Table 1.1 – Types of hydrolase, with their complete name, short name and function in *S. aureus*.

COMPLETE NAME	SHORT NAME	FUNCTION
Acetylmuramyl-l-alanine amidase	Amidase	Separates the glycan backbone and uncross-linked peptides, by the amide bond
Carboxyl- and endopeptidase	Peptidase	Cleaves bonds between DD- and LD- of the peptide
L-acetylglucosaminidases	Glucosaminidases	Cleaves the link between two disaccharide MurNac-GlcNac
N-acetyl- β -d-muramidases	Muramidases	Cleaves the 1,4- β linkages between MurNac and GlcNac from each disaccharide

Hydrolases are of such importance that there are several enzymes with overlapping functions. When one non-essential hydrolase is lacking for some reason, there is an overproduction of others. There is also a huge variety between species, but all bacteria would have some hydrolases for each of these types. *S. aureus* has a total of 19 known putative hydrolases. There are four glucosaminidases which as a group are essential for survival: SagA, SagB, ScaH and Atl.[65] However, the role of most of the remaining hydrolases is still unknown and require future study. Atl is one of the best characterized hydrolases from *S. aureus*,[65]–[67]. It has been shown, that there is a correlation between the localization of Atl and WTA, as mentioned above. [68]

The hydrolases are not only essential for cell division, but also for the normal transformation from nascent peptidoglycan to mature peptidoglycan as the cell cycle progresses. It has been shown that the CW after division (nascent material) is stiffer than the older parts of the cell. Glucosaminidases, cut long glycan chains into shorter strands, allowing the CW to be softer and expand to prepare for the next division cycle. The most important glycosaminidase in this process is SagB, because lack of this enzyme results in stiffer cells which are not able to grow as well as the WT. [65]

1.3.3.3 Cell division

The division mechanism is a very complex and variable process throughout different species. Most bacteria divide by binary transverse fission. [69] However, there is a big difference between *rod* and *cocci*-shaped bacteria. The *rod*-shape bacteria have a division machinery composed of several enzymes (*i.e.* the divisome) together with an

elongation mechanism that allows them to grow in length before division (*i.e.* the elangosome). In contrast, *cocci*-shaped bacteria only have the divisome, after division there are several enzymes that reorganize the nascent CW to allow the cell to achieve the appropriate volume by having a more spherical shape. Other bacterial species with alternative shapes such as oval or spiral have vastly different division mechanisms which are beyond the scope of this work. Here, only the division mechanism of *S. aureus* will be explained.

The septum is the area where the new cell wall is mostly synthesised before the cell splits and divide into two daughter cells. The peripheral ring,[70] also named Piecrust, is the initial stage of septal formation that will guide the rest of the synthesis (see *Figure 1.9*).

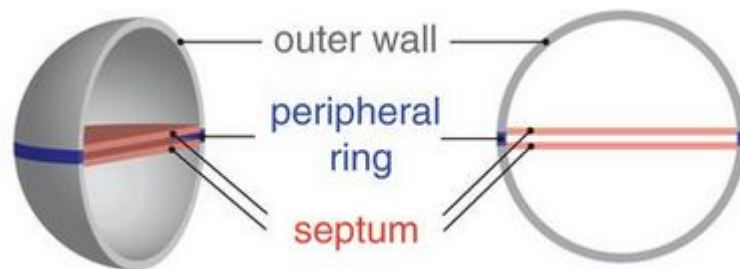


Figure 1.9 – Different parts of the cell wall: the outer wall that forms the major area of the cell (grey), the peripheral ring (blue), and the new PG formed at the septum (red). Reproduced with permission from [70]

The divisome is a large collection of proteins that localise at the division site (on the septum area). Some of the components have been identified in many organisms. However, each of their precise roles are not fully understood. The divisome can be divided into the group of enzymes that synthesise the new PG (the most important ones being the PBPs, see *section 1.3.3.1*); the second group of enzymes coordinate the activity of the first ones, and guides them through the Z-ring which is formed by the most important enzyme of the divisome, FtsZ.[71] The assembly of the Z-ring, which is regulated by EzrA,[72] acts as a scaffold for the rest of the divisome proteins to synthesise new PG on the septal plate. [73]–[76]

Using single molecule localization fluorescence microscopy the different stages of septation in *S. aureus* have been shown by mapping the PG newly incorporated and the location of FtsZ and EzrA. [77] It was observed before, that the leading edge. [78] of the septal plate does not have a uniform thickness. It forms a more triangular shape from a

cross-section point of view (see *Figure 1.10 iii*). However, this was never previously understood, until this study, where they explained that given the limited available surface area of the triangular leading edge, the synthesis of new PG occurs everywhere else on the septal plate, given that FtsZ and EzrA do not show a localization on the leading edge.[77] Once the septal plate has been completed, the machinery finishes synthesis so that all the septal plate acquires the same thickness, finally the piecrust is hydrolysed and the cell splits into two daughter cells. The splitting happens in only a few microseconds. [70] However, the whole process of cell division takes between 20-30 min. Contrary to previous models,[72], [79]–[82] the main focus of PG incorporation is not the leading edge of the septal plate but throughout the septum and during the rest of the cell cycle. [77]

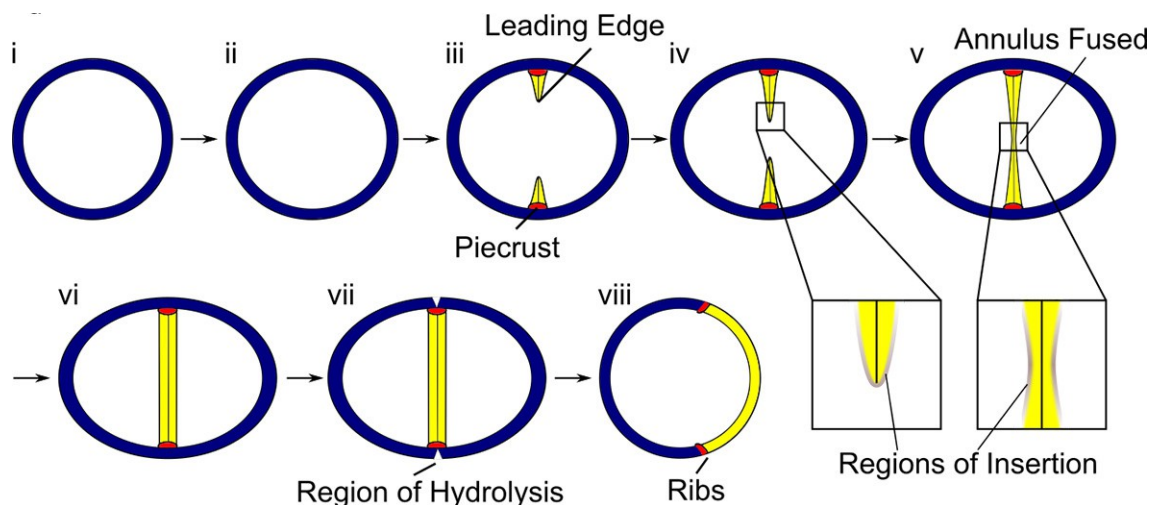


Figure 1.10 – (i, ii) Cell size increase before septum formation begins; (iii) Septum formation begins at the piecrust; (iv)The septum is thinnest at the leading edge; (v) Annulus fuses; (vi) Synthesis continues to complete a septal plate of homogenous thickness; (vii) mechanical crack; (viii)cell division. Reproduced with permission from [77]

Another important question is where does *S. aureus* place its septal plate? This is a complex mechanism because division is occurring in consecutive orthogonal planes from the previous division.[46] The peptidoglycan architecture forming the previous piecrust still remains on the daughter cells after division. These features, called ribs, mark the division planes depending on the age of the previous division. The place where two former ribs collide is called a T-junction (*Figure 1.11*). The division machinery start forming the septum perpendicular to the rib from the last division. [46]

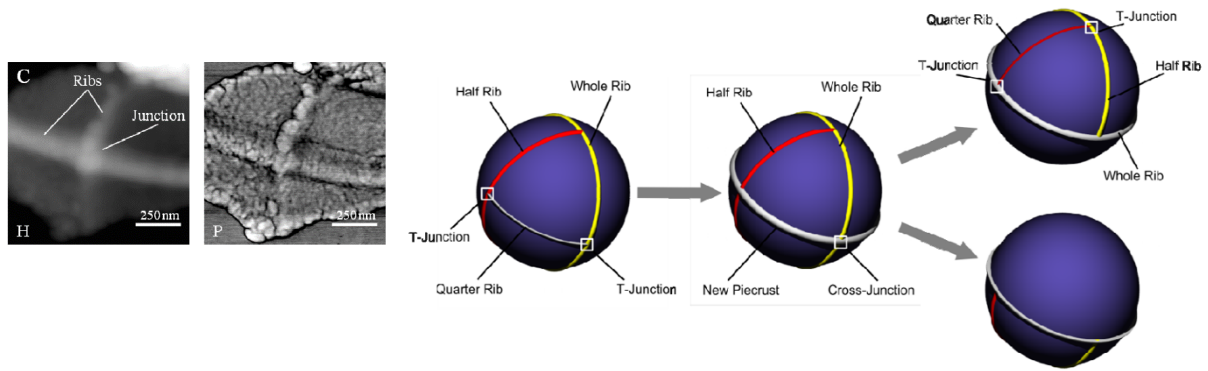


Figure 1.11 – Structural inheritance of division plane, peptidoglycan features such as ribs and junctions are used by *S. aureus* to guide next placement of the septal plate, perpendicular to the previous rib. Adapted with permission from [46]

This discovery that the placement of the division planes was guided by the peptidoglycan architecture forming the piecrust and its remnants was made using a direct imaging technique, AFM [46]. In this previous work, purified PG was imaged in a dried environment which allowed the piecrust, ribs and junctions to be clearly studied. Moreover, information was gained about the two distinguishable external architectures: the mature knobbls and the nascent rings (see section 3.2).

There is a lot of information about the biological mechanism that governs *S. aureus* division mechanisms and most recently, the first hints about the septum morphology and location have been determined. However, there is no experimental data regarding the peptidoglycan architecture at the region of the septum. It is unknown whether the septal PG architecture differs from other regions of the cell.

1.3.4 Cell wall function and target for main antibiotics

Throughout this section the importance of the CW for cell survival has been clear. Specifically the PG layer, which has unique biophysical properties that make it such a crucial biopolymer for bacterial cells. The most important function of PG is its barrier behaviour between the cytoplasm and the environment, preventing turgor pressure to lyse the cell. Controversially, it also acts as a permeable layer that allows interchange of nutrients and small molecules between the cell and its environment. These two functions seem to be antagonistic with each other. However, the unique chemical structure and the molecular organization of the PG components in the CW allows this

layer to be unbreakable by the turgor pressure and at the same time porous enough to allow an extracellular connection to the environment. [24]

The PG layer possesses the required thickness to hold the turgor pressure for each bacterial species. For example, for the rod-shaped *B. subtilis* the thickness is 10-20 nm (measured by cryo-TEM [48] and AFM [49]) for an indirectly measured turgor pressure of 20 atm. [83] Meanwhile, for *S. aureus* the CW is thicker with 20-40 nm (measured by cryo-TEM and AFM) for a higher turgor pressure of 20-25 atm. Turgor pressure from *S. aureus* was measured by a different method,[84] which is even more indirect than the used in *B. subtilis*. [83] However, even a small increase in turgor pressure implies a great difference in CW thickness of about 10-20 nm, which could indicate a strong relationship between thickness and strength.

Another interesting property of the CW is its elastic capabilities. In the *rod-shaped (E. coli)*, the Young's Modulus was used as a measure of its elasticity upon deformation. Lower values of Young's Modulus have been shown to exist in the direction of the long axis relative to the short axis. This finding portrays anisotropy in elasticity of the PG layer. [44], [85] Recent studies have shown a correlation between this anisotropy and PG structure in *E. coli*. [86]

Regarding the role of PG as a diffusion barrier, it has been suggested in a few studies that molecules could be accessing the cell through large pores, with diameters of 50-60 nm on *S. aureus*,[87] which have been observed by AFM. In contrast, Demchick and Koch [88] stained purified PG with fluorescence-label dextrans of different sizes to determine the average pore size of the PG mesh network with 2.06 nm diameter in *E. coli* and 2.12 in *B. subtilis*. The authors estimated the molecular weight of uncharged proteins able to penetrate the CW, which was found as approximately 22-50 kDa, if the PG layer was stretched. [88] Currently, in the field, there is no consensus about the three-dimensional architecture of the PG layer from different bacterial species. However, it is clear from these early studies that studying the porosity of this material and its function is biologically relevant.

PG is a very common target for several antibiotic classes because this biomolecule and its enzymatic machinery are not present in mammalian cells, allowing for very specific

recognition of bacterial infections inside a host. Having a better understanding of peptidoglycan would bring us one step closer to defeating AMR.

A combination of three main microscopy techniques has been used in the past to study the structure and properties of the cell wall: super-resolution fluorescence microscopy, electron microscopy (including TEM, SEM and cryo-EM) and finally, AFM. These three techniques each have strengths and weaknesses. The main problem with super-resolution fluorescence microscopy is the size of fluorescent probes (usually ranging 10-15 nm) attached to target molecules. [89] Even for state-of-the-art techniques (*e.g.* STORM) and instruments their resolution still cannot go beyond 10 nm under most of the experimental conditions used to study biological samples.[90] On the other hand, the EM microscopy family is not applicable to living cells due to its high-energy transfer to the sample. In terms of resolution, EM can achieve resolution of a few angstroms in certain samples.[91] However, when dealing with a disordered, insoluble macromolecule such as peptidoglycan, there is a lack of contrast on the images due to the low signal-to-noise ratio.[92][93] Therefore, AFM is the only of these three microscopy techniques that can directly image both live and dead cells in liquid environment with resolutions on the order of a few nm.

1.4 Atomic Force Microscopy

Atomic Force Microscopy (AFM) is the most versatile type of scanning probe microscopy (SPM). SPMs were invented by Binnig and Rohrer in 1980.[94] Later in 1986, AFM technology was patented by Gerd Binnig, although Quate and Gerber were also involved in their discovery.[95] All SPM techniques are based on building an image of a nanometric sample by sensing the interactions between the sample and a needle with a tip radius of the size of the features in the sample. This type of microscopy does not involve the use of light or electrons, it is purely a physical technique based on force sensing. The first SPM technique ever invented was called Scanning Tunnelling microscopy (STM) [94] which was based on the quantum mechanics tunnelling effect, by reading the electronic interaction between a conductive sample and the final atom of the STM tip. This atomic resolution technique has a major downside: it is only useful to study conductive samples. Therefore, the AFM was invented as a non-charged version of the STM, and the working mechanism had to be modified. Being a relatively young

technique, compared to the other major microscopy techniques, the working principle of AFM is still under development nowadays, with improvements in acquisition time and force sensitivity. AFM is still being tailored towards specific applications. Here, only commercially available AFM equipment has been used, as such this Thesis does not focus on improving AFM instrumentation. [95]

The main strength of AFM with respect to other microscopy techniques is the possibility to image biological samples in their native environment without damaging them; together with the ability to image a huge range of sample dimensions, from single atoms and single molecules to whole cells. In terms of resolution, in normal conditions, AFM can achieve lateral resolution in the order tens of nanometres (well below the optical diffraction limit encountered in light microscopy).[96] For example, AFM has been extensively used in the biophysics field to study Deoxyribonucleic acid (DNA) [97] and resolve complex protein structure.[98] AFM has also been used in extreme conditions, under very low temperatures and vacuum, to resolve the atomic organization of small molecules (such as phenyl rings,[99] vanadyl-phthalocyanine chemical reactions [100]). It is incredible to think that just 50 years ago, the famous physicist Richard Feynman said “There is plenty of room at the bottom...”[101] meaning that the step forward for technology was atomic manipulation (or bottom-up).[102] Now, this is a reality, as real atomic manipulation has been performed using STM [103] and AFM.[104] This shows the huge versatility of this technique and its multiple applications. Force spectroscopy is another branch of AFM research that focuses on studying the nanomechanical properties of the samples.[105] It does this by applying controlled force with the AFM tip and sensing the material response. In conclusion, AFM is an efficient tool to study biological samples because of the possibility of working under physiological environment, it does not deform or affect the sample (if operated by an experienced user), it is label free and allows for nanomechanical manipulation.[106], [107]The type of samples that can be studied with AFM are no longer limited to conductive samples, as they were with the STM. AFM can image samples with sizes ranging from atoms,[108] small molecules,[109] individual proteins,[98] whole bacterial[110] and eukaryotic cells,[111] all the way to plants[112] and bulk materials. [113]

1.4.1 Atomic force microscopy working principle

The principle of AFM is based on the mechanical interaction between a nanometric sharp tip attached to a flexible cantilever (AFM probe) and the surface of the sample (see *Figure 1.12*). Sometimes, this microscope is considered to be inspired by Braille writing, because when an object cannot be seen by light, its dimensions and properties can still be characterized using the sense of touch.[114] The development of nanofabrication lead to the creation of AFM tips small enough (a few nanometres) to interact with nanometric objects.

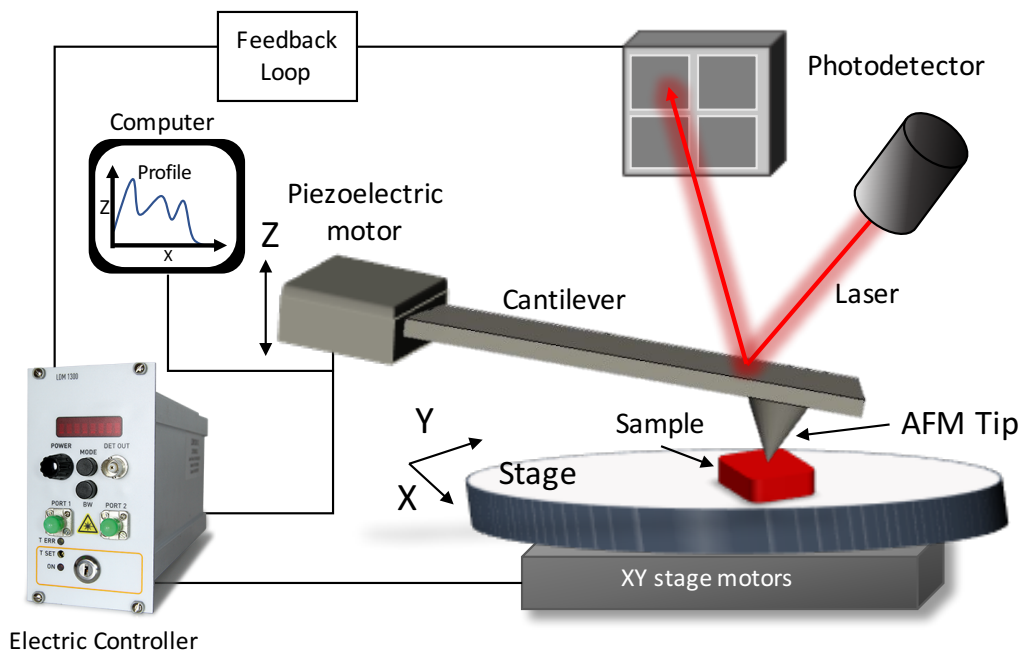


Figure 1.12 – Scheme of the main components of an AFM set-up: cantilever with the AFM tip at the end, sample to scan on the stage (controlled by the XY stage motors), laser shines on photodetector, sends signal to the feedback loop and the electric controller moves the piezoelectric motor, which produces the profile visualized on a computer.

Generally, the AFM consists of four main components: an AFM probe; piezoelectric[115] motors which control the movements in X, Y and Z directions; an optical sensing system with a monitoring laser, a photodetector,[116] and a feedback loop; and finally, a computer to control and display the results. When the AFM tip, attached at the free end of the cantilever, approaches the surface, it is affected by different interaction forces with the surface of the sample (van der Waals and electrostatic forces, see *section 1.4.2* below). These interactions with the surface cause the whole cantilever to bend. This bending, also known as deflection, is detected by the laser beam, which reflects on the back of the cantilever and is collected on a photodetector (see *Figure 1.12*). The position sensitive photodetector sends a current to the computer indicating the intensity and location of the laser spot. The feedback system is an electronic circuit that modifies the

vertical position (Z) of the cantilever to move following the topography of the surface. This is achieved by comparing the detected value of deflection to a constant value controlled by the AFM user (the setpoint).[117] Finally, a topographic image of a given sample is obtained by plotting the vertical modifications (Z) of the cantilever at each pixel, by scanning over the sample surface (in X and Y directions) building all the image pixels together line by line. Sample features will cause the cantilever to deflect and the vertical movement of the cantilever will mimic the height of those features. This topographic, or also called height, image represents the three-dimensional profile of the sample surface.[118]

In this thesis, only the imaging capabilities of the AFM will be explored, and no experiments were performed to study the nanomechanical properties of the samples in this work. Therefore, only the imaging working principle is tackled here.

1.4.2 Surface interactions

The AFM cantilever bends when approaching the sample surface due to a combination of different interaction forces with the tip. The different types of interaction forces will be explained in more detail, these are crucial to understanding AFM operability in its different imaging modes, and also provide accurate image interpretation and sample preparation.

1.4.2.1 Origin of short-range and long-range forces

It is well-established that our universe is governed by four distinct forces. The *strong* and *weak* interactions are the two forces that act between elementary particles such as neutrons, protons and electrons. The first attempt at identifying intermolecular forces was in 1873, when the physicist J.D van der Waals considered the effect of attractive forces between molecules. Later on, these intermolecular forces would be known as *van der Waals* forces. In parallel, the development of quantum mechanics lead to a unifying theory, the Schrödinger equation, which could be used to explain the interaction between molecules. But, it is virtually impossible to solve for complex systems of individual atoms, let alone macromolecules.

This lead to independent disciplines solving these problems using different approximations. Since the discoveries were made by different disciplines, new

nomenclature was used that essentially meant the same across disciplines, leading to huge confusion in the field of intermolecular forces. For example, in chemistry and biology the focus is placed on *short-range* force fields around atoms and molecules (usually only accounting for one or two atomic distances). Within this term of *short-range* forces, differentiation for specific cases has led to terms such as molecular packing, specific binding sites, lock and key mechanisms, etc. In the field of soft matter and colloidal science usually the emphasis is on the *long-range* forces which include terms like double-layer forces, van der Waals, steric polymer interactions, etc. In these regimes, the *short-range* forces are usually negligible. Currently, the old barriers between certain areas such as physics, chemistry and biology are increasingly disappearing as advances in nanotechnology arise. In the near future, science will present us with problems where these old disciplines cannot work independently. [119]

In the AFM community, the term *short-range* forces refers to the van der Waals interactions with a range between the 0.2 to 10 nm. Meanwhile, *long-range* forces refer to the electrostatic double-layer forces which have a range on the order of 10s of nm to 100s of nm. Finally, when the *contact repulsive* forces (below 0.2 nm) are mentioned this term includes interactions such as: Coulomb potential, hydrogen bonds, and atomic orbitals overlapping. [118]

1.4.2.1.1 *Van der Waals interaction*

This interaction is less straightforward to understand than purely electrostatic interactions. The van der Waals interaction is present between all atoms and molecules independently of their electric charge or valency. These interactions are also known as dispersion forces, London forces, charge-fluctuation, electrodynamic forces and induced-dipole forces.[120]–[124] They can be either repulsive or attractive depending on the overall system where they are acting. These forces are nonadditive, meaning that the interaction between two bodies will not be affected by other bodies nearby. [119]

The origin of this interaction is quantum electrodynamics. Briefly, the reason why a non-polar (neutrally charged) atom such as helium is affected by this may seem contradictory. However it is because the positional variation of its electrons versus its protons causes a finite dipole moment. This dipole generates an electric field that polarizes the other non-polar atoms in the vicinity generating opposing instantaneous

dipoles creating an attractive force between the two atoms. In the case where the atoms or molecules are similar, the van der Waals force is attractive. When comparing two nanoscopic surfaces such as an AFM tip and the sample, they will be assumed as similar objects and this force will always be assumed as attractive. [119]

1.4.2.1.2 *The double-layer force*

This force has an origin on the charging of neutral surfaces in liquids. Any water-based liquid, even pure water, contains free ions, H_3O^+ and OH^- . These ions can either be adsorbed by an uncharged surface or ionize the surface carboxylic groups ($\text{COOH} \rightarrow \text{COO}^- + \text{H}^+$) ultimately charging the surface negatively. Whatever the final surface charge of co-ions, it will always be balanced by an equal but opposite charged region of counterions. Some of the counterions are bound to the surface within the so-called Helmholtz layer, while others form a diffuse counterion atmosphere close to the surface, also known as the diffuse electric double-layer. [125] The reason why the counterions in solution accumulate at a surface is simply to minimise the repulsion between them. This entropically resulting repulsion dominates, maintaining the double layer close to the surface. If another identically surface approaches, some of the counterions will be pushed closer together, creating a net repulsive entropic force between the two surfaces known as the electrostatic double-layer forces.[119]

Derjaguin, Landau, Verwey, Overbeek (DLVO) theory [126] provides equations to predict the types of interaction potentials that can occur between two similarly charged surfaces or colloidal particles in a 1:1 electrolyte solution. At a nanoscale separation, this system is governed by the combined action of the Double-layer forces (F_{el}) and the van der Waals force (F_{vdW}).

1.4.2.2 *The ideal tip-sample interaction*

The interaction between two smooth and planar surfaces is the most relevant example to AFM. The first surface is a negatively charged biological macromolecule. [127] The second surface of the system is the end of the tip which is usually made of silicon nitride (Si_3N_4). In water, the net charge of the tip surface is negative. The DLVO theory allows the forces between a biological sample and the tip to be described quantitatively. [119]

The van der Waals force (F_{vdW}) per unit area is given in *Equation 1.1*.

$$F_{vdW}(z) = -H_a 6\pi z^3 \quad (\text{Eq. 1.1})$$

Where z is the separation of the two surfaces. H_a is the Hamaker constant characterizing the interaction of the two surfaces across a media in between. As an example for silicon oxide surfaces in water the Hamaker constant, H_a is 8.3×10^{-21} J. [119]

The overlap between the two diffuse electric double-layers (EDL) corresponding to the two surfaces creates the electrostatic double-layer forces (F_{el}) which is *Equation 1.2*.

$$F_{el}(z) = \frac{2\sigma_S\sigma_P}{\epsilon_e\epsilon_0} e^{-z/\lambda_D} \quad (\text{Eq. 1.2})$$

Where λ_D is the Debye length, ϵ_0 is the vacuum dielectric permittivity, ϵ_e is the dielectric permittivity of the electrolyte, and σ_S and σ_P represent the surface charge densities of the sample and the probe (tip), respectively. The thickness of the EDL layer can be represented by the Debye length, which depends on the valency (q_i) and the concentration (c_i) of electrolyte in the media. According to Muller *et al.* [128] this length can be calculated using *Equation 1.3*.

$$\lambda_D = \sqrt{\frac{\epsilon_e\epsilon_0 kT}{e^2 \sum_i c_i q_i^2}} \quad (\text{Eq. 1.3})$$

Where; k is the Boltzmann constant, T is the absolute temperature, e is the unit charge, ϵ_0 is the permittivity of the vacuum and ϵ_e is the dielectric permittivity of the electrolyte.

Finally, the total force (F_{DLVO}) that drives the interaction between the tip and the sample is the sum of the double-layer force (long-range) and the van der Waals forces (short-range) from the Equations 1.1 and 1.2, [128] resulting in *Equation 1.4*.

$$F_{DLVO}(z) = F_{el}(z) + F_{vdW}(z) = \frac{2\sigma_S\sigma_P}{\epsilon_e\epsilon_0} e^{-z/\lambda_D} - H_a 6\pi z^3 \quad (\text{Eq. 1.4})$$

This was modelled considering that all the available surface area at the end of the tip interacts with the sample. The global tip radius can typically be between 40-200 nm. However, some of the images obtained in similar experimental conditions as presented here, have shown subnanometer resolution of 2D planar protein lattices. [128][129] This resolution could only be explained if a small protrusion from the tip with a local radius of 2 nm was interacting with the sample. In that case, there are two different situations at play simultaneously: (i) the $F_{DLVO}(z)$ between the local protrusion and a spherical protein (for example) of a similar radius ($R_{loc} = 2$ nm) and (ii) the interaction between the

global tip with a radius of 40-200 nm and a planar surface that is composed of the small proteins organized as a lattice. If we model this situation as a microscopic half sphere located on a macroscopic tip (see *Figure 1.13*) then the total DLVO force between the tip and the surface can be expressed in *Equation 1.5*. [129]

$$F_{DLVO}(z) \approx F_{DLVO}^{glo}(z) + \frac{1}{2} F_{DLVO}^{loc}(z) \quad (\text{Eq. 1.5})$$

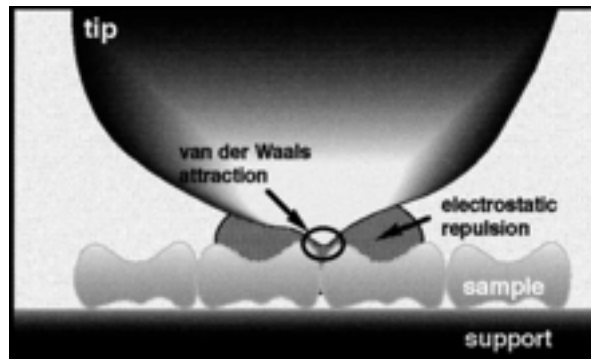


Figure 1.13 – Forces interacting between tip and surface in electrolyte solution, adapted with permission from [129]

According to *Equation 1.4* the long-range forces component (F_{el}) cannot be eliminated completely because the attraction from the short-range van der Waals force would deform the sample. Therefore, by adjusting the pH and the electrolyte concentration these two force components can be equilibrated to achieve the ideal AFM-sample interaction. [118]

1.4.3 Atomic force microscopy modes of operation

As shown above, the interaction between the tip and the sample will have a huge impact in the accuracy of the final image. However, the motion of the AFM tip performs when approaching and retracting from the sample is also crucial. There are different AFM modes available for generating topographical images based on the movement of the tip. The two most commonly used modes to obtain topographic images are: Contact and intermittent contact. [118] There are other modes more advanced and less commonly used (*e.g.* PeakForce, [131] frequency modulation[132]).

1.4.3.1 Contact mode

Contact mode, as its name states, consists of a continuous contact between the AFM tip and the surface of the sample. The movement of the cantilever is controlled by the feedback system. It can be either fixed by a parameter that controls a constant

separation between the sample and the tip (contact mode at constant height); or by the deflection that is a direct measurement of the interaction force between the tip and the sample (contact mode at a constant force).[118] The latter approach, is the most commonly used mode when the AFM is operated in contact mode. Firstly, a deflection set-point is established by the AFM user. During the approach (or engage), the AFM approaches the sample and when it makes contact with the surface it continues to increase the force until the deflection reaches the set-point. Once engaged, the scanning begins. The surface topography will cause the cantilever to deflect more or less (see *Figure 1.14 b*). This deflection changes the position of the laser on the photodetector (see *Figure 1.14 a*).

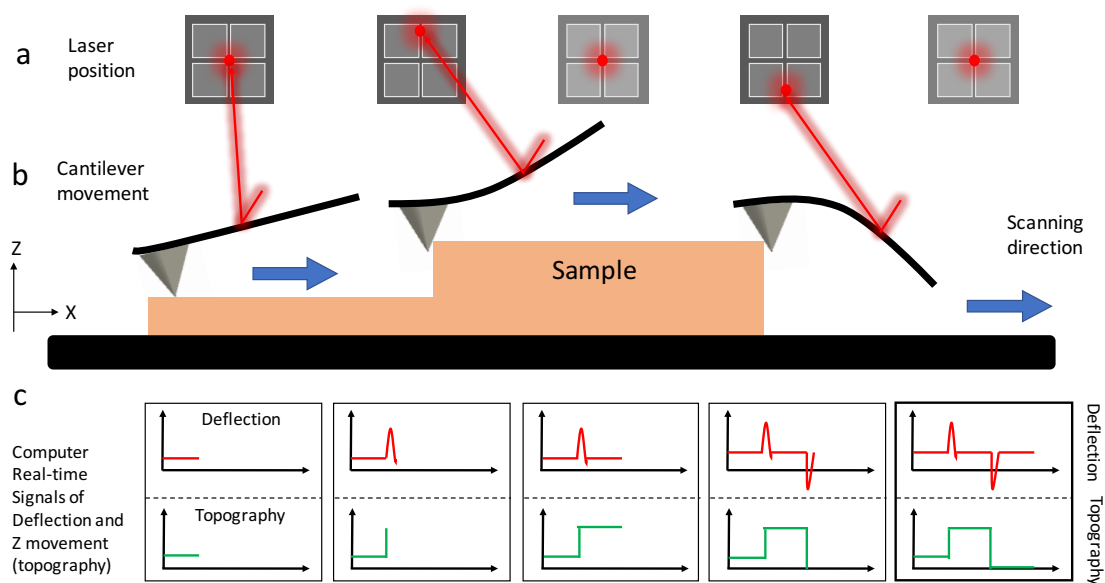
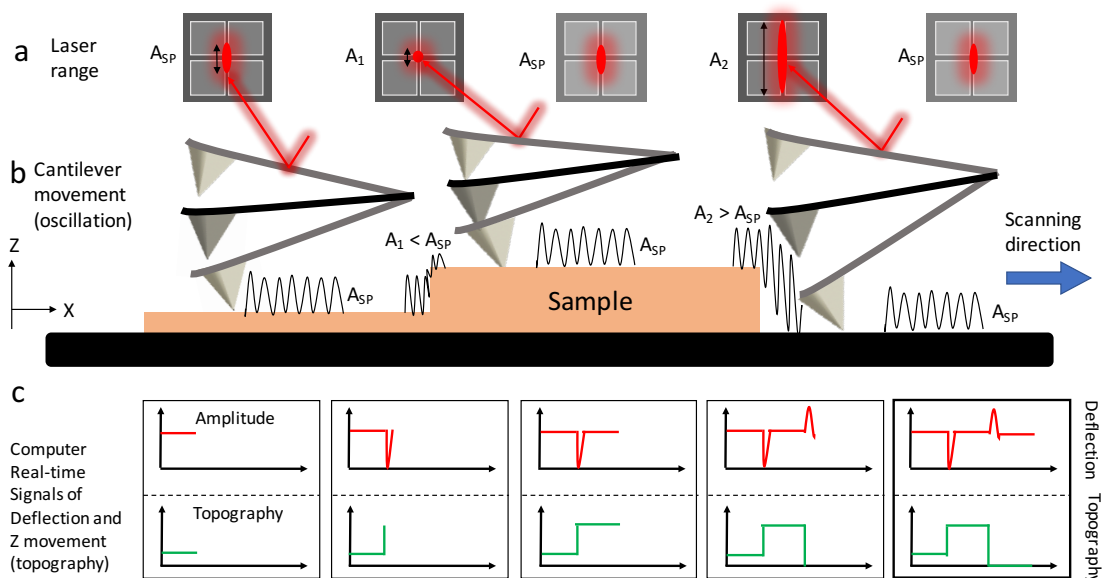


Figure 1.14 - Scheme explaining how a profile is created in contact mode, a) the laser position on the photodetector changes according to the deflection of the cantilever; b) as the cantilever follows the sample it changes deflection; c) the real-time signals of deflection and Z movement are recorded in the computer to build a profile of the topography

Following this, the feedback loop continuously adjusts the vertical position of the cantilever using the Z piezoelectric motor to maintain the real-time cantilever deflection as close as possible to the set-point. This vertical control signal is used to build the topographical image of the surface. And the deflection signal is used to build the deflection error channel (see *Figure 1.14 c*). In addition to the inherent interaction forces between the tip and the sample, this mode will cause a significant lateral force along the scanning direction. This imaging mode was the first to be invented, and is good for quickly imaging relatively topographic samples in air or liquid environment. [95]

1.4.3.2 Intermittent contact - Tapping™ mode

Intermittent contact or Tapping™ mode (IC-AFM) was first invented in 1993 by Veeco (Bruker).[133] This technique consists of scanning the surface by oscillating the cantilever near its resonance frequency, the AFM tip is intermittently in contact with the surface at the minimum point of each oscillation (see *Figure 1.15 b*). During scanning, the sample surface attracts the tip due to short-range forces, dissipating energy from the periodic oscillations of the tip, causing the amplitude oscillation to be reduced or augmented (see A_1 and A_2 in *Figure 1.15 b*). The working principle of IC-AFM is the same as Contact mode. However, instead of keeping the deflection constant, the amplitude of oscillation is kept constant by the feedback loop, using an amplitude set-point value (A_{SP}) chosen by the user (see *Figure 1.15 a* and *Figure 1.15 d*). The topographic image is also generated by recording the positions of the Z motor over time (see *Figure 1.15c*). Conceptually for the user, this mode works contrary to Contact mode, because in Tapping™ mode a decrease in the amplitude set-point means an increase in interaction force between the surface and the sample (see how the red curves in *Figure 1.14 c* and *1.15 c* are inverted).[118]



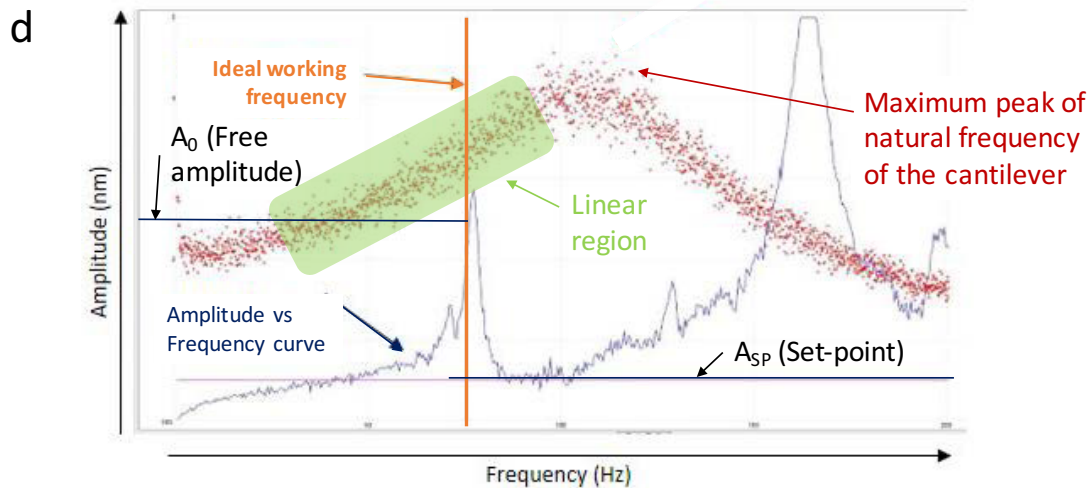


Figure 1.15 – Scheme explaining how a profile is created in IC-AFM mode, a) the laser amplitude on the photodetector changes according to the oscillation of the cantilever; b) as the cantilever follows the sample it changes amplitude of oscillation; c) the real-time signals of amplitude and Z movement are recorded in the computer to build a profile of the topography; d) Tuning parameters extracted from a real experiment with a FastScanD probe in liquid using the Dimensions FastScan.

This imaging mode is more complex and requires more parameters to be optimized by the AFM user. In contrast to contact mode, here the cantilever has to be tuned to control its oscillation prior to engaging the tip with the sample. This tuning consists in choosing an appropriate operating frequency, which is usually close to the maximum natural frequency of the cantilever (see ideal frequency in *Figure 1.15 d*). The voltage of the acoustic excitation is then adjusted to control the free amplitude (see A_0 in *Figure 1.15 d*). This is the oscillation amplitude of the cantilever when it is far away from the surface. This value has to be higher than the desired set-point for the AFM to engage

Additionally, another type of signal can be acquired from the IC-AFM. The phase image gives information about the heterogeneity of the sample, which can be useful when working with certain samples (*e.g.* different phases in a polymer with similar morphology). This signal is obtained by monitoring the difference between the phase of the drive frequency of oscillation and the phase of the cantilever response. [118]

The suitability of these two operation modes depends on sample characteristics. For example, for very robust and highly topographical samples, starting with Contact in air is a good approach. However, delicate samples such as biological materials, are much less deformed or damaged when imaged with IC-AFM, because the lateral force is greatly reduced as the tip is not always in contact with the surface. Usually, when liquid imaging is required the first approach is to use IC-AFM in liquid. Depending on the mode,

the type of cantilever used is different because they have different values of spring constant (k). The value of k defines the ratio between the force applied at the end of the cantilever and its deflection; k indicates whether the cantilever is softer or stiffer under the same tip-sample interaction.[134] For imaging in air, IC-AFM requires higher spring constant cantilevers than for Contact mode because in each oscillation the cantilever has to overcome the capillary forces [118][135] exerted by the microscopic water and contamination layer covering the surfaces. When imaging in liquid with IC-AFM, the same tips used for Contact in air with lower spring constant can be used, because when everything is covered in liquid, there are no capillary forces.

1.4.3.3 Alternative imaging modes and PeakForce

A different modality of AFM was invented for the first time in 1997 named pulse-force mode (PFM),[136] which offered topographic imaging and simultaneous mapping of physical properties. The working principle of this method was to introduce a sinusoidal modulation of the Z piezo at frequencies much lower than the resonance frequency of the cantilever. Then, in each image pixel, a complete force-distance cycle is performed (see *Figure 1.16 a*). The force signal is similar to what would be obtained from conventional force-distance curves acquired using the “force volume” AFM modality [137] (curves similar to the red line in *Figure 1.13 b*).

Moving closer to the surface the tip snaps by feeling the attractive van der Waals forces (see snap in *Figure 1.16 a*). Once the tip is in contact with the surface the cantilever feels the electrostatic Coulomb repulsive forces and deflects until arriving to a maximum (see F_{\max} in *Figure 1.16 a*). When the piezo moves back the tip experiences sample adhesion (see adhesion peak in *Figure 1.16 a*). Finally, the tip loses contact causing free oscillation, once this reaches the baseline, the cycle is repeated. In order to follow the surface and obtain a topographic image, this mode uses F_{\max} as the setpoint for the feedback loop to keep constant. Then, in each pixel the z piezo moves to the appropriate height to achieve the force setpoint value. [138]

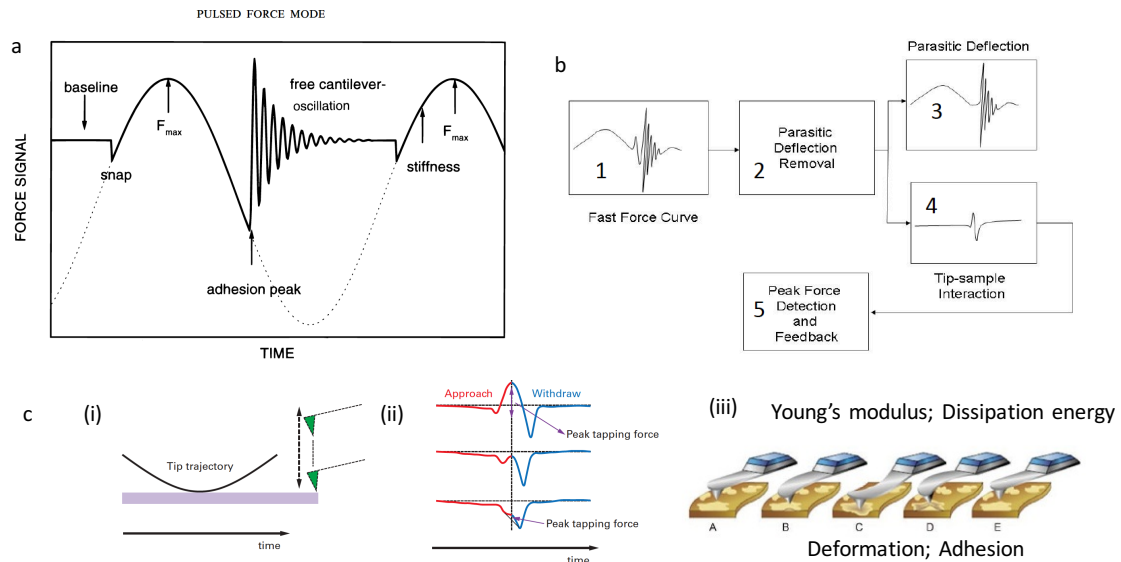


Figure 1.16 – a) Pulse-force mode schematics of an oscillation cycle. Reproduced with permission from [138]; b) steps taken by the software in PeakForce mode to clean the raw data from the Parasitic Deflection; c) movement of the AFM tip during PeakForce. ‘b’ and ‘c’ reproduced and adapted with permission from [131]

The PFM was invented as an analogue module to be added to any commercial AFM allowing access to the force signal, to modify the z modulation. In 1998 another similar mode was proposed named jumping mode. [139][140] The main difference was the lack of sinusoidal z modulation, instead the system works with a closed feedback loop and when the tip approaches the surface to detect the topography, then it changes to an open feedback loop when retracting the tip to a certain distance from the surface. These types of mode were used for many applications in the 10 years following their discovery.[140]–[142] However, at that time tapping mode still provided the highest performance in most of the samples in comparison to these alternative modes.

In 2010 Veeco developed a Quantitative mechanical property mapping mode called PeakForce QNM and the corresponding imaging mode called PeakForce Tapping.[131] This was inspired by the pulse-force mode. In PeakForce the AFM probe periodically taps the sample and the interaction forces are measured directly by the deflection of the cantilever. Then, the feedback loop keeps the peak force fixed according to the set-point chosen by the user. PeakForce has a digital software control due to advances in electronics. The main difference with PFM is the range of interaction forces at which it can operate (on the order of piconewtons). This was achieved by removing the parasitic deflections, which are uncontrolled movements of the tip, such as the ringing motion already detected on the PFM. PeakForce QNM can capture several force-curves per

millisecond. However, this increases the amount of parasitic disruptions on the system because these disruptions are more prominent when the acceleration of the cantilever movement is larger as most of them come from the inertia of the cantilever. The most important disruptions are: the coupling movement of the piezo with the cantilever deflection in the z-axis; the cantilever resonance oscillation caused during the pull-off adhesive part of the cycle (almost negligible in liquid); and the viscous force, either in ambient or liquid conditions. Veeco developed a control system to first identify the type of parasitic disruption (system ID) and then parameterize and characterize them using fast digital control. [143] The original data obtained from the force sensor is a superimposition of the tip-sample interaction with the parasitic movements. The control system separates the two types of data and only the data corresponding to the tip-sample interaction is sent to the feedback system (see *Figure 1.16 b*). This improved the force sensitivity of the PFM from <20 nN to <100 pN in PeakForce. This low force control is the most important factor in achieving high-resolution imaging. Another difference with the PFM was the real-time analysis of each force curve. Four main properties were analysed: (i) the retraction curve was used to fit the DMT model and obtain the Young's modulus, (ii) the calculation of the dissipation energy, (iii) the deformation of the sample and (iv) the adhesion (see *Figure 1.16 c*).

In summary, PeakForce QNM/Tapping [131] provides a real-time quantitative data for four important physical properties and improved topographical resolution due to instrumental control of low forces between tip and sample. The lateral forces in this imaging technique are greatly reduced, as the tip steps away from the surface in each oscillation. This mode can only be operated on Bruker machines, however other companies have designed similar modes such as Quantitative Imaging in the JPK machines. [144]

1.4.4 High resolution imaging

Obtaining AFM images at relatively low-resolution (scan size greater than $1 \mu\text{m}^2$, with resolution bigger than 50 nm) is fairly straightforward and widely used for quality control of nanostructures. [118] However, obtaining high-resolution (on the order of 5 nm or less) is considered very demanding because a large number of factors must be

optimized, specifically for each sample. In the following paragraphs, some of these factors are highlighted.

From the theoretical point of view, under liquid conditions where the capillary forces are negligible, the ultimate lateral resolution achievable by AFM operating in Tapping mode will be determined by the tip-sample contact diameter (a), (see *Equation 1.6*).

$$a = 3 \frac{F_{TS} r_{tip}}{4E^*} \quad (\text{Eq. 1.6})$$

Where: F_{TS} is the tip-sample interaction at the point of contact, r_{tip} is the radius at the very end of the tip and E^* is the sample Young's modulus. [145][146]

The first obvious parameter to take into account when trying to achieve the highest resolution possible is the tip radius. By using a very clean and sharp probe, the chances of high-resolution will increase significantly. However, when imaging a very demanding sample, tip contamination and or deformation can be an issue, even when using the best commercially available tips. One way to test whether the probe is the problem is by imaging probe sharpness characterization samples, such as Polycrystalline titanium roughness sample with small features of 10-20 nm. This sample is compatible with the Tip Qualification tool from Nanoscope™ Analysis software.[147] If the tip performs poorly on that sample, it will not work on the sample of interest.

The only other parameter that can be controlled from Eq.1 is the F_{TS} ; a smaller tip-sample diameter will be achieved by reducing this force, hence leading to better image resolution. In the ideal conditions described here, using intermittent contact tapping in liquid, the interaction force between the tip and sample $\langle F_{TS} \rangle$ at the point of contact in each oscillation is described by *Equation 1.7*. [148], [149]

$$\langle F_{TS} \rangle = \frac{k}{2Q} \sqrt{(A_0^2 - A_{SP}^2)} \quad (\text{Eq. 1.7})$$

Where: k is the spring constant of the cantilever, Q is the quality factor (it is approximately 1 in liquid), A_0 is the free amplitude and A_{SP} is the amplitude set-point. The difference between the free amplitude and the amplitude set-point should be minimised to apply gentle forces.

The optimal conditions to minimize a and $\langle F_{TS} \rangle$ from Eq.5 and 6 have to be combined with an acceptable level of thermal noise from the probe $\langle \delta_0 \rangle$, see *Equation 1.8*.

$$\langle \delta_0 \rangle = \sqrt{\frac{2k_B T Q}{\pi k f_0}} \quad (\text{Eq. 1.8})$$

Where: k_B is Boltzmann constant ($1.23 \cdot 10^{-23} \text{ J}\cdot\text{K}^{-1}$), T is the temperature of the operating conditions, Q is the quality factor, k is the spring constant of the cantilever and f_0 is the resonance frequency of the cantilever. [146]

In order for the cantilever to be able to detect features on the surface of the sample with high-resolution, the thermal noise of the cantilever must be significantly smaller than the difference between $A_0^2 - A_{SP}^2$. If $\langle \delta_0 \rangle$ is too large the Brownian motion of the cantilever will dominate the sensor and obscure the real signal that results from small forces.[148] Thus, the ideal cantilever should keep the spring constant as small as possible while the resonant frequency should be as high as possible to reduce the thermal noise.

Based on this theoretical approach, Kumar *et al.* [150] used small cantilevers (FastScan-D with $k = 0.25 \text{ N m}^{-1}$ and $f_0 = 100 \text{ kHz}$ with $16 \mu\text{m}$ of length) to obtain high resolution images of the native architecture of chromatophores. [150] FastScan-D were the best commercially available cantilevers that minimize all three Equations 1.6-1.8. The relatively low k in combination with the high frequency gives better control over the forces and thermal noise. Smaller cantilevers also contribute to decreasing the noise caused by laser power fluctuations. Once the noise threshold was significantly reduced compared to conventional cantilevers, a free amplitude (A_0) of up to 1 nm was used. The amplitude set-point (A_{SP}) was kept as close as possible to the free amplitude (90%) to use low forces while maintaining the signal-to-noise ratio. Another parameter that was optimized was the scanning speed. Other parameters were optimized to achieve better images: researchers performed scans at a line rate of $4\text{-}8 \text{ Hz}$, allowing them to overcome small amounts of sample drift. The Z-range of the piezoelectric motor was reduced to decrease the noise in the high voltage amplifier. This experiment was performed with the Dimension FastScan from Bruker (the same model used in this thesis).

There are several factors that will influence the resolution of the images that are completely independent of the cantilever or the scanning parameters. External factors cause mainly sample drift and temperature changes. The sample must be as well-fixed

to the AFM stage as possible, to avoid movements. If this is not the case, it will cause sample drift. This issue can be spotted by observing huge deformations of the features from consecutive images at the same position. The best approach to solve this is using epoxy adhesive as sample mounting method. When working with a rotation stage, the sample should be located in the centre to avoid residual movements. Another important factor is the external vibration and noise caused by unnecessary light sources or electronic equipment close to the AFM. The best conditions of isolation are usually achieved with a combination of a vibration-damped table and an acoustic hood. [151] However, these isolation conditions have a major drawback, as the temperature inside is usually much higher than the ambient room temperature. Thus, thermal equilibration is crucial to achieve high-resolution, as the system needs to be thermally stable. Leaving the system to equilibrate for a few hours inside the acoustic hood, prior to image acquisition, can solve this problem. [118]

1.4.4.1.1 *Screening of electric double-layer*

Many studies have shown that in order to achieve the best possible resolution possible with AFM there needs to be an appropriate balance between long-range forces (van der Waals) and short-range forces (electrostatic double-layer forces). As mention above, the only way to control this interaction is by modifying the electrostatic double-layer forces. This type of force can be controlled by changing the pH and using the appropriate concentration of counterions in the media, making the interaction between the tip and the sample close to the theoretically ideal case. [119]

The counterions have to be present in sufficient quantity in order to prevent the tip from crashing into the sample and deforming its surface, but cannot be too concentrated, so that there is too much repulsion between the tip and sample. Several experiments, have shown the direct relationship between counterions concentration and tip-sample interaction. However, there is no universal value, and each experimental sample will have its ideal media conditions that will provide the best possible resolution. This is called, an imaging buffer. In general, increasing the salt concentration and the use of divalent ions in the imaging buffer improves the resolution of the images. For example, the imaging buffer of pH 8.2, 10 mM Tris-HCl and 150 mM KCl was the best media to study 2D lattices of the water channel-forming protein aquaporin-1 (AQP1). [128] Other

studies have been performed on opened liposomes and 2D lattice crystals of Porin OmpF. Each had an optimized imaging buffer by increasing its KCl concentration: pH 7.2, 10 mM Tris-HCl and 150 mM KCl for liposomes and pH 7.2, 20 mM Tris-HCl and 300 mM KCl for OmpF sheets.[128] The introduction of divalent counterions was found to have a greater effect. For example, for studying of hexagonally packed intermediate (HPI), which is a typical bacterial surface protein, the optimal buffer was 50 mM MgCl₂ and 300 mM KCl (10 mM Tris-HCl at pH 7.6).[129] More recently, a similar buffer was used: 300 mM KCl plus 20 mM MOPS and 10 mM MgCl₂ at pH 7.4 to study the native architecture of chromatophores.[150]

The best method to optimize the imaging buffer when faced with a new sample is vary the electrolyte concentrations and pH and record the force-distance [129] or amplitude-distance curves.[150] By studying the shape of these curves, it can be clear which buffer reduces the double-electronic layer force the most (see examples in *Figure 1.17*).

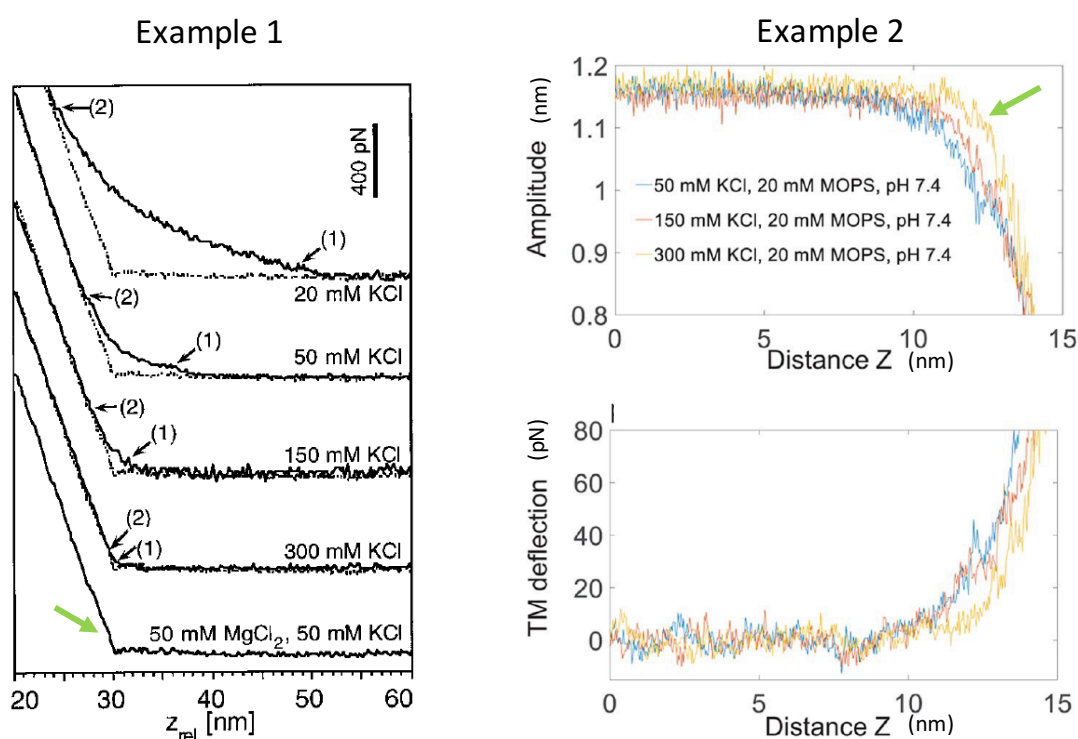


Figure 1.17 – Force curves at different buffers from Muller (example 1) and Amplitude curves from Kumar (example 2), adapted with permission from [129] and [150] respectively.

Figure 1.17 shows different force-distance curves taken from the same sample, but at different buffer concentrations. When the electrolyte concentration increases, the curves indicate that the tip is becoming into contact with the surface at a shorter distance. The distance between the AFM tip and a biological sample depends on both

the force applied and the imaging buffer. The amount of force cannot be infinitely increased, as applying a force greater than 0.1 nN could deform the samples (for example individual proteins, each sample will have a different threshold). [129] Therefore, these curves will be different for each experiment, and for examples 1 and 2, the best conditions are indicated with green arrows.

In this thesis the buffer conditions are similar to previous work performed on living cells with AFM in our group (see *Chapter 3*). However, whenever the buffer used was not appropriate, optimization followed using the guidelines given above.

All of these factors are assuming the sample is perfect. However, biological samples are challenging and can cause additional and unexpected problems. Thus, achieving high lateral-resolution of the order of a few nanometres with AFM in biological samples is a demanding experiment with low throughput compared to other microscopy techniques.

1.4.5 Study of bacteria using AFM

AFM has been extensively used to image biophysical samples obtaining much better resolution than other techniques. Another great advantage of AFM with respect to other more invasive techniques is the potential to image living organisms in their own environment without disrupting them.[96], [152], [153] Bacteria cells can be imaged with AFM with great versatility: either by directly imaging live bacterial cells or studying the purified cell wall material.

1.4.5.1 Living bacteria

The first time AFM was used to image bacterial cells was in 1991 by Hiroshi *et al.* when they looked at *E. coli* whole cells.[154] However, it was not until 2004 that the first high resolution images of peptidoglycan on living bacteria were obtained by Touhami and his group.[87] The specimen under study was *S. aureus*, the experimental results were consistent with previous SEM data. Thus, AFM images provided structural information at higher resolution and could differentiate between mature (see *Figure 1.18 a*) and nascent peptidoglycan regions (see *Figure 1.18 b*) on the cell surface with two distinct architectures. Another group [155] also showed the two distinct architectures on the same cell. Under their experimental conditions, a quarter of the cell corresponded to mature peptidoglycan (see yellow arrow in *Figure 1.18 c*) and the rest of the cell surface

was covered by nascent peptidoglycan from the two most recent divisions (see green arrows in *Figure 1.18 c*).[155] Most recently, using small cantilevers and soft tapping mode together with the optimal buffer conditions to screen the surface charges, the highest resolution AFM images of *S. aureus* live cells have been obtained in our group (see *Chapter 3*).[156]

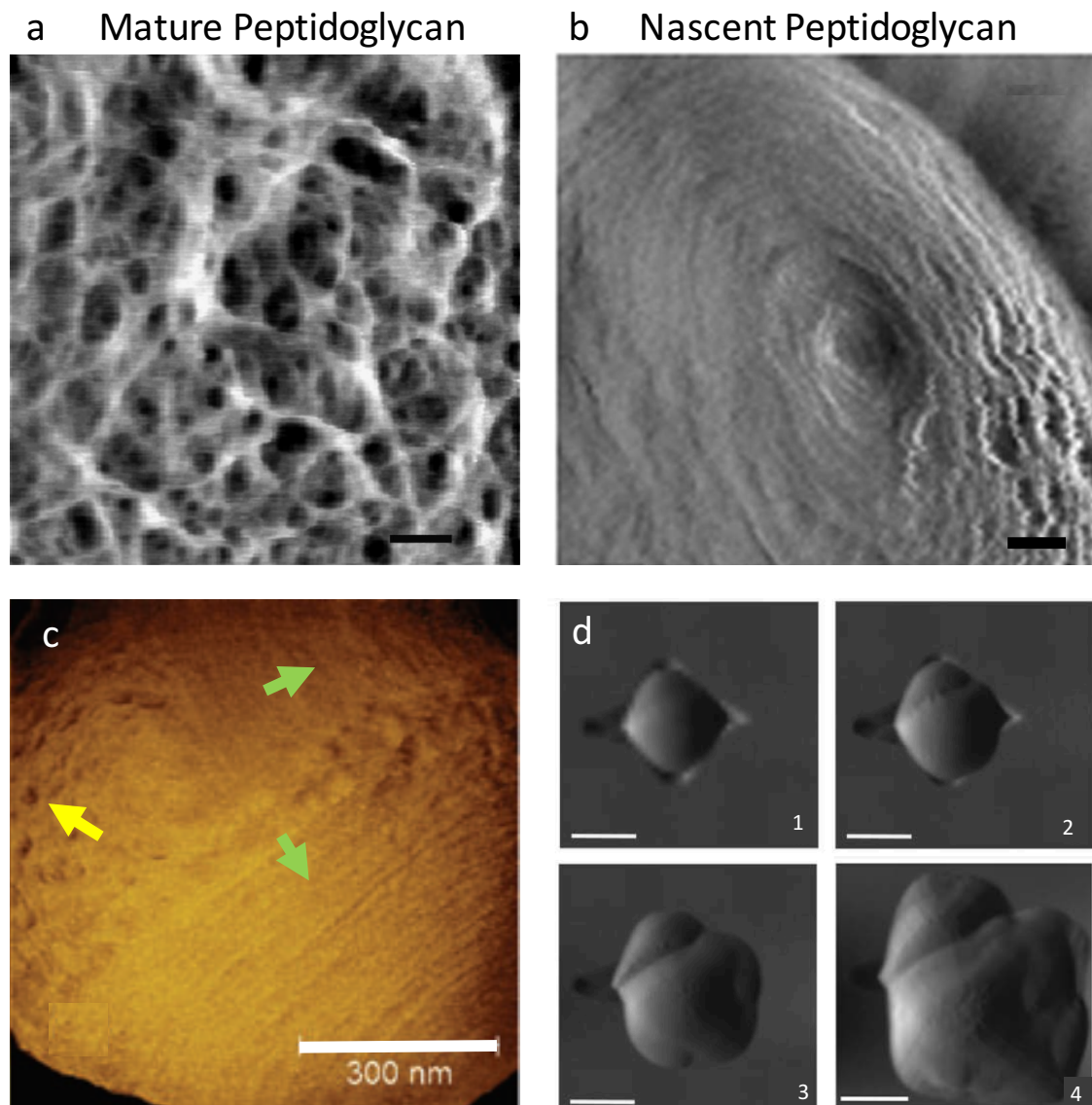


Figure 1.18 – height images in intermittent contact mode in liquid: a, b) S. aureus mature and nascent peptidoglycan regions, adapted with permission from [87]; c) S. aureus (NCTC 8532) living cell with mature area (yellow arrow) and three quarters of the cell being covered by nascent material (green arrows), adapted with permission from [155]; d) consecutive images of an S. aureus cell undergoing division, adapted with permission form [110]

Moreover, AFM is a suitable technique to study dynamic processes such as cell division (see *Figure 1.18 d*). In this study, [110] they improved the entrapment of the cells, which allowed them to grow and divide whilst still being imaged by AFM. The most common bacterial entrapment methods in the field are; miliporous filter membranes [87], [155]

and silicon wells etched into different shapes: four point star [110] and most recently circular. [156]

Another study focused on the *in situ* dynamic structural changes of *S. aureus* CW, this was after the addition of the PG directed enzyme lysostaphin. [157] For the first time, CW digestion by lysostaphin was directly observed. Causing swelling of the cells, nanoscale perforation and an increase in surface roughness.[157] This proves that AFM is the ideal microscopy technique to study the assembly of peptidoglycan and its response to enzymes and potentially to antibiotic drugs. [153], [158]

All of the examples presented so far concerned study of the pathogen *S. aureus*. However, many other studies have used AFM as the main tool to understand the surface architecture and mechanical properties of other microorganisms. Other Gram-positive bacteria such as *Group B Streptococcus* [159] and *Lactococcus lactis* [160] have been studied by AFM, to image the PG arrangement and polysaccharides cell envelope respectively. Another Gram-positive lactic acid bacteria, *Lactobacillus plantarum* was the focus of a study that combined fluorescence and AFM to determine the relationship between the WTA location and PG architecture.[36] The dynamics and structure of a single germinating spore from *Bacillus atrophaeus* were also studied by AFM. [161] The nascent spore PG architecture was similar to the mature PG from *S. aureus*. [156] By contrast, other work has have focused on the possibility to follow dynamic processes by AFM; including the disruption of the Gram-negative bacteria *E. coli* upon treatment of antimicrobial peptide; [162] and the host-immune cells killing mechanism creating pores on the surface of *E. coli* by the membrane attack complex. [163] The Gram-positive *mycobacteria sp. strains JLS, KMS and MCS* have been objects of study for their adhesion behaviour during division from the mother cells to its descendants. [164] Another species, *Mycobacterium smegmatis* was the focus of a study following their growth and division over multiple generations using PeakForce mode AFM. [165] Further work has been conducted regarding the nano-mechanics and the nanostructure of the CW of *mycobacterium JLS* upon ethambutol treatment.[166] The researchers found an inhibition of the contractile ring formation inducing cell death and decreasing nanomechanical values upon ethambutol treatment together with different sensitivity depending on the division phase of each individual bacterium. [166]

1.4.5.2 Sacculi samples

The approach outlined above is limited to external analysis of the cell wall because AFM as it is a surface technique. However, the molecular architecture of the inner side of the cell wall is of great interest because it has close proximity to the internal lipid membrane of the cell. Therefore, a second approach was developed by purifying only the peptidoglycan component of the cell wall (*i.e.* sacculi).

AFM was used for the first time to image bacteria sacculi in 2008, when the long-term collaboration commenced between Professor Foster and Professor Hobbs. [49] *B. subtilis* sacculi were studied because it is a Gram-positive bacterial species, as these were already extensively studied in a laboratory setting. *B. subtilis* sacculi were imaged by AFM after being dried on a flat surface. The result was a rather unexpected and elegant PG architecture, which consisted of a rough external CW and a highly ordered internal CW with “cable-like” protrusions separated by approximately 50 nm. The researchers measured the length of purified glycan strands which has a maximum length of 5 μm . They studied the septa formation resulting in a thick outer band surrounding centripetal rings along the septal disc. As the septa progressed, cross-striations with a 25 nm periodicity appeared. These results lead to a proposed model of *B. subtilis* CW architecture (see *Figure 1.19 a*) which contradicted the scaffolded model and previous data obtained by Cryo-EM.[48]

More recently, an independent study of *B. subtilis* dried sacculi elucidated further information on the different architectures per cell cycle and septa formation. [167]

A similar approach was used in 2010 to study sacculi of *S. aureus* with AFM. [46] Previously there was a consensus in the field about *S. aureus* external CW being heterogenic, comprising at least two different architectures. Studies by SEM had previously shown a highly ordered concentric rings architecture and a more disordered structure.[53] By imaging dried sacculi using AFM, it was shown that the concentric rings correspond to the nascent PG material. The other disordered architecture was rough and forming knobbls which were associated with the older PG material. No description of the internal CW architecture was achieved due to lack of resolution at the time. However, a major breakthrough was made, establishing a direct relationship between the cellular division mechanism and specific spatial organization of the PG in certain

parts of the CW. The main feature was called piecrust, the location of which regulates the orientation of the orthogonal division planes (see *section 1.3.3.3*). [46] A parallel study, combined with fluorescence measured the increase in volume from hemispherical to spherical cells. This finding suggested that the volume of the cell increases leading to an increase in CW surface area,[47] but without further synthesis of peptidoglycan, requiring a reduction in peptidoglycan density. The remodelling of peptidoglycan from concentric rings to knobles occurs by lateral expansion of peptidoglycan by discontinuous autolysis along the rings, produced by peptidoglycan hydrolases.[65] From these studies, a model of CW architecture from *S. aureus* was proposed (see *Figure 1.19 b*).

In Gram-negative bacteria species such as *E. Coli* sacculi were also studied by AFM, [44] revealing a more disordered structure than previously thought. Researchers have shown that the PG single layer is a porous three-dimensional biopolymer network without any overall orientation of PG strands with respect to the membrane of the cell. Additionally, they hypothesize that PG is organized into bands of higher or lower porosity levels. The latter is responsible for synthesising new PG material in the middle region between external and internal CW. More recently, molecular-resolution of *E. coli* has been achieved by imaging with AFM in a liquid environment. [86] The relationship between the PG architecture and the cell shape was shown. Rod-shaped *E. coli* displayed longer glycan chains and much more ordered PG than mutated spheroid *E. coli*. These studies can be summarized in their proposed model (see *Figure 1.19 c*).

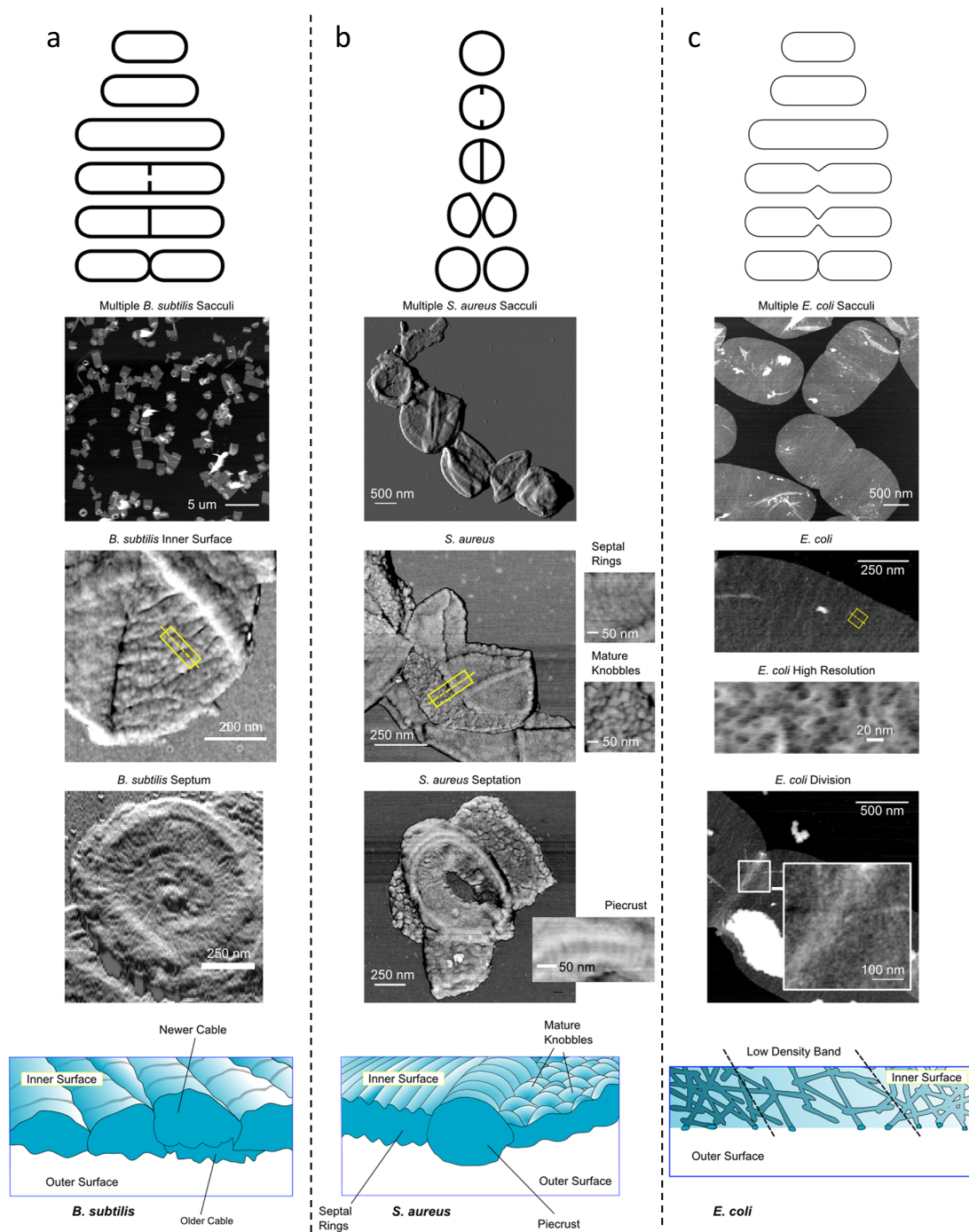


Figure 1.19 – Peptidoglycan architecture from a) *B. subtilis*; b) *S. aureus* and c) *E. coli* sacculi. Reproduced with permission from [23]

Finally, other bacterial species have also been the focus of sacculi studies. AFM was used to study the CW architecture of *Lactococcus lactis* [160] in living cells, as previously described. However, sacculi fragments from *Lactococcus lactis* were used to determine the absence of rings-like structures upon dehydration and purification of the CW. They concluded that the best approach to understand the CW architecture is using living cells, because the purification process needed to produce a sacculi sample can alter the CW

structure. [36], [160] Another study combined AFM of sacculi with super-resolution microscopy to determine the cell wall dynamics and the PG architecture of four ovococcal bacterial species: *Streptococcus pneumoniae* (R6 strain), *Erococcus faecalis* (JH2-2 strain) and *Lactococcus lactis* (MG1363 and VES5751 strains). [47] They found structural features such as the equatorial Ring and the septum location which differ from other Gram-positive bacteria such as *B. subtilis* and *S. aureus*.

All the aforementioned studies performing AFM on bacterial sacculi used a dehydrated environment with the notable exception of the most recent work on *E. coli* which was performed in tapping mode in liquid. [86]

1.5 Project aims

The increasing amount of AMR strains together with a striking decrease in the discovery of new antimicrobial compounds creates a pessimistic picture of the world health for the future if no action is taken. This is why, together with screening new antibiotic compounds, fundamental research on the growth and death of bacteria is necessary.

One of the main differences between eukaryotic and prokaryotic cells is the cell wall. This is a component unique to bacterial cells, it is crucial for their survival as without it the cell does not have a define shape anymore and it dies. The cell wall also performs a really important function of interaction with their environment and it guides cell division. The main component of the cell wall is a macromolecule called peptidoglycan. Although there is a lot of data supporting its chemical composition and structure, the three dimensional architecture of this molecule around the cell at the molecular level is still unknown. The cell wall is one of the most common target for antibiotics, because of its specificity to bacteria and the crucial role it has in bacteria survival. However, how can the correct next steps to design a better antibiotic against the cell wall be taken if there is a knowledge gap with respect to its molecular organization? This project is focused on deciphering the three dimensional architecture of the Gram-positive bacterial cell wall.

The technique chosen to obtain molecular resolution structures of peptidoglycan is atomic force microscope. Despite being a young microscopy technique, we believe it might overcome most of the limitations from the main microscopy techniques when

studying bacterial cell walls. In the literature, there is plenty of work performed by fluorescence and electron microscopy. These techniques have limitations in terms of resolution and signal to noise ratio respectively. Atomic force microscopy is a high resolution technique (of a few nanometres) which consist of a direct interaction between a sharp tip and the surface of the sample. It is label free and can work in the native environment of the cells without damaging them.

There has been many studies in the past which focused on the cell wall architecture of different bacteria using the atomic force microscope. There has been several works on whole live bacteria with limited resolution. In order to achieve more details of the cell wall, purified peptidoglycan was also studied with this technique. However, none of these were performed successfully in liquid with the exception of a recent work in *E. coli*. Here, we aim to complete the work previously done in our group on living bacteria with imaging purified peptidoglycan in liquid also using atomic force microscopes.

Firstly, a new method to image purified material from Gram-positive bacteria in liquid has to be optimized. Then, the information extracted from these experiments will be compared with the available data on living *S. aureus* in *Chapter 3*. [87], [110], [155], [156] In *Chapter 4*, the main focus will be determining the structure of the internal PG, which is key to provide a complete structural picture of the *S. aureus* CW. The main synthases such as PBPs are located between the cell membrane and the internal surface of the CW. Moreover, the internal PG surface is the first barrier to control turgor pressure. Having a three dimensional structural map of the CW would be crucial to build the first PG model of *S. aureus* based on direct data.

Secondly, once the healthy CW has been mapped, a comprehensive comparison with different strains with CW mutations will be performed in *Chapter 5*. The PG phenotype from strains lacking non-essential hydrolases or synthases will be characterised. From these phenotypes, we can infer their role in normal PG growth in a healthy cell. This will allow us to stablish a direct relationship between enzymatic functions and the resultant PG architecture.

B. subtilis will be studied in *Chapter 6* using the methodologies developed during previous chapters. This will provide a second example of Gram-positive bacteria. Given *B. subtilis* is a rod-shaped bacteria species, the three dimensional PG architecture will

be examined for shape-dependent features. Then, additional work will be performed on *B. subtilis* live cells to complete the data set for both species. If there are different PG organisation according to cell shape, crucial enzymes responsible for the rod-shape will be studied following the same approach as in *Chapter 5*.

Finally, the question about what is the effect of different antibiotics on the cell wall architecture will be tackled in *Chapter 7*. After the cell wall is completely defined for both species, cell wall bactericidal antibiotics will be tested in *S. aureus* to understand how do antibiotics break the CW ultimately killing the cells. This work will finally allow us to answer the question of how do antibiotics kill Gram-positive bacteria. This problem has been unanswered for several decades. We will obtain information about this process at molecular level using a direct microscopy technique. This will help fill the knowledge gap necessary to advance in our battle against antimicrobial resistance.

1.6 Bibliography

- [1] K. M. Joan L. Slonczewski, John W. Foster, "Microbiology: An Evolving Science (2nd Edition)," *IEEE Trans. Wirel. Commun.*, 2017.
- [2] E. Y. Furuya and F. D. Lowy, "Antimicrobial-resistant bacteria in the community setting," *Nat. Rev. Microbiol.*, vol. 4, no. 1, pp. 36–45, 2006.
- [3] E. J. Zasowski, J. M. Rybak, and M. J. Rybak, "The β -Lactams Strike Back: Ceftazidime-Avibactam," *Pharmacotherapy*. 2015.
- [4] R. Sharma, T. Eun Park, and S. Moy, "Ceftazidime-Avibactam: A Novel Cephalosporin/ β -Lactamase Inhibitor Combination for the Treatment of Resistant Gram-negative Organisms," *Clinical Therapeutics*. 2016.
- [5] The Review on Antimicrobial Resistance, "The Review on Antimicrobial Resistance," 2016.
- [6] A. Holmes, L. Moore, A. Sundsfjord, M. Steinbakk, S. Regmi, A. Karkey, P. Guerin and L. Piddock, "Understanding the mechanisms and drivers of antimicrobial resistance," *The Lancet*. 2016.
- [7] WHO, "Antimicrobial resistance. Global report on surveillance," *World Heal. Organ.*, 2014.
- [8] M. Ferri, E. Ranucci, P. Romagnoli, and V. Giaccone, "Antimicrobial resistance: A global emerging threat to public health systems," *Crit. Rev. Food Sci. Nutr.*, 2017.
- [9] M. Woolhouse, M. Ward, B. Van Bunnik, and J. Farrar, "Antimicrobial resistance in humans, livestock and the wider environment," *Philos. Trans. R. Soc. B Biol. Sci.*, 2015.
- [10] C. Kirchhelle, "Pharming animals: a global history of antibiotics in food production (1935–2017)," *Palgrave Commun.*, 2018.
- [11] A. Pantosti and M. Venditti, "What is MRSA?," *European Respiratory Journal*. 2009.
- [12] R. Köck, K. Becker, B. Cookson, J. van Germert-Pijnen, S. Harbatch, J. Kluytmans, M. Mielke, G. Peters, R. Skov, M. Struelens, E. Tacconelli, A. Torné, W. Witte, A. Friedrich, "Methicillin-resistant *Staphylococcus aureus* (MRSA): Burden of disease and control challenges in Europe," *Eurosurveillance*. 2010.
- [13] R. J. Gordon and F. D. Lowy, "Pathogenesis of Methicillin-Resistant *Staphylococcus aureus* Infection," *Clin. Infect. Dis.*, 2008.
- [14] J. Stokes, K. Yang, K. Swanson, W. Jin, A. Cubillos-Ruiz, N. Donghia, C. MacNair, S. French, L. Carfrae, Z. Bloom-Ackerman, V. Tran, A. Chiappino-Pepe, A. Badran, I. Andrews, E. Chory, G. Church, E. Brown, T. Jaakkola, R. Barzilay and J. Collins, "A Deep Learning Approach to Antibiotic Discovery," *Cell*, 2020.

- [15] M. Wilhelm, J. Sheffield, M. Sharifian, Y. Wu, C. Spahr, G. Gonella, B. Xu and H. Dai "Gram's Stain Does Not Cross the Bacterial Cytoplasmic Membrane," *ACS Chem. Biol.*, vol. 10, no. 7, pp. 1711–1717, 2015.
- [16] W. Jacobson, "Gram's discovery of his staining technique," *J. Infect.*, 1983.
- [17] C. Gram, "Untersuchungen über die Grösse der rothen Blutkörperchen im Normalzustande und bei verschiedenen Krankheiten," *Fortschr. Med.*, vol. 2, no. 2, 1884.
- [18] C. Friedländer, *Die mikrokokken der pneumonie*. 1883.
- [19] R. N. Stijn Blot, K. Vandewoude, and F. Colardyn, "Staphylococcus aureus infections," *N. Engl. J. Med.*, 1998.
- [20] S. Y. C. Tong, J. S. Davis, E. Eichenberger, T. L. Holland, and V. G. Fowler, "Staphylococcus aureus infections: Epidemiology, pathophysiology, clinical manifestations, and management," *Clin. Microbiol. Rev.*, vol. 28, no. 3, pp. 603–661, 2015.
- [21] Office of National Statistics, "Deaths involving MRSA, 2008 to 2012," no. August, pp. 1–16, 2013.
- [22] F. D. Lowy, "Secrets of a superbug," *Nature Medicine*. 2007.
- [23] R. D. Turner, W. Vollmer, and S. J. Foster, "Different walls for rods and balls: The diversity of peptidoglycan," *Molecular Microbiology*. 2014.
- [24] W. Vollmer, D. Blanot, and M. A. De Pedro, "Peptidoglycan structure and architecture," *FEMS Microbiol. Rev.*, vol. 32, no. 2, pp. 149–167, 2008.
- [25] W. Vollmer and S. J. Seligman, "Architecture of peptidoglycan: more data and more models," *Trends Microbiol.*, vol. 18, no. 2, pp. 59–66, 2010.
- [26] S. M. Desmarais, M. A. De Pedro, F. Cava, and K. C. Huang, "Peptidoglycan at its peaks: How chromatographic analyses can reveal bacterial cell wall structure and assembly," *Mol. Microbiol.*, vol. 89, no. 1, pp. 1–13, 2013.
- [27] S. J. Kim, J. Chang, and M. Singh, "Peptidoglycan architecture of Gram-positive bacteria by solid-state NMR," *Biochim. Biophys. Acta - Biomembr.*, vol. 1848, no. 1, pp. 350–362, 2015.
- [28] B. A. Dmitriev, F. V. Toukach, O. Holst, E. T. Rietschel, and S. Ehlers, "Tertiary structure of Staphylococcus aureus cell wall murein," *J. Bacteriol.*, vol. 186, no. 21, pp. 7141–7148, 2004.
- [29] S. Taheri-Araghi, S. Bradde, J. Sauls, N. Hill, P. Levin, J. Paulsson, M. Vergassola and S. Jun, "Cell-size control and homeostasis in bacteria," *Curr. Biol.*, 2015.
- [30] D. C. Yang, K. M. Blair, and N. R. Salama, "Staying in Shape: the Impact of Cell Shape on Bacterial Survival in Diverse Environments," *Microbiol. Mol. Biol. Rev.*, 2016.
- [31] I. G. Boneca, Z. H. Huang, D. A. Gage, and A. Tomasz, "Characterization of Staphylococcus aureus cell wall glycan strands, evidence for a new β -N-acetylglucosaminidase activity," *J. Biol. Chem.*, 2000.
- [32] J. J. ARMSTRONG, J. BADDILEY, and J. G. BUCHANAN, "Structure of the ribitol teichoic acid from the walls of Bacillus subtilis," *Biochem. J.*, 1960.
- [33] M. G. Percy and A. Gründling, "Lipoteichoic Acid Synthesis and Function in Gram-Positive Bacteria," *Annu. Rev. Microbiol.*, 2014.
- [34] S. Brown, J. P. Santa Maria, and S. Walker, "Wall Teichoic Acids of Gram-Positive Bacteria," *Annu. Rev. Microbiol.*, 2013.
- [35] S. Brown, Y. H. Zhang, and S. Walker, "A Revised Pathway Proposed for Staphylococcus aureus Wall Teichoic Acid Biosynthesis Based on In vitro Reconstitution of the Intracellular Steps," *Chem. Biol.*, 2008.
- [36] G. Andre, M. Deghorain, P. Bron, I. Van Swam, M. Kleerebezem, P. Hols and Y. Dufrêne, "Fluorescence and atomic force microscopy imaging of wall teichoic acids in lactobacillus plantarum," *ACS Chem. Biol.*, 2011.
- [37] V. R. F. Matias and T. J. Beveridge, "Lipoteichoic acid is a major component of the Bacillus subtilis periplasm," *J. Bacteriol.*, vol. 190, no. 22, pp. 7414–7418, 2008.
- [38] W. Fischer, "Bacterial Phosphoglycolipids and Lipoteichoic Acids," in *Glycolipids, Phosphoglycolipids, and Sulfoglycolipids*, 1990.
- [39] S. J. Kim, M. Singh, M. Preobrazhenskaya, and J. Schaefer, "Staphylococcus aureus peptidoglycan stem packing by rotational-echo double resonance NMR spectroscopy," *Biochemistry*, 2013.
- [40] S. Sharif, S. J. Kim, H. Labischinski, J. Chen, and J. Schaefer, "Uniformity of glycyl bridge lengths in the mature cell walls of fem mutants of methicillin-resistant Staphylococcus aureus," *J. Bacteriol.*, 2013.
- [41] S. Meroueh, K. Bencze, D. Heseck, M. Lee, J. Fisher, T. Stemmler and S. Mobashery, "Three-dimensional structure of the bacterial cell wall peptidoglycan," *Proc. Natl. Acad. Sci.*, 2006.

- [42] B. A. Dmitriev, F. V. Toukach, K. J. Schaper, O. Holst, E. T. Rietschel, and S. Ehlers, "Tertiary structure of bacterial murein: The scaffold model," *J. Bacteriol.*, 2003.
- [43] V. R. F. Matias, A. Al-Amoudi, J. Dubochet, and T. J. Beveridge, "Cryo-transmission electron microscopy of frozen-hydrated sections of *Escherichia coli* and *Pseudomonas aeruginosa*," *J. Bacteriol.*, 2003.
- [44] R. D. Turner, A. F. Hurd, A. Cadby, J. K. Hobbs, and S. J. Foster, "Cell wall elongation mode in Gram-negative bacteria is determined by peptidoglycan architecture," *Nat. Commun.*, 2013.
- [45] V. R. F. Matias and T. J. Beveridge, "Native cell wall organization shown by cryo-electron microscopy confirms the existence of a periplasmic space in *Staphylococcus aureus*," *J. Bacteriol.*, vol. 188, no. 3, pp. 1011–1021, 2006.
- [46] R. D. Turner, E. C. Ratcliffe, R. Wheeler, R. Golestanian, J. K. Hobbs, and S. J. Foster, "Peptidoglycan architecture can specify division planes in *Staphylococcus aureus*," *Nat. Commun.*, vol. 1, no. 3, p. 26, 2010.
- [47] R. Wheeler, S. Mesnage, I. G. Boneca, J. K. Hobbs, and S. J. Foster, "Super-resolution microscopy reveals cell wall dynamics and peptidoglycan architecture in ovococcal bacteria," *Mol. Microbiol.*, vol. 82, no. 5, pp. 1096–1109, 2011.
- [48] V. R. F. Matias and T. J. Beveridge, "Cryo-electron microscopy reveals native polymeric cell wall structure in *Bacillus subtilis* 168 and the existence of a periplasmic space," *Mol. Microbiol.*, vol. 56, no. 1, pp. 240–251, 2005.
- [49] E. J. Hayhurst, L. Kailas, J. K. Hobbs, and S. J. Foster, "Cell wall peptidoglycan architecture in *Bacillus subtilis*," *Proc. Natl. Acad. Sci.*, vol. 105, no. 38, pp. 14603–14608, 2008.
- [50] S. J. Kimi, L. Cegelski, M. Preobrazhenskaya, and J. Schaefer, "Structures of *Staphylococcus aureus* cell-wall complexes with vancomycin, eremomycin, and chloroeremomycin derivatives by $^{13}\text{C}\{^{19}\text{F}\}$ and $^{15}\text{N}\{^{19}\text{F}\}$ rotational-echo double resonance," *Biochemistry*, 2006.
- [51] S. J. Kim, M. Singh, and J. Schaefer, "Oritavancin Binds to Isolated Protoplast Membranes but not Intact Protoplasts of *Staphylococcus aureus*," *J. Mol. Biol.*, 2009.
- [52] K. D. Young, "Too many strictures on structure," *Trends in Microbiology*. 2006.
- [53] K. Amako, A. Umeda, and K. Murata, "Arrangement of peptidoglycan in the cell wall of *Staphylococcus*," *J. Bacteriol.*, 1982.
- [54] A. Typas, M. Banzhaf, C. A. Gross, and W. Vollmer, "From the regulation of peptidoglycan synthesis to bacterial growth and morphology," *Nature Reviews Microbiology*. 2012.
- [55] A. L. Lovering, S. S. Safadi, and N. C. J. Strynadka, "Structural Perspective of Peptidoglycan Biosynthesis and Assembly," *Annu. Rev. Biochem.*, 2012.
- [56] T. Mohammadi, V. Van Dam, R. Sijbrandi, T. Vernet, A. Zapun, A. Bouhss, M. Diepeveen, M. Nguyen-Distéche, B. De Kruijff and E. Breukink, "Identification of FtsW as a transporter of lipid-linked cell wall precursors across the membrane," *EMBO J.*, 2011.
- [57] N. Ruiz, "Bioinformatics identification of MurJ (MviN) as the peptidoglycan lipid II flippase in *Escherichia coli*," *Proc. Natl. Acad. Sci. U. S. A.*, 2008.
- [58] J. B. Ward and H. R. Perkins, "The direction of glycan synthesis in a bacterial peptidoglycan," *Biochem. J.*, 1973.
- [59] E. Fuchs Cleveland and C. Gilvarg, "Oligomeric intermediate in peptidoglycan biosynthesis in *Bacillus megaterium*," *Proc. Natl. Acad. Sci. U. S. A.*, 1976.
- [60] P. Macheboeuf, C. Contreras-Martel, V. Job, O. Dideberg, and A. Dessen, "Penicillin binding proteins: Key players in bacterial cell cycle and drug resistance processes," *FEMS Microbiology Reviews*. 2006.
- [61] J. W. Kozarich and J. L. Strominger, "A membrane enzyme from *Staphylococcus aureus* which catalyzes transpeptidase, carboxypeptidase, and penicillinase activities," *J. Biol. Chem.*, 1978.
- [62] P. Reed, H. Veiga, A. M. Jorge, M. Terrak, and M. G. Pinho, "Monofunctional transglycosylases are not essential for *Staphylococcus aureus* cell wall synthesis," *J. Bacteriol.*, 2011.
- [63] A. Taguchi, M. Welsh, L. Marmont, W. Lee, M. Sjodt, A. Kruse, D. Kahne, T. Bernhardt and S. Walker, "FtsW is a peptidoglycan polymerase that is functional only in complex with its cognate penicillin-binding protein," *Nat. Microbiol.*, 2019.
- [64] W. Vollmer, B. Joris, P. Charlier, and S. Foster, "Bacterial peptidoglycan (murein) hydrolases," *FEMS Microbiology Reviews*. 2008.
- [65] R. Wheeler, R. Turner, R. Bailey, B. Salamaga, S. Mesnage, S. Mohamad, E. Hayhurst, M. Horsburgh, J. Hobbs, and S. Foster, "Bacterial cell enlargement requires control of cell wall stiffness mediated by peptidoglycan hydrolases," *MBio*, 2015.

- [66] S. J. Foster, "Molecular characterization and functional analysis of the major autolysin of *Staphylococcus aureus* 8325/4," *J. Bacteriol.*, 1995.
- [67] L. Pasztor, A. Ziebandt, M. Nega, M. Schlag, S. Haase, M. Franz-Wachtel, J. Madlung, A. Nordheim, D. Heinrichs and F. Götz, "Staphylococcal major autolysin (Atl) is involved in excretion of cytoplasmic proteins," *J. Biol. Chem.*, 2010.
- [68] R. Biswas, N. Göhring, M. Schlag, M. Josten, G. Xia, F. Hegler, C. Gekeler, A. Gleske, F. Götz, H. Sahl, A. Kappler and A. Peschel, "Proton-binding capacity of *Staphylococcus aureus* wall teichoic acid and its role in controlling autolysin activity," *PLoS One*, 2012.
- [69] J. J. Perry, J. T. Staley, and S. Lory, *Microbial life*. Sinauer Associates Incorporated, 2002.
- [70] X. Zhou, D. Halladin, E. Rojas, E. Koslover, T. Lee, K. Huang and J. Theriot, "Mechanical crack propagation drives millisecond daughter cell separation in *Staphylococcus aureus*," *Science (80)*, 2015.
- [71] D. W. Adams and J. Errington, "Bacterial cell division: Assembly, maintenance and disassembly of the Z ring," *Nature Reviews Microbiology*. 2009.
- [72] V. R. Steele, A. L. Bottomley, J. Garcia-Lara, J. Kasturiarachchi, and S. J. Foster, "Multiple essential roles for EzrA in cell division of *Staphylococcus aureus*," *Mol. Microbiol.*, 2011.
- [73] C. A. Hale and P. A. J. De Boer, "Direct binding of FtsZ to ZipA, an essential component of the septal ring structure that mediates cell division in *E. coli*," *Cell*, 1997.
- [74] P. A. Levin, I. G. Kurtser, and A. D. Grossman, "Identification and characterization of a negative regulator of FtsZ ring formation in *Bacillus subtilis*," *Proc. Natl. Acad. Sci. U. S. A.*, 1999.
- [75] J. A. Thanassi, "Identification of 113 conserved essential genes using a high-throughput gene disruption system in *Streptococcus pneumoniae*," *Nucleic Acids Res.*, 2002.
- [76] K. Wacnik, "Dissecting cell division in the human pathogen *Staphylococcus aureus*." University of Sheffield, 2016.
- [77] V. Lund, K. Wacnik, R. Turner, B. Cotterell, C. Walther, S. Fenn, F. Grein, A. Wollman, M. Leake, N. Olivier, A. Cadby, S. Mesnage, S. Jones and S. Foster, "Molecular coordination of *Staphylococcus aureus* cell division," *Elife*, vol. 7, pp. 1–31, 2018.
- [78] V. R. F. Matias and T. J. Beveridge, "Cryo-electron microscopy of cell division in *Staphylococcus aureus* reveals a mid-zone between nascent cross walls," *Mol. Microbiol.*, 2007.
- [79] A. L. Bottomley, A. F. Kabli, A. F. Hurd, R. D. Turner, J. Garcia-Lara, and S. J. Foster, "*Staphylococcus aureus* DivIB is a peptidoglycan-binding protein that is required for a morphological checkpoint in cell division," *Mol. Microbiol.*, 2014.
- [80] S. J. Holden, T. Pengo, K. L. Meibom, C. F. Fernandez, J. Collier, and S. Manley, "High throughput 3D super-resolution microscopy reveals *Caulobacter crescentus* *in vivo* Z-ring organization," *Proc. Natl. Acad. Sci. U. S. A.*, 2014.
- [81] M. Jacq, V. Adam, D. Bourgeois, C. Moriscot, A. Di Guilmi, T. Vernet and C. Morlot, "Remodeling of the Z-ring nanostructure during the *Streptococcus pneumoniae* cell cycle revealed by photoactivated localization microscopy," *MBio*, 2015.
- [82] J. Buss, C. Coltharp, G. Shtengel, X. Yang, H. Hess, and J. Xiao, "A Multi-layered Protein Network Stabilizes the *Escherichia coli* FtsZ-ring and Modulates Constriction Dynamics," *PLoS Genet.*, 2015.
- [83] A. M. Whatmore and R. H. Reed, "Determination of turgor pressure in *Bacillus subtilis*: A possible role for K⁺ in turgor regulation," *J. Gen. Microbiol.*, 1990.
- [84] P. MITCHELL and J. MOYLE, "Permeability of the Envelopes of *Staphylococcus aureus* to some Salts, Amino Acids, and Non-Electrolytes," *J. Gen. Microbiol.*, 1959.
- [85] X. Yao, M. Jericho, and D. Pink, "Thickness and Elasticity of Gram-Negative Murein Sacculi Measured by Atomic Force Microscopy," vol. 181, no. 22, pp. 6865–6875, 1999.
- [86] R. D. Turner, S. Mesnage, J. K. Hobbs, and S. J. Foster, "Molecular imaging of glycan chains couples cell-wall polysaccharide architecture to bacterial cell morphology," *Nat. Commun.*, vol. 9, no. 1, 2018.
- [87] A. Touhami, M. H. Jericho, and T. J. Beveridge, "Atomic Force Microscopy of Cell Growth and Division in *Staphylococcus aureus*," *Society*, vol. 186, no. 11, pp. 3286–3295, 2004.
- [88] A. L. Koch, P. Demchick, and A. L. Koch, "The permeability of the wall fabric of *Escherichia coli* and *Bacillus subtilis*," *Journal of bacteriology : JB.*, vol. 178, no. 3. [Washington, DC] :, pp. 768–773, 1996.
- [89] J. Tam and D. Merino, "Stochastic optical reconstruction microscopy (STORM) in comparison with stimulated emission depletion (STED) and other imaging methods," *Journal of*

- Neurochemistry*. 2015.
- [90] R. Henriques, C. Griffiths, E. H. Rego, and M. M. Mhlanga, "PALM and STORM: Unlocking live-cell super-resolution," *Biopolymers*, 2011.
- [91] A. Bartesaghi, S. Banerjee, V. Falconieri, P. Rao, A. Merk, M. Davis, R. Pragani, M. Boxer, L. Earl, J. Milne and S. Subramaniam, "Breaking Cryo-EM Resolution Barriers to Facilitate Drug Discovery," *Cell.*, vol. 165, no. 7. Cambridge, Mass. :, pp. 1698–1707, 2016.
- [92] M. Beeby, J. C. Gumbart, B. Roux, and G. J. Jensen, "Architecture and assembly of the Gram-positive cell wall," *Mol. Microbiol.*, 2013.
- [93] L. Gan, S. Chen, and G. J. Jensen, "Molecular organization of Gram-negative peptidoglycan," *Proc. Natl. Acad. Sci.*, 2008.
- [94] H. ROHRER, "THE SCANNING TUNNEL MICROSCOPE," *Zeitschrift fur Kristallographie.*, vol. 162, no. 1–4. p. 23, 1983.
- [95] G. Binnig, C. F. Quate, and C. Gerber, "Atomic force microscope," *Phys. Rev. Lett.*, vol. 56, no. 9, p. 930, 1986.
- [96] P. Parot, Y. Dufrêne, P. Hinterdorfer, C. Le Grimmellec, D. Navajas, J. Pellequer and S. Scheuring, "Past, present and future of atomic force microscopy in life sciences and medicine," in *Journal of Molecular Recognition*, 2007.
- [97] Y. L. Lyubchenko, L. S. Shlyakhtenko, and T. Ando, "Imaging of nucleic acids with atomic force microscopy," 2011.
- [98] D. J. Muller, "AFM: A nanotool in membrane biology," *Biochemistry*, vol. 47, no. 31, pp. 7986–7998, 2008.
- [99] D. de Oteyza, P. Gorman, Y. Chen, S. Wickenburg, A. Riss, D. Mowbray, G. Etkin, Z. Pedramrazi, H. Tsai, A. Rubio, M. Crommie and F. Fischer, "Direct Imaging of Covalent Bond Structure in Single-Molecule Chemical Reactions," *Science (80)*, vol. 340, no. 6139, pp. 1434–1437, 2013.
- [100] K. Kaiser, L. Gross, and F. Schulz, "A Single-Molecule Chemical Reaction Studied by High-Resolution Atomic Force Microscopy and Scanning Tunneling Microscopy Induced Light Emission," *ACS Nano*, vol. 13, no. 6, pp. 6947–6954, Jun. 2019.
- [101] R. P. Feynman, "There's plenty of room at the bottom," *Miniaturization*, pp. 282–296, 1959.
- [102] J. M. Tour, "Top-down versus bottom-up fabrication of graphene-based electronics," *Chem. Mater.*, vol. 26, no. 1, pp. 163–171, 2014.
- [103] P. A. Sloan and R. E. Palmer, "Two-electron dissociation of single molecules by atomic manipulation at room temperature," *Nature*, vol. 434, no. 7031, pp. 367–371, 2005.
- [104] O. Custance, R. Perez, and S. Morita, "Atomic force microscopy as a tool for atom manipulation," *Nat. Nanotechnol.*, vol. 4, no. 12, p. 803, 2009.
- [105] O. Sahin, S. Magonov, C. Su, C. F. Quate, and O. Solgaard, "An atomic force microscope tip designed to measure time-varying nanomechanical forces," *Nat. Nanotechnol.*, vol. 2, no. 8, p. 507, 2007.
- [106] Y. Dufrêne, T. Ando, R. Garcia, D. Alsteens, D. Martinez-Martin, A. Engel, C. Gerber and D. Müller, "Imaging modes of atomic force microscopy for application in molecular and cell biology," *Nat. Nanotechnol.*, vol. 12, no. 4, pp. 295–307, 2017.
- [107] A. Viljoen, S. J. Foster, G. E. Fantner, J. K. Hobbs, and Y. F. Dufrêne, "Scratching the Surface: Bacterial Cell Envelopes at the Nanoscale," *MBio*, vol. 11, no. 1, 2020.
- [108] K. Iwata, S. Yamazaki, P. Mutombo, P. Hapala, M. Ondráček, P. Jelínek and Y. Sugimoto "Chemical structure imaging of a single molecule by atomic force microscopy at room temperature," *Nat. Commun.*, vol. 6, no. 1, p. 7766, 2015.
- [109] A. L. B. Pyne and B. W. Hoogenboom, "Imaging DNA structure by atomic force microscopy," in *Chromosome Architecture*, Springer, 2016, pp. 47–60.
- [110] L. Kailas, E. C. Ratcliffe, E. J. Hayhurst, M. G. Walker, S. J. Foster, and J. K. Hobbs, "Immobilizing live bacteria for AFM imaging of cellular processes," *Ultramicroscopy*, vol. 109, no. 7, pp. 775–780, 2009.
- [111] L. Chopinet, C. Formosa, M. P. Rols, R. E. Duval, and E. Dague, "Imaging living cells surface and quantifying its properties at high resolution using AFM in QI™ mode," *Micron*, vol. 48, pp. 26–33, 2013.
- [112] A. R. Kirby, A. P. Gunning, K. W. Waldron, V. J. Morris, and A. Ng, "Visualization of plant cell walls by atomic force microscopy," *Biophys. J.*, vol. 70, no. 3, pp. 1138–1143, 1996.

- [113] P. Vettiger, M. Despont, U. Drechsler, U. Durig, W. Haberle, M. Lutwyche, H. Rothuizen, R. Stutz, R. Widmer and G. Binnig, "The 'Millipede'—More than thousand tips for future AFM storage," *IBM J. Res. Dev.*, vol. 44, no. 3, pp. 323–340, 2000.
- [114] A. Pataquiva-Mateus and E. R. Dorantes, "Teaching Nanotechnology as a Framework of Social Inclusion, Empowerment, and Deep Learning," in *International Conference on Interactive Collaborative Learning*, 2016, pp. 468–478.
- [115] Y. E. Pak, "Crack extension force in a piezoelectric material," 1990.
- [116] J. P. Coffin IV, T. J. Gerhardt, M. A. Mills, and M. E. Kiani, "Photodiode detector with integrated noise shielding." Google Patents, 06-Feb-2001.
- [117] J. K. Hobbs, N. Mullin, C. H. M. Weber, O. E. Farrance, and C. Vasilev, "'Watching' processes in soft matter with SPM," *Mater. Today*, vol. 12, no. 7–8, pp. 26–33, 2009.
- [118] P. Eaton and P. West, *Atomic Force Microscopy*. 2010.
- [119] J. N. Israelachvili, *Intermolecular and surface forces*. Academic press, 2015.
- [120] E. F. Haugh and J. O. Hirschfelder, "Pi-electron forces between conjugated double bond molecules," *J. Chem. Phys.*, vol. 23, no. 10, pp. 1778–1796, 1955.
- [121] B. W. Ninham and V. A. Parsegian, "van der Waals Forces across Triple-layer Films," *J. Chem. Phys.*, vol. 52, no. 9, pp. 4578–4587, 1970.
- [122] J. N. Israelachvili, "The nature of van der Waals forces," *Contemp. Phys.*, vol. 15, no. 2, pp. 159–178, 1974.
- [123] H. Margenau, "NR Kestner in Theory of Intermodular Forces." Pergamon Press, New York (and references therein), 1971.
- [124] E. A. Moelwyn-Hughes, *States of Matter*. Oliver and Boyd, 1961.
- [125] R. Prasanna Misra, S. Das, and S. K. Mitra, "Electric double layer force between charged surfaces: Effect of solvent polarization," *J. Chem. Phys.*, vol. 138, no. 11, p. 114703, 2013.
- [126] B. V. Derjaguin, N. V. Churaev, and V. M. Muller, "The Derjaguin—Landau—Verwey—Overbeek (DLVO) theory of stability of lyophobic colloids," in *Surface Forces*, Springer, 1987, pp. 293–310.
- [127] H. K. Christenson, "DLVO (Derjaguin—Landau—Verwey—Overbeek) theory and solvation forces between mica surfaces in polar and hydrogen-bonding liquids," *J. Chem. Soc. Faraday Trans. 1 Phys. Chem. Condens. Phases*, vol. 80, no. 7, pp. 1933–1946, 1984.
- [128] D. J. Müller, M. Amrein, and A. Engel, "Adsorption of biological molecules to a solid support for scanning probe microscopy," *J. Struct. Biol.*, vol. 119, no. 2, pp. 172–188, 1997.
- [129] D. J. Müller, D. Fotiadis, S. Scheuring, S. A. Müller, and A. Engel, "Electrostatically balanced subnanometer imaging of biological specimens by atomic force microscope," *Biophys. J.*, vol. 76, no. 2, pp. 1101–1111, 1999.
- [130] K. W. Kolasinski, *Surface science: foundations of catalysis and nanoscience*. John Wiley & Sons, 2012.
- [131] B. Pittenger, N. Erina, and C. Su, "Quantitative Mechanical Property Mapping at the Nanoscale with PeakForce QNM," *Bruker Appl. Note AN128*, vol. AN128, 2010.
- [132] F. J. Giessibl, "Advances in atomic force microscopy," *Rev. Mod. Phys.*, vol. 75, no. 3, p. 949, 2003.
- [133] Q. Zhong, D. Inniss, K. Kjoller, and V. B. Elings, "Fractured polymer/silica fiber surface studied by tapping mode atomic force microscopy," *Surf. Sci. Lett.*, vol. 290, no. 1–2, pp. L688–L692, 1993.
- [134] D. Fotiadis, S. Scheuring, S. A. Müller, A. Engel, and D. J. Müller, "Imaging and manipulation of biological structures with the AFM," *Micron*, vol. 33, no. 4, pp. 385–397, 2002.
- [135] L. Zitzler, S. Herminghaus, and F. Mugele, "Capillary forces in tapping mode atomic force microscopy," *Phys. Rev. B*, vol. 66, no. 15, p. 155436, 2002.
- [136] A. Rosa-Zeiser, E. Weilandt, S. Hild, and O. Marti, "Simultaneous measurement of elastic, electrostatic and adhesive properties by scanning force microscopy: Pulsed-force mode operation," *Meas. Sci. Technol.*, vol. 8, no. 11, pp. 1333–1338, 1997.
- [137] H. J. Butt, B. Cappella, and M. Kappl, "Force measurements with the atomic force microscope: Technique, interpretation and applications," *Surface Science Reports*. 2005.
- [138] H. Krottil, T. Stifter, H. Waschipky, K. Weishaupt, S. Hild, and O. Marti, "Pulsed force mode: a new method for the investigation of surface properties," *Surf. Interface Anal.*, vol. 27, no. 56, pp. 336–340, 1999.
- [139] P. J. De Pablo, J. Colchero, J. Gómez-Herrero, and A. M. Baró, "Jumping mode scanning force microscopy," *Appl. Phys. Lett.*, vol. 73, no. 22, pp. 3300–3302, 1998.
- [140] J. Sotres, A. Lostao, C. Gómez-Moreno, and A. M. Baró, "Jumping mode AFM imaging of

- biomolecules in the repulsive electrical double layer," *Ultramicroscopy*, vol. 107, no. 12, pp. 1207–1212, 2007.
- [141] F. Moreno-Herrero, J. Colchero, J. Gómez-Herrero, and A. M. Baro, "Atomic force microscopy contact, tapping, and jumping modes for imaging biological samples in liquids," *Phys. Rev. E - Stat. Nonlinear, Soft Matter Phys.*, vol. 69, no. 3 1, pp. 1–9, 2004.
- [142] F. Moreno-Herrero, P. J. De Pablo, R. Fernández-Sánchez, J. Colchero, J. Gómez-Herrero, and A. M. Baró, "Scanning force microscopy jumping and tapping modes in liquids," *Appl. Phys. Lett.*, vol. 81, no. 14, pp. 2620–2622, 2002.
- [143] O. Sahin, "Harnessing bifurcations in tapping-mode atomic force microscopy to calibrate time-varying tip-sample force measurements," *Rev. Sci. Instrum.*, 2007.
- [144] JPK Instruments, "QI™ mode - Quantitative Imaging with the NanoWizard® 3 AFM," *Tech. Note (JPK Instruments)*, 2011.
- [145] P. Hansma, J. Cleveland, M. Madmacher, D. Walters, P. Hillner, M. Bezanilla, M. Fritz, D. Vie, H. Hansma, C. Prater, J. Massie, L. Fukunaga, G. Gurley and V. Elings, "Tapping mode atomic force microscopy in liquid," *Appl. Phys. Lett.*, vol. 64, no. 13, pp. 26–28, 1994.
- [146] R. García, *Dynamic atomic force microscopy methods*, vol. 47, no. 6–8, 2002.
- [147] Bruker Corporation, "NanoScope Analysis 1.50 manual," no. page 13.
- [148] T. Fukuma, K. Onishi, N. Kobayashi, A. Matsuki, and H. Asakawa, "Atomic-resolution imaging in liquid by frequency modulation atomic force microscopy using small cantilevers with megahertz-order resonance frequencies," *Nanotechnology*, vol. 23, no. 13, p. 135706, 2012.
- [149] J. P. Cleveland, F. Ohnesorge, D. A. Walters, P. K. Hansma, and T. E. Scha, "Studies of vibrating atomic force microscope cantilevers in liquid," vol. 80, no. April, pp. 0–5, 1996.
- [150] S. Kumar, M. Cartron, N. Mullin, P. Qian, G. Leggett, C. Hunter and J. Hobbs, "Direct Imaging of Protein Organization in an Intact Bacterial Organelle Using High-Resolution Atomic Force Microscopy," *ACS Nano*, 2017.
- [151] M. Pfreundschuh, D. Martinez-Martin, E. Mulvihill, S. Wegmann, and D. J. Muller, "Multiparametric high-resolution imaging of native proteins by force-distance curve-based AFM," *Nat. Protoc.*, 2014.
- [152] D. Fotiadis, S. Scheuring, S. A. Müller, A. Engel, and D. J. Müller, "Imaging and manipulation of biological structures with the AFM," *Micron*. 2002.
- [153] Y. F. Dufrêne, "Using nanotechniques to explore microbial surfaces," *Nature Reviews Microbiology*. 2004.
- [154] R. Azumi, M. Matsumoto, Y. Kawabata, T. Ichimura, T. Mizuno, and H. Miyamoto, "Atomic Force Microscopic Study of Vesicles of Synthetic Surfactant, Vesicles of Thylakoid Membrane, and Whole Cells of Bacteria," *Chem. Lett.*, 1991.
- [155] R. D. Turner, N. H. Thomson, J. Kirkham, and D. Devine, "Improvement of the pore trapping method to immobilize vital coccoid bacteria for high-resolution AFM: A study of *Staphylococcus aureus*," *J. Microsc.*, vol. 238, no. 2, pp. 102–110, 2010.
- [156] J. M. Burns, "High Resolution Atomic Force Microscopy Imaging of Living Bacterial Surfaces," University of Sheffield, 2017.
- [157] G. Francius, O. Domenech, M. P. Mingeot-Leclercq, and Y. F. Dufrêne, "Direct observation of *Staphylococcus aureus* cell wall digestion by lysostaphin," *J. Bacteriol.*, 2008.
- [158] Y. F. Dufrêne, "Towards nanomicrobiology using atomic force microscopy," *Nat. Rev. Microbiol.*, vol. 6, no. 9, pp. 674–680, 2008.
- [159] R. Saar Dover, A. Bitler, E. Shimon, P. Trieu-Cuot, and Y. Shai, "Multiparametric AFM reveals turgor-responsive net-like peptidoglycan architecture in live *streptococci*," *Nat. Commun.*, 2015.
- [160] G. Andre, S. Kulakauskas, M. Chapot-Chartier, B. Navet, M. Deghorain, E. Bernard, P. Hols and Y. Dufrêne, "Imaging the nanoscale organization of peptidoglycan in living *Lactococcus lactis* cells," *Nat. Commun.*, 2010.
- [161] M. Plomp, T. J. Leighton, K. E. Wheeler, H. D. Hill, and A. J. Malkin, "In vitro high-resolution structural dynamics of single germinating bacterial spores," *Proc. Natl. Acad. Sci. U. S. A.*, 2007.
- [162] G. E. Fantner, R. J. Barbero, D. S. Gray, and A. M. Belcher, "Kinetics of antimicrobial peptide activity measured on individual bacterial cells using high-speed atomic force microscopy," *Nat. Nanotechnol.*, 2010.
- [163] D. Heesterbeek, B. Bardoel, E. Parsons, I. Bennett, M. Ruyken, D. Doorduijn, R. Gorham, E. Berends, A. Pyne, B. Hoogenboom and S. Rooijackers, "Bacterial killing by complement requires membrane attack complex formation via surface-bound C5 convertases," *EMBO J.*, 2019.

- [164] Y. Wu and A. Zhou, "Fluctuations in adhesion behavior of dividing/budding mycobacterium sp. strains JLS, KMS, MCS: An AFM evaluation," *Micron*, 2010.
- [165] H. Eskandarian, P. Odermatt, J. Ven, M. Hannebelle, A. Nievergelt, N. Dhar, J. McKinney and G. Fantner, "Division site selection linked to inherited cell surface wave troughs in mycobacteria," *Nat. Microbiol.*, 2017.
- [166] Y. Wu, R. C. Sims, and A. Zhou, "AFM resolves effects of ethambutol on nanomechanics and nanostructures of single dividing mycobacteria in real-time," *Phys. Chem. Chem. Phys.*, 2014.
- [167] K. Li, X. Yuan, H. Sun, L. Zhao, R. Tang, Z. Chen, Q. Qin, X. Chen, Y. Zhang and H. Su, "Atomic force microscopy of side wall and septa peptidoglycan from *Bacillus subtilis* reveals an architectural remodeling during growth," *Front. Microbiol.*, vol. 9, no. MAR, pp. 1–6, 2018.

Chapter 2 Materials and Methods

2.1 Materials

2.1.1 Bacterial strains

Bacterial strains were taken from Microbank™ storage beads (Pro Lab) kept at -80 °C and grown on solid media plates (see *section 2.2.1*). The plates were incubated overnight at 37 °C and stored at 4 °C for up to 4 weeks. All the strains used in this study are listed in *Table 2.1*.

Table 2.1 – Bacterial strains used in sections and chapters of this thesis

<i>Specie</i>	<i>Strain (SJF collection)</i>	<i>Genotype/marker</i>	<i>Sections</i>	<i>Source</i>
<i>S. aureus</i>	SH1000 (682)	Functional rsbU ⁺ derivative of 8325-4	Chapters 3,4 and 7	Horsburgh <i>et al.</i> [1]
<i>S. aureus</i>	SH1000 <i>tarO</i> (5290)	<i>tarO::ermB/pCU1-tarO⁺</i>	Section 5.1	Foster Lab
<i>S. aureus</i>	SH1000 <i>ItaS</i> (5159)	Δ <i>ItaS</i> <i>gdpP::kan</i>	Section 5.2	Foster Lab
<i>S. aureus</i>	SH1000 <i>sagB</i> (4167)	<i>sagB::kan</i>	Section 5.3	Weeler-Turner <i>et al.</i> [2]
<i>S. aureus</i>	SH1000 <i>pbp3</i> (4425)	<i>pbp3</i> disrupted by insertion of Tn	Section 5.4	K. Wacknik [3]
<i>S. aureus</i>	SH1000 <i>pbp4</i> (4421)	<i>pbp4</i> disrupted by insertion of Tn	Section 5.5	K. Wacknik [3]
<i>B. subtilis</i>	168 (1)	Standard lab strain HR <i>trpC2</i>	Chapter 6	Howard Crossley & Howard Rogers
<i>B. subtilis</i>	4264 (5149)	<i>trpC2</i> Δ <i>rsgl::</i> (<i>neo:spc</i>)	Section 6.3	Schirner-Errington <i>et al.</i> [4]
<i>B. subtilis</i>	4277 (5150)	<i>trpC2</i> Ω <i>neo3427</i> Δ <i>mreB</i> Δ <i>mbI::cat</i> Δ <i>mreBH::erm</i> Δ <i>rsgl::</i> (<i>neo:spc</i>) - Strictly Mg ²⁺ dependent	Section 6.3	Schirner-Errington <i>et al.</i> [4]

2.1.2 Antibiotics

Methicillin (Sigma, 51454-50MG) 10 mg ml⁻¹ stock solution was prepared in distilled water (dH₂O). Then, it was filter sterilized (0.22 μ m pore) and stored at -20 °C in 1 ml aliquots until further use. Vancomycin (Sigma, 1404-93-9) 10 mg ml⁻¹ stock solution was prepared in dH₂O. Then, it was filter sterilized (0.22 μ m pore) and stored at -20 °C in 1 ml aliquots until further use.

2.1.3 Buffers and solutions required for cell wall purification

2.1.3.1 Tris buffer

To prepare Tris buffer (50 mM, pH 7), first add 3 g of Tris base (Fisher Bioreagents, BP154-1) to 500 mL of dH₂O. Adjust to pH 7 using 1 M hydrochloric acid (HCl). Autoclave and store at room temperature.

2.1.3.2 Sodium dodecyl sulfate

To prepare a sodium dodecyl sulfate (SDS, Sigma-aldrich) solution (5 % w/v): Add 250 mL of dH₂O to 12.5 g of SDS in a suitable container and mix. Do not autoclave. Store at room temperature.

2.1.3.3 Pronase solution

To prepare a pronase stock solution of 20 mg ml⁻¹, first make a 1 M Tris buffer at pH 7.5 using 1 M HCl to adjust the pH. Then, make a 4 M sodium chloride solution. Combine 50 ml of dH₂O, 0.5 ml of 1 M Tris buffer and 0.125 ml 4M sodium chloride solution together with 1g of Pronase stock (Merck, 10165921001). Pronase is a mixture of several nonspecific endo- and exoprotease enzymes extracted from *Streptomyces griseus* that digest proteins down to single amino acids. This solution must be incubated at 31°C for 1 h. Then, filter sterilize the solution using a 0.22 µm filter and split it into 1 ml aliquotes and store at -20 °C for further use during cell wall purification protocol.

2.1.4 Buffers for Atomic force microscopy experiment

2.1.4.1 Imaging buffer for sacculi

Concentrations ranging 150-300 mM potassium chloride (KCl) buffer were used. To prepare this buffer dilute appropriate concentrations from 1 M KCl stock and add 10 mM Tris-HCl to achieve pH 7.8. Usually final volumes used were between 10-20 ml. The buffer was filtered with 0.22 µm pore filter and stored until further use at room temperature. Every buffer was used a maximum length of time of 1 month. The night before an experiment the buffer was put inside the AFM isolation chamber.

2.1.4.2 – Imaging buffer for living cells

For *S. aureus*, an imaging buffer with concentrations ranging 200-300 mM potassium chloride (KCl) plus 10 mM Tris-HCl (pH 7.8) was used. For *B. subtilis*, an imaging buffer of 5 mM Tris-HCl (pH 7.8) was used. These buffers were prepared following *section 2.1.4.1*.

2.1.4.2 Buffers for surface coatings

To prepare 0.1 M of Sodium Bicarbonate (NaHCO₃, Sigma) add 0.25 g into 30 ml of dH₂O and mix well. To prepare 1 M of Sodium hydroxide (NaOH, Sigma) add 1.2 g into 30 ml of dH₂O and mix well. Then, the buffers should be filtered with a 0.22 μm pore filter and stored until further use at 4°C.

2.1.5 Substrates for Atomic force microscopy experiments

2.1.5.1 Mica discs

Mica is a natural mineral from various deposits (the highest quality muscovite mica deposit is located in India). The density of this mineral is approximately 3 g cm⁻³ with the chemical formula K₃Si₃O₁₀(OH)₂. This is the ideal substrate for AFM experiments because this material cleaves on the <001> plane producing a clean substrate to deposit samples, even atomically thin objects like graphene. Commercially available mica sheets (ProSciTech, WSL) vary in thickness from 0.15-0.21 mm. In terms of properties, it is a dielectric material, stable in water, solvents and inert to most acids. This allows for a robust performance when working with biological samples which sometimes require certain treatments, non-damaging to the mica.

2.1.5.2 Glass coverslips

High precision glass coverslip (Marienfeld) were used as flat substrate for both purified CW and living cells. The most appropriate dimensions were 24x24 mm square coverslips with 170 μm thickness. Circular 28 mm gridded glass coverslips of 170 μm thickness (Ibidi, cells in focus) with an area of 50x50 μm² for each grid were used for colocalization experiments. The glass surface from these coverslips is flat and clean, but to avoid small glass irregularities, all the coverslips undergo a cleaning protocol before being used for AFM purposes (see *section 2.3.1.2*).

2.1.5.3 Silicon grids

Silicon grids custom made (NuNano) using laser-writing technique were used for *S. aureus* live cell trapping. The dimensions of the grids were approximately 1.4 μm diameter and 700 nm deep separated by a distance of 4 μm both in the horizontal and vertical directions. These grids were not highly efficient trapping *tarO* cells because the distance between each hole was too big, causing the AFM probe to go blunt upon scanning large areas to find an appropriately attached cell. The same dimensions with less distance between the holes would be ideal for future experiments.

2.1.5.4 Complementary materials for substrate preparation

Several materials are used routinely for AFM sample preparation. One key element when preparing flat surfaces for AFM is the glue between the elements must be tight and stable without causing dilation or other movements over time. A green rubber used as metrology casting material is the ideal adhesive that ensures the best performance for AFM imaging because it cures almost instantly (in 2-4 min) and leaves no space between components. This green adhesive (Thin pour, Reprorubber, Flexbar) is made of PDMS copolymer with SiO_2 filler. This two-part yellow and blue adhesive (green glue), has been used throughout this thesis. Circular metallic stubs of 9-14 mm diameter (ProSciTech) were used to support other fragile substrates like mica discs or silicon grids. Then, the substrate and the sample can be magnetically attached to the AFM stage.

2.1.6 Surface Coatings for Atomic force microscopy experiments

2.1.6.1 Poly-L-Lysin (PLL)

Poly-L-Lysin (PLL, Sigma-aldrich) is a polymer formed by consecutive lysin (Lys) amino-acid. It is compatible with biological material and it forms a thin network of positively charged chains that spread uniformly onto the supporting surface.

2.1.6.2 Cell-Tak™ tissue adhesive

Cell-Tak™ tissue adhesive in 5% acetic acid (Cell-Tak, Corning) is a synthetic product based on polyphenolic proteins extracted from marine mussels. These proteins are responsible for the marine mussels to firmly attach to rocks through a high number of weak interactions. These proteins were used in many other studies specially involving

eukaryotic cells. This coating has been used to attach eukaryotic cells onto flat surfaces.[5]

2.1.7 Atomic force microscopy probes

All probes used in this thesis were commercially available (Bruker AFM Probes). The different probes used according to the experiment are described below in *Table 2.2*.

Table 2.2 – AFM probes with their names and physical characteristics

<i>Probe name</i>	<i>Environment</i>	<i>Nominal resonant frequency (kHz)</i>	<i>Nominal spring constant ($N m^{-1}$)</i>	<i>Length (μm)</i>	<i>Nominal tip radius (nm)</i>
<i>Tespa-V2</i>	Air	320	37	123	7
<i>FastScan-A</i>	Air	1400	18	27	5
<i>MLCT (E)</i>	Liquid	38	0.1	140	20
<i>ScanAsyst-Fluid</i>	Liquid	150	0.7	70	20
<i>FastScan-D</i>	Liquid	110	0.25	16	5

2.1.8 Sacculi dilutions and batches

The sacculi from bacterial strains was prepared in different days, each corresponds to a different batch (see *Table 2.3*). The same strain (e.g. SH1000) can be prepared in different batches, representing independent biological repeats. Most of the strains on this thesis were only prepared once. Many technical repeats were performed by imaging in different AFM sessions or preparing different samples attached to a substrate. Those have not been classified here.

Table 2.3 – Sacculi batches prepared independently from different strains and conditions

<i>Batch name</i>	<i>Strain</i>	<i>Date finished</i>	<i>Conditions</i>
<i>Batch 1</i>	SH1000	09.01.2017	Stock A and B; $OD_{600} = 0.5$
<i>Batch 2</i>	SH1000	04.05.2017	Stock A; $OD_{600} = 1.2$
<i>Batch 3</i>	SH1000	09.05.2017	Stock A and B; $OD_{600} = 0.5$
<i>Batch 4</i>	SH1000	22.07.2017	Stock A; $OD_{600} = 0.5$
<i>Batch 5</i>	SH1000	20.11.2017	Stock A; Different ODs
<i>Batch 6</i>	SH1000	24.01.2018	Stock A; Methicillin
<i>Batch 7</i>	SH1000 WT & sagB	June 2018	Stock A; Vancomycin
<i>Batch 8</i>	SH1000 ltaS	February 2019	Stock A;
<i>Batch 9</i>	SH1000 pbp3 & pbp4	March 2019	Stock A; $OD_{600} = 0.5$
<i>Batch 10</i>	168	23.03.2018	Stock A;
<i>Batch 11</i>	4264 & 4277	27.02.2019	Stock A;

The stock batches were not suitable for AFM imaging and dilutions have to be done with the OD₆₀₀ values summarized in *Table 2.4*.

Table 2.4 – Sacculi dilutions and their optical dispersity values

<i>Dilution name</i>	<i>OD₆₀₀</i>
<i>Dilution 1</i>	0.29
<i>Dilution 2</i>	0.73
<i>Dilution 3</i>	1.68
<i>Dilution 4</i>	2.35
<i>Dilution 5</i>	3.78
<i>Dilution 6</i>	7.49

2.2 Microbiology protocols

2.2.1 Cell growth conditions and growth/killing curves

2.2.1.1 Optical Density

To monitor cell growth in-situ, the cell density, or optical density (OD) of a liquid culture is measured using a spectrophotometer. To check the OD, first transfer 1 ml of the media used for growing the cells into a 1.6 ml polystyrene micro cuvette (Fisherbrand) which will serve as blank. Introduce the blank cuvette onto a Spectrophotometer programmed to measure at 600 nm wavelength (Biochrom, WPA Biowave) and press the Tare button. Then, transfer 1 ml of cell suspension into another cuvette a press the green button to measure to obtain the OD₆₀₀ value.

2.2.1.2 Growth conditions for *S. aureus*

All media were prepared using deionized water (dH₂O) and autoclaved at 125 °C for 20 min. For solid medium Bacteriological agar (VWR) 1.5% (w/v) was added to Tryptone soy broth (TSA, Oxoid) with a final concentration of 30 g l⁻¹. Cell colonies were grown on solid media at 37 °C without shaking for a minimum of 18 h. For liquid medium only Tryptone soy broth (TSB) with a concentration of 30 g l⁻¹ was prepared. Cell culture overnight was grown on liquid media at 37 °C with constant horizontal movement with shaking speeds between (180-250 rpm with open shaker) 21-40 g for a minimum of 16 h, achieving stationary phase.

2.2.1.3 Growth conditions for *B. subtilis*

For solid medium nutrient agar (NA, sigma-aldrich) with a final concentration of 28 g l⁻¹ was prepared. Cell colonies were grown on solid media at 37 °C without shaking for a minimum of 15 h. For liquid medium nutrient broth (NB, Oxoid) with a concentration of 13 g l⁻¹ was prepared. Cell culture overnight was grown on liquid media at 37 °C with constant horizontal movement with shaking speeds between (180-250 rpm with open shaker) 21-40 g for a minimum of 14 h, achieving stationary phase.

2.2.1.4 Growth conditions for *S. aureus* mutant strains

The strain Δ *ltaS gdpP::kan* in SH1000 background was grown on solid medium: bacteriological agar 1.5% (w/v) with Tryptone soy broth 30 g l⁻¹ together with selection antibiotics: Erythromycin (Ery) 5 µg ml⁻¹ and Kanamycin (Kan) 50 µg ml⁻¹. Cell colonies were grown on solid media at 37 °C without shaking for a minimum of 18 h. For liquid medium Tryptone soy broth 30 g l⁻¹ with selection antibiotics: Ery 5 µg ml⁻¹ and Kan 50 µg ml⁻¹ was prepared. Cell culture overnight was grown with the same conditions as *S. aureus* SH1000.

The strain *sagB::kan* in SH1000 background was grown on solid medium: bacteriological agar 1.5% (w/v) with Tryptone soy broth 30 g l⁻¹ together with the antibiotic, Kan 50 µg ml⁻¹ and Neomycin (Neo) 50 µg ml⁻¹. Cell culture overnight was grown with the same selection antibiotics. Cell growing conditions and liquid media were the same as *S. aureus* SH1000 (see section 2.2.1.2).

The strains *tarO*, *pbp3::Tn* and *pbp4::Tn* in SH1000 background were grown with the same conditions as *S. aureus* SH1000 (see section 2.2.1.2).

2.2.1.5 Growth conditions for *B. subtilis* mutant strains

The strain Δ *mreB* Δ *mbi* Δ *mrBH* in a *rsgI::spec* background was grown on solid medium: nutrient agar 28 g l⁻¹ together with a selection antibiotic: Ery 1 µg ml⁻¹ and 20 mM MgSO₄ to produce Mg⁺² ions. To check all the mutations were expressing correctly, another plate was prepared with the same conditions plus the following selection antibiotics: Kan 5 µg ml⁻¹, Chloramphenicol (Cm) 5 µg ml⁻¹ and Spectinomycin (Spec) 50 µg ml⁻¹. For liquid medium Nutrient broth 13 g l⁻¹ with 20 mM MgSO₄ to produce Mg⁺² was prepared. Cell culture overnight was grown with same conditions as *B. subtilis* 168 (see 2.2.1.3).

The strain *rsgl::spec* in *B. subtilis* 168 background was grown on solid medium: nutrient agar 28 g l⁻¹ together with a selection antibiotic: Spec 50 µg ml⁻¹. For liquid medium Nutrient broth 13 g l⁻¹ was prepared. Cell culture overnight was grown with same conditions as *B. subtilis* 168 (see 2.2.1.3).

2.2.1.6 Growth curves

A growth curve is performed to study the growth rate of bacterial cell cultures. The lag, exponential and stationary phases of *S. aureus* SH1000 growth have been extensively studied using standard growth conditions: culture volume= 50 ml; rotation= 40 g; inoculation from pre-cultured exponential phase cells. However, if the conditions change, the dynamics of the liquid movement might be different, potentially affecting the timing of the different phases. A growth curve with the same conditions used for peptidoglycan purification was performed: culture volume= 1000 ml; rotation= 26 g; starting OD₆₀₀=0.05; inoculation from overnight (stationary phase cells). First, prepare 1L of TSB and 300 ml of TSA, 2 days prior to the growth curve. Prepare 11 plates of TSA and store at 4 °C. Use stationary cells from overnight to inoculate a 2 L flask containing the 1 L liquid media with a starting OD₆₀₀=0.05. Start growth curve, measure the OD₆₀₀ every 15 min while simultaneously plating the cell suspension with serial PBS dilutions (10⁻² to 10⁻¹²) every 45 min. Total time of growth: 8h and 45 min. Each OD₆₀₀ measurement to build the growth curve was the arithmetic mean of three measurements. The plates were left to grow overnight at 37 °C and the colonies were counted obtaining the colony forming unit (CFU) ml⁻¹. In each dilution area (sixth of a plate) there were three droplets each containing 10 µl of cell suspension at each dilution. For example, if in the 10⁻⁶ dilution there were a mean number of 7 colonies, that represents 7x10⁸ CFU ml⁻¹. Finally, the OD₆₀₀ vs minutes and CFU ml⁻¹ vs minutes were plotted with the Log₁₀ of the y axis, as established in the microbiology community.

2.2.1.7 Killing curves with SDS

B. subtilis cells were challenged with different SDS concentrations to test which concentration will kill the cells within 1-2 h. First, a stock of SDS 10 % w/v was prepared. Then, different SDS concentrations were calculated to be added to 8 ml cell culture in

50 ml plastic tubes. *Equation 2.1* was used to calculate the volume of stock required in each tube to achieve the concentrations: 5, 2.5, 1, 0.5, 0.1, 0.05 and 0.01 % SDS.

$$V_{stock_SDS10\%} = \frac{C_{SDS} \cdot 8 \text{ ml}}{10 - C_{SDS}} \quad (\text{Eq. 2.1})$$

A total of 8 tubes with 10 ml cell culture were grown from an overnight inoculation to $OD_{600} \sim 0.55$. Then, 1 ml of cell culture from each tube was used to perform OD_{600} measurements and plates with serial PBS dilution ($0, 10^{-1}$ to 10^{-8}) as time 0 h. An extra 1 ml of cell culture from each tube was transferred to 1.5 ml plastic tubes and kept static at room temperature. Next, the respective amounts of SDS were added to 7 different tubes (with only 8 ml of cell culture remaining) and the killing started. The 7 tubes with SDS together with a control without SDS were kept under conventional microbiology conditions: 37 °C and continuous shaking at 250 rpm. After 1 h of SDS treatment OD_{600} measurements and plates were performed. At the same time, the tubes containing 1 ml of cell culture that were kept static at room temperature (which represents the conditions mimicking the AFM experiments) had 0, 5, 1, 0.1 and 0.01% SDS added. Immediately after, 200 μ l of cell suspension with SDS were used to form a droplet onto a high precision 24x24 mm glass coverslip and after 2h the total volume of sample was recovered from the glass coverslip and plated using the same serial dilution as the tubes. Finally, the OD_{600} vs minutes and $CFU \text{ ml}^{-1}$ vs minutes were plotted with the Log_{10} of the y axis for the SDS treatment in liquid under conventional microbiology conditions. $CFU \text{ ml}^{-1}$ vs minutes curve was plotted for the SDS treatment on a glass coverslip.

2.2.2 Cell Wall purification protocols

2.2.2.1 Cell Wall purification protocol for *S. aureus*

The purification of *S. aureus* cell wall was initially performed following the established protocol. [6] First an overnight 20 ml culture was prepared the day before from a single colony in a solid Agar plate. The next morning, the overnight culture is used to inoculate 1 L of bacterial culture (on a 2 L autoclaved conical flask) to an starting OD_{600} of 0.05 and grow to an OD_{600} of 0.5 under 37 °C and lateral shaking at 26 g. Then, the whole flask is chilled on ice. Centrifuge all the contents at 15,950 g for 10 min. After removing supernatant, the pellet is suspended with 1 ml of PBS buffer. The cell suspension is then split into approximately four 1.5 ml tubes. The tubes are boiled in a water bath for 10

min to kill the cells. Then, the contents are transferred to 2 ml Lysing matrix tubes with 0.1 mm silica beads (M.P. Biomedical, B 6911-100). The FastPrep-24™ 5G (M.P. Biomedical) is an homogenizer usually used to break organs and other biological materials. The tubes are treated 6 times with the FastPrep-24™ at predetermined speed of 6 during 30 s. Between each cycle leave at least 1 min for the machine to cool down. Check the breakage by optical microscopy, if 95% of the cells have not broken perform more FastPrep-24™ cycles if necessary. Spin down for 30 s at 170 g to separate the breaking beads (pellet) from broken cells (supernatant). Transfer supernatant to 1.5 ml tubes. Then, centrifuge for 3 minutes at 20,000 g and discard supernatant. This will allow only the heaviest part of the broken cells (the peptidoglycan) to remain on the pellet. Next, the pellets were resuspended into 1 ml of SDS 5 % (w/v) and boiled for 25 min to disrupt the lipid membrane (it is crucial the pellets are well resuspended). Centrifuge again for 3 min at 20,000 g and discard supernatant. Resuspend pellet again with 1 ml of SDS 5 % (w/v) and boiled for 15 min to ensure nothing more than the CW components remain in the pellet. After the SDS treatment, all the remaining SDS must be removed by centrifuging and resuspending pellets with distilled water five times. At the last cycle, the pellets are resuspended in 0.9 ml Tris-HCL (50 mM, pH 7) buffer, plus 0.1 ml of pronase stock solution. The mixture is incubated at 60 °C for 90 minutes, to digest any remaining surface proteins attached to the CW. Centrifuge again for 3 min at 20,000 g and resuspend pellet with distilled water. Centrifuge again and discard supernatant. Resuspend in minimal amount of HPLC-grade water (0.1 ml) and store at -20 °C until further use. If the protocol stops here, a purification of PG + WTA sacculi has been achieved. What has been labelled in this thesis as Stock A.

2.2.2.2 With and without wall teichoic acids (stocks A and B)

When experiments require working with purified PG without any teichoic acids, the same protocol as stated above is performed but after the last step before adding the minimal amount of HPLC-grade water, the following steps are followed to remove the teichoic acids from the PG. This part of the protocol is identical for any Gram-positive strains. Carefully observing local security and waste disposal measures, resuspend the pellet in 0.25 ml of hydrofluoric acid (HF). Incubate for 48 h at 4 °C. Centrifuge for 3 minutes at 20,000 g and safely discard supernatant and resuspend pellet in HPLC until

the supernatant is at least pH=5. Resuspend in minimal amount of HPLC-grade water (0.1 ml) and store at -20 °C until further use. This protocol purifies PG sacculi, what has been labelled in this thesis as Stock B.

2.2.2.3 Improvements from established protocol

The established protocol in *sections 2.2.2.1 and 2.2.2.2* was followed, except some changes were introduced early on and then followed throughout the rest of the thesis. First of all, after the 1 L of cell culture has been grown to OD₆₀₀ of 0.5 the liquid was poured into 50 ml falcon tubes and directly boiled in the water bath to immediately stop growth. Then, the tubes were centrifuged and the pellets were resuspended in 0.33 ml PBS and transferred to 1.5 ml tubes (as many as you need according to pellet volume). This change in order between boiling and centrifuging allows for a better control of the growth of the cells. In some cases (*e.g.* antibiotic treatment) this allows for a better control of the exact time-point needed for an experiment. Then, centrifuge centrifuge for 3 min and 30 s at 20,000 g, discard supernatant and resuspend in PBS to transfer into the minimal amount possible of FastPrep tubes. Then, during the FastPrep treatment, the cycle was repeated 11 times producing optimal breakage for *S. aureus* WT. Unless otherwise stated, the rest of the *S. aureus* strains were prepared with the same repetition number. This consistently produced good samples without the need to check the breakage percentage with the optical microscopy during the purification protocol. Leave tubes on ice a minimum of 3 min and 30 s between FastPrep cycles to avoid overheating the machine. After performing all the FastPrep cycle, spin down for 1 min at 170 g to separate the breaking beads from broken cells, the beads pellet moves if the tube is rotated, repeat this step as many times as necessary to obtain a sample free of beads. Finally, the last change from the established protocol is the storing conditions of the sample. Instead of keeping the sacculi at -20 °C, the sacculi stocks were kept at 4 °C to avoid aggregation between sacculi fragments. Then the stock must be diluted and tip sonicated (2.3.2.1) to obtain enough single layers to perform the experiments.

2.2.2.4 Cell Wall purification protocol for *B. subtilis*

The purification of *B. subtilis* cell wall is very similar as *S. aureus* except for the breakage method. According to [6] *B. subtilis* being a rod-shaped bacteria requires to be broken

with French Press method instead of FastPrep. However, due to technical difficulties using French Press, *B. subtilis* cells were broken with FastPrep. After an optimisation experiment, the optimal number of cycles was 15. The rest of the protocol was performed identically as *S. aureus* (see section 2.2.2.1) including the changes on section 2.2.2.3 (except for the FastPrep cycles). Unless otherwise stated, the rest of the *B. subtilis* strains were prepared following the same protocol.

2.2.2.5 Cell Wall purification for antibiotic treated cells

This experiment was never performed before. However, SIM microscopy of cells treated with antibiotics for several time-points was performed by Dr Milena L Von Und Zur Muhlen. [7] To obtain a direct comparison between AFM and SIM microscopy results, some parameters were matched exactly. The protocol of *S. aureus* cell wall purification explained in sections 2.2.2.1-3 was followed with the following exceptions.

An overnight culture from the desired strain is used to inoculate 1 L of bacterial culture to an starting OD₆₀₀ of 0.05 and grow to an OD₆₀₀ of 0.2-0.3. Then, the appropriate amount of antibiotic is added to a final concentration of 10 times the MIC concentration. For example, for Methicillin which has an MIC of 4µg/ml for *S. aureus*, the working concentration was 40µg/ml which for a 1 L volume it meant 4 ml of 10 mg/ml. These values will have to be adapted depending on the antibiotic to be used and their MIC concentration for the desired strain. Once the antibiotic is added, the cell culture continues to be in the same growing conditions of 37 °C and lateral shaking at 21 g. After the desired treatment time (e.g. 30 min) a partial volume of 300 ml is extracted and rapidly transferred to falcon tubes, which are immediately put on a water bath to boil for 10 min. This step substitute the glutaraldehyde fixing used in SIM microscopy, which has to be avoided for AFM imaging due to molecular perturbations to the PG architecture. The rest of the culture is kept undisturbed until the following time-point is required. From the initial volume, no more than 70 % of volume is used overall to purify all the different time-points. The rest of the protocol continues as normal.

2.3 Atomic Force Microscopy protocols

2.3.1 Substrate preparation

2.3.1.1 Mica discs

First, 9 mm diameter mica discs were either cut with a mica cutter from a bigger sheet. Alternatively, 9 mm mica discs can be obtained commercially. Then, the mica disc must be firmly attached to a metal stub using epoxy green glue. A minimal amount of green glue freshly mixed should be placed on the centre of the metal stub. Next, the mica disc is pressed against the stub uniformly distributing the glue underneath. Finally, after 2-4 min the glue is dry and the top layer of the mica disc can be cleaved using cello tape (magic scotch tape). The surface is then ready for coating or directly sample deposition.

2.3.1.2 High precision glass coverslip and glass etched grids

Firstly, the glass surfaces must be clean. This cleaning protocol works for the squared 24x24 mm high precision glass coverslip and the circular glass etched grids.

First, 150 ml of 1 M potassium hydroxide (KOH) is prepared in a 250 ml beaker, the coverslips are fit in a hard plastic rack and placed inside the beaker. They are washed with the 1 M KOH inside the ultrasound water bath during 15 min. Secondly, the whole rack is rinsed extensively with Milli-Q water (up to 4 times the volume used with the KOH). Then, submerged the rack with the glass coverslips in Milli-Q water while sonicating in the ultrasound water bath during 15 minutes. Finally, exchange the water and leave submerged in fresh Milli-Q for storage.

When a coverslip is needed for an AFM experiment, it has to be removed from the rack and dried with gentle N₂ flow. Then, the square coverslips are attached to a rectangular microscopy glass slide with green glue surrounding all the edges. The circular glass grids are attached to a mini petri dish of 60 mm diameter using the green glue around the edges. Finally, let the glue dry for 2-4 min and they are ready for coating or sample deposition.

2.3.1.3 Silicon grids

The commercial silicon grids (NuNano) are made in groups of 7 in a 11 cm diameter silicon wafer, the 5x5 mm grids must be cut and separated from the rest of the wafer with a diamond knife. Then, the grids are glued to a 9 mm metal stub with minimal amount of epoxy green glue. Finally, they should be washed with Milli-Q water and

inorganic solvent such as 70% Ethanol or 2-Propanol. The grids must be rinsed with extensive Milli-Q water and blow dried with N₂. Exception: if the silicon grid is custom made using photolithography and the last step to etch the silicon has not been performed, the rinsing step with inorganic solvent should be entirely avoided. Without the etching of the silicon, the grid pattern is created by the photo-resin which is soluble with inorganic solvent and the pattern would be erased completely.

2.3.2 Surface mounting and buffer for imaging of purified cell wall

2.3.2.1 Sacculi dilution and tip sonicating

After performing the cell purification protocols (see *section 2.2.2*) the resultant samples is a concentrated sacculi stock with OD₆₀₀ = 7 – 45. This sacculi must be diluted to obtain an appropriate sample distribution on the surface for AFM experiments. After optimization and testing of several concentrations, the optimal working concentration must have an OD₆₀₀ = 2.5 – 7.5 (see *Table 2.4*). Therefore, depending on the OD₆₀₀ of the stock the sample must be diluted more or less. Depending on the sample (*e.g.* with or without antibiotics) it might be required to further break the sacculi fragments using tip ultrasonic disintegrator technique. The sacculi dilution should have a minimal volume of 100 µl then. The smallest probe available from the tip disintegrator (Soniprep 150 plus, MSE). For *S. aureus* WT sacculi, the sacculi dilution should be sonicated for 3 cycles of 30 seconds at 2 mA, leaving at least 1 min between cycles to avoid overheating. For *B. subtilis* WT sacculi it should be 2 cycles of 10 seconds at 2 mA.

2.3.2.2 PLL coated surfaces for mounting sacculi in liquid

2.3.2.2.1 PLL coated glass

Firstly, a high-precision glass coverslip is cleaned according to (*section 2.3.1.2*) then 50 µl of commercially available 0.01% PLL (Sigma-Aldrich) is incubated for no more than 20 min. Then, the PLL is rinsed with water and blow dry it.

For Gram-negative bacteria (*e.g. E. coli*): put 5 µl of sacculi dilution on top of the PLL coated glass, add 15 µl of 10 mM Tris (pH=7.8), incubate for 20 min. Then, gently rinse with ~200-400 µl of 10mM Tris. For Gram-positive bacteria (*e.g. S. aureus and B. subtilis*): put 10 µl of sacculi dilution on top of the PLL coated glass and incubate for 90

min. Then, gently rinse with 1 ml HPLC-grade water. Do not let dry the sample at any point during this protocol.

The final step for all types of bacteria is to add an additional ~200 µl of the appropriate imaging buffer and place on AFM stage to be imaged in liquid.

2.3.2.2.2 *PLL coated mica*

Gram-positive bacteria can be attached to PLL coated mica by following the same protocol as PLL coated glass, just interchanging the glass coverslip for freshly cleaved mica (according to 2.3.1.1). For both substrates, the PLL coating only works to attach sacculi from Stock A (PG containing WTA). When, stock B was (PG without WTA) even incubated for more than 90 min, the sacculi attachment was too poor for both PLL coated glass and mica to perform high resolution imaging in liquid. If PLL wants to be used as coating, it is required to perform the drying step (see section 2.3.2.4).

2.3.2.3 Cell-Tak™ coated surfaces for mounting sacculi in liquid

2.3.2.3.1 *Cell-Tak™ coated glass*

In summary, the glass coverslip is cleaned according to (section 2.3.1.2), then the Cell-Tak™ is applied as recommended by the fabricant. The Cell-Tak™ will only be activated at a neutral pH (that is why it is diluted in acetic acid, pH 3). To achieve the change in pH, first add 285 µl of 0.1 M NaHCO₃ (pH=7) to the glass, then 10 µl of Cell-Tak™ and finally add 5 µl of 1 M NaOH (pH=14) to activate the adhesive properties of the Cell-Tak™. Do not incubate for more than 30 min (to avoid protein aggregation), ideally incubating for 25-30 min creates a uniform surface coating. Rinse the excess of Cell-Tak™ with 1 ml of HPLC-grade water and blow dry it. Then, put 10 µl of sample and incubate during 60 min for Stock A and 120 min for Stock B. Finally, gently rinse with 1 ml HPLC-grade water. Do not let the sample dry at any point during this protocol. Add an additional ~200 µl of the appropriate imaging buffer and place on AFM stage to be imaged in liquid.

2.3.2.3.2 *Cell-Tak™ coated mica*

The protocol to prepare a sample on Cell-Tak™ coated mica is very similar as the Cell-Tak™ coated glass by interchanging glass for freshly cleaved mica. The only exceptions

are the volumes used to coat the surface with Cell-Tak are smaller because of the reduced surface area from the mica with respect to the glass. Add 171 μL of 0.1 M NaHCO_3 (pH=7) to the mica, then 6 μL of Cell-TakTM and finally add 3 μL of 1 M NaOH (pH=14) to activate the adhesive properties of the Cell-TakTM.

Given that Cell-TakTM coated surfaces provide better attachment in general than PLL, to obtain consistency in the future, it was decided that all the experiments regarding Gram-positive sacculi in liquid should be performed using Cell-TakTM coated surfaces. Glass coverslips should be used only to perform correlative experiments with fluorescence microscopy.

2.3.2.4 Surface mounting in ambient conditions of purified cell wall

If the purified CW has to be imaged only in ambient conditions, the sacculi stock should be diluted using dilution 1 from *Table 2.4*. Then, 5 μL of sample should be added to a freshly cleaved mica surface. Carefully, use ~ 20 μL of HPLC-grade water to distribute the sample across the surface. Then dry the sample using N_2 flow.

By contrast, if the purified CW has to be imaged in both ambient conditions and liquid, the mica surface should be coated with Cell-Tak. Then, the same protocol used for liquid imaging is followed (*section 2.3.2.3.2*) but after the last rinsing step with 1 ml HPLC-grade water, dry the sample with N_2 flow. This step will produce higher attachment between the sacculi and the surface. The sample is then ready to be imaged in air and then rehydrated in liquid with no particular order. This protocol is known throughout the thesis as 'the drying step'.

2.3.2.5 Air to liquid correlation methods

Here are the correlation methods that were not very successful in correlating individual sacculi fragments. First, the gridded glass coverslips (2.1.5.2) were used. However, there is a difficulty to localize a specific sacculus, which has a surface area of approximately $1.5 \mu\text{m}^2$, within an area of $50 \times 50 \mu\text{m}^2$. Then, permanent ink marks were made on a squared glass coverslip prior to sample deposition. These marks guide where to locate the AFM tip with a smaller range of approximately $30 \times 30 \mu\text{m}$, easier to locate individual sacculi. The same approach was taken using mica as a substrate to avoid the drift problems caused by the air layers between the glass coverslip and the glass slide. The

permanent ink mark must be drawn after coating the mica surface but prior to sample deposition. Alternatively, the mark can be drawn after attaching the sample to the surface using the drying step (2.3.2.4).

2.3.3 Surface mounting to image live cells

2.3.3.1 *S. aureus* SH1000 live cells in silicon grids

Overnight cells were grown to an early exponential phase $OD_{600} = 0.5$. Approximately 10 ml of cell suspension were centrifuged for 5 min at 20,000 g and the supernatant was discarded. The pellet was rinsed with 10 mM Tris buffer three times and the final resuspension was done in 250 μ l of imaging buffer (2.1.4.2). Then 10 μ l of cell suspension was incubated for 10 min onto the silicon grids. Then, the droplet was almost completely dried using very gentle N_2 flow. Finally, 1 ml of HPLC-grade water was used to rinse the excess of non-attached cells. The silicon grid was glued down to the AFM stage with green glue and no more than 250 μ l of imaging buffer was added.

2.3.3.2 *S. aureus* SH1000 *tarO* live cells in silicon grids

The same protocol as 2.3.3.1 was followed. However, *tarO* cells did not attach to the surface without some extra steps after depositing the cell suspension onto the silicon grid. A custom made device was built with a 1.5 ml plastic tube, green glue and a mica disc. The mica disc serve as a support glued inside the tube. Then, green glue is added on one side of the mica disc to put the silicon grid with the cell suspension. Once the glue is dry and the grid is firmly attached, the tube is left open and the cells get incubated onto the grids for 40 min. Then, close the tube and centrifuge for 1 min at 42 g (do two cycles re-centring the cell droplet in between), do a last cycle of 170 g for 1 min. Remove the silicon grid from the tube using sharp tweezers and glue it down to a rectangular glass slide. Dry the rest of the droplet onto the grids with N_2 flow and proceed with the same protocol as SH1000 WT cells.

2.3.3.3 *B. subtilis* live cells in Cell Tak coated mica

Exponential phase cells were grown up to an $OD_{600}=0.3-0.5$. Approximately 4 ml of cell suspension were centrifuged for 5 min at 20,000 g and the supernatant was discarded. The pellet was rinsed with 5 mM Tris buffer three times and the final resuspension was

done in 100 μl of imaging buffer (2.1.4.2). Incubate 50-100 μl on Cell-Tak coated mica during 45 min. Finally, rinse 5 times with 100 μl of 5 mM Tris.

2.3.3.3.1 Imaging *B. subtilis* live cells with SDS treatment

After performing the protocol to image healthy *B. subtilis* cells and obtaining high-resolution images of several cells, the working liquid volume is between 150-200 μl . Using Eq. 2.1, approximately 55 μl from 10 % SDS stock should be added directly to the sample on the AFM stage to obtain a concentration of 2.5 %. Focus on a cell using aspect ratio 4 and use the video capture mode to constantly save the images. Then, add the appropriate amount of SDS to the solution and keep imaging in the same location to record the dynamic changes. A similar approach was taken to perform the 5 % SDS.

2.3.4 Achieve the highest resolution possible with Atomic force microscopy

2.3.4.1 Sacculi in liquid

When imaging sacculi in liquid it is crucial to use PeakForce/QNM mode instead of tapping. The best AFM probe to use is FastScan-D with laser spot 'small low thermal' (if the sum of the laser is too low it is better to change to 'Small' laser spot). Leave to thermally equilibrate the tip with the sample in 200 μl of buffer for at least 1 h. The day before imaging the buffer tube and the mica containing the sample should be kept inside the closed AFM chamber for at least 12 h. Although PeakForce mode does not require cantilever tuning, a calibration of the spring constant of the cantilever will allow a more controlled Peak Force setpoint value. However, the calibration method that requires force-curves against a hard surface should be avoided at all costs because it would damage the tip or make it blunt. Once the equilibration and calibration is complete start imaging with a small scan area of $5 \times 5 \mu\text{m}^2$. Do not perform too large scans. Use initially 1 nN as set-point and control the gains manually to reduce the noise. Once a sacculi of interest has been found zoom gradually (do not change from bigger scan sizes to smaller ones suddenly). Then, to perform the best close up image possible, keep adjusting the set-point, gains and PeakForce amplitude and lift height until the best combination of parameters is found. This will vary with each experiment. The Z piezo range can be reduced to 0.5 μm but a lower value will produce resonance problems.

2.3.4.2 Living cells

Most of the general advice from sacculi can be applied here. For *B. subtilis* consistent results have been obtained with PeakForce, although the highest lateral resolution of 0.5-1 nm has been achieved with soft tapping mode. For both *B. subtilis* and *S. aureus* live cells, the best approach to resolution is tapping mode using the FastScan-D on the Bruker Dimensions FastScan microscope. The same advice regarding stabilization and noise are applied here. In addition to thermally stabilize the sample prior to imaging, during the imaging session keep constantly checking the optical image of the AFM probe and its surroundings. Most likely non-attached bacterial cells in suspension will attach to the tip and could block the path of the laser. If that starts to happen, extremely carefully add a minimal amount of imaging buffer close to the AFM tip. For the ideal tuning of the cantilever for imaging in tapping mode follow the example from *Figure 1.15 d*. Regarding the parameters, usually free amplitude of 1-2 nm and set-point of 0.8-1.5 nm are used. These values should be constantly checked and changed if needed during the experiment, together with the integral and proportional gains which should be changed depending on the image size and the pixel number. Not always more pixels mean better definition of the features of interest, because the noise could overpower the signal. The Z range of the piezoelectric motor can be reduced to 0.2 μm .

2.4 References

- [1] M. J. Horsburgh, J. L. Aish, I. J. White, L. Shaw, J. K. Lithgow, and S. J. Foster, " δb modulates virulence determinant expression and stress resistance: Characterization of a functional rsbU strain derived from *Staphylococcus aureus* 8325-4," *J. Bacteriol.*, 2002.
- [2] R. Wheeler, R. Turner, R. Bailey, B. Salamaga, S. Mesnage, S. Mohamad, E. Hayhurst, M. Horsburgh, J. Hobbs, and S. Foster, "Bacterial cell enlargement requires control of cell wall stiffness mediated by peptidoglycan hydrolases," *MBio*, 2015.
- [3] K. Wacnik, "Dissecting cell division in the human pathogen *Staphylococcus aureus*." University of Sheffield, 2016.
- [4] K. Schirner and J. Errington, "The cell wall regulator σl specifically suppresses the lethal phenotype of *mbl* mutants in *Bacillus subtilis*," *J. Bacteriol.*, 2009.
- [5] A. Bisson-Filho, Y. Hsu, G. Squyres, E. Kuru, F. Wu, C. Jukes, Y. Sun, C. Dekker, S. Holden, M. Van Nieuwenhze, Y. Brun and E. Garner, "Treadmilling by FtsZ filaments drives peptidoglycan synthesis and bacterial cell division," *Science (80)*, 2017.
- [6] J. M. Walker, *Cell Wall Homeostasis*. 2016.
- [7] M. L. V. U. Zur Muhlen, "Life and Death: Cell Wall Antibiotic killing of *Staphylococcus aureus*," University of Sheffield, 2019.

Chapter 3 The external peptidoglycan architecture of *Staphylococcus aureus*

The focus of this chapter is to use AFM to study, for the first time, sacculi in liquid environment, which mimics the native environment of *S. aureus* better than the current dry studies. The robustness of this method was assessed through quantitative analysis, comparing the known structure of the external surface of the cell wall from living bacterial cells and the novel external structure of sacculi in liquid. Defining the external structure of hydrated purified peptidoglycan is a crucial first step on the goal of a full characterisation of the PG physical structure.

3.1 The external cell wall architecture of living bacteria

AFM has been previously used to describe the PG structure of *S. aureus* with molecular resolution on living cells. [1] The protocol optimised by a former group member who performed this work [1] can be found in *section 2.3.3.1*.

The cell division mechanism for *S. aureus* proceeds through consecutive orthogonal planes, creating two differentiated structures along the cell surface (see *1.3.3.3* and *Figure 3.1 a*). The PG synthesis machinery deposits the nascent material as concentric rings, this structure covers approximately a third of the cell surface defining the parallel surfaces of the two daughter cells after division (see *Figure 3.1 b*). [1]–[4]

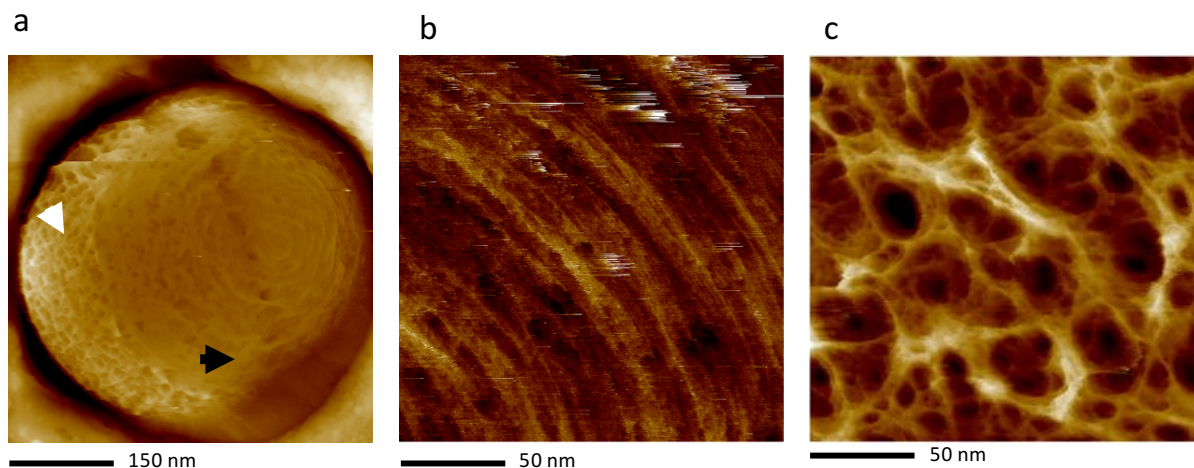


Figure 3.1 – a) Image of an entire S. aureus living cell with the two structures clearly differentiated, the mature structure (see white arrow) and the concentric rings from the nascent material (see black arrow); b) Nascent material structure of concentric rings of a living cell; c) Mature structure of a living cell (Mesh); Images taken by Dr Jonathan Burns [1]

Images from *Figure 3.1* were taken using the following experimental conditions [1] (see *Table 3.1*). See *section 2.1.7* for AFM probes properties and *section 2.1.4* for buffer preparation.

Table 3.1 – Experimental conditions used in Figure 3.1. Work performed by Dr Jonathan Burns [1].

	AFM TYPE	AFM PROBE	AFM MODE	SAMPLE TYPE	ENVIRONMENT	SURFACE	SPECIFIC CONDITIONS
FIGURE 3.1 A	Bruker Fast Scan	Fast Scan - D	Soft Tapping	<i>S. aureus</i> WT live cells	300mM KCl + 10mM Tris pH=7.8	Silicon grid	Exponential phase cells O. D. ₆₀₀ ~ 0.5
FIGURE 3.1 B, C	Bruker Fast Scan	Fast Scan - D	Soft Tapping	<i>S. aureus</i> WT live cells	200mM KCl + 10mM MgCl ₂ 10mM Tris pH=7.8	Silicon grid	Exponential phase cells O. D. ₆₀₀ ~ 0.5

This data is in good agreement with previous transmission electron microscopy (TEM), scanning electron microscopy (SEM) and cryogenic electron microscopy (cryo-EM) studies. [5]–[7] The second structure corresponds to the mature PG which is the material that had been deposited in the rest of the cell in previous generations and organizes itself in a randomly oriented network of fibres, formed by a few glycan chains and peptide cross-linked typically between 3-5 nm in diameter, forming a porous gel structure, see *Figure 3.1 c*, (see *section 3.5.4.1*, for quantitative analysis of the fibres). [1]–[3], [8]

3.2 Purified peptidoglycan in ambient conditions

A major limitation on the study of bacterial cells by AFM is the lack of access to the internal CW surface due to the closed topology of cells. To achieve this objective *S. aureus* purified PG (*i.e.* sacculi) was studied. [4], [9]–[13] The main workflow to perform AFM images of sacculi, either under liquid or ambient environment is summarized in *Figure 3.2*. This scheme is based on the protocol used in the previous work [4] together with a few educated guesses about possible improvements needed to perform the experiments under liquid conditions.

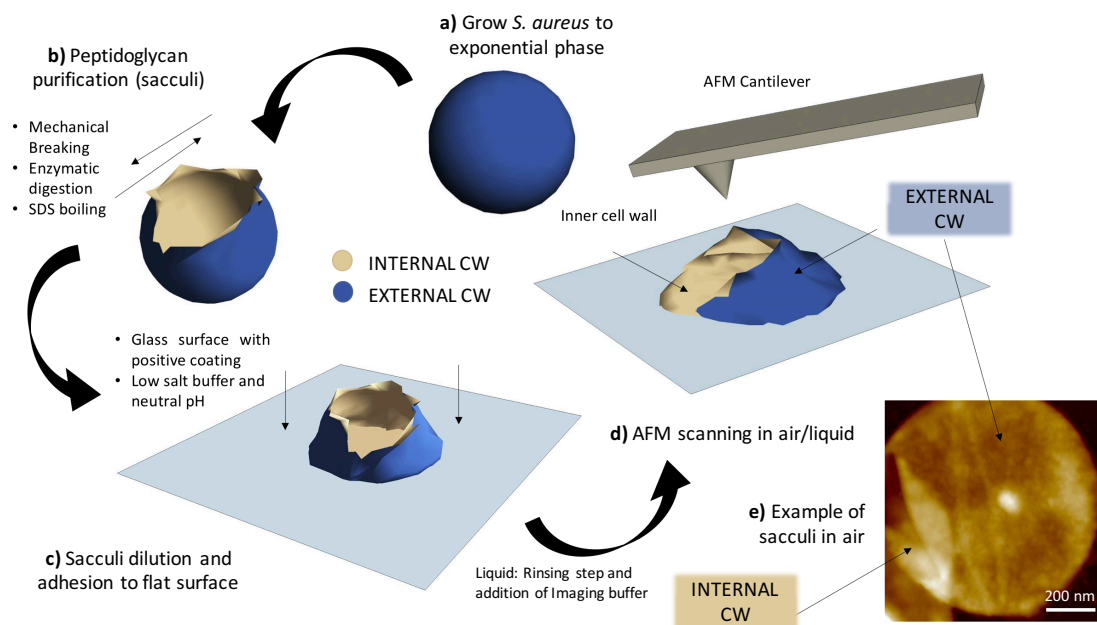


Figure 3.2 – Schematics of the sacculi sample preparation for AFM (made using a 3D drawing program called sketch-UP), a) grow *S. aureus* to exponential phase; b) then start peptidoglycan purification protocol producing a sacculi stock; c) make the appropriate sacculi dilution and prepare the surface with the chosen coating, incubate sacculi dilution during a fixed incubation time; d) rinse the sample after the incubation time and put imaging buffer, ready to image with AFM; e) example of sacculi imaged in air, where no rinsing step was taken.

Figure 3.2 a-b represent the steps to purify PG from *S. aureus* cells according to the reported method [14] including some improvements (see section 2.2.2.3). Next, the highly concentrated sacculi stock must be diluted and deposited on a flat substrate. For experiments in ambient conditions the sample is dried with nitrogen flow, Figure 3.2 c. For experiments in liquid conditions the sample must be rinsed instead of dried (see section 2.3.2.4), then perform the AFM to obtain three-dimensional topographic images, Figure 3.2 d.

Before performing experiments with sacculi in liquid environment, in the early stages of this project the previous published work [4] in ambient conditions was repeated. Two distinctive architectures have been reported: the ‘knobbles’ and ‘concentric rings’, corresponding respectively to mature and nascent peptidoglycan (see Figure 3.3).

The experimental conditions used to produce images from Figure 3.3 did not allow the optimal resolution in the topography images (H). However, the phase (P) images (see section 1.4.3.2) provided more contrast allowing the features to be defined.

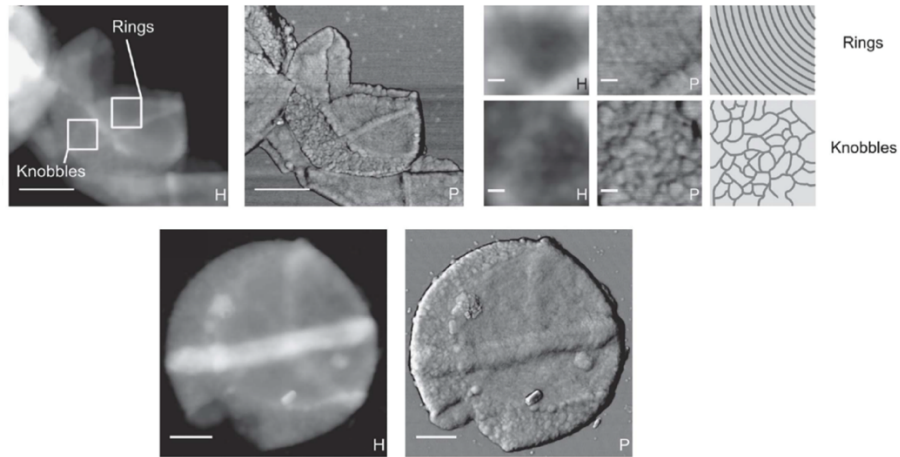


Figure 3.3 – AFM images of purified peptidoglycan from *S. aureus* in ambient conditions. Adapted with permission from [4]

In the initial stage of this project, the focus was only the external surface. To ensure the sacculi fragments have the external surface upwards to be imaged by AFM, only partially broken sacculi that kept its spherical shape, [4], [10]–[13] (see Figure 3.2 e) were imaged in more detail. See Figure 3.4 for examples of purified peptidoglycan in ambient conditions.

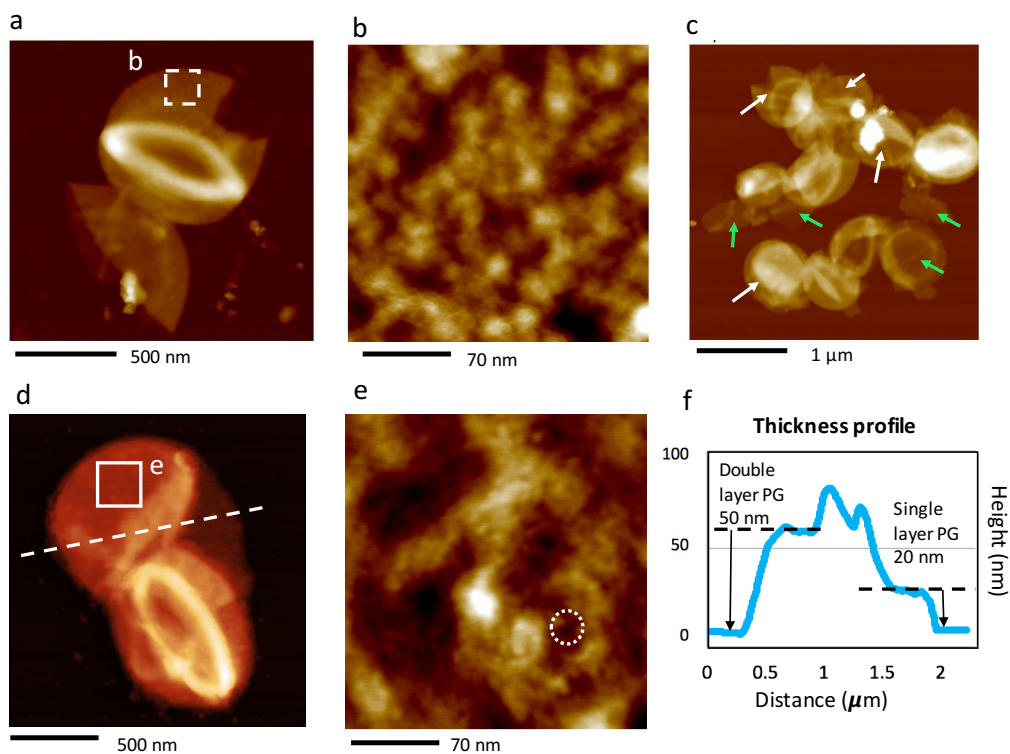


Figure 3.4 – Topography (H) images of *S. aureus* sacculi in ambient environment - a) partially broken sacculus only from one side of the cell, showing the external structure of mature peptidoglycan intact; b) Zoom from 'a' showing the finer structure of knobbles corresponding to previous data of the mature peptidoglycan in air environment; c) overview of sacculi sample with some of them totally broken and some of them only partially broken (put arrows), d) Partially broken sacculi showing a recent division site, e) zoom image from the top of sacculi 'e' showing the finer

structure of concentric rings from purified peptidoglycan in air environment; f) profile from dashed white line in 'd' showing a double PG layer with 50 nm thickness and a single PG layer with 20 nm thickness.

The experimental conditions used to replicate the results presented in *Figure 3.3* was the same as previously described [4], [14] but without rinsing. This experimental conditions are presented below in *Table 3.2* and in *section 2.3.2.4*.

Table 3.2- Experimental conditions used when images from Figure 3.4 were taken. For information about the sacculi batch and dilution see sections 2.1.8, 2.3.2.1. and 3.3.2.

AFM TYPE	AFM PROBE	AFM MODE	SAMPLE TYPE	ENVIRONMENT	SURFACE	SPECIFIC CONDITIONS
BRUKER FAST SCAN	Tespa-V2	Soft Tapping in air	WT sacculi Batch 1 Stock A, Dilution 1	Air (no rinsing step was performed)	Freshly cleaved Mica	Stock was kept at -20°C

In *Figure 3.4*, the results presented were in accordance with the previous structure types summarized in *Figure 3.3*. [4] *Figure 3.4 a-b* show the mature external surface, the 'knobbles' are characterized by a set of protrusions on the peptidoglycan of different sizes and disordered in space. *Figure 3.4 d-e* show the nascent external surface, the concentric rings are also formed by protrusions but ordered radially to a centre area (see white circle). Single PG layers are going to be the focus of this thesis, they are individual layers with thickness of approximately 20 nm in air (see *Figure 3.4 f*). *Figure 3.4 c* shows the difference between partially broken sacculi (white arrows) and other conformations (green arrows).

Remarkably, this data seemed to suggest that the two clearly distinguishable structures on the external surface, named *mesh* in living cells and *knobbles* in purified PG under ambient environment (see *Figure 3.3-3.4*), corresponded to mature peptidoglycan. See *Table 3.3* for a summary of PG structures previously identified in sacculi and living bacteria cells.

Table 3.3 – Summary of established PG structures identified using AFM in different samples

	Nascent Peptidoglycan	Mature Peptidoglycan
<i>Living bacteria PG structure</i>	Concentric Rings	Randomly orientated mesh
<i>Dried purified PG structure</i>	Concentric Rings	'knobbles'
<i>Hydrated purified PG structure</i>	Unknown	Unknown

This disagreement between living cells and sacculi data respect the mature peptidoglycan could have two possible explanations: the PG purification process affects

the mature architecture; or it could be caused by a drying artefact. Probably the difference in environment is responsible for this. There are other examples of biomaterials that imaged with AFM under liquid versus ambient conditions significant structural differences were observed (*e.g. Bacillus cereus* exosporium). [15] To answer this question, the purified PG has to be imaged with high resolution in liquid and the mature PG architecture determined.

3.3 Optimization process of sacculi adhesion in liquid conditions

To obtain high resolution images of sacculi in liquid it was necessary to optimize the adhesion conditions of the sacculi onto a supporting surface. Here some unsuccessful protocols and the optimization process will be summarized.

The sacculi dilutions can be prepared either containing wall teichoic acids (PG+WTA, *i.e.* Stock A) or without them (PG, *i.e.* Stock B), see *section 2.2.2.2*. Both samples have been used throughout in this chapter. In order to mimic as much as possible the WT living cell native environment, [16]–[18] the first optimization attempts were performed with Stock A.

3.3.1 Poly-L-Lysine coated glass

Poly-L-Lysine (PLL) coated [19], [20] surfaces work to attach Gram-negative bacteria *E. coli* in liquid. [21] A high-precision glass coverslip coated with PLL (see *section 2.3.1.2*) was used to deposit a more concentrated *S. aureus* sacculi dilution than the sample used for imaging in air, *Table 3.2*. See *section 2.3.2.2.1* for the protocol. For the first time a successful attachment of sacculi to a surface in liquid was obtained, the best results are summarize in *Figure 3.5*.

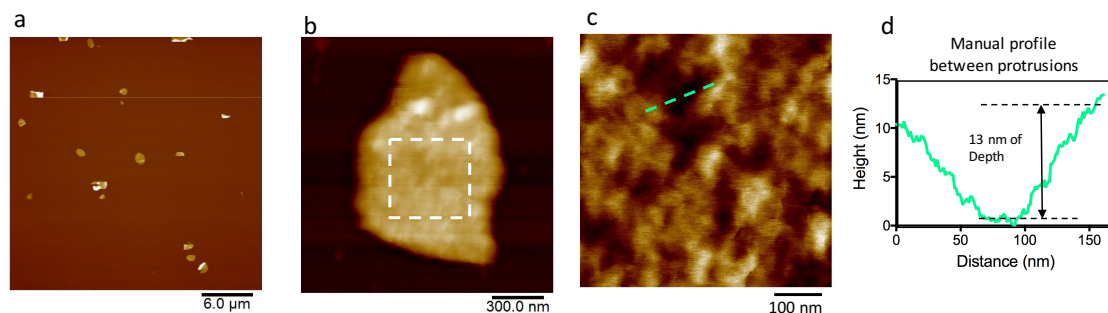


Figure 3.5 - S. aureus sacculi on PLL coated glass - a) overview of the system with many different sacculi attached to the surface, taken in Contact mode; b) zoomed imaged taken with tapping mode in liquid; b) Zoom image from 'b'

showing a potential mature cell wall structure; d) profile across features from image 'c' the depth measured was no bigger than 15nm.

The images from *Figure 3.5* were performed under the experimental conditions summarized below in *Table 3.4*.

Table 3.4 - Experimental conditions used when images from Figure 3.5 were taken. See section 2.3.2.2.1

AFM TYPE	AFM PROBE	AFM MODE	SAMPLE TYPE	ENVIRONMENT	SURFACE	SPECIFIC CONDITIONS
DIMENSIONS 3100 (BRUKER)	MLCT (E)	Contact and Tapping	WT sacculi Batch 1 Stock A Dilution 2	10 mM Tris pH 7.8	Glass coated with PLL	60 min incubation on Glass

Figure 3.5 a shows a distribution of individual pieces of purified PG from *S. aureus*. This image was taken in contact mode in liquid (see *section 1.4.3.1*). This AFM mode produces high lateral forces, ensuring that the sacculi was firmly immobilized on the surface. Then, it was required to change to tapping mode (see *section 1.4.3.2*) to obtain more details (see *Figure 3.5 b-d*). However, the image resolution was not better than in ambient conditions as the resolved features with similar dimensions (*e.g.* 13 deep and 60 nm wide). Moreover, the number of sacculi fragments attached to the surface had to be increased.

3.3.2 Optimized sacculi concentration

There are two possible explanations for a low concentration of sample on the surface: the sacculi concentration being too low or the sacculi not being uniformly distributed across the surface. The latter, is hardly addressable, as it is inherent to the nature of the technique. The sacculi concentration can be tuned by diluting the sacculi stock. Different stock dilutions were tested (see *Table 3.5*).

Table 3.5 – Details of the different dilutions 1-6 which were used to test the optimal sacculi concentration

Dilution name	Dilution v/v	V_{stock} (μ l)	V_{final} (μ l)	<i>O.D.</i> ₆₀₀
<i>Dil 1</i>	1:80	5	400	0.29
<i>Dil 2</i>	1:40	10	400	0.73
<i>Dil 3</i>	1:20	10	200	1.68
<i>Dil 4</i>	1:12,5	10	125	2.35
<i>Dil 5</i>	1:7,6	15	115	3.78
<i>Dil 6</i>	1:2,7	40	150	7.49
<i>Stock</i>	1:1	50	50	30.56

The stock corresponding to this experiment had an Optical Density at 600 nm of wavelength (OD_{600}) of 30.56. [22] However, when other sacculi batches were prepared to obtain independent biological repeats (see *section 2.1.8*), the stock OD_{600} varied from 7-45 depending on the quality of the purification process and the initial volume of cells used. Therefore, the stock volumes and dilutions v/v from *Table 3.5* are only applicable in this experiment, the important measurement is the $O.D._{600}$ from the dilutions (see *Table 2.4*). The results obtained using these conditions for four different dilutions are summarized in *Figure 3.6*. No other variable was changed.

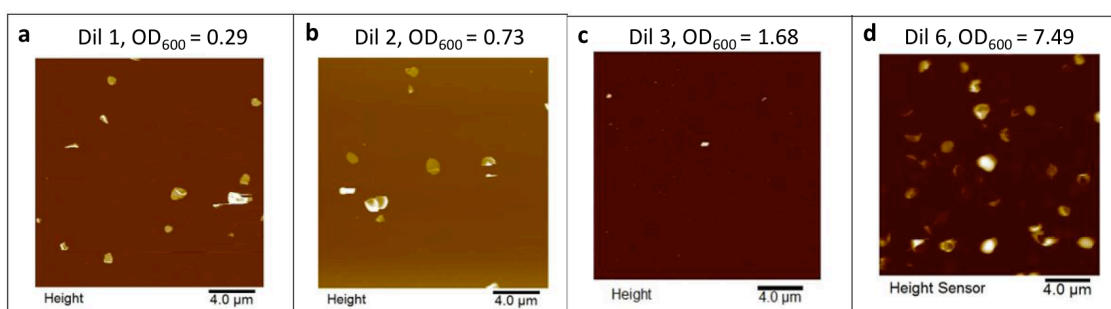


Figure 3.6 – Optimizing S. aureus sacculi concentration in PLL coated glass - a) The most diluted concentration Dil 1, with $OD_{600} = 0.29$ shows some single layer sacculi attached to the surface; b) The next concentration tested Dil 2, with $OD_{600} = 0.73$ with no apparent different from ‘a’; c) image Dil 3 with with $OD_{600} = 1.68$ which showed less amount of sacculi attached to the surface than ‘a’ and ‘b’; d) Finally the most concentrated sample tested was Dil 6 with $OD_{600} = 7.49$ which shows an increased number of sacculi attached to the surface.

In conclusion, the appropriate concentration for a batch 1 (see *Table 2.3*) was Dilution 6 with $OD_{600} = 7.49$, *Figure 3.6 d*. For other stocks with low volume available, Dilutions 5 and 4 from *Table 3.5* were also used with similar results as Dilution 6. Therefore, the appropriate dilution to perform experiments in liquid environment has **OD_{600}** between **2.34-7.49**.

3.3.3 Sacculi attach to Cell-Tak™ coated Glass

One major impediment to achieve better resolution than in ambient conditions was the poor attachment of the single PG layers the surface. Especially when scanning smaller areas the continuous interaction with the tip was causing lateral displacements of PG fragments, observable when comparing trace and retrace. To test single PG layer attachment, Cell-Tak™ tissue adhesive was used as an alternative coating.

The complete protocol initially used to attach sacculi on Cell-Tak coated glass can be found in *section 2.3.2.3.1*. The sample is added to Cell-Tak™ coated glass and incubated

for 60 min, rinsed with 1 ml HPLC-grade water and rinsed with imaging buffer. A comparison with PLL coated glass is shown in *Figure 3.7*.

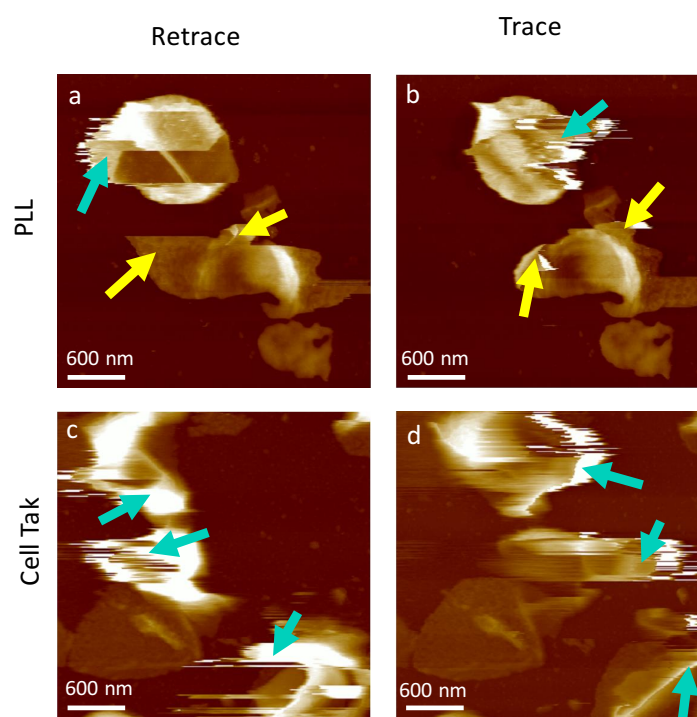


Figure 3.7 – Top left to right images were taken with PLL in liquid corresponding to retrace and trace, showing double layers moving (blue arrows) and single layers moving as well (yellow arrows). Bottom left to right images were carried out with Cell Tak in liquid corresponding to retrace and trace with double layers moving as well (blue arrows).

Figure 3.7 a-b show the two channels corresponding to the trace and retrace signals from the AFM scanning. The PG double layers moved in both cases (see blue arrows). The PG single layers (see yellow arrows) moved when imaged on PLL coated glass but not when Cell-Tak™ was the coating agent. In conclusion, Cell-Tak™ provides better fixation for sacculi in liquid environment, avoiding perturbations of single PG layers during AFM imaging.

3.3.4 Sacculi attach to Cell-Tak™ coated Mica

The high-precision glass set-up has many air interphases between the sample and the stage, increasing the mechanical vibrations of the sample and producing instability and drift problems (see *section 1.4.4*). Therefore, a more stable substrate was sought. The widely used AFM set-up of mica attached to a metal stub (*section 2.3.1.1*) was tested producing better results with less drift. Cell-Tak™ coated mica protocol (see *section 2.3.2.3.2*) requires some adjustments with respect to Cell-Tak™ coated glass.

3.3.5 Sample incubation optimization

The optimized sample incubation time using Cell-Tak™ coated mica was determined to be 60 min for the **Stock A** samples (see *Figure 3.7 c-d*). However, when the same protocol was attempted using the **Stock B** there was poor attachment of sacculi. This could be explained because the lack of WTA might affect the net charge of the sacculi and hence reduced its attachment which is ultimately based on an electrostatic interaction.

Therefore, the incubation time for **Stock B** was optimized using Dilution 5 (corresponding to $OD_{600} = 3.78$). Three different incubation times were tested: **45, 90, 135 min**, *Figure 3.8*.

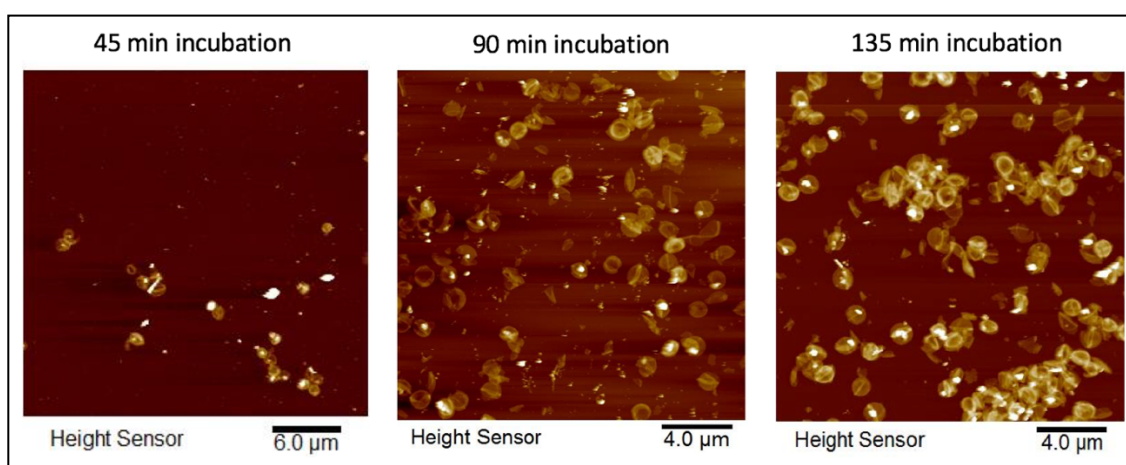


Figure 3.8 – Optimization of incubation time of sacculi from stock B with dilution 5 on Cell-Tak™ coated mica.

The AFM images presented in *Figure 3.8* were performed with the experimental conditions summarized in *Table 3.6*. From here on, all the images in this thesis have been acquired from the AFM type: Bruker Fast Scan, so this will be removed from the experimental tables.

Table 3.6 – Experimental conditions from images presented in Figure 3.8. See section 2.3.2.3.2

AFM PROBE	AFM MODE	SAMPLE TYPE	ENVIRONMENT	SURFACE	SPECIFIC CONDITIONS
TESPA – V2	Tapping	WT sacculi Batch 3 Stock B, Dilution 5	Air	Mica coated with Cell-Tak™	Rinsed and blow dried prior to image

The optimal incubation time was between 90 min and 135 min. Finally, the established time for stock B is **120 min incubation** on Cell-Tak™ coated mica.

3.4 Nascent purified peptidoglycan in liquid environment

3.4.1 Molecular resolution of nascent peptidoglycan

The nascent structure of hydrated purified peptidoglycan was the first focus of our investigation to complete the unknown structures in *Table 3.3*.

S. aureus sacculi was prepared using the protocol 2.3.2.3.1 which did not involve any drying step throughout. The hydrated sacculi was imaged using small amplitude tapping mode (*sections 1.4.3.2, 1.4.4*). [23]–[27] Tapping mode was also used to obtain high resolution images of living cells (see *Figure 3.1 b*) [1]. The best set of images of nascent peptidoglycan structure are summarized in *Figure 3.9*.

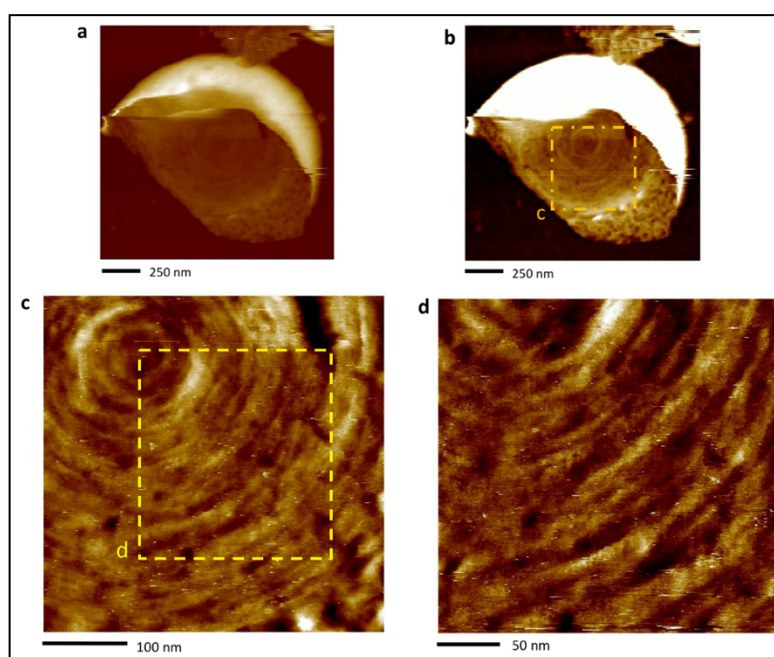


Figure 3.9 – a) Image of AFM in liquid of a flat single layer attached to the surface with a double layer on the top part (brightest colour), b) same image but different colour scale highlighting the ring structure; c) zoom image from 'b' showing the concentric rings (see dashed yellow box); d) finer structure of rings.

In *Figure 3.9* it can be observed that the nascent peptidoglycan in hydrated sacculi had indeed the same structure as the living cells and the dried sacculi concentric rings.

The images from *Figure 3.9* were performed under the conditions summarized in *Table 3.7*.

Table 3.7 - Experimental conditions for the visualization of nascent purified peptidoglycan in liquid environment

AFM PROBE	AFM MODE	SAMPLE TYPE	ENVIRONMENT	SURFACE	SPECIFIC CONDITIONS
FAST SCAN -D	Soft Tapping	WT sacculi Batch 3 Stock A Dilution 4	300mM KCl + 10mM Tris pH=7.8	Glass (grid) coated CellTak	Leave stabilize for 1h

At this point it became apparent that the comparison between the structures determined from different biological samples required a quantitative method instead of a qualitative visual comparison. This would allow us to confidently establish if the purification of PG induced any structural changes to the sample. The concentric rings have a distance between them dependant on their cell cycle.[28] Nanoscope Analysis™ and Gwyddion [29] (open source) softwares can be used to analyse the images. Several profiles were performed and the Peak to Peak (PtP) method was used to measure the distance between the rings. [30] The separation between concentric rings in *S. aureus* living cells is $2.7 \text{ nm} \pm 0.5$ (n=16).[1], [28]

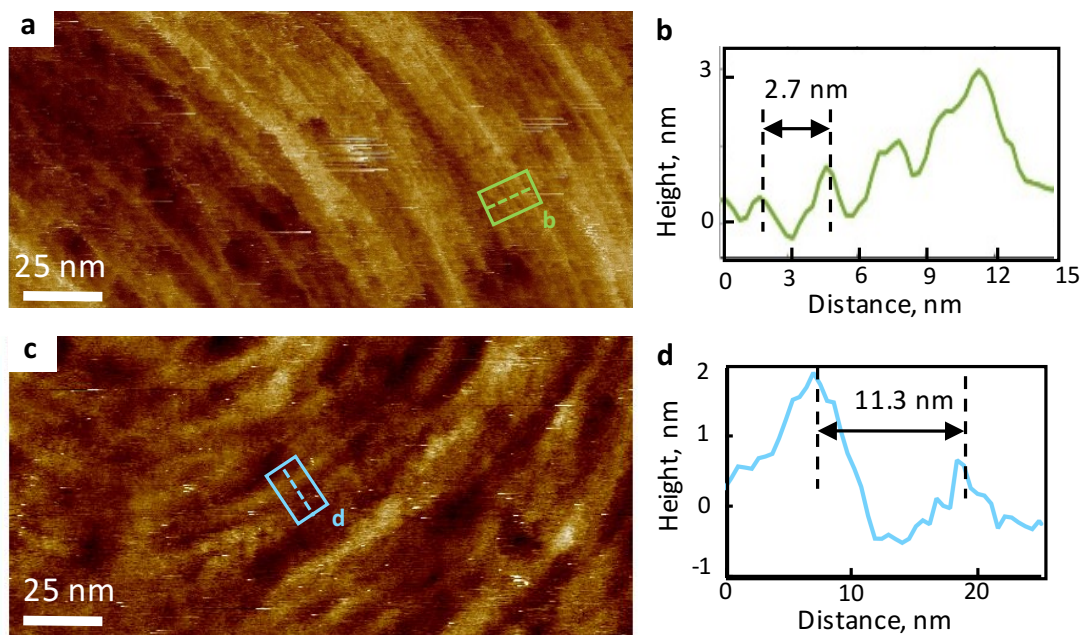


Figure 3.10 - Quantitative comparison between living cells and hydrated purified PG architectures on the nascent region (Concentric Rings). a) concentric rings from living *S. aureus*, adapted with permission from [28]; b) profile from green dashed line in 'a' showing the distance between consecutive rings; c) Concentric rings from *S. aureus* sacculi, bottom region of 'Figure 3.9 d'; d) profile from blue dashed line in 'c' showing the distance between consecutive rings.

Figure 3.10 shows the measurement of distance between the rings taken from living bacteria (Figure 3.10 a-b) and hydrated sacculi (Figure 3.10 c-d). It can be seen by comparing the graphs from Figure 3.10 b and d that the smallest feature that could be resolved in the sacculi sample was much larger than the smallest feature in living cells, implying the resolution of the images are not comparable. Therefore, more optimization was necessary.

Performing experiments in Cell-Tak™ coated mica decrease the drift causing less noise (see section 3.3.4). [19], [31] The small amplitude tapping mode was causing too much

interaction with the surface preventing the topography of the sample to be revealed with the appropriate resolution. Usually, when there is a strong attraction between the AFM tip and the sample, the use of high ionic strength buffer might reduce this interaction (see *section 1.4.4.1*). [27] This use of imaging buffer with (150-300 mM KCl) throughout this thesis caused no visible improvement. The AFM tip lateral forces are dominating the attractive interaction with the sample, rather than long-range forces (see *section 1.4.2*). Therefore, PeakForce mode was tested because the lateral forces are greatly reduced, see *section 1.4.3.3*. See *Figure 3.11* for high resolution images of nascent external PG.

The images from *Figure 3.11* were performed under the experimental conditions summarized in *Table 3.8*.

Table 3.8 - Experimental conditions for high resolution of nascent purified peptidoglycan in liquid environment

AFM PROBE	AFM MODE	SAMPLE TYPE	ENVIRONMENT	SURFACE	SPECIFIC CONDITIONS
FAST SCAN -D	PeakForce Tapping	WT sacculi Batch 3 Stock B Dilution 5	300mM KCl + 10mM Tris pH=7.8	mica coated Cell-Tak™	Leave stabilize for 30min

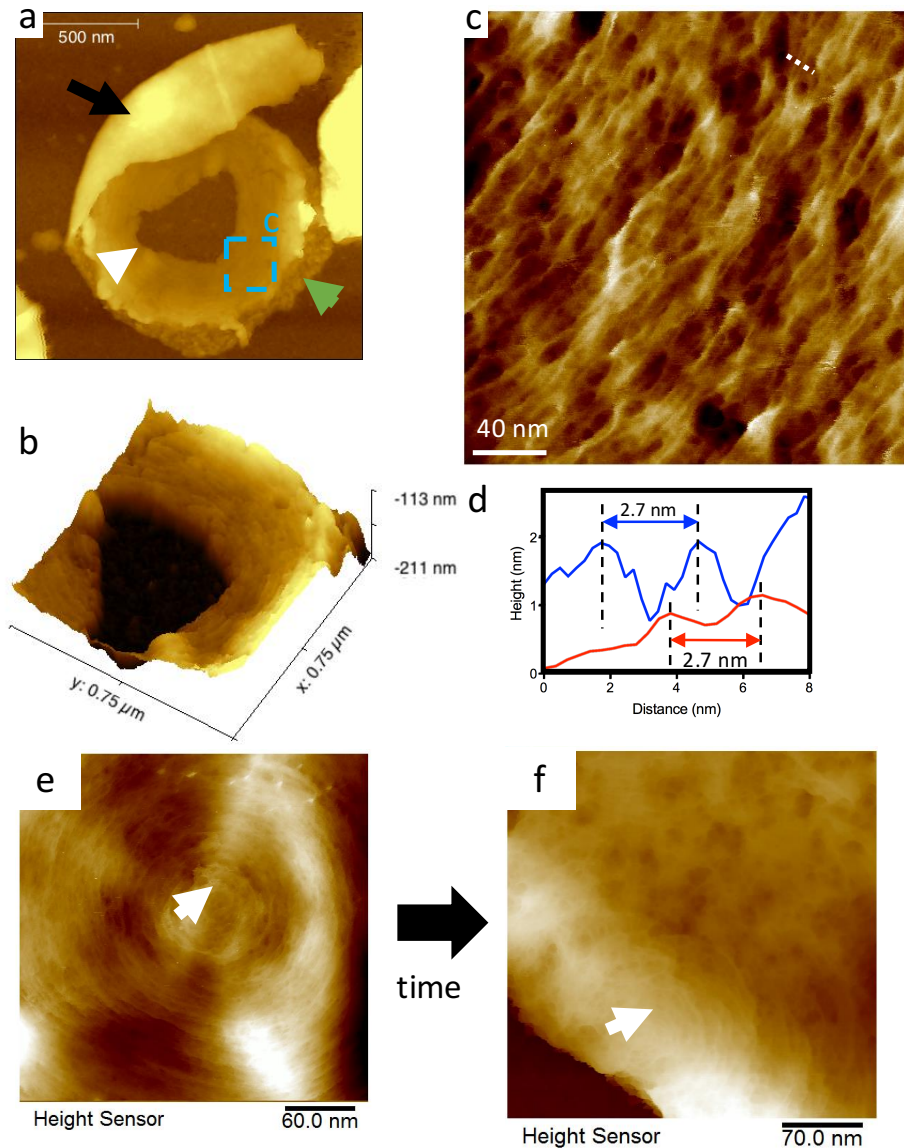


Figure 3.11 - a) sacculus broken from the middle of the rings (white arrow) showing the rest of the older material around them (green arrow) and the internal PG surface flipped over (black arrow); b) three-dimensional representation of the internal site of 'a' where the rings can be visualized all around the striation; c) high resolution image of rings was obtained from the zoomed area in 'a' showing small features such as the profile highlighted in 'd' (see red line); d) graph showing two profiles: the red line represent the profile from dashed white line in 'c' with a separation $PtP=2.7\text{nm}$, the blue line represents a section of the profile from 'a'; e) concentric rings at an early stage of the cell cycle; f) concentric rings at a more advance stage of the cell cycle.

Figure 3.11 a has an unusual conformation, after analysing a wider set of data it was possible to identify the nascent external surface surrounding a big scar (white arrow and 3D representation on Figure 3.11 b), with other structures present which were not the focus at this point (black and green arrow). Image Figure 3.11 c is a zoomed from Figure 3.11 a from the nascent PG region showing as expected, concentric rings. After comparing two profiles (Figure 3.11 d red from sacculi and blue from living cells [1] from Figure 3.10 a), it was determined that both images had comparable resolution. It has been described [28] that tight concentric rings (see Figure 3.11 e) correspond to early

stages of division; and looser rings with higher distance between them (see *Figure 3.11 f*) correspond to a later division stage. The central depression (see white arrows in *Figure 3.11 e-f*) was used to find rings.

3.4.2 Periodicity along glycan strands

A set of periodic features were observed either between the Rings (see *Figure 3.12 a-c*) or along the glycan strands (see *Figure 3.12 d-j*). These features might be the uncross-linked peptide stems attached to the glycan backbone (see *section 1.3.2*). The peptidoglycan chemical structure has been described as having a helical pitch with a periodicity distance of $\sim 40 \text{ \AA}$ (4 nm) (see *Figure 3.12 l*). [32]–[36]

The results from *Figure 3.12* were obtained using the experimental conditions summarized in *Table 3.9*.

Table 3.9 - Experimental conditions for Figure 3.12. Images g-h taken by Dr Jonathan Burns

	AFM PROBE	AFM MODE	SAMPLE TYPE	ENVIRONMENT	SURFACE	SPECIFIC CONDITIONS
<i>FIGURE 3.12 A-E</i>	Fast Scan D	PeakForce Tapping	WT sacculi Batch 3 Stock B Dilution 5	300mM KCl + 10mM Tris pH=7.8	MICA coated CellTak	Location 5 /Stabilized for 30min
<i>FIGURE 3.12 G-H</i>	Fast Scan D	Soft Tapping	<i>S. aureus</i> WT live cells	200mM KCl + 10mM MgCl ₂ + 10mM Tris pH = 7.8	Silicon Grids	Adapted with permission from [28]

Figure 3.12 shows two data sets: hydrated purified PG, *Figure 3.12 a-f* and living cells, images taken by Dr. Jonathan Burns (*Figure 3.12 g-j*). [1], [28] There is similarity between the two sets of data because both have periodic features 3.5-4.5 nm apart (see example profiles in *Figure 3.12 f, i*). This corroborates the periodicity is intrinsic from PG chemical structure and does not get altered during the purification process. Another set of periodic were found between neighbouring glycan strands in hydrated sacculi (see *Figure 3.12 a-c*) which could be cross-links. The data from *Figure 3.12* represents the first non-averaging tool to be able to directly visualize the peptidoglycan chemical structure. However, there is not enough solid evidence at this point, because larger data sets are required. Technical improvements such as using different AFM probes with tip radius $\sim 3-5 \text{ nm}$ (e.g. Ando cantilever [37], [38]) could improve image resolution and

increase the reproducibility of the results. These probes are mounted in a chip too small to fit in the Bruker FastScan, but they could fit in the AFM head designed by the Fantner group [39]–[41] which our group is acquiring in the near future.

In summary, there is still room for improvement but the current preliminary data provides a good foundation to build a more solid set of data in the near future.

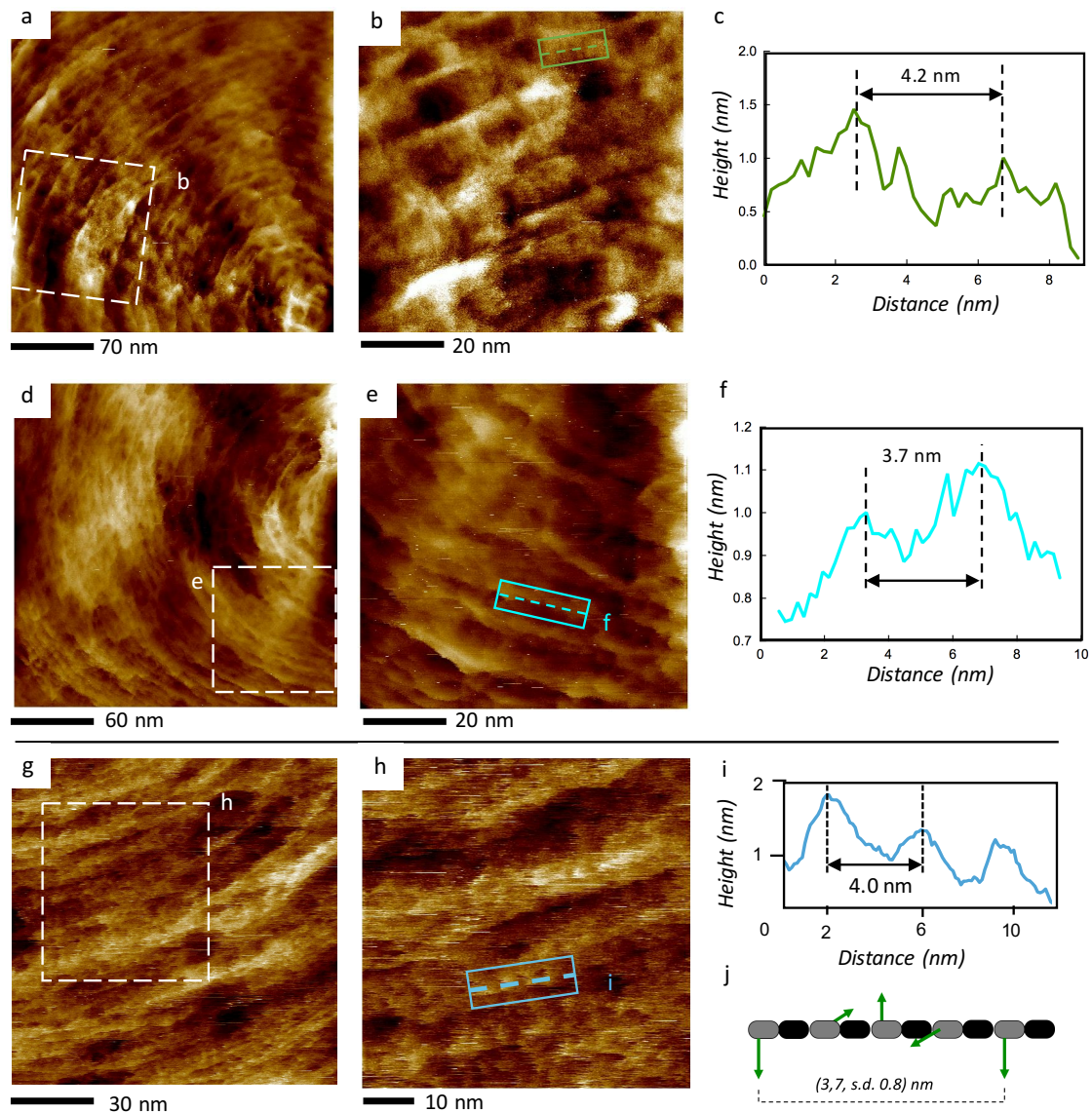


Figure 3.12- Periodic features between and along the glycan strands in the concentric rings of *S. aureus* - a) Concentric rings from hydrated purified PG; b) zoomed image from 'a' showing some periodic features between the concentric rings; c) profile extracted from the green dashed line in 'b' with a measured PtP distance = 4.2 nm; d) Concentric rings from another purified sacculus; e) zoomed image from 'd' showing periodic protrusions along the glycan strands; f) profile extracted from the light blue dashed line in 'e' with a measured PtP distance = 3.7 nm; g) Image by J Burns, Concentric rings from a recently divided surface from a living cell; h) zoomed image from 'g' showing up close a series of periodic protrusions along the glycan strands of the living cell; i) profile extracted from the blue dashed line in 'h' with a measured PtP distance = 4.0 nm; j) representation of the meaning of the periodicity along the glycan strands, where black and grey blocks represent the disaccharide unit forming the peptidoglycan backbone and the green arrows represent the uncross-linked side peptides. g-j Adapted from [28]

3.5 Mature purified peptidoglycan in liquid environment

The mature PG surface is created when the concentric rings at later stages of division rearrange completely to a more disordered structure, called mesh (see *Figure 3.1 c*) formed by random oriented fibres and pores of various sizes. This highly porous structure is called mesh. By contrast, the mature PG architecture of the purified dried sacculi (knobbles [4]) is characterized by a set of disordered protrusions of different sizes (see *Figure 3.4 b*). The purified PG has to be imaged with high resolution in liquid and determine which is the mature PG architecture under these conditions. Probably transforming the last unknown structure from *Table 3.3* into a defined structure.

3.5.1 Hydrated mature sacculi in tapping mode

Mature hydrated purified peptidoglycan became the focus and some images collected while focusing on concentric rings (see *Figure 3.9*) also contained sacculi fragments with a different architecture, summarised in *Figure 3.13*.

The images from *Figure 3.13* were performed under the same experimental conditions as *Figure 3.9* summarized in *Table 3.7* except for the imaging buffer.

Figure 3.13 c, f show randomly orientated architectures with more similarities to the randomly orientated fibred mesh corresponding to the living cells (see *Figure 3.1 c*) rather than the 'knobbles' obtained in dried sacculi (see *Figure 3.4 b*). The minimum distinguishable features were 8-10 nm wide, not comparable to the resolution achieved in living cells using the same technique, which was 1-2 nm. Achieving equivalent resolutions is required to quantitatively compare AFM images from two different samples.

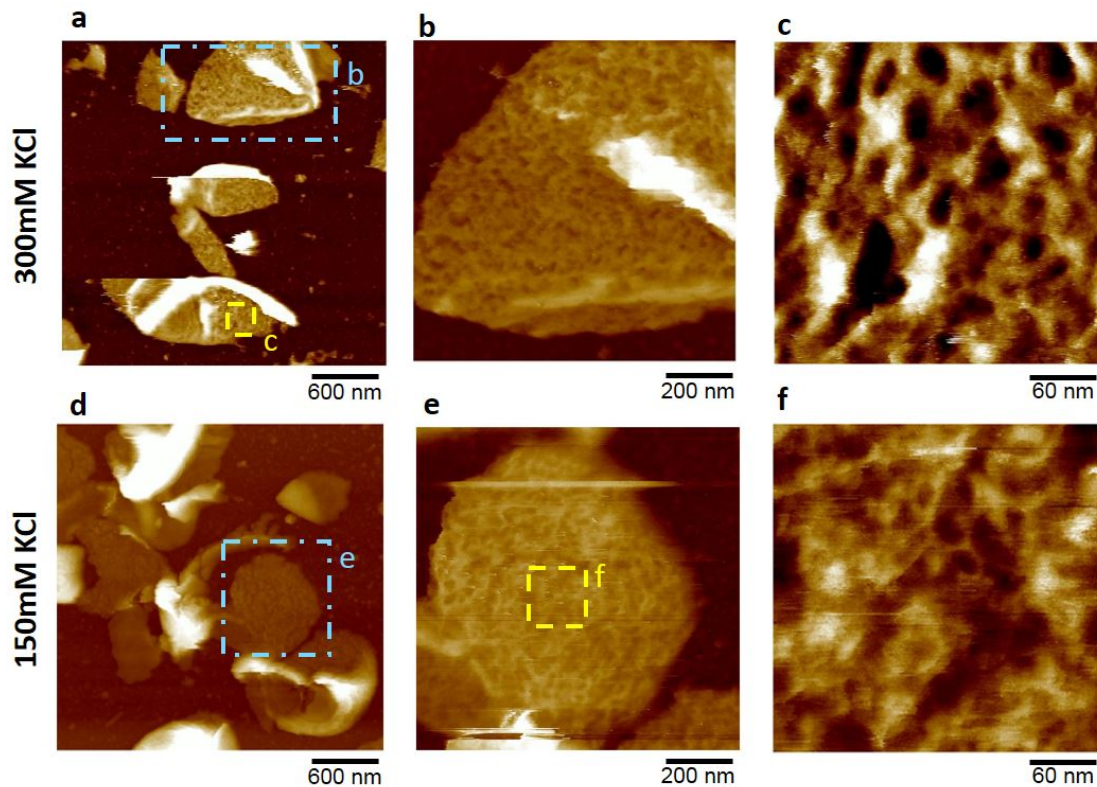


Figure 3.13 – Mature PG hydrated sacculi with Tapping mode - a) Sacculi distribution of single layer PG on top of glass surface, image taken under 300mM KCl + 10mM Tris; b) zoomed image from 'a' which is a reminiscence of the mature peptidoglycan structure of a living cell (see dashed blue box in 'a'); c) zoomed image from area marked in 'a' (see yellow box) of a mature peptidoglycan area showing a randomly orientated structure like 'a' in Fig 3.1; d) sacculi distribution of single layer PG on top of glass surface, image taken under 150mM KCl + 10mM Tris; e) zoomed image from 'd' which is similar to 'b' (see dashed blue box in 'd'); f) zoomed image from area marked in 'e' (see dashed yellow box) of a mature peptidoglycan area.

3.5.2 Hydrated mature sacculi in PeakForce mode

Why the same type of PG architecture could be imaged with Tapping achieving the resolution needed in living cells but it does not work with sacculi? We suggest that purified PG has been released of all pressure is a relaxed filamentous network different from heavily stretched network in its native environment (*i.e.* living cells). [42]–[45]

Therefore, reducing the lateral force by using PeakForce™ mode resulted in less disturbance of this filamentous mesh. Moreover, Cell-Tak™ coated mica instead of glass was used.

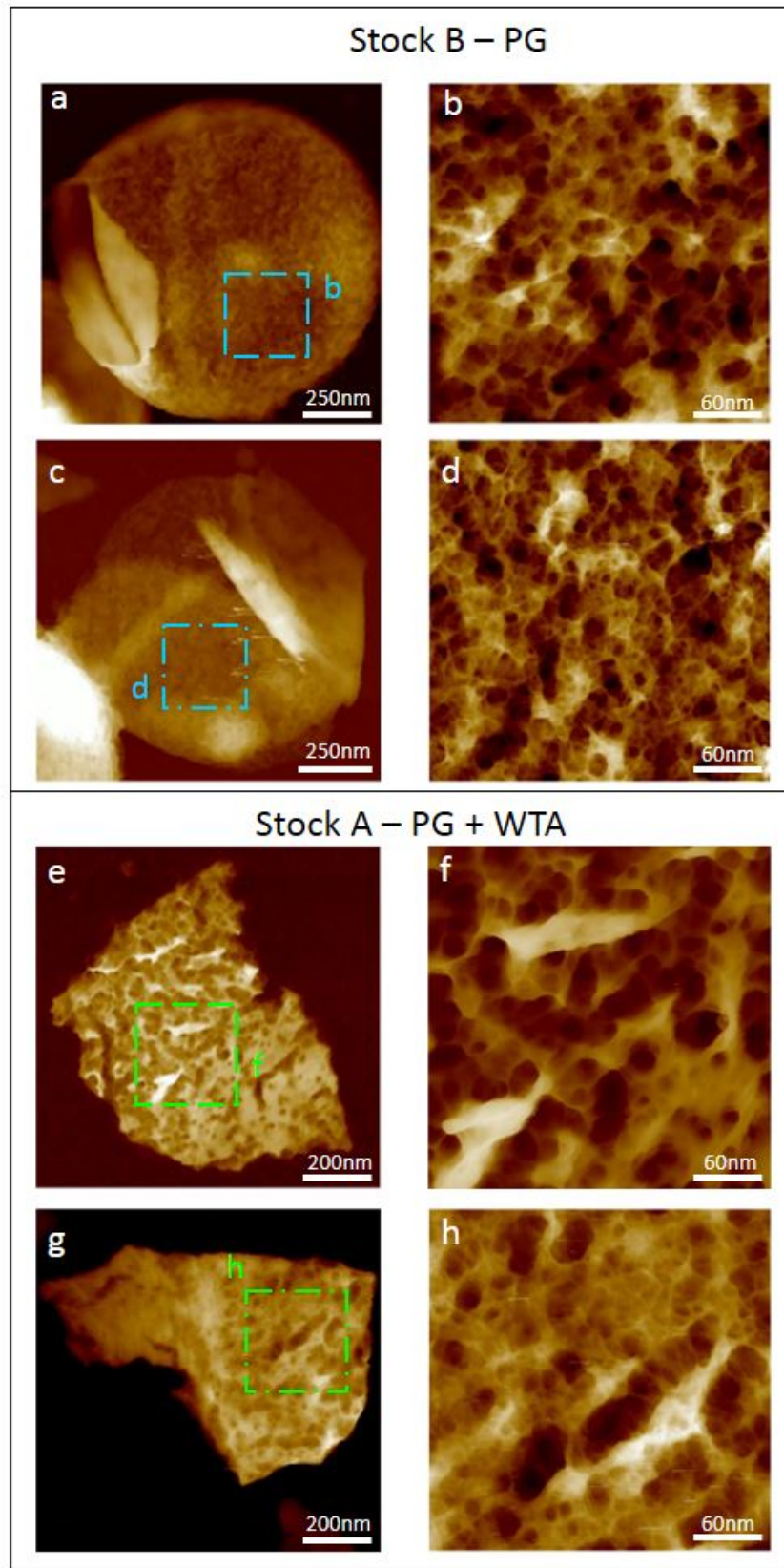


Figure 3.14 – a,c) Sacculi partially broken on one side, with the external surface occupying the majority of the sacculus area; b,d) zoomed image from 'a' and 'c' corresponding to the mature peptidoglycan structure (see dashed blue boxes in 'a' and 'c'); e,g) sacculus fragments showing the external structure upwards, this sample has not been treated with HF to remove the WTA; f,h) zoomed images from 'e' and 'g' (see dashed green boxes) showing a randomly orientated structure corresponding to the mature PG.

The images from *Figure 3.14* were performed under the experimental conditions summarized in *Table 3.10*. The AFM probe, mode and surface are the same as *Table 3.8*.

Table 3.10 – Experimental conditions for the visualization of sacculi in liquid environment in Figure 3.14

	SAMPLE TYPE	ENVIRONMENT	SPECIFIC CONDITIONS
FIGURE 3.14 A-D	WT sacculi Batch 3 Stock B Dilution 5	300mM KCl + 10mM Tris pH=7.8	Leave stabilize for 30min
FIGURE 3.14 E-F	WT sacculi Batch 4 Stock A Dilution 5	300mM KCl + 10mM Tris pH=7.8	Leave stabilize for 2h
FIGURE 3.14 G-H	WT sacculi Batch 5 Stock A Dilution 4	200mM KCl + 10mM Tris pH=7.8	Leave stabilize for 1h

Figure 3.14 show four examples of high resolution images of mature PG consisting of a random orientated mesh of fibres and pores of different sizes (see *Figure 3.14 right column*) taken from different sacculus fragments (see *Figure 3.14 left column*).

3.5.3 Comparison of mature peptidoglycan in different environments

The high resolution images of mature PG in hydrated sacculi showing a mesh structure instead of knobbls, proves they were not a result of the purification process. To test if the knobbls are created when sacculi is exposed to ambient conditions a direct correlation was made.

3.5.3.1 Optimization of correlating methods

3.5.3.1.1 Gridded glass coverslip

The glass grids are physically etched grids on high precision glass coverslips (see *Figure 3.15 a*). To work with them, they required the same cleaning treatment as the squared glass coverslips (see *section 2.3.1.2*). They also required being glued down to a plastic petri dish, which later must be glued down to the AFM stage using green glue (see *Figure 3.15 b*).

Each grid square comprises 50x50 μm of surface area, usually the biggest sacculi AFM images consist of 20x20 μm , meaning there will be a low correlation throughput each grid. Some sacculi were co-localized in air and in liquid, after several hours of trial and error (see *Figure 3.15 c*). Moreover, there was another drawback in this set-up: the etching of the grid lines meant that most of the sacculi were trapped at the lines instead

of being attached to the flat surface of the glass (see green arrow and dashed circles in *Figure 3.15 d*). There are two approaches to solve this problem: reverse the grid using the flat side, or increase the sacculi concentration.

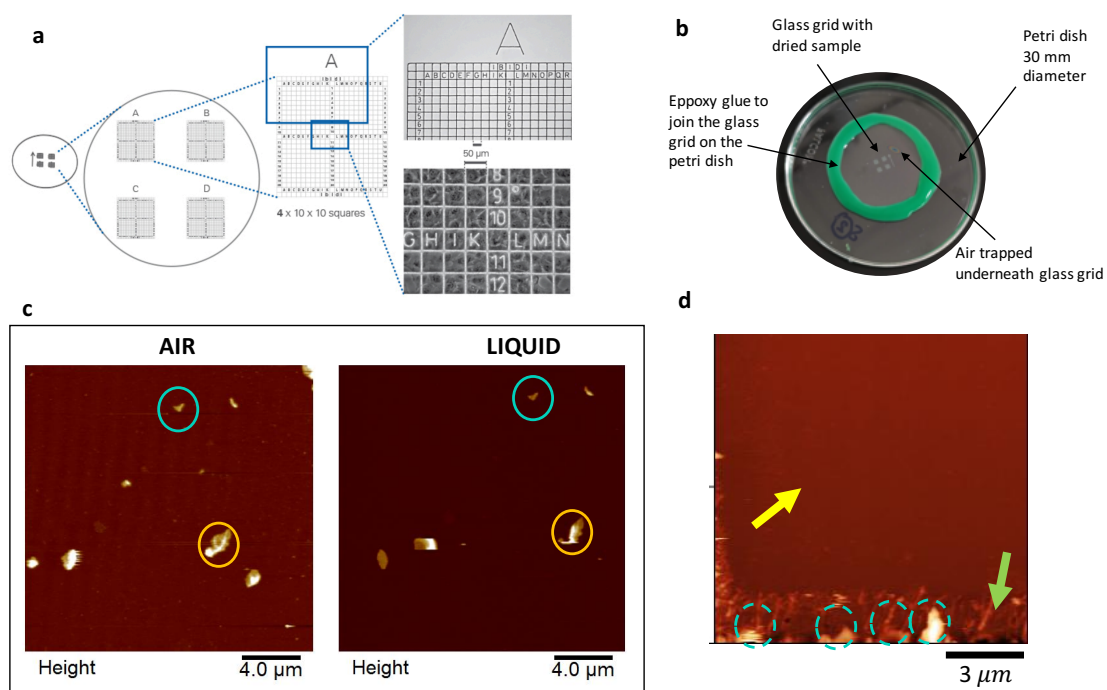


Figure 3.15 – Glass grid correlation method, set-up and results. A) Glass grids’ distribution and sizes, adapted with permission from [46] ; b) glass-grid set-up on the AFM stage; c) First results of correlation with the reverse grid, blue and orange circles represent the same sacculus in air and liquid; d) image of the side of the edge of one grid (green arrow), most of the sacculi are on top of the lines (blue dashed circles) whereas no sacculi are attached on the main area of the grid (yellow arrow).

In conclusion, this method was not very effective for all the reasons stated above and other correlation methods were sought. However, the gridded glass coverslip might be useful for other experiments, [19] especially for correlation with fluorescence microscopy. [47]

3.5.3.1.2 Marks on Mica

Another approach was to perform manual ink marks on top of the mica surface (*section 2.3.2.5*). The marks guide where to locate the AFM tip within approximately 30x30 μm region, increasing the sample throughput. Moreover, working with mica solves the etches trapping the sample and the drift and stability problems as shown above (*sections 3.3.4, 3.4.1 and 3.5.1*).

3.5.3.2 Mesh to Knobbles correlation

The approach to correlate the mature PG structure from hydrated sacculi was to first image the sample under liquid and then in ambient conditions by localizing the same area using marks on mica. The best results following this protocol are presented below in *Figure 3.16*.

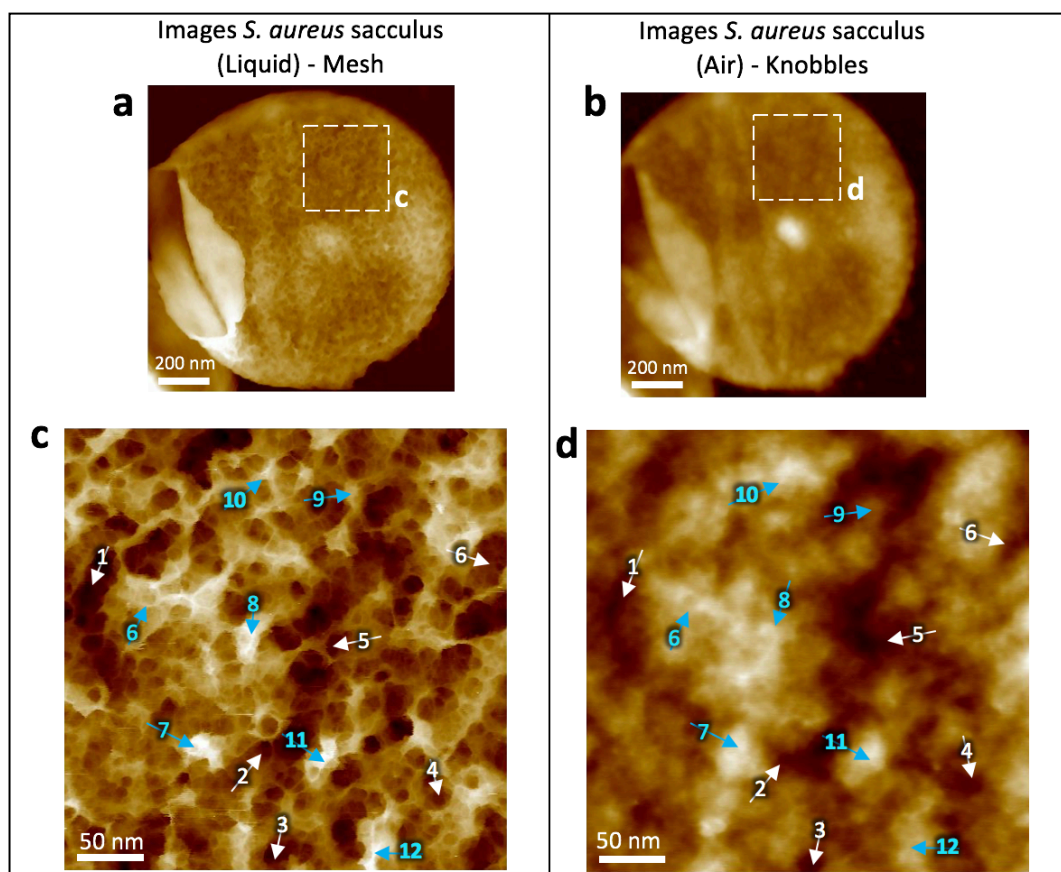


Figure 3.16 - a) Height image of a sacculus that has been broken just on the left side and emptied of all its content, showing clearly the different structures on the external and internal PG surfaces; b) Same exact sacculus as 'a' but imaged in ambient conditions (rinsed with HPLC water and dried with nitrogen flow); c) zoomed image from 'a' of mature PG in buffer conditions, white arrows (1-6): lower regions on the image, blue arrows (7-12): higher regions on the image; d) Image of the same location of mature PG in ambient conditions, zoom area from 'b' corresponding to the same area as 'c', the arrows were manually placed to point to the corresponding features as 1-12 in 'c'.

The images from *Figure 3.16* were performed under the experimental conditions summarized in *Table 3.11*. The surface was Cell-Tak™ coated mica.

Table 3.11 - Experimental conditions for sacculi in liquid environment and correlation in air environment

	AFM PROBE	AFM MODE	SAMPLE TYPE	ENVIRONMENT	SPECIFIC CONDITIONS
IMAGES IN AIR (B,D)	Tespa-V2	Tapping	WT sacculi Batch 3 Stock B Dilution 5	Air	Location 5 (by mark on Mica)
IMAGES IN LIQUID (A,C)	Fast Scan D	PeakForce Tapping	WT sacculi Batch 3 Stock B Dilution 5	300mM KCl + 10mM Tris pH=7.8	Location 5 /Stabilized for 30min

Figure 3.16 a shows a sacculus that has been partially broken on the left side exposing the internal PG surface (see Chapter 4) and the external PG surface covering most of the sacculus. *Figure 3.16 b* is the exact same sacculus as ‘a’ but in ambient conditions. *Figure 3.16 c* is a zoomed image from ‘a’ showing a randomly oriented mesh of fibres, very similar to previous examples (see *Figure 3.14*). The white arrows (1-6) correspond to lower features on the image, blue arrows (7-12) mark higher features on the image. *Figure 3.16 d* shows the same region as ‘c’ in a dry environment, which are knobbls [4] (see *Figure 3.4 b*). The arrows in this image were manually placed to point to the corresponding features as 1-12 in ‘c’. The resolution in air is lower because under normal humidity conditions a thin layer of water molecules is formed on the interface between surfaces and air, therefore when performing tapping, the AFM tip must exert enough force to surpass the capillary forces caused by the water layer. The AFM probe must be stiffer to withstand these forces (see *section 1.4.3.2*), which increases the tip-sample force, causing the resolution to decrease (see *Eq. 1.6*). Additionally, when the tip interacts with the sample the water of the interface forms a meniscus around the tip. This effect increases the length scale of the tip-sample interaction, effectively blunting the tip. Therefore, the knobbls features cannot be resolved in air as well as in liquid.

Table 3.12– Complete summary of established PG structures identified using AFM in different samples

	Nascent Peptidoglycan	Mature Peptidoglycan	Origin of data
<i>Living bacteria PG structure</i>	Concentric Rings	Randomly orientated mesh	[1]
<i>Dried sacculi structure</i>	Concentric Rings	Knobbls	[4]; this study
<i>Hydrated sacculi structure</i>	Concentric Rings	Randomly orientated mesh	This study

Table 3.12 shows a complete summary of all the different PG structures described by AFM from previous studies [1], [4] and the results from this study. Several samples were imaged first in liquid then in air and rehydrated again obtaining in all the cases a reversible transformation. Another important conclusion that can be extracted from this experiment is the corroboration that having a drying step before imaging in liquid does not affect the structure of the sacculi after rehydration. Therefore, from this point

onwards a drying step was always introduced to help attach the sacculi to the surface (see *section 2.3.2.4*). Therefore, Cell-Tak™ and PLL are used equally in this thesis.

3.5.3.3 Hydrogel behaviour

Besides the change in structure upon hydration, the sacculi suffered a radical increase in thickness, indicating that peptidoglycan has an hydrogel behaviour by absorbing water and integrating it to its composition. This hydrogel behaviour was quantified by measuring the thickness of PG single layers in air and liquid environments.

Using the marks on mica correlation methodology (2.3.2.5), scanning areas between 10x10 and 20x20 μm size were imaged in liquid then in air. Then the images were cropped off-line into smaller regions of approximately 5x5 μm containing a few PG single layers (see *Figure 3.17 a*). Then, a mask was applied using the Gwyddion tool 'mark grains by threshold' (see *Figure 3.17 b*). The background tilt was corrected applying a 1st order plane fit (excluding the masked areas). An individual sacculus is highlighted at a time and its thickness distribution plotted using the Gwyddion tool 'calculate 1D statistical functions'. The program plots two distributions, the highest peak corresponds to the background and the other to the sacculus fragment height distribution. The sacculus thickness is calculated by fitting two Gaussian functions to these peaks and returning the difference between the two expected values (X_0), see *Figure 3.17 c*. This is a reproductive and objective method especially in liquid, where the thickness distribution of sacculi is very broad, see *Figure 3.17 d*. It is important to highlight that the interaction force between the tip and the sample has a big influence in the sacculi thickness (see examples in *Figure 3.17 e*). There is a critical thickness for each sacculus from which if more force is applied, the material ruptures (e.g. 25.5nm, see *Figure 3.17 e*). The PeakForce set-point was always kept at the minimum.

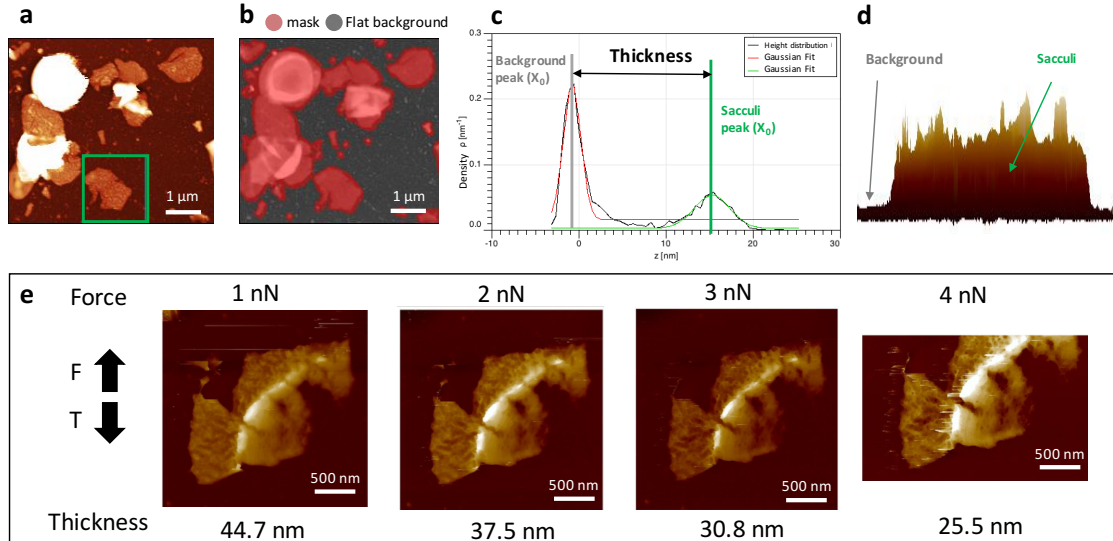


Figure 3.17 – a) Height AFM image of an Stock A sacculi sample in liquid with several PG single layers (see green arrows), one sacculus fragment selected (see green box); b) Same AFM image as ‘a’ marked with mask using grains by threshold), the grey background is flattened; c) Height distribution curve from image ‘b’, where the first peak corresponds to the background and the second peak corresponds to the sacculi fragments, thickness is difference between them; d) Side representation of the 3D image of the sacculus fragment from ‘a’, green box; e) Dependence between PeakForce set-point and the thickness of the same sacculus fragments.

Two types of sample were studied, the purified PG containing WTA (stock A) and the purified PG without WTA (stock B). For both, the procedure described above was followed. The results are summarized in Figure 3.18.

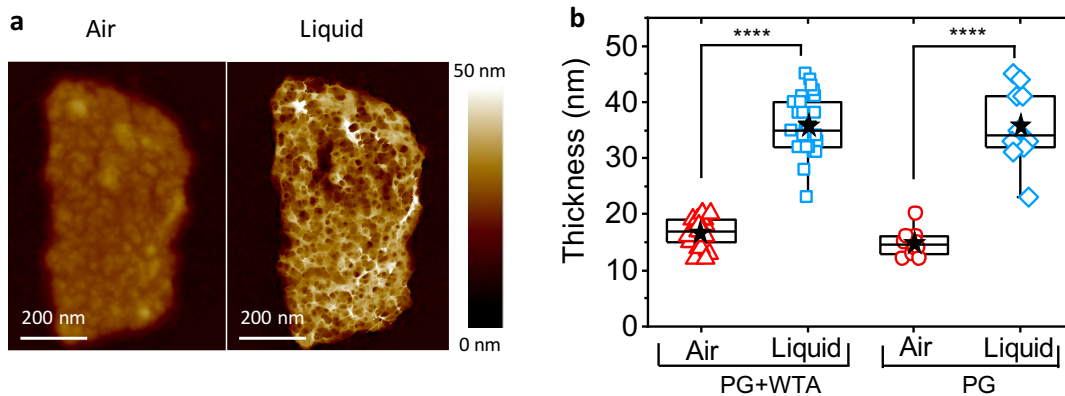


Figure 3.18– a) The same sacculus fragment in air and liquid with the same data scale = 50 nm; b) Thickness in liquid and air before (left, $n = 25$ sacculi) and after (right, $n = 10$ sacculi) removal of WTAs, using a paired, two-tailed t-test: $****p = 2.4 \cdot 10^{-5}$ (left) and $****p = 8.3 \cdot 10^{-6}$ (right). The boxes represent the 25–75% percentile, the center line indicates the median, the black stars show the mean and the error bars represent the minimum and maximum values. PG, peptidoglycan. Adapted from [28]

The AFM images taken to produce Figure 3.18 were performed under the experimental conditions summarised in Table 3.13.

Table 3.13 - Experimental conditions for the thickness measurement of sacculi in liquid and air from Figure 3.18

	AFM PROBE	AFM MODE	SAMPLE TYPE	ENVIRONMENT	SURFACE	SPECIFIC CONDITIONS
IMAGES IN LIQUID	Fast Scan -D	PeakForce Tapping	WT sacculi Batch 3 Stock A&B Dilution 5&6	300mM KCl + 10mM Tris pH=7.8	CellTak™ Coated MICA	No drying steps were taken
IMAGES IN AIR	Fast Scan -A	Tapping	WT sacculi Batch 3 Stock A&B Dilution 5&6	Air	CellTak™ Coated MICA	Rinse and blow dry to remove buffer

There is a significant difference in both samples between the thickness of sacculi in air and upon hydration. A paired, two-tailed student t-test was used, determining a difference of **** $p = 2.4 \cdot 10^{-5}$ for stock A and **** $p = 8.3 \cdot 10^{-6}$ for stock B. There was no significant difference between stock A and B thickness in liquid with $p = 0.95$. However, a slightly difference was found between the two stocks thickness in air with * $p = 0.03$. The results presented in *Figure 3.18 b* from left to right are: PG+WTA in air has a thickness of 17 ± 2 nm (mean \pm standard deviation, *s.d.*); PG+WTA in liquid has a thickness of 36 ± 5.3 nm (mean \pm *s.d.*); PG in air has a thickness of 15 ± 2 nm and PG in liquid has a thickness of 36 ± 6.9 nm (mean \pm *s.d.*).

In conclusion, these results show that *S. aureus* sacculi has an increase of thickness when hydrated of approximately 47% which means it has an hydrogel behaviour. This data agrees with previous cryo-EM studies showing a ~50% increase in cell wall thickness from live cells to extracted, hydrated sacculi.

3.5.4 Different approaches of analysis of mature peptidoglycan

The external peptidoglycan architecture of *S. aureus* is now well defined and with consistent results in both living bacteria and hydrated purified PG. Therefore, a quantitative method to compare these images must be developed.

3.5.4.1 Manual profiles measuring depth of pores and width of fibres

A random orientated mesh structure has two important features to focus on: the fibres that compose the lattice of the mesh and the pores formed between these fibres.

Regarding the pores, several things can be measured: area of pores, number of pores or depth of pores. Manually using the profiling tool the depth of the pores was measured for living cells and sacculi (see *Figure 3.19* for example).

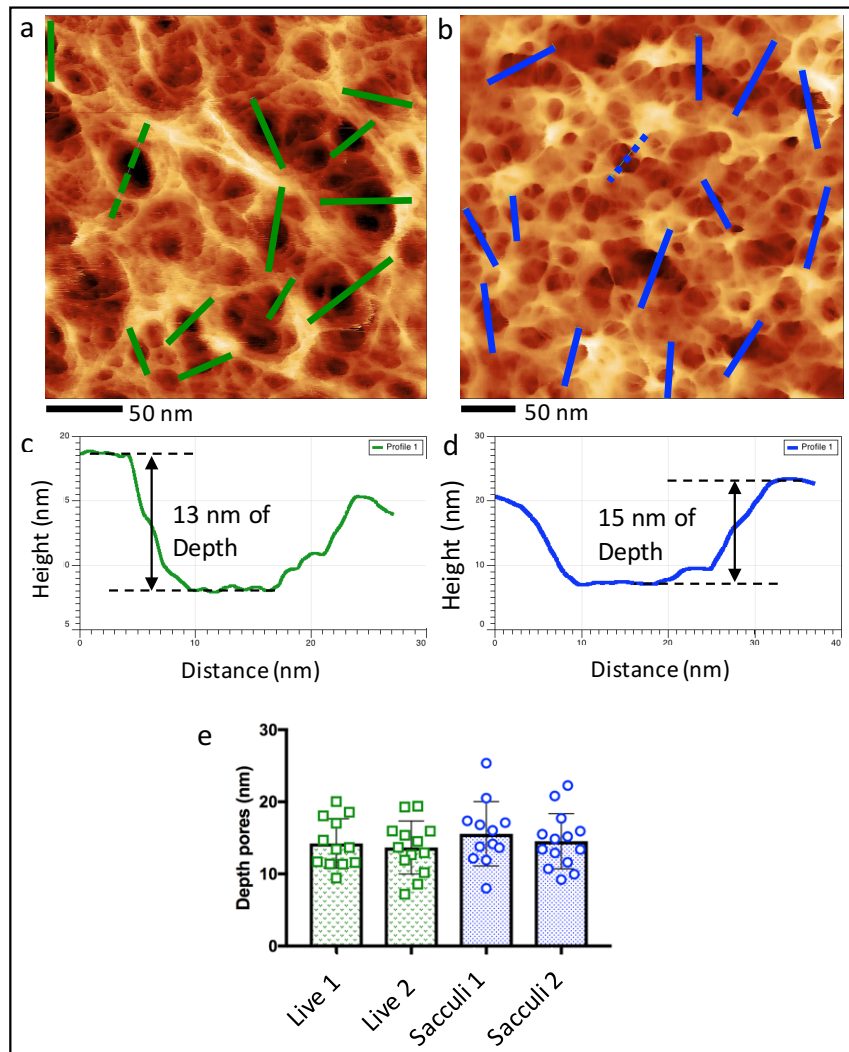


Figure 3.19 – a) Manual profiling analysis to calculate depth of pores from the external mature PG structure of a living cell adapted from [1]; b) Manual profiling analysis to calculate depth of pores from the external mature PG from an individual sacculus; c) profile representing an example measurement from a total of $n=12$ made in this image, see dashed green line in 'a', the calculated depth was 13 nm in this case; d) profile representing an example measurement from a total of $n=12$ made in this image, see dashed blue line in 'b', the calculated depth was 15 nm in this case; e) Results from two images of live cells (green) and sacculi (blue).

In *Figure 3.19* this manual process is summarized. First several lines were drawn in random directions across similar number of pores for both images, then two cursors are placed between the end of a pore and the highest point possible extracting the depth of a pore. This same process was repeated for two images of hydrated sacculi and from living cells [1]. The results are summarized in *Figure 3.19 e*.

The main disadvantages of this technique are the loss of pores not analysed and the high level of subjectivity, leading to poor reproducibility. Regarding the fibre width, the same profiling tool was applied as above. Using the full width at half maximum (FWHM) [26], [30], [48] (see *Figure 3.20* for an example).

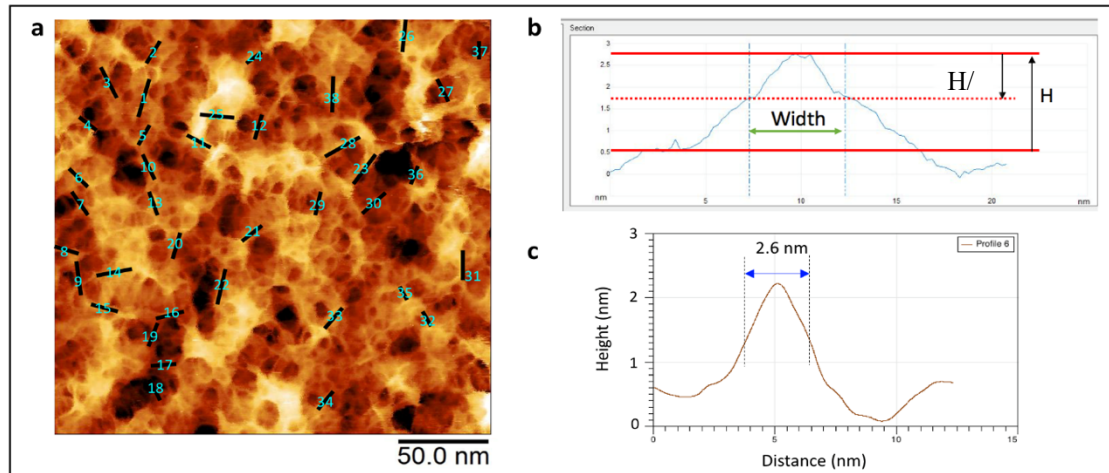


Figure 3.20 – a) AFM image of a hydrated sacculi with numbers assigned to each fibre (marked with black lines); b) Analysis method of fibre width using manual profiling tool, basic principle of Full width at half maximum (FWHM); c) Example profile from image ‘a’ corresponding to the profile 6, width marked with blue arrow (2.6 nm).

Figure 3.20 shows an example of how the FWHM method was applied in a mature PG AFM image of hydrated sacculi. Fibres to be analysed were chosen based on their distinguishability from neighbouring features, including various orientations and sizes (see *Figure 3.20 a*). Systematic errors were reduced by performing three independent profiles perpendicular to each fibre and determining the geometric mean.

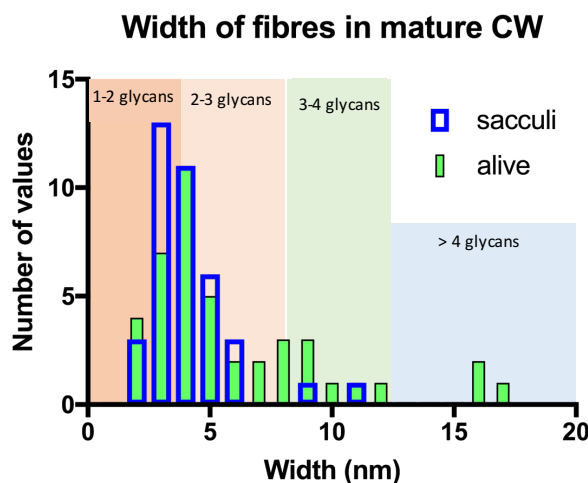


Figure 3.21- Results from the manual profiling calculation of width of the fibres taken using images of CW from different samples: hydrated sacculi (blue, n= 2 images, n= 70 fibres) and living cells (green, n= 2 images, n= 65 fibres)

Figure 3.21 shows two histograms of fibre widths (for hydrated sacculi, blue and live cells in green [1]). It was suggested that all these measurements can be grouped in four

different categories according to their number of glycans in each fibre. The estimation of number of glycans per fibre was made using the value of glycan to glycan spacing from the living cells data (2.7 ± 0.5 nm, see *section 3.4.1*). The fibres that were 1-4 nm wide, probably corresponded to individual or double glycan chains see dark orange area in *Figure 3.21*. The fibres that were 4-8 nm wide corresponded to strands interchanged together formed by two to three glycan chains and so on. The median values were 4.5 ± 3.8 nm for live cells and 3.6 ± 1.9 nm for hydrated sacculi. A significant difference (with $p=0.0096$) between the two populations was found, after performing a non-paired *student t* test. The majority of the analysed fibres were compressed between the first and second group, between 2-3 glycans. But in live cells some fibres were comprised of more than 4 glycan chains. The randomness nature of the mesh structure could have its origin in this huge variety of fibre's width.

Regarding the method of analysis, it is reliable because a representative number of fibres was analysed for each image. Even if this approach is very time consuming it is well established in the AFM community [26], [30], [48]. All the results obtained with the manual profiling approach are summarized in *Table 3.14*. The results from the pores depth are not reliable and need to be supported by other analysis approaches.

Table 3.14 – Summary of the results obtained from the analysis of random orientated mesh (mature PG) using the manual profiling method for both living bacteria and hydrated purified PG.

	Living bacteria PG structure	Hydrated purified PG structure
<i>Pores depth (not reliable)</i>	13.9 ± 3.4 nm	15.1 ± 3.9 nm
<i>Fibre width</i>	4.5 ± 3.8 nm	3.6 ± 1.9 nm

3.5.4.2 Two-dimensional sectioning (depth maps)

Here an alternative approach to characterize the pores from the mature peptidoglycan structure is presented. This analysis is an adaptation from [1]. The two-dimensional sectioning or depth map approach consists on dividing the AFM image into several two-dimensional sections at the XY planes along the Z axis, convert each section into binary highlighting only the pores and then put all the sections together one on top of another. The final stack is colour coded by depth (see *Figure 3.22*).

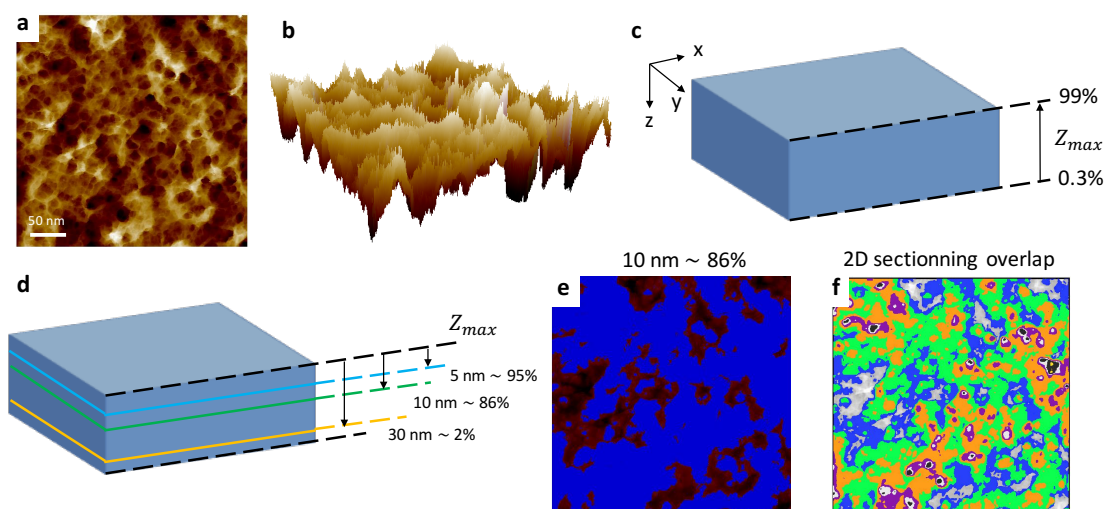


Figure 3.22 – a) AFM image with the height as the colour, top view in 2D; b) AFM image in a side three dimensional view; c) simplification of all the information contained in image ‘b’, the Z_{max} is calculated neglecting the areas below 0.3% and above 99% because they might contain artefacts and signal errors from the AFM; d) two dimensional sectioning at the XY plane going down from the Z_{max} a certain amount of nm; e) example of binary selection of the pores at 86% of one image; f) final result of the AFM image analysis colour coding the pores: blue = 5 nm deep, green = 10 nm, orange = 15 nm, purple = 20 nm, white = 23 nm, black = 25 nm and yellow = 30 nm.

Figure 3.22 shows a schematic representation of the steps required to perform the two-dimensional sectioning method. First, it is necessary to know the maximum Z value of the image: Z_{max} , which is calculated by neglecting approximately 0.3% from the bottom of the image and above 99% of the image, to exclude artefacts caused by uncontrolled cantilever movements (see Figure 3.22 c). Then, choosing a set of depth values from the Z_{max} down, the percentage of the image is calculated corresponding to each depth (see Figures 3.22 d). Then, the open source software ImageJ/Fiji [49] is used to perform the two-dimensional (XY) binary sections at each percentage. Finally, all the sections are stack together on top of the grey scale AFM image (see Figures 3.22 f). This analysis is performed with minimal subjectivity, analyses all the pores in each image and it is very reproducible.

In Figure 3.23 the two sets of data are compared visually (sacculi and living cells). Moreover, ImageJ/Fiji [49] returns the number of pores in each slice after performing ‘Analyse particles’. The number of pores at a certain depth can be calculated by subtracting the number of pores in a deeper section.

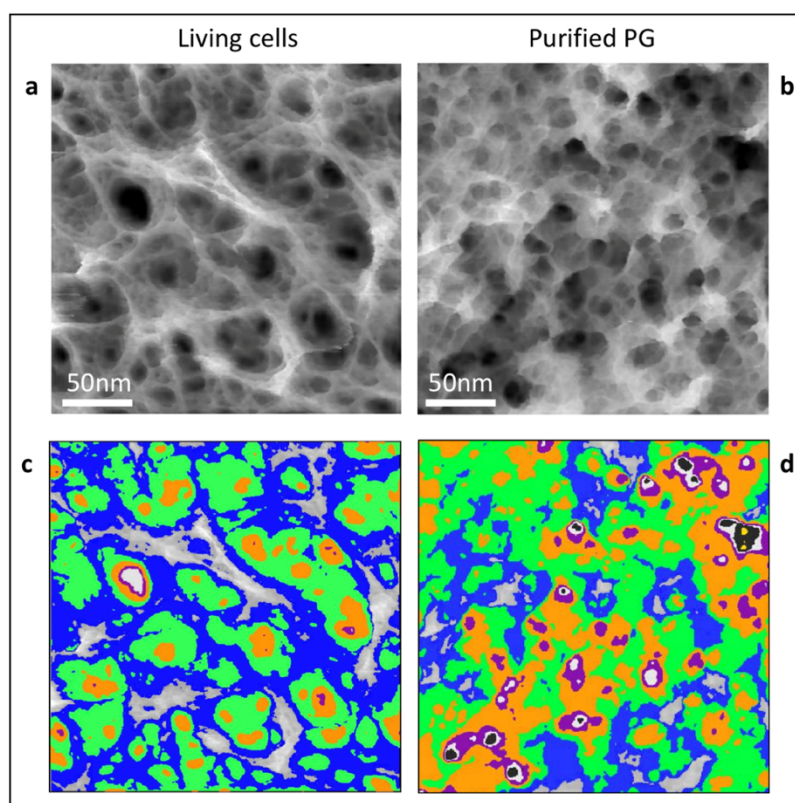


Figure 3.23 – a-b) Grey scale of the AFM images for both living cells (adapted from [1] and purified PG; c-d) coloured sections from the 99% of total depth of the image down. In order: 5 nm - blue areas, 10 nm - green areas, 15 nm – orange areas, 20 nm- purple areas, 23 nm – white areas, 25 nm – black areas, 30 nm – yellow areas.

Therefore, for each image the pores can be sorted in the set of depths chosen for the analysis. Then an average was calculated from $n = 2$ images for each sample, summarising them in *Table 3.15*.

Table 3.15 – Summary of the two-dimensional comparison between living bacteria and hydrated purified PG from *S. aureus*. The colours of the left column on the table correspond to the same colours displayed in Figure 3.23.

	Living bacteria PG structure (number pores/250x250)	Hydrated purified PG structure (number pores/250x250 nm)
Blue = 5nm deep	17	2
Green = 10nm deep	61	22
Orange = 15nm deep	40	52
Purple = 20nm deep	7	21
White = 23nm deep	2	11
Black = 25nm deep	0	4
Yellow = 30nm deep	0	1

The results presented in *Table 3.15* show that the majority of the pores in an area of 250x250 nm are at least **as deep as 10 nm for living cells and 15 nm for hydrated purified PG**, meaning the PG changes its nanometric dimensions when it is removed of its native environment.

Another striking conclusion, there is a small number of pores **as deep as 23 nm** in living cells which represents all the thickness of the cell wall *in vivo*. [1], [50] In this sacculus example the deepest pore is **30 nm** deep, which is much deeper than the CW in its native environment. The reason for this difference is probably because the PG relaxes when the tension is released after the turgor pressure is lost.

3.5.4.3 From AFM image to 3D representation using Avizo

Atomic Force Microscopy images have a disadvantage when it comes to data interpretation. AFM images contain three dimensional information but the data usually is presented with a two dimensions perspective with the colour being the third dimension. [25], [26], [30], [31] (see for example *Figure 3.22 a*). The AFM software can tilt the image to a side view where the Z information will be available but then the lateral resolution (X-Y) is lost (see example in *Figure 3.22 b*). To address the main objective of this chapter, decipher the three-dimensional architecture of the external PG of *S. aureus*, a new method of visualizing and interpreting these images is required. A new routine was developed using binary thresholding where the areas of interested are highlighted (*i.e.* the pores) along the Z axis of the image (~ 30 slices), these slices are fused together into a binary stack of images and visualized in three-dimensions using a 3D rendering software such as Avizo™ [51] or ImageJ/Fiji™ [49].

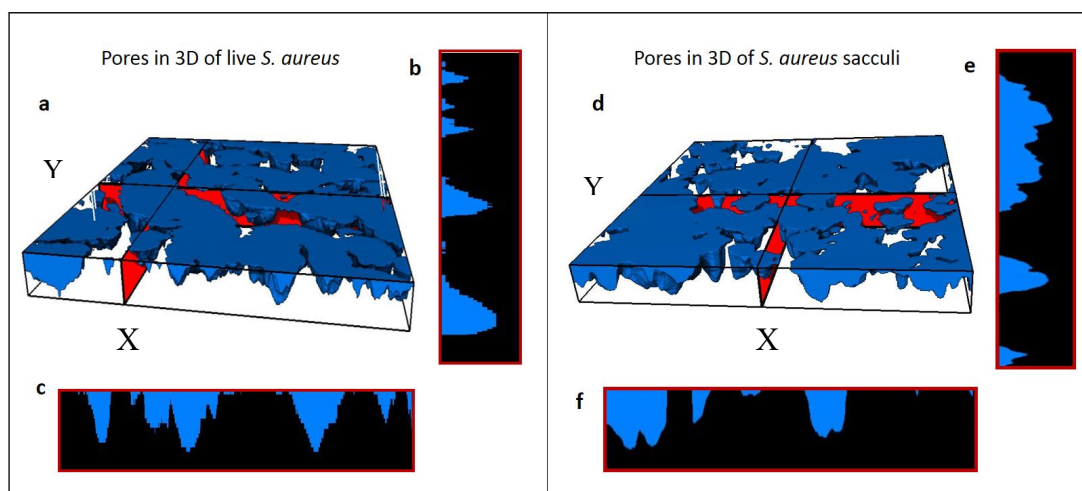


Figure 3.24 – 3D representation with Avizo of a) pores from a living S. aureus cells, from the top down, the pores are filled with blue colour; b) XZ slice extracted from the marked area in red from ‘a’, the blue areas represent the pores from that line; c) YZ slice extracted from the marked area in red from ‘a’; d) pores from a S. aureus sacculi, from the top down; e) XZ slice extracted from the marked area in red from ‘d’, the blue areas represent the pores from that line; f) YZ slice extracted from the marked area in red from ‘d’.

Figure 3.24 a is the 3D rendering from living bacteria mesh where the pores are shown as blue volumes. Figure 3.24 d is the 3D rendering from a sacculi image. This is a purely a qualitative representation but it maintains the XY resolution as well as providing Z information. Both softwares (Avizo™ and ImageJ™) can provide multi-ortho slices in the XZ and YZ planes (see Figure 3.24 b-c and e-f), resulting in a lateral vision of the PG pores as function of its thickness showing a range of sizes and depths depending on the position of the lateral slices (see red areas in Figure 3.24 a).

Then, by colour coding the slices of interested in the XY plane from the complete stack (~ 30 slices) three-dimensional maps were produced highlighting the set of depths (Figure 3.23 and Table 3.15). The best results are summarized in Figure 3.25 comparing data from living bacteria and purified PG.

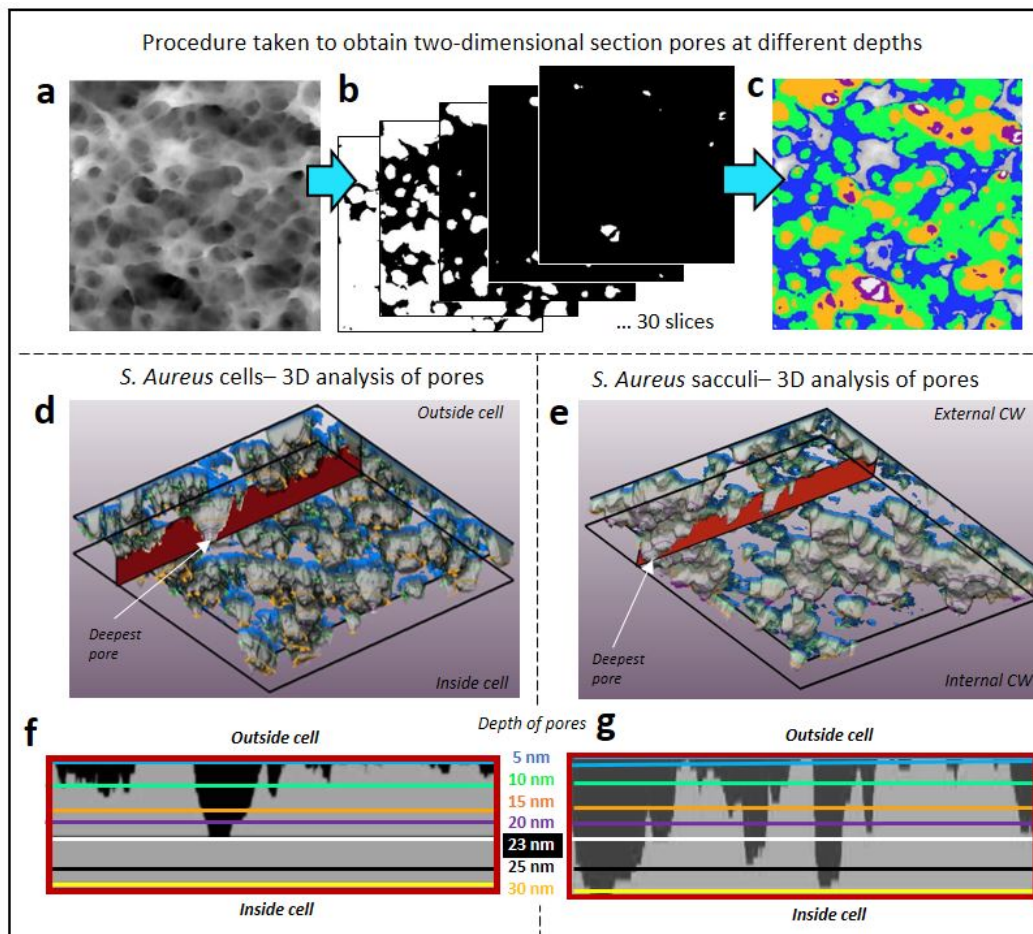


Figure 3.25 – Summary of the complete three dimensional images from living bacteria and sacculi comparison. a) AFM image of mature sacculi in grey scale; b) creation of >30 slices of different depths (every 3% of image); d) two-dimensional slices reconstruction highlighting only five depths with different colours; e) 3D Avizo™ representation from the complete stack of *S. aureus* live cells. Pores with 5 depths highlighted; f) same representation from a hydrated sacculi sample with 7 depths highlighted; g) XZ slice marked with a red area in 'e' highlighting the profile of the pores; h) same profile marked with a red area in 'f'. Adapted from [28]

Figure 3.25 a-c show the steps necessary to obtain a stack of binary images with the chosen depths colour coded. *Figure 3.25 d-e* are the same as *Figure 3.24 a, d* but from a different perspective and with the edges of the pores colour coded by depth. *Figure 3.25 f-g* are XZ slices from the red regions marked in *Figure 3.25 d-e*. These slices are a direct comparison of the pores characteristics between living cells and hydrated sacculi. The results presented in *Figure 3.25* shows the same information as *Figure 3.23* and *Table 3.15* combined, introducing a 3D representation of this data. To conclude, the peptidoglycan changes the depth of the pores when relaxed in the sacculi sample with respect to the native environment in the living cells. This striking result could explain how the CW fulfils its functions as permeable barrier and allows a certain degree of deformation during the cellular division process. Another biological implication of the peptidoglycan being a porous hydrogel deformable under pressure is that the cell might be able to squish and deform itself to survive in difficult environments such as inside the immune cells of the host organism or to overcome severe desiccation periods. [52]–[54]

3.6 Discussion

In this chapter, the external peptidoglycan structure has been characterized for both hydrated purified PG and living cells.

The first conclusion that can be extracted is the nascent peptidoglycan material has the same structure in the living cells as the hydrated sacculi. This structure, that appears on the external surface of the CW when the bacterium has just finish dividing, is a set of concentric rings orientated along the current division plane and perpendicular to the most recent division plane (see *Figure 3.11* for summary of results). [1]–[4], [55] The finer structure of the rings is the glycan strands forming the backbone of the rings with the peptide side chains organized with helical pitch of 4 nm periodicity as protrusions either along the rings or between them (see *Figure 3.12*). The AFM presented, in *section 3.4.2*, is presumably a direct measure of this periodicity, [1], [28] the resultant values are in agreement with other indirect techniques such as NMR and HPLC. [32]–[36], [56] Although the helical pitch was found in both hydrated sacculi and living bacteria, not enough results were obtained to confirm this solidly. Thus, more images of higher resolution would be needed using technological improvements to the AFM.

The second conclusion is the mature PG structure on the external surface of the living cell is a random orientated mesh, consistent with the results obtained from hydrated sacculi (see *Figure 3.14*, and *section 3.5.2*),. Clarifying the controversy that appeared when dried sacculi was studied in the past [4] when a different structure called ‘knobbles’ was associated to the mature PG structure (see *Table 3.12*). In *section 3.5.3.2*, it has been shown that these two structures correlate perfectly: when an area of a sacculus showing a mesh architecture in liquid is imaged under a dry environment, *knobbles* appear instead on the same area (see *Figure 3.16*). This is a reversible transition, the same sacculus was imaged first in air, then in liquid and finally in air again, showing reversible transitions between ‘knobbles’ and ‘mesh’ (see *Figure 3.16*). During this analysis on different environments, a significant increase in thickness was found in hydrated sacculi. This was observed in both samples (with and without WTA, see *Figure 3.18*). Showing that this hydrogel behaviour is an intrinsic property of the peptidoglycan material (see *section 3.5.3.3*).

Further quantitative analysis from the mature PG structure led to several conclusions. In one hand, the peptidoglycan is organized in fibres of different widths, some of them are probably single glycan strands and other fibres are a bundle of several strands (see histogram in *Figure 3.22*). On the other hand, these fibres are randomly oriented and interlink with themselves in a way that pores are formed across the thickness of the peptidoglycan. The analysis and characterization of these pores is crucial because it gives insights into the relationship between structure and function of the cell wall of bacteria. It is believed, the pores must have a main role in the permeability function of the CW, allowing nutrients and other molecules to pass through its external barrier. [28]

The three-dimensional renderisation method with Avizo™ [51] was discovered during the optimization process to find a method of analysis that allows quantitative and reproducible characterization of the pores. This is a novel way to interpret and visualize the AFM images (see *Figure 3.24-26*). Providing a three-dimensional representation with only the highlighted information of the features of interest in contrast to conventional AFM analysis software that only provides good visualization in two-dimensions. Using this novel approach, the previous data from living cells [1] and the data of hydrated sacculi obtained in this project were compared (see *Figure 3.23-3.25*). The pore depth

comparison for both samples lead to the conclusion that peptidoglycan is a flexible material that depending on the environment conditions and the amount of pressure that is supporting can rearrange its bulk structure without changing its chemical composition.

To finalize this chapter, the three-dimensional renderisation method can be used to visualize the AFM images of the external PG in yet another representation. As said above, by selecting the area of interest of an AFM image and stack it along the Z axis, a .tiff file can be created and Avizo™ can interpret it as a 3D structure. [51] If the peptidoglycan material is chosen instead of the pores, the inverse image will be created highlighting the same features we see in the AFM image but without visualizing the pores or anything else. All different structures were represented in this way forming a model of the external CW of *S. aureus* (Figure 3.26 b).

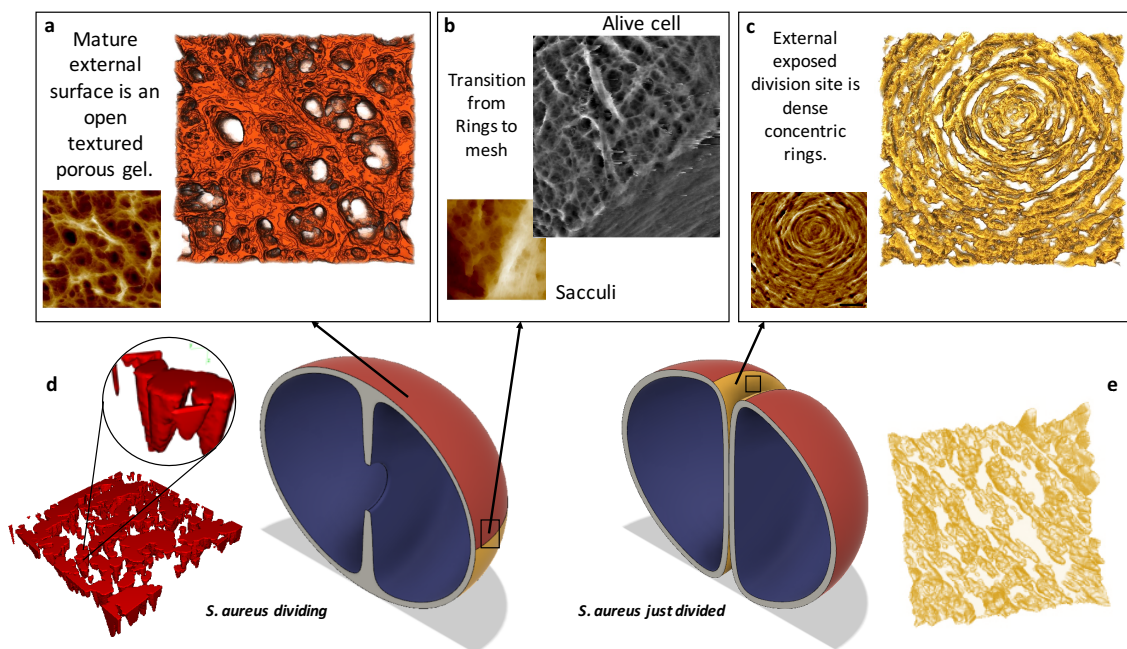


Figure 3.26 – Summary scheme of external PG structure of *S. aureus* both living cell and purified peptidoglycan – a) Model of mature external PG structure in red from living cells, obtained from AFM image (bottom); b) Sudden transition between mature mesh and nascent rings, grey image is from living cells, bottom image is from sacculi; c) Model of nascent external PG structure in yellow from living cells, obtained from image (bottom); d) Model of external mesh from sacculi in red; e) Model of nascent rings from sacculi in yellow; Centre 3D schemes adapted from [28] provided by Dr Robert Turner

Figure 3.26 shows a schematic of all the different structures that composed the external surface of the cell wall of *S. aureus* at different cycle stages. The big coloured images of mesh, transition and rings are extracted from the AFM images using the method described above (shown smaller on the side). Figure 3.26 d, e represents the same

structures on hydrated sacculi to summarize that all the structures had an agreement with the native environment.

In conclusion, the sample of hydrated purified peptidoglycan provides a perfect platform to study the cell wall of bacteria at high resolution, providing high throughput and the main advantage is that allows access to the internal cell wall structure never studied before. This sample has been shown in this chapter to be highly effective providing consistent results for the external PG structure agreeing with the living cells results, this means the same approach can be applied to study the internal PG structure of *S. aureus*.

3.7 References

- [1] J. M. Burns, "High Resolution Atomic Force Microscopy Imaging of Living Bacterial Surfaces," University of Sheffield, 2017.
- [2] R. D. Turner, N. H. Thomson, J. Kirkham, and D. Devine, "Improvement of the pore trapping method to immobilize vital coccoid bacteria for high-resolution AFM: A study of *Staphylococcus aureus*," *J. Microsc.*, vol. 238, no. 2, pp. 102–110, 2010.
- [3] A. Touhami, M. H. Jericho, and T. J. Beveridge, "Atomic Force Microscopy of Cell Growth and Division in *Staphylococcus aureus*," *Society*, vol. 186, no. 11, pp. 3286–3295, 2004.
- [4] R. D. Turner, E. C. Ratcliffe, R. Wheeler, R. Golestanian, J. K. Hobbs, and S. J. Foster, "Peptidoglycan architecture can specify division planes in *Staphylococcus aureus*," *Nat. Commun.*, vol. 1, no. 3, p. 26, 2010.
- [5] K. Amako, "Arrangement of Peptidoglycan in the Cell Wall of *Staphylococcus*," *Chem. Anal.*, vol. 150, no. 2, pp. 844–850, 1982.
- [6] J. Monteiro, P. Fernandes, F. Vaz, A. Pereira, A. Tavares, M. Ferreira, P. Pereira, H. Veiga, E. Kuru, M. Vannieuwenhze, Y. Brun, S. Filipe and M. Pinho, "Cell shape dynamics during the staphylococcal cell cycle," *Nat. Commun.*, vol. 6, 2015.
- [7] P. Giesbrecht, T. Kersten, H. Maidhof, and J. Wecke, "Staphylococcal cell wall: morphogenesis and fatal variations in the presence of penicillin.," *Microbiol. Mol. Biol. Rev.*, vol. 62, no. 4, pp. 1371–414, 1998.
- [8] G. Francius, O. Domenech, M. P. Mingeot-Leclercq, and Y. F. Dufrêne, "Direct observation of *Staphylococcus aureus* cell wall digestion by lysostaphin," *J. Bacteriol.*, vol. 190, no. 24, pp. 7904–7909, 2008.
- [9] G. Andre, S. Kulakauskas, M. Chapot-Chartier, B. Navet, M. Deghorain, E. Bernard, P. Hols and Y. Dufrêne, "Imaging the nanoscale organization of peptidoglycan in living *Lactococcus lactis* cells," *Nat. Commun.*, vol. 1, no. 3, 2010.
- [10] K. Li, X. Yuan, H. Sun, L. Zhao, R. Tang, Z. Chen, Q. Qin, X. Chen, Y. Zhang and H. Su, "Atomic force microscopy of side wall and septa peptidoglycan from *Bacillus subtilis* reveals an architectural remodeling during growth," *Front. Microbiol.*, vol. 9, no. MAR, pp. 1–6, 2018.
- [11] E. J. Hayhurst, L. Kailas, J. K. Hobbs, and S. J. Foster, "Cell wall peptidoglycan architecture in *Bacillus subtilis*," *Proc. Natl. Acad. Sci.*, vol. 105, no. 38, pp. 14603–14608, 2008.
- [12] R. Wheeler, S. Mesnage, I. G. Boneca, J. K. Hobbs, and S. J. Foster, "Super-resolution microscopy reveals cell wall dynamics and peptidoglycan architecture in ovococcal bacteria," *Mol. Microbiol.*, vol. 82, no. 5, pp. 1096–1109, 2011.
- [13] R. D. Turner, A. F. Hurd, A. Cadby, J. K. Hobbs, and S. J. Foster, "Cell wall elongation mode in Gram-negative bacteria is determined by peptidoglycan architecture," *Nat. Commun.*, vol. 4, p. 1496, 2013.
- [14] J. M. Walker, *Cell Wall Homeostasis*. 2016.
- [15] L. Kailas, C. Terry, N. Abbott, R. Taylor, N. Mullin, S. Tzokov, S. Todd, B. Wallace, J. Hobbs, A. Moir and P. Bullough, "Surface architecture of endospores of the *Bacillus cereus*, anthracis, thuringiensis family at the subnanometer scale," *Proc. Natl. Acad. Sci.*, vol. 108, no. 38, pp. 16014–

- 16019, 2011.
- [16] S. Brown, J. P. Santa Maria, and S. Walker, "Wall teichoic acids of gram-positive bacteria.," *Annu. Rev. Microbiol.*, vol. 67, pp. 313–36, 2013.
- [17] M. Schlag, R. Biswas, B. Krismer, T. Kohler, S. Zoll, W. Yu, H. Schwarz, A. Peschel and F. Götz, "Role of staphylococcal wall teichoic acid in targeting the major autolysin Atl," *Mol. Microbiol.*, vol. 75, no. 4, pp. 864–873, 2010.
- [18] G. Andre, M. Deghorain, P. Bron, I. Van Swam, M. Kleerebezem, P. Hols and Y. Dufrêne, "Fluorescence and atomic force microscopy imaging of wall teichoic acids in *Lactobacillus plantarum*," *ACS Chem. Biol.*, vol. 6, no. 4, pp. 366–376, 2011.
- [19] R. Louise Meyer, X. Zhou, L. Tang, A. Arpanaei, P. Kingshott, and F. Besenbacher, "Immobilisation of living bacteria for AFM imaging under physiological conditions," *Ultramicroscopy*, vol. 110, no. 11, pp. 1349–1357, 2010.
- [20] L. Sigma-Aldrich Co., "Poly-L-lysine solution," 2015, p. 2, 2015.
- [21] R. D. Turner, S. Mesnage, J. K. Hobbs, and S. J. Foster, "Molecular imaging of glycan chains couples cell-wall polysaccharide architecture to bacterial cell morphology," *Nat. Commun.*, vol. 9, no. 1, 2018.
- [22] C. Begot, I. Desnier, J. D. Daudin, J. C. Labadie, and A. Lebert, "Recommendations for calculating growth parameters by optical density measurements," *J. Microbiol. Methods*, vol. 25, no. 3, pp. 225–232, 1996.
- [23] D. J. Müller and Y. F. Dufrêne, "Atomic force microscopy: A nanoscopic window on the cell surface," *Trends Cell Biol.*, vol. 21, no. 8, pp. 461–469, 2011.
- [24] D. J. Muller, "AFM: A nanotool in membrane biology," *Biochemistry*, vol. 47, no. 31, pp. 7986–7998, 2008.
- [25] Y. F. Dufrêne, T. Ando, R. Garcia, D. Alsteens, D. Martinez-Martin, A. Engel, C. Gerber and D. Müller., "Imaging modes of atomic force microscopy for application in molecular and cell biology," *Nat. Nanotechnol.*, vol. 12, no. 4, pp. 295–307, 2017.
- [26] T. R. Rodríguez and R. García, "Tip motion in amplitude modulation (tapping-mode) atomic-force microscopy: Comparison between continuous and point-mass models," *Appl. Phys. Lett.*, vol. 80, no. 9, pp. 1646–1648, 2002.
- [27] S. Kumar, M. Cartron, N. Mullin, P. Qian, G. Leggett, C. Hunter and J. Hobbs, "Direct Imaging of Protein Organization in an Intact Bacterial Organelle Using High-Resolution Atomic Force Microscopy," *ACS Nano*, vol. 11, no. 1, pp. 126–133, 2017.
- [28] L. Pasquina-Lemonche, J. Burns, R. Turner, S. Kumar, R. Tank, N. Mullin, J. Wilson, B. Chakrabarti, P. Bullough, S. Foster and J. Hobbs, "The architecture of the Gram-positive bacterial cell wall," *Nature*, vol. 582, no. 7811, pp. 294–297, 2020.
- [29] D. Nečas and P. Klapetek, "Gwyddion: An open-source software for SPM data analysis," *Cent. Eur. J. Phys.*, vol. 10, no. 1, pp. 181–188, 2012.
- [30] R. R. L. De, D. A. C. Albuquerque, T. G. S. Cruz, F. M. Yamaji, and F. L. Leite, "Measurement of the Nanoscale Roughness by Atomic Force Microscopy: Basic Principles and Applications," *At. Force Microsc. - Imaging, Meas. Manip. Surfaces At. Scale*, 2012.
- [31] R. García, *Dynamic atomic force microscopy methods*, vol. 47, no. 6–8, 2002.
- [32] W. Vollmer, D. Blanot, and M. A. De Pedro, "Peptidoglycan structure and architecture," *FEMS Microbiol. Rev.*, vol. 32, no. 2, pp. 149–167, 2008.
- [33] S. J. Kim, J. Chang, and M. Singh, "Peptidoglycan architecture of Gram-positive bacteria by solid-state NMR," *Biochim. Biophys. Acta - Biomembr.*, vol. 1848, no. 1, pp. 350–362, 2015.
- [34] W. Vollmer and S. J. Seligman, "Architecture of peptidoglycan: more data and more models," *Trends Microbiol.*, vol. 18, no. 2, pp. 59–66, 2010.
- [35] R. D. Turner, W. Vollmer, and S. J. Foster, "Different walls for rods and balls: The diversity of peptidoglycan," *Mol. Microbiol.*, vol. 91, no. 5, pp. 862–874, 2014.
- [36] S. M. Desmarais, M. A. De Pedro, F. Cava, and K. C. Huang, "Peptidoglycan at its peaks: How chromatographic analyses can reveal bacterial cell wall structure and assembly," *Mol. Microbiol.*, vol. 89, no. 1, pp. 1–13, 2013.
- [37] T. Ito, N. Kodera, and T. Ando, "A high-speed atomic force microscope for studying biological macromolecules," *Seibutsu Butsuri*, vol. 41, no. supplement, p. S92, 2017.
- [38] M. Shibata, T. Uchihashi, T. Ando, and R. Yasuda, "Long-tip high-speed atomic force microscopy for nanometer-scale imaging in live cells," *Sci. Rep.*, vol. 5, pp. 1–7, 2015.
- [39] A. P. Nievergelt, J. D. Adams, P. D. Odermatt, and G. E. Fantner, "High-frequency multimodal

- atomic force microscopy," *Beilstein J. Nanotechnol.*, vol. 5, no. 1, pp. 2459–2467, 2014.
- [40] J. D. Adams, A. Nievergelt, B. W. Erickson, C. Yang, M. Dukic, and G. E. Fantner, "High-speed imaging upgrade for a standard sample scanning atomic force microscope using small cantilevers," *Rev. Sci. Instrum.*, vol. 85, no. 9, 2014.
- [41] G. E. Fantner, R. J. Barbero, D. S. Gray, and A. M. Belcher, "Kinetics of antimicrobial peptide activity measured on individual bacterial cells using high-speed atomic force microscopy," *Nat. Nanotechnol.*, vol. 5, no. 4, pp. 280–285, 2010.
- [42] J. Foolen, T. Yamashita, and P. Kollmannsberger, "Shaping tissues by balancing active forces and geometric constraints," *J. Phys. D: Appl. Phys.*, vol. 49, no. 5, 2015.
- [43] R. Silva, B. Fabry, and A. R. Boccaccini, "Fibrous protein-based hydrogels for cell encapsulation," *Biomaterials*, vol. 35, no. 25, pp. 6727–6738, 2014.
- [44] P. Grimmer and J. Notbohm, "Displacement Propagation in Fibrous Networks Due to Local Contraction," *J. Biomech. Eng.*, vol. 140, no. 4, p. 041011, 2018.
- [45] E. Frey, "Physics in cell biology: On the physics of biopolymers and molecular motors," *ChemPhysChem*, vol. 3, no. 3, pp. 270–275, 2002.
- [46] I. Cells in focus, "Gridded Glass Coverslips Grid-50," *Ibidi company*. .
- [47] R. Tank, V. Lund, R. Turner, S. Kumar, L. Pasquina-Lemonche, N. Mullin, S. Foster and J. Hobbs, "STORM-force and the study of *B. subtilis*," *Nat. Commun.*, vol. In preparation, 2020.
- [48] K. Umemura, T. Hayashida, D. Nii, Y. Yamaguchi, and T. Kawashima, "Structures of hybrids of DNA and carbon nanotubes in air and in liquids," *Fourth Int. Conf. Smart Mater. Nanotechnol. Eng.*, vol. 8793, no. August 2013, p. 87931W, 2013.
- [49] J. Schindelin, I. Arganda-Carreras, E. Frise, V. Kaynig, M. Longair, T. Pietzsch, S. Preibisch, C. Rueden, S. Saalfeld, B. Schmid, J. Tinevez, D. White, V. Hartenstein, K. Eliceiri, P. Tomancak and A. Cardona, "Fiji: an open-source platform for biological-image analysis," *Nat. Methods*, vol. 9, no. 7, pp. 676–82, 2012.
- [50] V. R. F. Matias and T. J. Beveridge, "Native cell wall organization shown by cryo-electron microscopy confirms the existence of a periplasmic space in *Staphylococcus aureus*," *J. Bacteriol.*, vol. 188, no. 3, pp. 1011–1021, 2006.
- [51] F. S. Thermo Fisher Scientific, "Thermo Scientific Avizo Software." Merignac Cedex, France.
- [52] D. Yang, Y. X. Ho, L. M. Cowell, I. Jilani, S. J. Foster, and L. R. Prince, "A genome-wide screen identifies factors involved in *S. Aureus* - Induced human neutrophil cell death and pathogenesis," *Front. Immunol.*, vol. 10, no. JAN, pp. 1–11, 2019.
- [53] E. Boldock, B. Surewaard, D. Shamarina, M. Na, Y. Fei, A. Ali, A. Williams, E. Pollitt, P. Szkuta, P. Morris, T. Prajsnar, K. McCoy, T. Jin, D. Dockrell, J. van Strijp, P. Kubes, S. Renshaw and S. Foster, "Human skin commensals augment *Staphylococcus aureus* pathogenesis," *Nat. Microbiol.*, vol. 3, no. 8, pp. 881–890, 2018.
- [54] K. D. Buchan, T. Prajsnar, N. Ogryzko, N. De Jong, M. Van Gent, J. Kolata, S. Foster, J. Van Strijp and S. Renshaw, "A transgenic zebrafish line for *in vivo* visualisation of neutrophil myeloperoxidase," *PLoS One*, vol. 14, no. 4, pp. 1–19, 2019.
- [55] V. Lund, K. Wacnik, R. Turner, B. Cotterell, C. Walther, S. Fenn, F. Grein, A. Wollman, M. Leake, N. Olivier, A. Cadby, S. Mesnage, S. Jones and S. Foster, "Molecular coordination of *Staphylococcus aureus* cell division," *Elife*, vol. 7, pp. 1–31, 2018.
- [56] B. A. Dmitriev, F. V. Toukach, O. Holst, E. T. Rietschel, and S. Ehlers, "Tertiary structure of *Staphylococcus aureus* cell wall murein," *J. Bacteriol.*, vol. 186, no. 21, pp. 7141–7148, 2004.

Chapter 4 The internal peptidoglycan architecture of *Staphylococcus aureus*

This chapter comprises a set of AFM experiments performed on purified peptidoglycan extracted from *S. aureus* healthy cells, which allowed us to set the structural framework of the internal surface of the cell wall for the first time.

4.1 Molecular resolution of internal cell wall

The internal surface of Gram-positive bacterial CW has a crucial role regarding the interaction with the biological processes that occur within the cell. Most of the proteins that have a transmembrane domain interact with the internal surface of the peptidoglycan network. The PBPs (see *section 1.3.3.1*) are of utmost interest because their active site is the target for β -lactam antibiotics. [1] PBPs have a domain attached to the membrane and other transmembrane domains, having direct contact with the internal surface of the cell wall.[2] One of the aims of this project is understanding the effect of antibiotics on the cell wall at nanometric level. To achieve this, the first step was deciphering the molecular architecture of the internal surface of the cell wall. As mentioned before, the main drawback of imaging *S. aureus* live cells with AFM is the lack of access to the internal surface of the cell. [3]–[6] However, the internal surface gets exposed when using purified PG. [7]–[12]

4.1.1 Imaging the internal cell wall under liquid conditions

In chapter 3, the external CW surface was characterized on hydrated purified PG. Here, the optimised protocol to image hydrated purified CW with AFM (*section 2.3.2.3.2*) was used, focusing on obtaining data from the internal CW.

It is crucial to be able to identify which surface is being imaged under the AFM. This was especially important at this stage of the research because the internal CW structure was still unknown and it was not possible to use the characteristic architecture of the internal CW as an indicator of the sacculus orientation. The best sacculi for this purpose were partially broken sacculus with both surfaces exposed to AFM imaging, while individual PG

layers were avoided. The internal CW surface was imaged at the highest magnification possible, see the best results in *Figure 4.2* below.

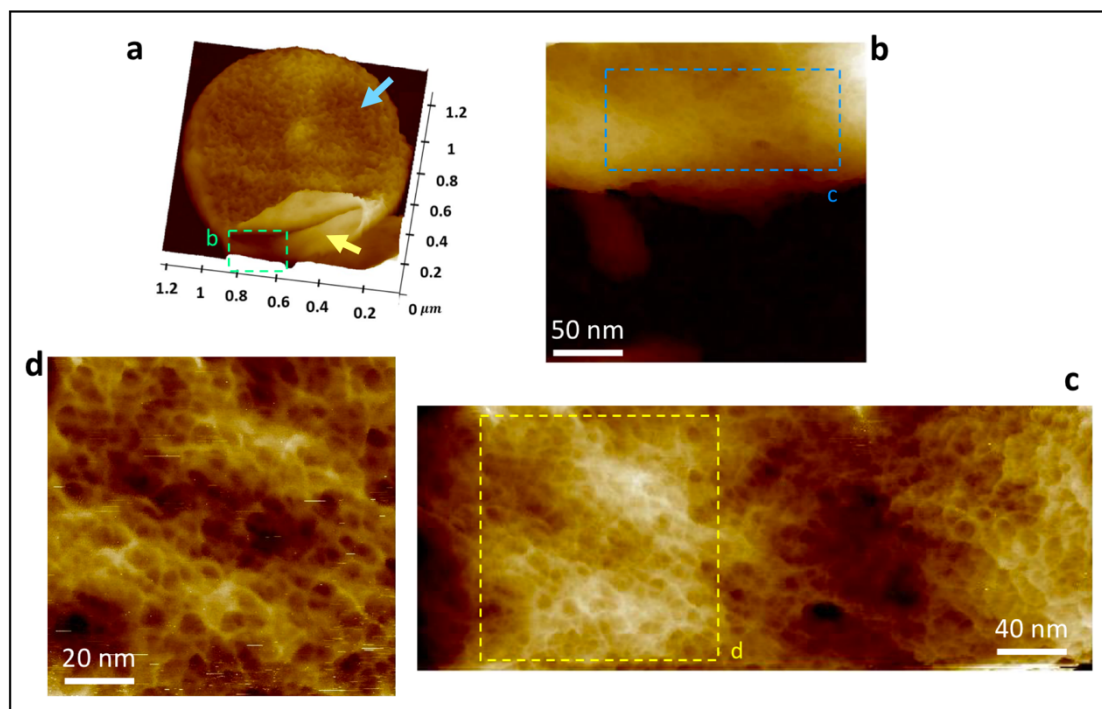


Figure 4.1 – a) the same sacculus as in Figure 3.16 a but represented using the 3D view in Nanoscope™, it is clear that it is only broken at the bottom, which is clearly the internal surface (see yellow arrow), while the rest of the sacculus has the external CW upwards (see blue arrow); b) zoomed image from the area marked with the green dashed boxed in 'a', showing a piece of internal surface on top of the flat background; c) zoomed image from 'b' from the dashed blue box, the contrast has increased enormously and details can be visualized better; d) zoomed image from the area marked with the yellow dashed box in 'c', showing the internal surface of a hydrated sacculi magnified in liquid. All height images.

The images from *Figure 4.1* were performed under the same experimental conditions summarized in *Table 3.10* (first row).

Figure 4.1 a shows a 3D representation of a sacculus fragment where the external PG corresponds to the majority of the area (blue arrow), while the small crack at the bottom shows the internal PG surface (yellow arrow). *Figure 4.1 b-d* show consecutive zooms from *Figure 4.1 a*. *Figure 4.2 c* shows small features which could easily get obscured by the grooves and wrinkles that form in the purified PG when attached to the surface. Higher magnification is required to reveal the finer PG architecture. *Figure 4.1 d* shows a densely packed mesh of fibres that are randomly orientated (see *section 4.4.3* for analysis). This is the first time this structure has been revealed.

The sacculus from *Figure 4.1* was rare and difficult to find among a very diverse sacculi sample. To give a more real representation of the typical samples used in this study, alternative conformations are presented in *Figure 4.2*.

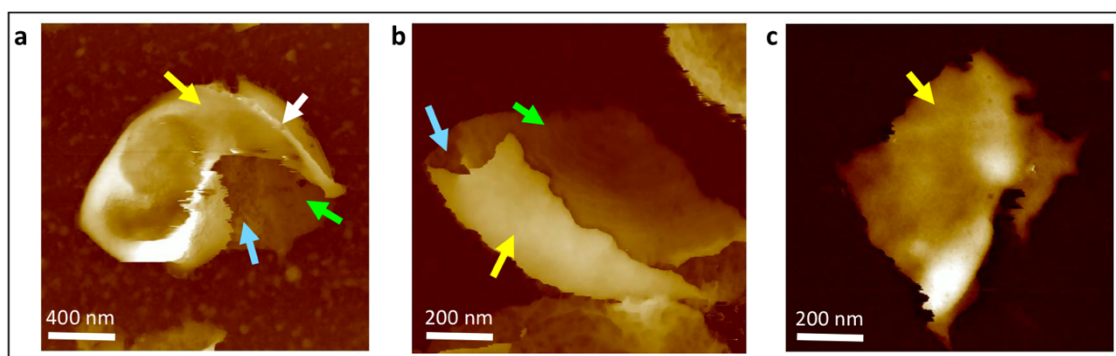


Figure 4.2 – a) sacculus which has been reversed with its internal CW covering most of its area (see yellow arrow), while the external CW corresponding to mesh (see blue arrow) and rings (see green arrow) are occupying less area. White arrow pointing probably to a rib, from a former division plane; b) sacculus with the flat area attached to the surface corresponding to rings (green arrow) and mesh (blue arrow), however the internal CW has been flipped over (yellow arrow); c) Individual fragment of CW with the internal smooth structure facing upwards (yellow arrow).

The images from *Figure 4.2* were performed under the experimental conditions summarized in *Table 4.1*.

Table 4.1 – Experimental conditions used to take the data from *Figure 4.2*. See section 2.3.2.3.2

AFM TIP	AFM MODE	SAMPLE TYPE	ENVIRONMENT	SURFACE	SPECIFIC CONDITIONS
FAST SCAN D	PeakForce Tapping	WT sacculi Batch 4 Stock A Dilution 5	300 mM KCl + 10mM Tris pH=7.8	CellTak™ Coated MICA	Dry step before imaging – 1h stabilization

Figure 4.2 a shows a reversed sacculus with its internal PG facing upwards and covering the majority of the area (yellow arrow), a small region of external PG can be visualized (see blue arrow pointing to mesh green arrow pointing to rings). Moreover, this sacculus contains an internal rib structure remnants of the previous piecrust (white arrow) [8]. The piecrust and ribs (see *section 1.3.3.3*) were never visualized on the external surface of live cells either. [3]–[6], [13] *Figure 4.2 b* shows a sacculus with an internal PG region flipped over the rest of the sacculus (see yellow arrow). Finally, *Figure 4.2 c* is an example of an individual fragment with its internal surface facing upwards (see yellow arrow).

Using the piecrust or ribs as an indication of an internal surface has a slight inconvenience when used on hydrated sacculi: the distinctive protrusions will appear even when the external surface is upwards. These features are so prominent that even

when facing down, the whole PG layer gets deformed. Therefore, a criteria was established to discern between these two scenarios. See examples in *Figure 4.3*.

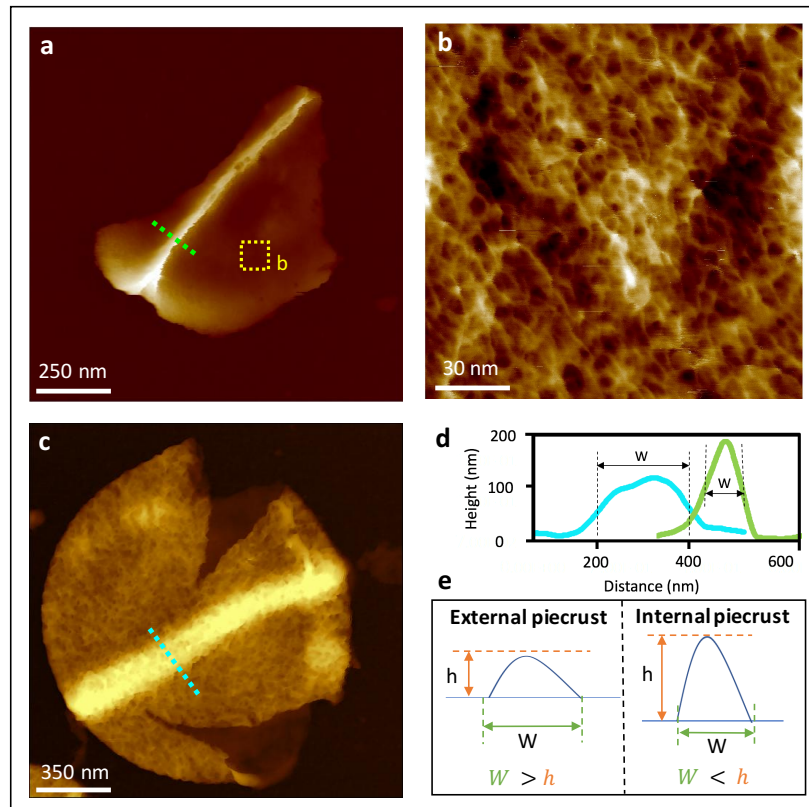


Figure 4.3– a) Sacculus fragment with a piecrust like feature diagonally across; b) Zoomed image from ‘a’ (see yellow dashed box) with a tight densely mesh structure; c) partially broken sacculus with external surface facing upwards; d) profiles taken from images ‘a’ and ‘c’ from green and blue dashed lines; e) schematics of the criteria established.

The images from *Figure 4.3* were performed under the same experimental conditions summarized in *Table 4.1*.

Figure 4.3 a shows a single PG layer with a prominent diagonal feature. This distinctive feature was identified as being the piecrust in early stages of formation. This was thought to correspond to the first scenario where the internal PG is facing upwards. To corroborate this, a higher magnification of the finer PG structure surrounding the piecrust was performed (see *Figure 4.3 b*). The PG was from the internal surface with tight densely packed mesh randomly orientated. The second scenario was explored in *Figure 4.3 c*, the external surface is facing upwards and there is a protrusion in the middle of the cell corresponding to the deformation from the piecrust underneath. This sacculus is partially broken, providing evidence that the top layer corresponds to the external surface. A major difference with respect to the first scenario is the texture of the protrusion being the same as the surrounding material (external mature PG). In

both scenarios, profiles were performed to measure the dimensions of the features. In *Figure 4.3 d* the green line is from *Figure 4.3 a* (see green dashed line) and the blue line is from *Figure 4.3 c* (see blue dashed line). The aspect ratio of the features is very different. The green profile from the internal PG shows a higher height than width, while the blue profile from the external surface has a bigger width than height. Consequently, the aspect ratio (A) from the 'piecrust' features was calculated using *Equation 4.1*. [14]

$$A = \frac{W}{h} \quad (\text{Eq. 4.1})$$

If the 'piecrust' is imaged from the internal surface, it would have $A < 1$; by contrast, if the piecrust is imaged from the external surface, $A > 1$. This criteria was defined for *S. aureus* sacculi (see schematization in *Figure 4.3 e*). The data from *Figures 4.1-4.3* are a small representation of hundreds of hydrated *S. aureus* sacculi.

4.2 Quantitative analysis of pores across the cell wall

Early in this project, it was clear that if the AFM was going to be a tool to gain insights into the relationship between function and structure of the CW, there were two main parts of the project with a similar importance. The first part, the experimental optimization in order to obtain comparable results in different samples and the second part was the optimization of an appropriate analysis method to be able to compare all the different samples included in this study.

4.2.1 Optimisation to analyse pore size

Novel approaches to analyse the size of the pores will be developed and applied to both external mature PG and internal PG architectures, complementing the previous analysis (*section 3.5.4*). It is crucial that these two architectures are quantitatively compared with a reproducible and non-biased method to be able to obtain meaningful information on the pores across the CW.

4.2.1.1 Manual measuring of individual pores for each image

Manual profiling was previous used to measure the depth of the pores in mature external images (see *section 3.5.4.1*), being poorly reproducible, subjective and time-consuming. However, the first time a new parameter is studied, performing a manual

analysis allow us to identify the limitations (if any) to be later implemented into a more automated routine. See the results for two images of each group in *Figure 4.4*.

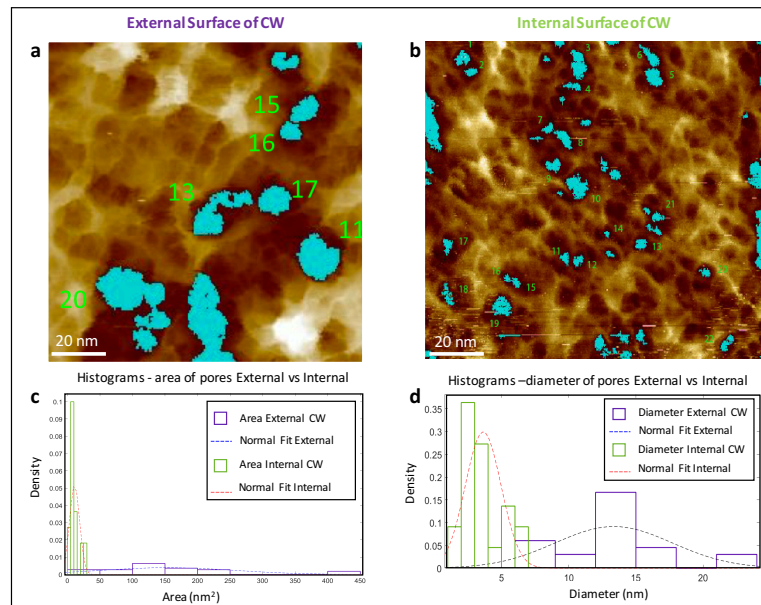


Figure 4.4 – a) External surface of the CW AFM image, where $n=22$ pores are highlighted in blue and numbered, using the particle analysis tool from the Nanoscope™ Analysis software; b) Internal surface image with also $n=22$ pores highlighted in the same way as in ‘a’; c-d) Histograms of the areas and diameter of all the pores from both images ‘a’ and ‘b’.

Figure 4.4 a shows the external surface of the CW where certain pores have been highlighted in blue and numbered with green labels ($n=22$, not all shown at this scale). This was done with the ‘particle analysis’ tool of the Nanoscope™ Analysis software, [15] the equivalent tool in Gwydion [16] is ‘mark grains by threshold’. First, a depth threshold was chosen so that at least 22 different pores were highlighted. Then, the pores were numbered and manually one by one was selected on the software, obtaining the area and maximum diameter of each individual pore. The same procedure was followed to analyse the pores from the internal surface, see *Figure 4.4 b*. The distributions of the area measurements are shown in *Figure 4.4 c* and the distribution of the diameters are shown in *Figure 4.4 d*. In both cases, there is a clear difference between the two populations. The median values are: $\text{Area}_{\text{median}} = 8.2 \pm 7.6 \text{ nm}^2$ and $\text{Diameter}_{\text{median}} = 3.6 \pm 0.2 \text{ nm}$ for the **internal surface** and $\text{Area}_{\text{median}} = 140.2 \pm 102 \text{ nm}^2$ and $\text{Diameter}_{\text{median}} = 13.4 \pm 0.93 \text{ nm}$ for the **external surface**. The internal PG is composed of smaller pores than the mature external PG in *S. aureus*.

4.2.1.2 Semi-automated method with final manual check

Two main problems were identified during the manual analysis: the number of pores must be increased and a better criteria for choosing the depth threshold should be established. The solution to solve these issues has to be as objective and reproducible as possible.

A semi-automated method of analysis was developed combining two analysis softwares: Image J/Fiji [17] and Nanoscope™ Analysis v1.20 [15] (Gwyddion can also be used) [16]. This method of analysis is similar to the “two-dimensional sectioning” explained in *section 3.5.4.2*. The aim is to measure the area of the pores from a 2D slice threshold at a certain percentage of the total thickness of the image. The target slice for the mature external images is where most of the pores start to be defined in the image (around 50% for all the images). However, for the internal surface the slice that allow for most of the pores to be selected was at 28% for all the images. The percentages are in proportion to the Z_{total} of each image, where the lowest point is 0% and the highest point is 100% (see *Figure 3.22* for more details). No other personal decision from the researcher was involved during the process aside from the thresholding. Using these guidelines the automated method is described step by step in *Figure 4.5* below.

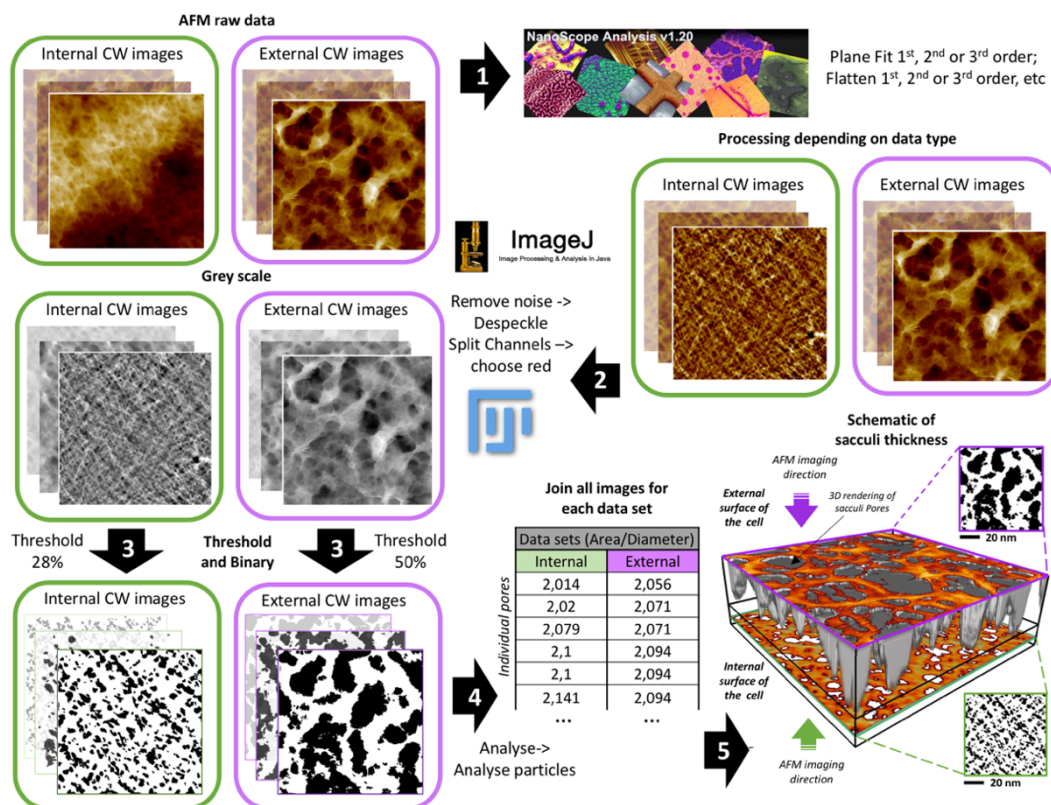


Figure 4.5 – Starting the method at the top left corner with the raw data from the AFM, Step 1: processing of the images using Nanoscope Analysis; Step 2: they are opened with Image J and converted to Grey scale; Step 3: then

the two sets of data have different thresholds to convert the images into binary, highlighting the pores in black; Step 4: measure the area of the pores using the analyse particles tool; Step 5: schematic of the sacculi thickness using real data by stacking an external CW image on top of an internal CW image.

Figure 4.5 shows a summarized scheme of the automated analysis methodology. Starting with the raw data from both sets (top left corner). The first step is to process these images to remove any tilt or curvature artefacts caused by the AFM imaging process using Nanoscope or Gwydion. [16] Both sets of images have to be processed accordingly (see *Figure 4.6* below). The second step is process the images with ImageJ/Fiji: convert the pixel size to nm, remove the noise and the convert the images to grey scale by splitting the colour channels and choosing the red channel. In step 3, the images have to be converted into binary 2D slices with ImageJ/Fiji: *Image -> adjust -> threshold* in ImageJ/Fiji. Choosing a 50% threshold for the external CW images and 28% for the internal CW images. The pores are highlighted in black and the rest of the image in white. In step 4, the binary images are measured: *Analyse -> analyse particles* which returns a list of individual pores with their corresponding area. Finally, after comparing the different data sets, a model of the CW across its thickness was built as shown after step 5 in the bottom right corner of *Figure 4.5*.

The sets of images were treated differently according to their topography. The set of external surface images was Plane Fit at 2nd order. This filter computes a single polynomial of 2nd order and subtracts it from the image to remove any bow tilt caused either by sample topology or artefactual tilt from the AFM. The set of internal surface was more challenging. Two treatments were tested in the same image with the results shown in *Figure 4.6*.

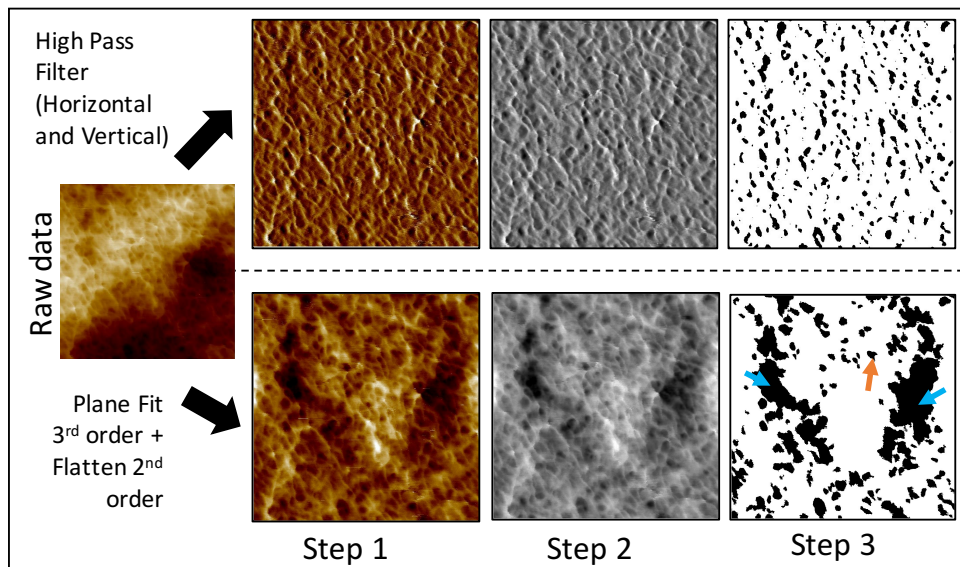


Figure 4.6 –Different outcomes of analysis depending on image treatment – The left panel shows an AFM raw data from the internal PG surface; The top row show steps 1-3 from Figure 4.5 applied to the previous image after being high pass filtered (horizontal and vertical with a filter size approximately of 20 nm); Bottom row show steps 1-3 from Figure 4.5 applied to the previous image after being treated with a plane fit filter at 3rd order and flattened at 2nd order.

Figure 4.6 shows two types of treatment using Nanoscope™ Analysis, one in each row. The bottom row shows a similar approach as the treatment of the external surface, a Plane Fit filter at 3rd order, then each line of the image was flattened using a 2nd order filter. Then steps 2 and 3 (from Figure 4.5) were performed. The resultant slice is not successful because: the pores from the centre of the image are not selected and big depressions dominate the analysis. The top row shows a high pass filter treatment instead. This filter flattens all the data points at the same level by removing any features bigger than a certain number ($\sim 4 \text{ nm}$). This latter contains the highest number possible of individual pores (see orange arrow).

After applying this analysis, the pore distributions have a larger number of pores but they are highly positively skewed due to abnormally big pores. After closer examination these were wrongfully merged neighbouring pores. Thus, they were removed from the distribution manually, by using the following steps. Figure 4.7 a shows a binary image obtained after step 3 in Figure 4.5. Then the black areas are transformed to transparent. Figure 4.7 b shows the overlap between the original image consisting of blue tones instead of grey tones. Using this raw data as guide, if a single area away from its neighbours contained a darker tone of blue, that means it was a single pore in the image and the analysis had selected it correctly (see pink arrows in Figure 4.7 b). However,

when there were multiple areas of darker blue tones (see yellow arrows in Figure 4.7b) selected under the same pore, that was categorised as wrongfully merged by the edges (see green arrows in Figure 4.7 b). This is a subjective classification of pores which has its limitations and might vary depending on the researcher performing the analysis.

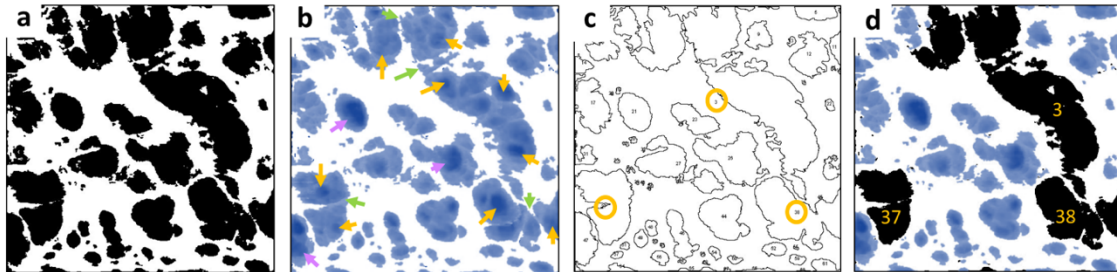


Figure 4.7 – a) Binary image extracted after applying step 3 from Figure 4.5; b) overlap of binary image where the black areas have been turned transparent with the grey image extracted from step 2 Figure 4.5 turned to blue scale (arrows indicate certain pores and artefacts identified manually); c) Outlines of the pores numbered obtained after applying step 4 Figure 4.6; d) Final manual removal in this case of pores 3, 37 and 38.

Then, using the resultant image from step 4 in Figure 4.5, the number label corresponding to the wrongfully merged pores is identified (e.g. 3, 37 and 38 Figure 4.7 c, d). Finally, these pores were removed from the final distribution. This semi-automated method allows less subjective measurements with higher throughput than using any manual method of analysis.

4.2.2 Quantitative comparison of internal and external cell wall

Now a quantitative comparison between the internal and external surface of the CW could be performed. A third data set was included, the images corresponding to the external mature PG from living *S. aureus* cells, [4] with permission of Dr Jonathan Burns. The final results after applying the optimized semi-automated analysis procedure are presented in Figure 4.8.

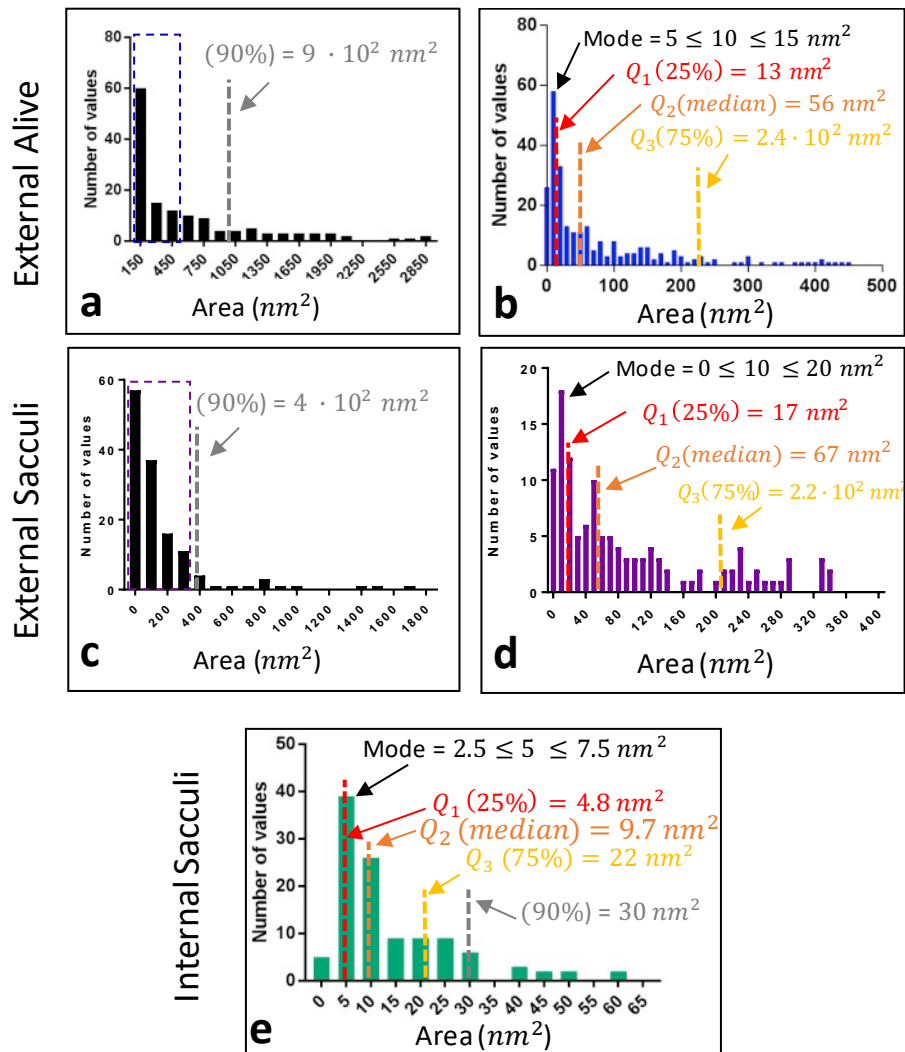


Figure 4.8 – a) Histogram of pore area from external live cells data; b) zoom from blue dotted box in ‘a’; c) Histogram of pore area from external sacculi data; d) zoom from blue dotted box in ‘c’; e) Histogram of pore area from internal sacculi.

Figure 4.8 shows the final results of all three data sets plotted as histograms. The distributions remained positively skewed even after the manual filtering of the wrongfully merged pores. However, the maximum area values that are achieved in this case are no bigger than 3000 nm² (see Figure 4.8 a, c). ImageJ/Fiji measures the area of individual pores. However, biologically, the diameter of the pores is more relevant because it can be compared to the molecular weight and size of the relevant moieties such as proteins of certain *kDa*, bacteriophages or antibiotic molecules. Although ImageJ/Fiji has the option to calculate the maximum diameter, it was not useful in this case because all pores have different shapes. Thus, the values of area were used to calculate the diameter of a hypothetically circular pore, using Equation 4.2.

$$d = 2 \cdot \sqrt{\frac{A}{\pi}} \quad (\text{Eq. 4.2})$$

Where; d is the diameter and A is the measured area of the pore.

The statistical characterization of the histograms presented in *Figure 4.8* and the calculation of the corresponding diameter values calculated with *Eq.4.2* are summarized in *Table 4.2*.

Table 4.2 – Summary of the results extracted from the Histograms in Figure 4.8 and using Eq.4.2 to calculate diameters.

Data set	Q ₁ (25%)		Q ₂ (50%) - Median		Q ₃ (75%)		90%	
	Area (nm ²)	Diameter (nm)	Area (nm ²)	Diameter (nm)	Area (nm ²)	Diameter (nm)	Area (nm ²)	Diameter (nm)
External Alive	13	4.1	56	8.4	240	17.5	900	33.8
External sacculi	17	4.6	67	9.2	220	16.7	400	22.6
Internal sacculi	4.8	2.5	9.7	3.5	22	5.3	30	6.2

From the second column, the **Diameter**_{median} values are in the same vicinity as the results from the manual approach, which were approximately 3.6 nm and 13.4 nm for internal and external pores respectively (*section 4.2.1.1*). Extracting the same conclusion from the results in *Table 4.2* is that the pores on the internal surface of the sacculi (presumably as well on the living cell) are much smaller than the pores on the external surface from sacculi or living cells.

The biological question that would be crucial to answer is: what is the more probable size of the pores on a living cell when a molecule lands on its surface? The statistical parameters presented in *Table 4.3* are mathematically accurate, but they do not answer this question. The area that each pore occupies will be related to the probability of a molecule landing in a surface and finding that specific pore, more than the number of pores of a specific size. The appropriate representation of data to express this concept is calculating the cumulative fraction of total area of the distribution and plot it by the area of each individual pore. The data treatment from the raw data to achieve this representation is summarized in *Figure 4.9*.

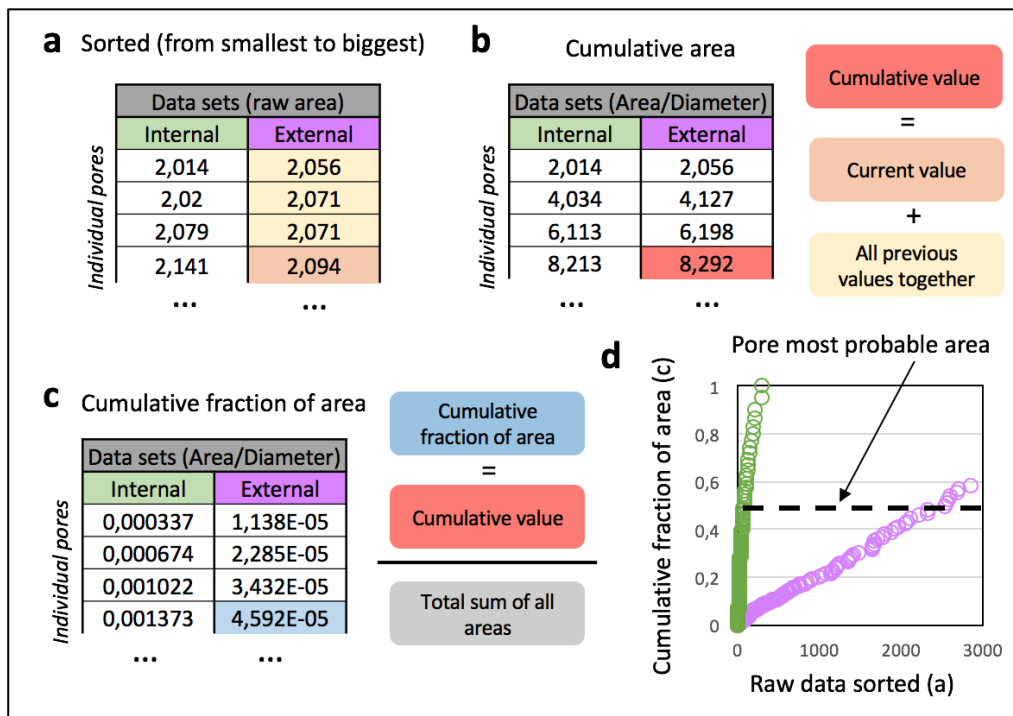


Figure 4.9 – a) raw data extracted from analysis for the two different data sets, it is sorted from the smallest value to the biggest value; b) Cumulative area calculated by adding the current value with all the previous values; c) cumulative fraction area calculated by dividing the cumulative area in 'b' by the total sum of all the areas for each data set; d) plot of 'c' versus 'a'.

Figure 4.9 shows the set of transformations from 'a' to 'c' necessary to produce a plot of the cumulative fraction of total area versus the area of each pore. The **half of the cumulative fraction of total area (HCFA)** represents the pore size that occupies half of the total area of all the pores summed together. If hypothetically a molecule lands randomly on the surface of *S. aureus* it is equally likely to land on a pore smaller or bigger than this value.

All data sets were plotted in this way and the HCFA values were compared, see Figure 4.10 a. Furthermore, instead of just studying the size of the pores at 50% of the external surface, different thresholds were tested, Figure 4.10 b.

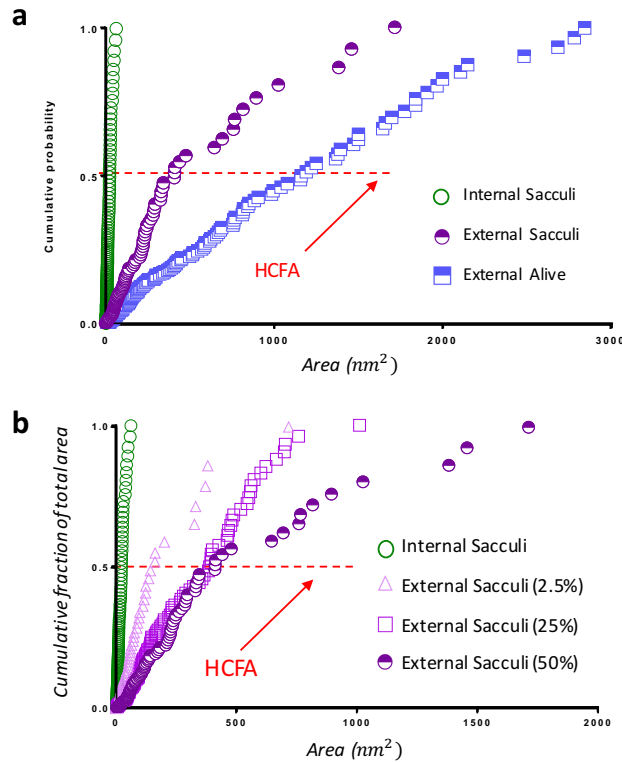


Figure 4.10 – a) direct comparison between Internal Sacculi, external surface of live cell and external surface of sacculi; b) Cumulative fraction of the total area of different two-dimensional sections at 50%, 25% and 2.5% of the external sacculi versus the internal sacculi.

Figure 4.10 a shows the final results of the three data sets together in one plot of cumulative fraction of total area versus area. It can be clearly distinguished how the distributions follow different slopes. The steeper a distribution is, the smaller the pores are. The external pores from live cells (blue squares) are larger than external sacculi (purple and white circles). The pore distribution of internal sacculi falls on the left of the graph, showing the smallest pores (see green circles). Figure 4.10 b shows the external sacculi surface at different depths by thresholding into the percentages: 50%, 25% and 2.5%. The pore sizes decrease as the pores get closer to the internal surface. Meaning the pores are not uniform across the CW thickness.

The HCFA values are summarized in Table 4.3 left column for all data sets.

Table 4.3 - Summary of the results extracted from the graphs in Figure 4.10 and using Eq.4.2 to calculate diameters.

Data sets	HCFA - Area (nm ²)	HCFD - Diameter (nm)
External Alive (50%, n=310)	1220	39
Internal sacculi (28%, n=112)	32.4	6.4
External sacculi (50%, n=292)	409	23
External sacculi (25%, n=223)	386	22
External sacculi (5%, n=176)	150	14

The half cumulative fraction of total diameter (HCFD) was calculated from the HCFA values and is the diameter of the most probable pore a moiety would encounter if it randomly landed on these surfaces. The first three rows of data have high similarities with the values corresponding to the 90% column in *Table 4.2* from the same data sets. This means that 90% of the pores are approximately smaller than the pores occupying 50% of the total area of the surface in all the data sets. Meaning there is only 10% of big pores occupying the other 50% of the total area. The results from the last three rows in *Table 4.3* show the pores from the mature PG get smaller as they go through the total CW thickness in sacculi.

4.3 Theoretical approach to turgor pressure equilibrium

The quantitative characterization of the pores across the CW performed in the previous section provides an experimental framework. The evidence presented in this work so far supports *S. aureus* cells having a much more complex CW architecture far from the more simplistic view from the currently established models (*i.e.* scaffolded and layered in *section 1.3.2*). This poses a problem because the current models explain very well how the PG macromolecule is able to keep the turgor pressure inside the cell. However, as the CW is much more porous than these models can predict, it raises the question of how the cell maintains its turgor pressure without a tight dense structure surrounding it?

To solve this question a theoretical estimation of the critical pore size to maintain the plasma membrane integrity was performed in collaboration with Dr Buddhapriya Chakrabarti (University of Sheffield). The calculation was based in the elastic deformation energy of a membrane given by the Helfrich-Canham form [18] (see *Eq. 4.3*).

$$F_H = \frac{\kappa}{2} \int H^2 dA \quad (\text{Eq. 4.3a})$$

$$H = \frac{1}{2} (c_1 + c_2) \quad (\text{Eq. 4.3b})$$

Where; κ is the bending modulus of the membrane, H , the mean curvature, dA the surface area element, c_1 and c_2 are the principal curvatures of the membrane. In other systems, there is an extra term called Gaussian curvature in *Eq. 4.3 b* corresponding to

a spontaneous curvature of the membrane. However, here it was considered to be zero according to the Gauss-Bonnet theorem, that states this term would result into a constant term in Eq. 4.3a for closed membranes. Thus, the elastic deformation term corresponding to the Gaussian curvature was neglected in Eq. 4.3 a.

The cell membrane was assumed to be a closed continuous sheet surrounded by a porous PG layer (the periplasm space was not taken into consideration during this calculation). Despite the PG layer being a porous material, only a pore of a critical size would allow an hemispherical bulge of radius R , critically rupturing the membrane and losing the turgor pressure. For a hemispherical bulge of radius R (where $c_1 = c_2$) the Helfrich-Canham free energy is given by Eq. 4.4.

$$F_H = \pi\kappa. \quad (\text{Eq.4.4})$$

The work done to cause the membrane to deform into a hemispherical bulge will be given by $P\Delta V$ where P here is the turgor pressure of the cell and ΔV is the volume associated with the bulge. This gives a critical pressure to form the hemispherical bulge of P_{crit} given by Eq. 4.5.

$$P_{crit} = \frac{3\kappa}{2R^3} \quad (\text{Eq. 4.5})$$

At pressures above this we expect the membrane would start to escape out through a hole of a critical size, ultimately leading to cell death. *i.e.* P_{crit} here is the maximum turgor pressure that the cell can sustain.

We calculate the maximum critical pore size for the expected cellular turgor pressure of approximately 20 bar. R is taken to be half the critical pore diameter. In this calculation the value for the bending modulus κ have to be defined. However, the experimental values of Gram-positive cell membranes are not found in the literature. Therefore, it was estimated κ to have a range of 20-70 $k_B T$, the lower value being the bending modulus for a supported lipid membrane, in line with Daly *et. al.* [19] and the upper value being the bending modulus for an eukaryotic cell membrane lacking anchoring to the actin cortex. [20] For a turgor pressure of 20 bar, using Eq. 4.5 this gives us an estimated critical pore diameter of $D_{crit} (2R) = 8-12 \text{ nm}$, implying that the pores seen

(6.4 nm, Table 4.3) are just small enough that membrane rigidity is able to maintain cell turgor.

4.4 The septum structure

Another advantage of study purified PG is the possibility to study the PG architectures corresponding to the septal plate. This was not possible in studies of living cells because of the lack of access to the internal surface. [3]–[6]

As mention in the introduction chapter (see section 1.3.3.3) *S. aureus* division process occurs by fabricating a septal plate (*i.e.* septum) in the middle of the parent cell composed of two CW and a space in between; there is a septal aperture in the middle, the diameter of which indicates the exact moment of the septal formation; then when the septal plate is finished and the aperture is closed, the whole septum gains uniform thickness and then the cell splits into two daughter cells. [13] There is a large amount of literature about the mechanistic pathways involve in this process of septum formation in *S. aureus*. [21]–[26] A super resolution microscopy study of division dynamics has provided evidence that the new PG material in between the septal plate is synthesized as concentric rings. [27] The PG surface inside the septal plate synthesised as rings will cover the nascent exposed external surface of the two daughter cells once they split. [28] This part of the septum will be referred as ‘external septal wall’ corresponding to two identical surfaces (one from each future daughter cell) facing each other with a separation between them [29] (see Figure 4.11 b). The other side of the external septal wall is called ‘internal septal wall’. This is the surface closer to the cytoplasmic membranes and it will remain facing the inside of the cell after division. However, as PG incorporation happens throughout the septal plate and during the rest of the cell cycle, it was suggested that the ‘internal septal wall’ (see Figure 4.11 a) would be synthesized differently resulting in an alternative PG architecture than the concentric rings.

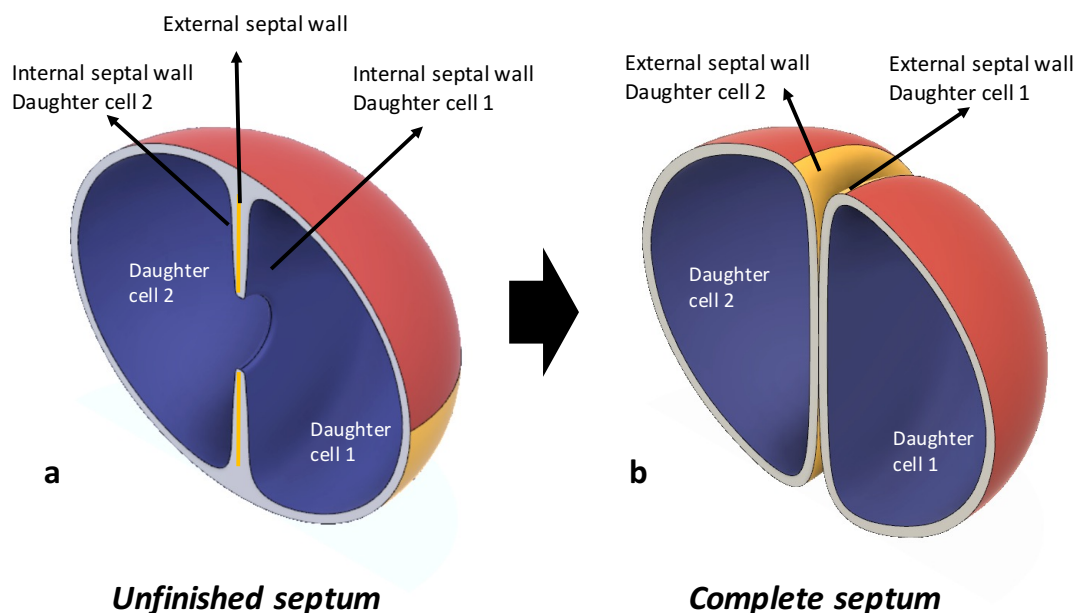


Figure 4.11 – 3D schematics of different stages of *S. aureus* cell division; a) Unfinished septum where the septal plate has three structures merged together: internal septal wall of the two daughter cells and the external septal wall; b) when the septum is complete the surface that was called “external septal wall” emerges to the surface to form the nascent material of the two daughter cells, whereas the internal septal wall becomes part of the internal surface of the new cells. Adapted from model provided by Dr Robert Turner.

4.4.1 Optimization of sample preparation to obtain more septa on AFM

The experimental conditions to image hydrated sacculi used throughout chapters 3 and 4 contained almost no septa, requiring at least 4-5 h to find a viable septum to perform high resolution imaging. The main reason for this lack of unfinished septa was the cell cycle desynchronization of the cells during exponential phase. From the cells that were purified during the division process, either they just started (showing the piecrust), [8] [13] or they recently divided. However, only the unfinished septa would provide useful structural information about septal plate formation.

Optimization of the sample preparation was required with the goal of obtaining a sacculi sample with high numbers of unfinished septa. The main adjustment might be the growth phase (*i.e.* lag, exponential and stationary phase) because the cells would divide different rates. The growth phases have been extensively studied for *S. aureus* Wild Type (WT) using standard growth conditions: culture volume= 50 ml; rotation= 40 g; inoculation from pre-cultured exponential phase cells. However, the growth conditions used during the PG purification process are different. Therefore, before preparing sacculi at different growth phases, a growth curve was performed using the sacculi purification conditions (*section 2.2.1.6*) to identify these phases, *Figure 4.12*.

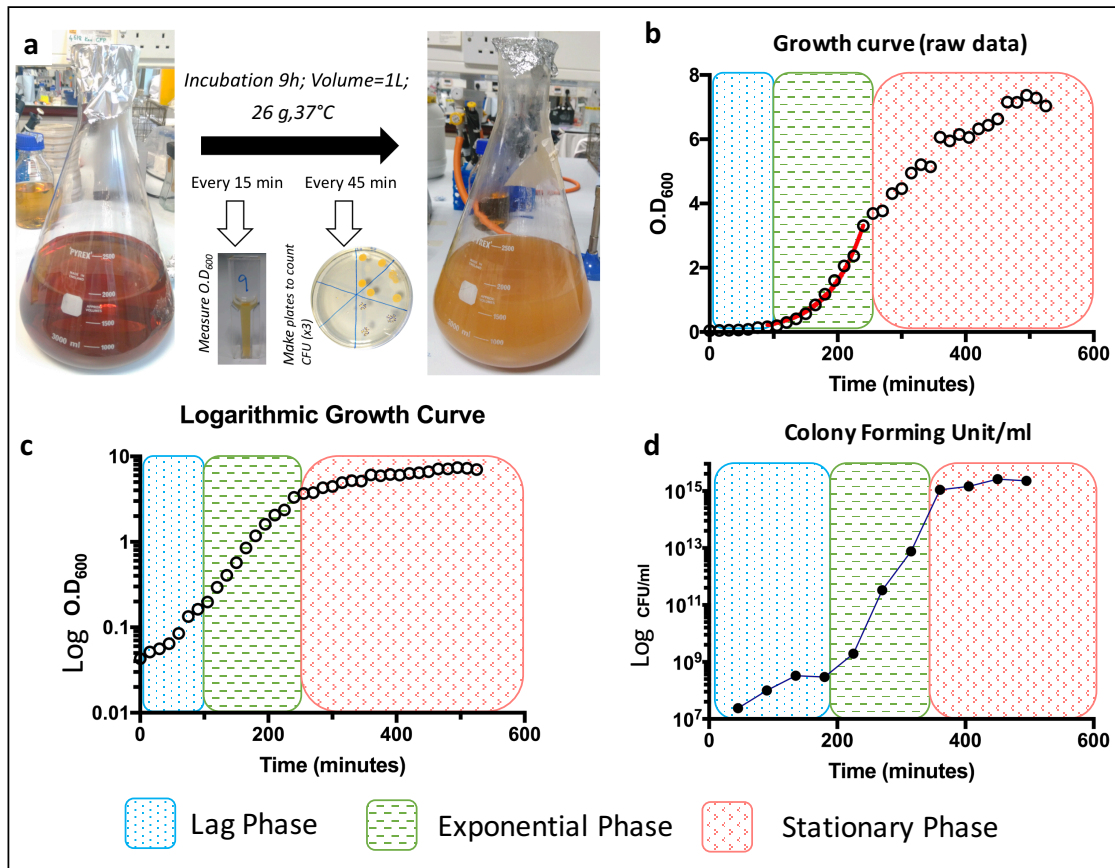


Figure 4.12 – a) schematics of the measurements performed during this experiment: OD every 15min and plate every 45min, the pictures of the 1L flask represent the time point 0min at the left and the final time point after 9h at the right; b) raw data of the OD_{600} measurements with a red line representing an exponential fitting on the exponential phase; c) Same data as 'b' but represented with a logarithmic scale on the OD_{600} axis; d) CFU/ml vs Time curve extracted after 24h of plate incubation, the colonies present were counted.

Figure 4.12 shows the results from the growth curve experiment. Figure 4.12 a shows the workflow followed to perform this experiment (see 2.2.1.6): 1 L of cell culture was continuously incubated during 9 h, every 15 min 1 ml was extracted from the culture to perform an OD_{600} measurement and every 45 min another 1ml was extracted to prepare $CFU\ ml^{-1}$ plates. Figure 4.12 b is the plot of the growth curve using the OD_{600} measurement over time, the red line is an exponential fit, marking the exponential phase. Figure 4.12 c is the OD_{600} measurements in logarithmic scale. Figure 4.12 d plots the logarithmic scale of $CFU\ ml^{-1}$ versus time, indicating the number of viable cells over time. The different coloured areas correspond to lag phase (blue), exponential phase (green) and stationary phase (red). The areas were manually placed in Figures 4.12 b-c using the exponential fitting from the raw data as a guide to identify where the exponential phase was. However, these phases are displaced in the CFU graph, Figure 4.12 d. This shift is probably due to the time delay to perform the plates (20-30 min) in each time-point. Therefore, the growth phases were defined using the OD_{600} graphs

(Figure 4.12 b-c). Another experiment was performed using the same exact conditions as in Figure 4.12. However, instead of extracting sample to plot the grow curves, three sacculi samples were prepared using 250 ml each, one corresponding to each phase, Table 4.4. They were all extracted from the same cell culture (1 L).

Table 4.4 – Different sacculi samples at specific time points and ODs for *S. aureus*

Sample name	Time Point (min)	OD ₆₀₀	Phase
S1	60	0,08	Lag
S2	135	0,5	Exponential
S3	315	5	Stationary

The only alteration in the purification protocol is the OD₆₀₀ at which the different samples were extracted. Then, AFM imaging was performed in ambient conditions for the three samples (S1, S2 and S3 from Table 4.4). Then, 15x15 μm scan areas were used to classify the different morphologies of the cells (see Figure 4.13).

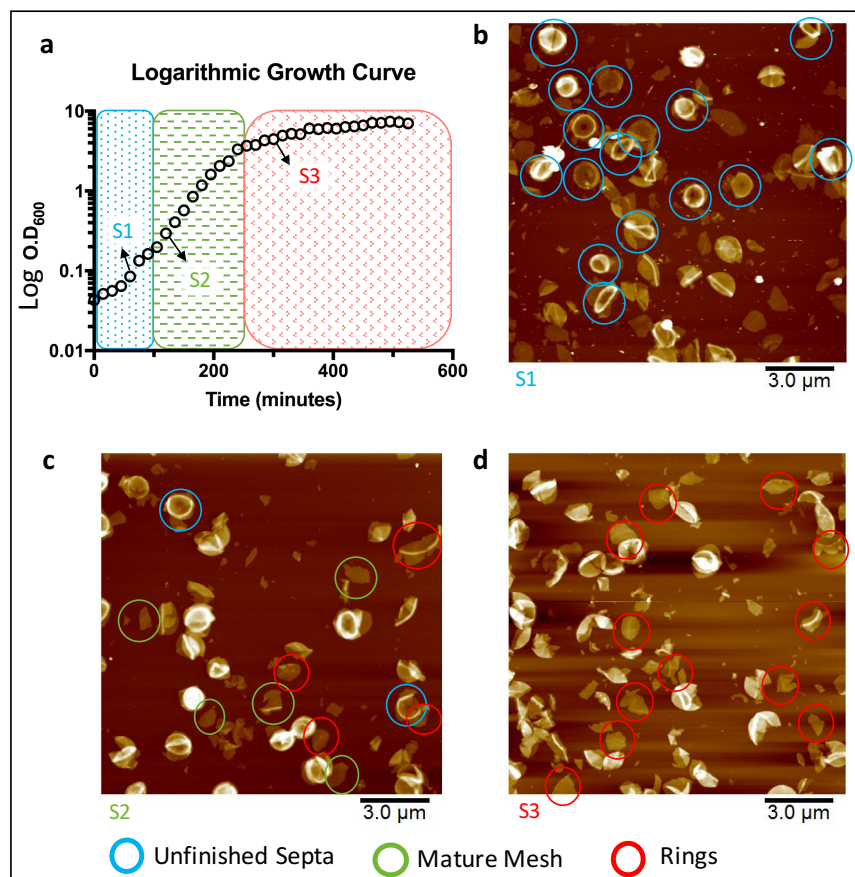


Figure 4.13 – a) same graph as Figure 12 c but showing the location of the different samples taken to compare different cell cycle time points (S1, S2 and S3); b) Sample prepared at Lag phase, unfinished septa blue circles; c) Sample prepared at exponential phase with septa (blue), mature mesh (green circles) and rings (red circles); d) Sample prepared at stationary phase: Rings are red circles. All sacculi were prepared the same day: Batch 5.

Figure 4.13 a shows the same growth curve as *Figure 4.12 a* with the time-points where samples from *Table 4.4* were taken from. Three different morphologies were counted throughout the samples: unfinished septa (blue circles), mature mesh (green circles) and nascent rings (red circles). *Figure 4.13 b* shows an AFM in air from sample S1 taken during the lag phase. This sample primarily contains unfinished septa. *Figure 4.13 c* shows an image from sample S2 taken during the exponential phase (this is the condition used in all previous sacculi samples). This sample contains mixture of all morphologies but mostly from mature mesh and nascent rings. *Figure 4.13 d* shows an image from sample S3 taken stationary phase with a high number of cells with tight concentric rings. The different PG architectures according to their cell cycle stage is not surprising as it has been reported in a similar study using TEM and Solid-state NMR spectroscopy to explore PG structural changes depending on their OD. [30]

To conclude, from the results summarized in *Figure 4.13* it was determined that the sample from *Table 4.4* that contained the higher number of unfinished septa was **S1**, at the middle of Lag phase with $OD_{600} = 0.08$. It was suggested the transition from the overnight to fresh growth media would synchronize the cells. When sample S1 is purified the cells are in lag phase and they are performing the septation process all at once.

4.4.2 The septal plate architecture inside out

As stated before above in *Figure 4.11*, there is two different structures of unfinished septa: the external and internal surface. However, when an unfinished septum attaches to a flat surface, only the 'internal septal wall' is exposed to AFM imaging, because the two septal walls do not split until the septum is complete.

4.4.2.1 Internal septal wall structure

Using the optimized conditions of the sacculi preparation and all the improvements of imaging sacculi in liquid explained in *Chapter 3* a sample at **lag phase (S1)** was prepared. Several unfinished septum were imaged. However, only a few were obtained at high resolution because of the challenging nature of imaging a non-flat surface, the best results are shown in *Figure 4.14*.

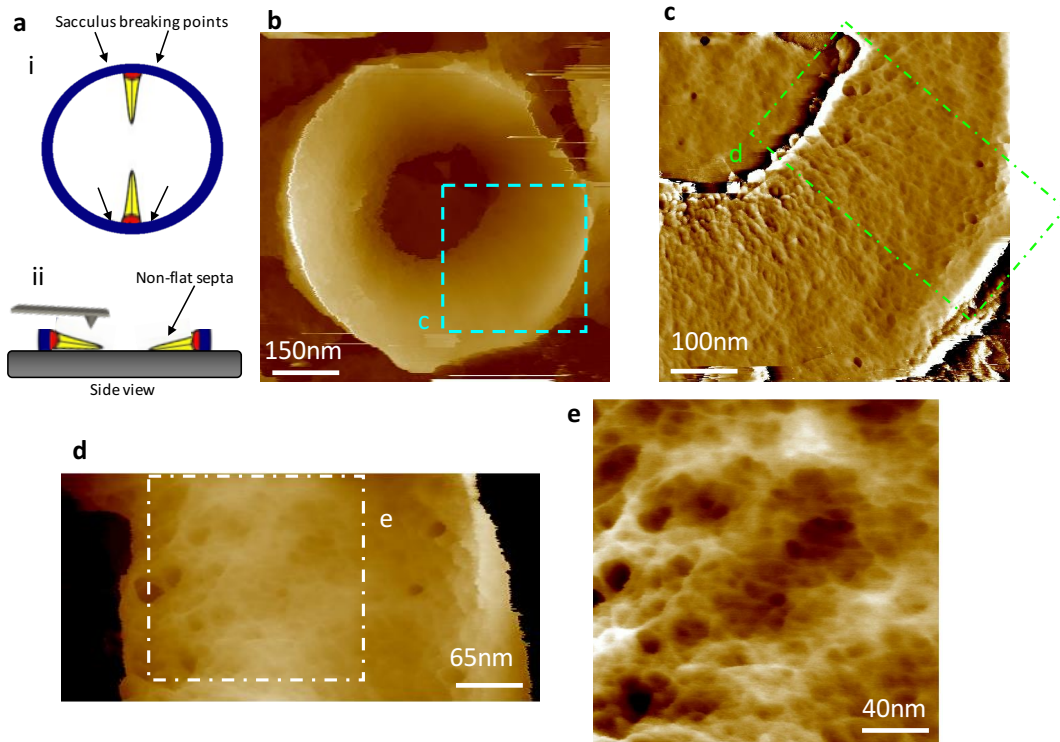


Figure 4.14 – a) scheme showing (i) the different parts of the unfinished septa (ii) and after PG purification is attached to the surface with the non-flat areas exposed to AFM imaging, adapted with permission from [13]; b) unfinished septum with its internal septal wall upwards; c) zoom from 'b' (blue box). High pass filtered; d) Zoomed from 'c', (green dotted box), angle 45°; e) Zoomed from 'd', see white box.

The images from Figure 4.14 were performed under the experimental conditions summarized in Table 4.5

Table 4.5 - Experimental conditions used to take the data from Figure 4.14.

AFM TIP	AFM MODE	SAMPLE TYPE	BUFFER/ ENVIRONMENT	SURFACE	SPECIFIC CONDITIONS
FAST SCAN - D	PeakForce Tapping	WT sacculi Stock A Batch 5 Dil 6	200mM KCl + 10mM Tris pH=7.8	MICA coated CellTak	cells purified at OD ₆₀₀ = 0.08 (S1)

Figure 4.14 shows the best results from imaging the internal septal wall of an unfinished septum. Figure 4.14 a(i) is a scheme of a cell on the early stages of division, with the piecrust (red area) and the septal walls (yellow), during the purification process this sacculus probably breaks on the marked areas (see black arrows). Then, Figure 4.14 a(ii) shows this unfinished septa attached to the surface, with the non-flat areas being imaged by the AFM, which makes it very challenging to achieve high resolution. Figure 4.14 b shows an unfinished septa. Figure 4.14 e shows the finer structure of the internal

septal wall is composed of a tight disordered mesh very similar to the internal architecture of the rest of the cell (see *Figure 4.1 d*).

A quantitative comparison of the size of the pores was performed between the internal septal wall and the internal PG from the rest of the cell. Following the methodology applied in *Figure 4.10* the area of pores was plotted against their cumulative fraction of total area.

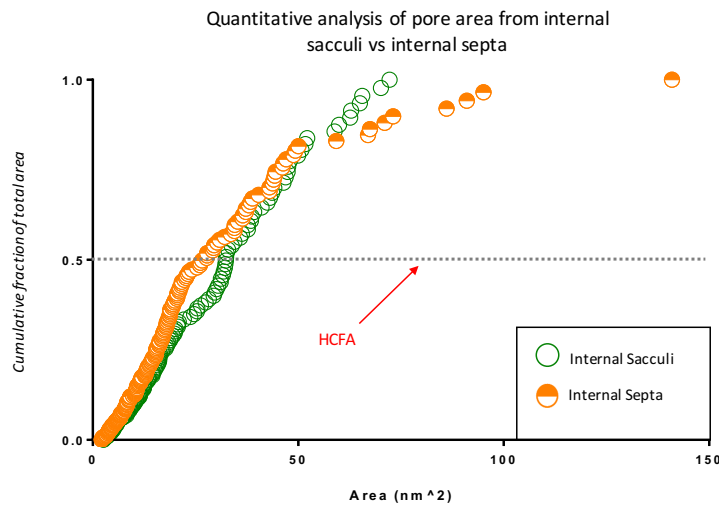


Figure 4.15 – Cumulative fraction of total area to compare the Internal sacculi and the internal septa.

From the quantitative representation in *Figure 4.15* it can be observed that both distributions follow a similar trend. However their HCFD values were calculated from the HCFA shown on the graph with $\text{HCFD}_{\text{Septa}} = 5.9 \text{ nm}$ versus $\text{HCFD}_{\text{Internal}} = 6.4 \text{ nm}$. However, there is a presence of some pores on the internal septal wall bigger than the maximum pore size of the internal sacculi from the rest of the cell. Considering the septum used to plot this data was incomplete, additional PG synthesis could still occur for filling the pores bigger than the critical size (8-12 nm, see *section 4.3*) up to the size like the rest of the internal mesh. This would avoid the cell bursting after division due to the turgor pressure and would explain the results from super resolution microscopy showing a unification of the septal plate thickness due to additional synthesis after the aperture of the septa has been closed (see *Figure 1.10, iv*).

To conclude, the internal septal wall PG structure is similar to the internal PG of the rest of the cell. This is the first time both these architectures have been directly visualized and characterized with such detail.

4.4.2.2 External septal wall structure

Once the internal septal wall was studied, the focus shifted to the external surface which was suggested to be concentric rings before the splitting as well as the nascent PG of a recent division. However, as mentioned above, unfinished septa would not split naturally. [28] Although some exceptions were found due to the mechanical shear the cells suffered during the purification treatment. The best examples of this latter scenario are shown in *Figure 4.16*. These images were performed under the same experimental conditions summarized in *Table 4.5*.

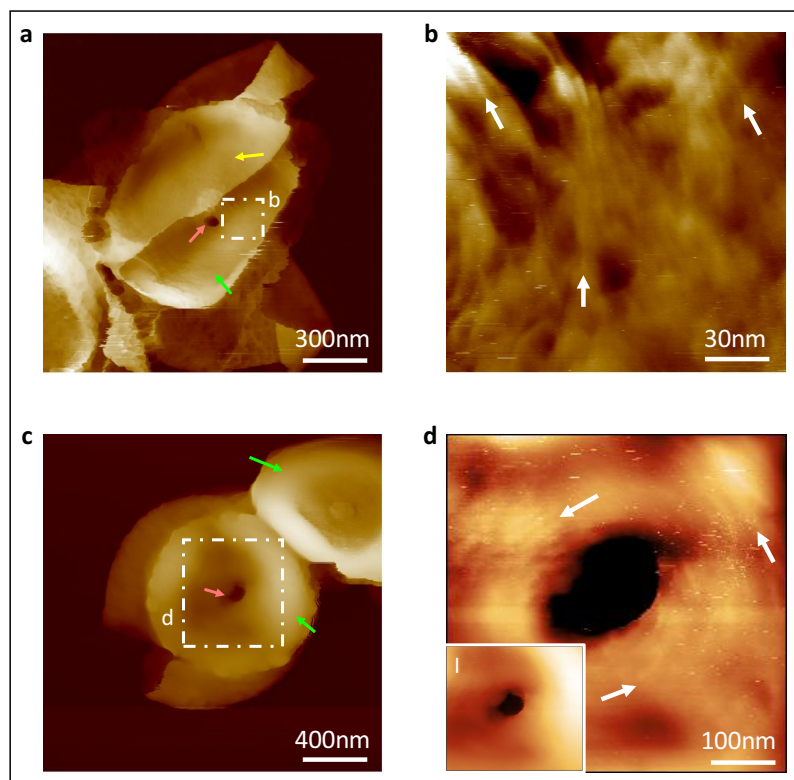


Figure 4.16 – a) septal plate ripped apart from one side. Internal septal wall (yellow arrow), external septal wall (green arrow), septal aperture (pink arrow); b) Zoom from ‘a’ external septal wall (see white box); c) Premature splitting of an unfinished septa with the external septal wall facing upwards (green arrow) and still having a septal cavity (pink arrow); d) Zoom from ‘c’ (see white box), high pass filtered, inset (l) showing the raw data.

As these occasions are very rare, high resolution was not achieved. However, the main features were visible. *Figure 4.16 a* shows the septal plate formed of two walls separated by a space between them. [29] This unfinished septa was broken in the middle, exposing the ‘external septal wall’ from daughter cell 1 (green arrow) which is underneath the smoother internal septal wall’ from daughter cell 2 (see yellow arrow). *Figure 4.16 b* is a zoomed image from the external septal wall showing ordered concentric rings (see white arrows). *Figure 4.16 c* shows another example where a

premature splitting caused the external septal wall from two daughter cells to separate (see green arrows). *Figure 4.16 d* is a zoomed image from the area surrounding the septal aperture (see pink arrow), showing concentric rings oriented around the aperture (see white arrows).

These results contradict some theories that the concentric rings are formed by the splitting enzymes appearing only after the division is finished. [31]–[34] However, they confirm the opposite hypothesis: the concentric rings being synthesized in progression with the septal plate formation in between the septal walls at the leading edge. [27]

4.4.3 Glycan strands orientation analysis

The internal septal wall structure presented in *section 4.4.2.1* raises controversy with published work, which suggested both sides of the septal wall from Gram-positive bacteria has concentric rings architecture. The concentric rings are often referred as a highly ordered structured. [3]–[6] There is evidence about FtsZ [35], [36] coordinating several proteins to synthesise PG concentric rings architecture using treadmilling dynamics. Consequently, when a disordered structure was found in the septal plate, coexisting with the ordered concentric rings, it was necessary to have strong proof of the degree of strand orientation to shed light into this controversy.

The orientation analysis of these strands was performed using a semi-automated method. The first step is to manually draw a skeletonized version of the image highlighting only the thinner strands (see *Figure 4.17 a-b*). Then, a program was coded in MATLAB™ [37] to automatically detect the straight black lines on a white background from the skeletonized image (see *Figure 4.17 c*) and calculate different angle orientations corresponding to each line (see supplementary information of [5] for the code) (see *Figure 4.17 d-e*).

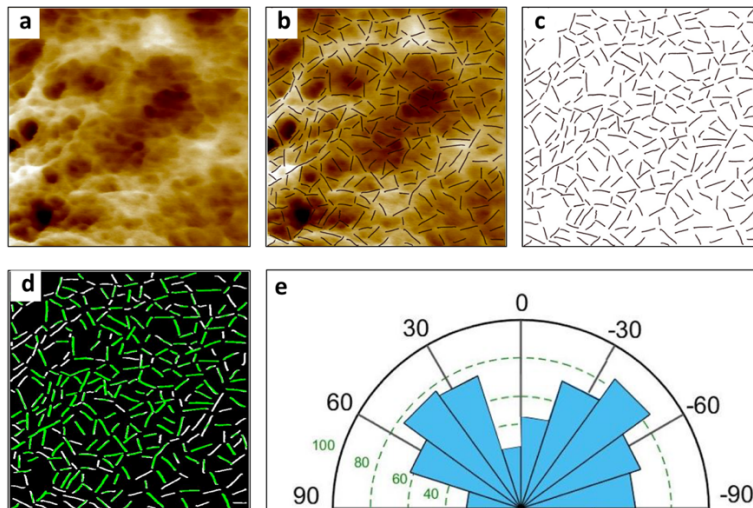


Figure 4.17 – a) Initial AFM image; b) Manual drawing of short lines along the strands; c) skeletonized version of the image; d) First output of the MATLAB program indicating how many line have been detected (green) and how many have not (white); e) Output of the angle distribution where the small green number represent the number of values.

It is important to highlight that the program [5] does not detect 100% of the lines from the skeletonized version of the image, but detects around 70% on average after performing analysis on several images (green lines in Figure 4.17 d). The resultant rose plot represents the density probability of angles obtained from the image.

This semi-automated method of analysis was applied to images from three different surfaces: the internal septal wall, the internal surface of the rest of the cell and the concentric rings. All images were taken using PeakForce™ mode AFM from sacculi. The results can be directly compare in Figure 4.18.

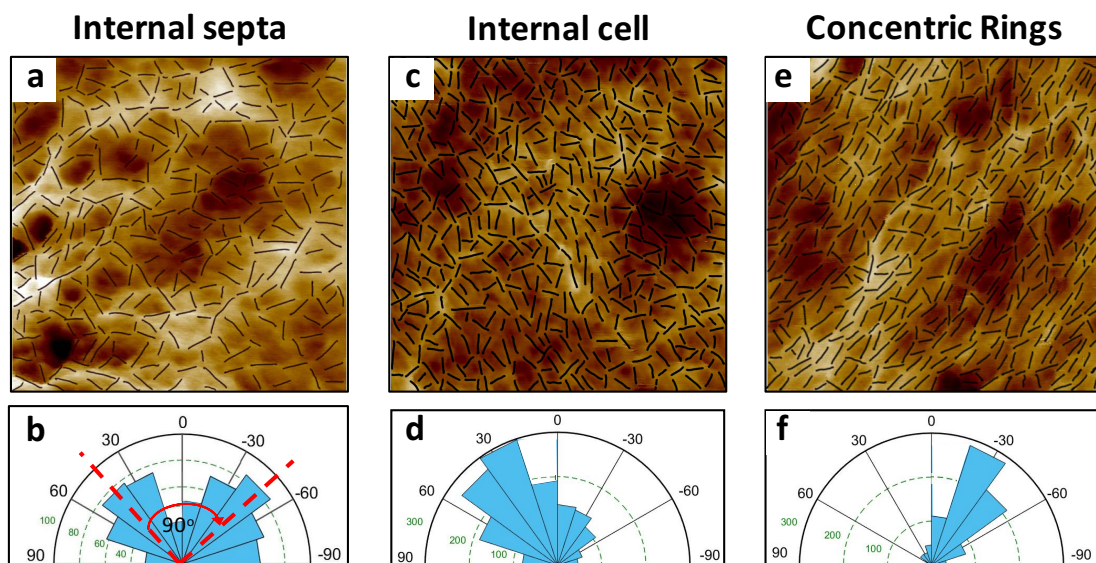


Figure 4.18 – a) Internal septal wall image with the manual drawing overlapped; b) resultant rose plot of angles from 'a'; c) Internal surface of an area away from septa with the manual drawing overlapped; d) resultant rose plot of angles from 'c'; e) Concentric Rings with the manual drawing overlapped; f) resultant rose plot of angles from 'e'.

Figure 4.18 a-d show a similar range of angles in the internal septal wall and the internal surface of the rest of the cell. The rose plot from the internal septal wall does not have a major angle of predominant orientation. Instead, there are two main peaks separated between each other at approximately 90° (see red dashed lines). On the other hand, the results from the concentric rings are clearly different with a predominant orientation of most of the glycan strands going along the rings and tangential to a circumference with centre point at the centre of the cells (see *Figure 3.11 c*).

To conclude, the semi-automated analysis has confirmed the qualitative observation that the internal septal wall does not have a predominant orientation; this means it is very unlikely to be an initial phase of the external concentric rings because this would require huge reverse reorganization of the glycan chains in the PG structure. It was interesting to find that instead of a random orientation of the glycans in the internal septal wall, a more complex structure is present with two major orientation angles separated by 90°. This could imply there are two sets of enzymes moving approximately perpendicular to each other synthesising this architecture. However, given the scarce number of high resolution images from septal walls, no strong conclusions can be extracted without performing further experiments.

4.5 Discussion

In this chapter the internal cell wall has been explored. The peptidoglycan architecture from the internal surface has been described with molecular resolution for the septal region and the rest of the cell, using *S. aureus* hydrated sacculi.

The first conclusion is that the peptidoglycan architecture from the internal surface for the majority of the cell has been described with molecular resolution. This architecture at lower magnification can be described as a smooth tight layer of material. Striking resolution of 1-2 nm was routinely achieved imaging hydrated sacculi with AFM. Using these high magnification images, the finer internal peptidoglycan structure can be better described as a disordered mesh of glycan fibres forming two dimensional pores, visibly smaller than the ones from the mature external surface. The necessary controls and criteria were defined to make sure the novel discovered architecture corresponded indeed to the internal CW surface (see *section 4.1*).

The second conclusion is that the current established analysis workflows do not allow an unbiased, quantitative and high throughput characterization of pore sizes across the CW thickness. Therefore, a novel semi-automatic analysis methodology was optimized (see *section 4.2.1*) to measure the pore size at a certain depth of an AFM image. This novel analysis was applied to compare the pore sizes between image sets of the internal and external PG structure from *S. aureus* sacculi and living cells. All the image sets analysed resulted in non-normal distributions of pore size. Therefore, to obtain a meaningful number predicting the most probable pore size from both regions of the cell, the cumulative fraction of total area was calculated. This data transformation allows us to visualize each individual pore area in a graph, and when different samples are plot together, a difference in the trend of the curves was appreciated. The pores from the external surface of both sacculi and living cells get smaller as they go through the CW. The half of the cumulative fraction of total area (HCFA) was calculated (see *Table 4.3*) because if a molecule would randomly land on the cell surface, it would encounter pores bigger than HCFA 50 % of the time and smaller than this value 50 % of the time. The HCFA values were transformed into diameter resulting into $HCFD_{\text{internal}} = 6.4 \text{ nm}$ and $HCFD_{\text{external}} = 23 \text{ nm}$ (see *section 4.2.2*).

The third conclusion is related to how the cell wall fulfils its role at maintaining turgor pressure. From the results presented in this thesis, so far, the PG seems to be a much more porous and complex material than any current model would predict. Therefore, the critical size of the pore from which the cell membrane would bulge through and turgor pressure would be lost was calculated. The Helfrich-Canham theory about the elastic deformation energy of a membrane was used together with other assumptions: the shape of the bulge would be hemispherical; and the bending modulus of the membrane was assumed to be between 20-70 $k_B T$ (values corresponding to a lipid bilayer and a eukaryotic cell). Using all these conditions and considering a turgor pressure of 20 bar, the critical pore diameter ranges between 8-12 nm. This implies that the pores from the internal PG surface are just small enough that membrane rigidity is able to maintain cell turgor (see *section 4.3*).

The last conclusion from this chapter is the high degree of complexity from the PG structure from the septal plate during cell division. The septal plate has two distinct

regions of interest. The internal septal wall which is closer to the cytoplasmic membrane, surprisingly has a randomly oriented tight mesh architecture, similar to the internal PG surface from the rest of the cell (see *section 4.4.2.1*). By contrast, the external septal wall that gets exposed to the exterior right after division has a concentric rings architecture, even when the septa is unfinished (see *section 4.4.2.2*). Additionally, a novel quantitative analysis of strand orientation was design to characterize the internal septal wall PG architecture (see *section 4.4.3*).

All the results collected up to this point, can be summarized in a 3D model of the internal PG architectures in *S. aureus*, see *Figure 4.19*.

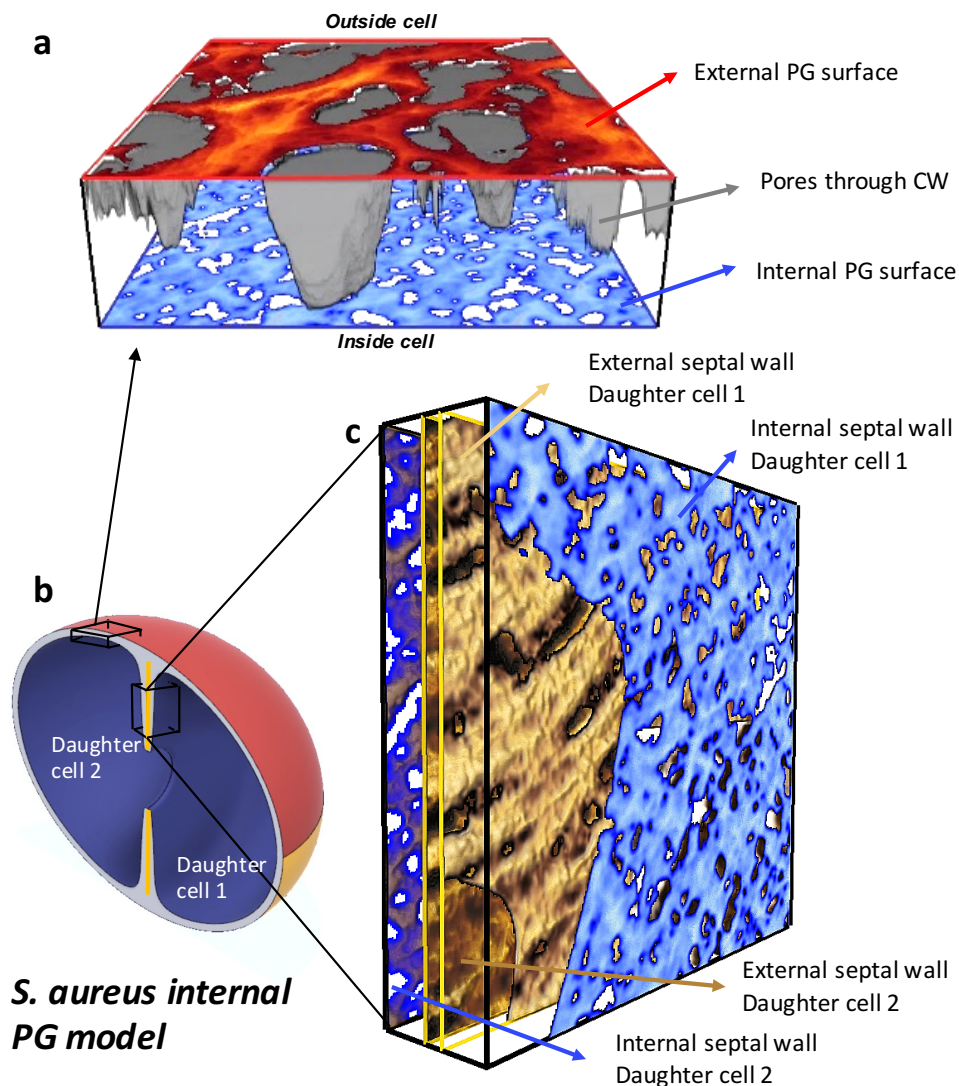


Figure 4.19 – a) Montage of an external mature PG image with the top surface (red) and the pores highlighted (grey), on top of the internal surface (blue); b) Same drawing from Figure 4.11 a, with a cross-section of the septal plate marked with a black box; c) zoom of this cross-section model of all the 2 different architectures cohabit this space: Internal septal wall (blue), external septal wall (yellow) from each daughter cell. This model was made by rendering AFM images with Avizo™.

This novel level of resolution achievable by AFM together with the capacity to explore the internal surface of the CW using hydrated sacculi, will allow further studies on cell division and studying the relationship between PG structure and function.

4.6 References

- [1] E. Sauvage, A. Powell, J. Heilemann, H. Josephine, P. Charlier, C. Davies and R. Pratt, "Crystal Structures of Complexes of Bacterial dd-Peptidases with Peptidoglycan-Mimetic Ligands: The Substrate Specificity Puzzle," *J. Mol. Biol.*, 2008.
- [2] P. Macheboeuf, C. Contreras-Martel, V. Job, O. Dideberg, and A. Dessen, "Penicillin binding proteins: Key players in bacterial cell cycle and drug resistance processes," *FEMS Microbiology Reviews*. 2006.
- [3] A. Touhami, M. H. Jericho, and T. J. Beveridge, "Atomic force microscopy of cell growth and division in *Staphylococcus aureus*," *J. Bacteriol.*, 2004.
- [4] J. M. Burns, "High Resolution Atomic Force Microscopy Imaging of Living Bacterial Surfaces," University of Sheffield, 2017.
- [5] L. Pasquina-Lemonche, J. Burns, R. Turner, S. Kumar, R. Tank, N. Mullin, J. Wilson, B. Chakrabarti, P. Bullough, S. Foster and J. Hobbs, "The architecture of the Gram-positive bacterial cell wall," *Nature*, vol. 582, no. 7811, pp. 294–297, 2020.
- [6] R. D. Turner, N. H. Thomson, J. Kirkham, and D. Devine, "Improvement of the pore trapping method to immobilize vital coccoid bacteria for high-resolution AFM: A study of *Staphylococcus aureus*," *J. Microsc.*, 2010.
- [7] R. D. Turner, W. Vollmer, and S. J. Foster, "Different walls for rods and balls: The diversity of peptidoglycan," *Mol. Microbiol.*, vol. 91, no. 5, pp. 862–874, 2014.
- [8] R. D. Turner, E. C. Ratcliffe, R. Wheeler, R. Golestanian, J. K. Hobbs, and S. J. Foster, "Peptidoglycan architecture can specify division planes in *Staphylococcus aureus*," *Nat. Commun.*, vol. 1, no. 3, p. 26, 2010.
- [9] R. D. Turner, A. F. Hurd, A. Cadby, J. K. Hobbs, and S. J. Foster, "Cell wall elongation mode in Gram-negative bacteria is determined by peptidoglycan architecture," *Nat. Commun.*, vol. 4, p. 1496, 2013.
- [10] R. D. Turner, S. Mesnage, J. K. Hobbs, and S. J. Foster, "Molecular imaging of glycan chains couples cell-wall polysaccharide architecture to bacterial cell morphology," *Nat. Commun.*, vol. 9, no. 1, 2018.
- [11] G. Andre, M. Deghorain, P. Bron, I. Van Swam, M. Kleerebezem, P. Hols and Y. Dufrêne, "Fluorescence and atomic force microscopy imaging of wall teichoic acids in *Lactobacillus plantarum*," *ACS Chem. Biol.*, vol. 6, no. 4, pp. 366–376, 2011.
- [12] E. J. Hayhurst, L. Kailas, J. K. Hobbs, and S. J. Foster, "Cell wall peptidoglycan architecture in *Bacillus subtilis*," *Proc. Natl. Acad. Sci.*, vol. 105, no. 38, pp. 14603–14608, 2008.
- [13] V. Lund, K. Wacnik, R. Turner, B. Cotterell, C. Walther, S. Fenn, F. Grein, A. Wollman, M. Leake, N. Olivier, A. Cadby, S. Mesnage, S. Jones and S. Foster, "Molecular coordination of *Staphylococcus aureus* cell division," *Elife*, vol. 7, pp. 1–31, 2018.
- [14] C. J. Murphy and N. R. Jana, "Controlling the aspect ratio of inorganic nanorods and nanowires," *Adv. Mater.*, 2002.
- [15] S. B. Kaemmar and Bruker Corporation, "Introduction to Bruker's ScanAsyst and PeakForce Tapping AFM Technology," *Bruker*, p. 12, 2011.
- [16] D. Nečas and P. Klapetek, "Gwyddion: An open-source software for SPM data analysis," *Cent. Eur. J. Phys.*, vol. 10, no. 1, pp. 181–188, 2012.
- [17] J. Schindelin, I. Arganda-Carreras, E. Frise, V. Kaynig, M. Longair, T. Pietzsch, S. Preibisch, C. Rueden, S. Saalfeld, B. Schmid, J. Tinevez, D. White, V. Hartenstein, K. Eliceiri, P. Tomancak and A. Cardona, "Fiji: an open-source platform for biological-image analysis," *Nat. Methods*, vol. 9, no. 7, pp. 676–82, 2012.
- [18] W. Helfrich, "Elastic Properties of Lipid Bilayers: Theory and Possible Experiments," *Zeitschrift für Naturforsch. - Sect. C J. Biosci.*, 1973.
- [19] K. E. Daly, K. C. Huang, N. S. Wingreen, and R. Mukhopadhyay, "Mechanics of membrane bulging

- during cell-wall disruption in Gram-negative bacteria," *Phys. Rev. E - Stat. Nonlinear, Soft Matter Phys.*, 2011.
- [20] R. Simson, E. Wallraff, J. Faix, J. Niewohner, G. Gerisch, and E. Sackmann, "Membrane bending modulus and adhesion energy of wild-type and mutant cells of *Dictyostelium* lacking talin or cortexillins," *Biophys. J.*, 1998.
- [21] V. R. Steele, A. L. Bottomley, J. Garcia-Lara, J. Kasturiarachchi, and S. J. Foster, "Multiple essential roles for EzrA in cell division of *Staphylococcus aureus*," *Mol. Microbiol.*, 2011.
- [22] K. Wacnik, "Dissecting cell division in the human pathogen *Staphylococcus aureus*." University of Sheffield, 2016.
- [23] J. A. Thanassi, "Identification of 113 conserved essential genes using a high-throughput gene disruption system in *Streptococcus pneumoniae*," *Nucleic Acids Res.*, 2002.
- [24] D. W. Adams and J. Errington, "Bacterial cell division: Assembly, maintenance and disassembly of the Z ring," *Nature Reviews Microbiology*. 2009.
- [25] C. A. Hale and P. A. J. De Boer, "Direct binding of FtsZ to ZipA, an essential component of the septal ring structure that mediates cell division in *E. coli*," *Cell*, 1997.
- [26] P. A. Levin, I. G. Kurtser, and A. D. Grossman, "Identification and characterization of a negative regulator of FtsZ ring formation in *Bacillus subtilis*," *Proc. Natl. Acad. Sci. U. S. A.*, 1999.
- [27] V. A. Lund, "Peptidoglycan Dynamics in *Staphylococcus aureus* using Super-Resolution Microscopy." University of Sheffield, 2016.
- [28] X. Zhou, D. Halladin, E. Rojas, E. Koslover, T. Lee, K. Huang and J. Theriot, "Mechanical crack propagation drives millisecond daughter cell separation in *Staphylococcus aureus*," *Science (80-.)*, 2015.
- [29] V. R. F. Matias and T. J. Beveridge, "Cryo-electron microscopy of cell division in *Staphylococcus aureus* reveals a mid-zone between nascent cross walls," *Mol. Microbiol.*, 2007.
- [30] X. Zhou and L. Cegelski, "Nutrient-dependent structural changes in *S. aureus* peptidoglycan revealed by solid-state NMR spectroscopy," *Biochemistry*, vol. 51, no. 41, pp. 8143–8153, 2012.
- [31] K. Amako and A. Umeda, "Scanning electron microscopy of *Staphylococcus*," *J. Ultrastruct. Res.*, vol. 58, no. 1, pp. 34–40, 1977.
- [32] V. A. Fischetti, R. P. Novick, J. J. Ferretti, D. A. Portnoy, and J. I. Rood, *Gram-positive pathogens.*, no. Ed. 2. ASM Press, 2006.
- [33] P. Giesbrecht, T. Kersten, H. Maidhof, and J. Wecke, "Staphylococcal Cell Wall: Morphogenesis and Fatal Variations in the Presence of Penicillin," *Microbiol. Mol. Biol. Rev.*, 1998.
- [34] S. Yamada, M. Sugai, H. Komatsuzawa, S. Nakashima, T. Oshida, A. Matsumoto and H. Suginaka, "An autolysin ring associated with cell separation of *Staphylococcus aureus*," *J. Bacteriol.*, 1996.
- [35] A. Bisson-Filho, Y. Hsu, G. Squyres, E. Kuru, F. Wu, C. Jukes, Y. Sun, C. Dekker, S. Holden, M. Van Nieuwenhze, Y. Brun and E. Garner, "Treadmilling by FtsZ filaments drives peptidoglycan synthesis and bacterial cell division," *Science (80-.)*, vol. 355, no. 6326, pp. 739–743, 2017.
- [36] J. Monteiro, A. Pereira, N. Reichmann, B. Saraiva, P. Fernandes, H. Veiga, A. Tavares, M. Santos, M. Ferreira, V. Macário, M. VanNieuwenhze, S. Filipe and M. Pinho, "Peptidoglycan synthesis drives an FtsZ-treadmilling-independent step of cytokinesis," *Nature*, 2018.
- [37] N. The MathWorks Inc, "MATLAB, version 7.10.0 (R2010a)." Massachusetts, 2010.

Chapter 5 *Staphylococcus aureus* mutants

In this chapter other strains than *S. aureus* WT (SH1000) will be studied more in depth and compared to the findings from *chapters 3* and *4*. The aim is to investigate how different mutations of non-essential cell machinery components can affect the three-dimensional PG architecture in *S. aureus*.

All the mutant strains below were constructed using *S. aureus* SH1000 as a background strain. The mutant strains were already available in the strain collection produced by members of *Prof Simon Foster's group*.

5.1 Removal of WTA (SH1000 *tarO*)

The first strain to be studied was the *tarO* (SH1000 *tarO*, see *section 2.1.1*). The disruption of *tarO* gene affects the biosynthesis machinery of WTA the second major component of the CW (see *section 1.3.1.1*).[1]–[4] This was a control, to corroborate that the features observed in *chapters 3* and *4* were created by peptidoglycan and not by other CW components such as WTA. Thus, *tarO* mutant cells were grown to exponential phase ($OD_{600}=0.5$) and trapped using silicon grids to ensure the images corresponded to the external PG architecture (see *section 2.1.5.3*). Images of *tarO* live cells are presented in *Figure 5.1*.

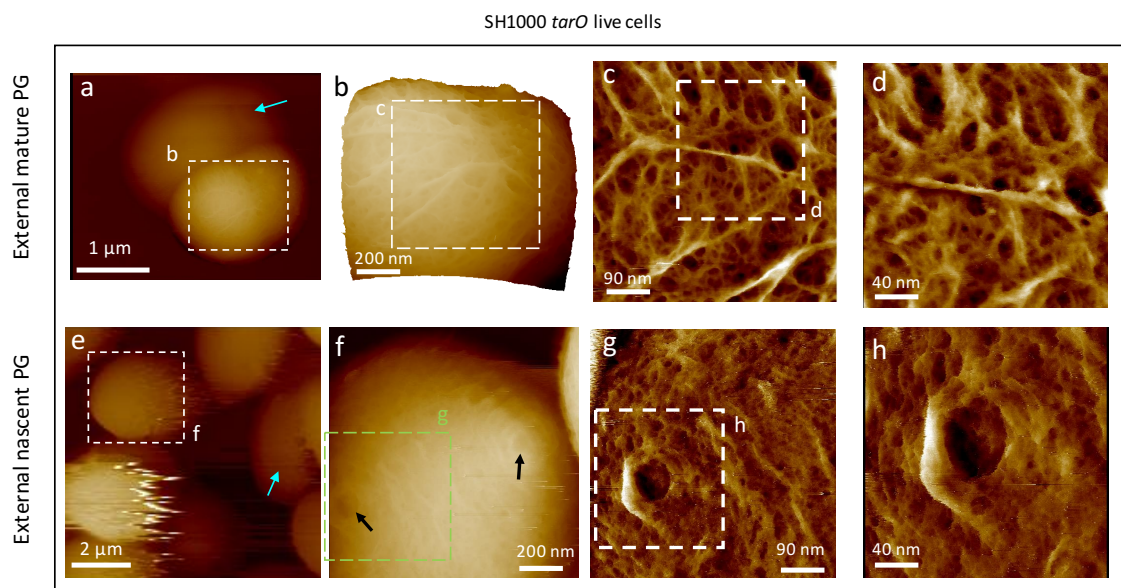


Figure 5.1 – *tarO* live cells trapped in silicon grids – a) Two *tarO* cells trapped in a silicon grid of 1 μm diameter; b) Zoom of one cell from 'a'; c) Zoomed image of external mature PG from 'b'; d) Zoomed from 'c'; e) Several *tarO* cells trapped in a silicon grid; f) Zoom of one cells from 'e' showing two regions of nascent CW with two opposite centre

of rings (see black arrows); g) Zoom from 'f' showing concentric rings; h) Zoom from 'g' with rings.

Table 5.1 – Experimental conditions used to obtain data from Figure 5.1 using tip FastScanD.

AFM MODE	SAMPLE TYPE	BUFFER/ ENVIRONMENT	SURFACE	SPECIFIC CONDITIONS
SOFT TAPPING	<i>S. aureus</i> SH1000 $\Delta tarO$ live cells	150 mM KCl + 10 mM MgCl ₂ 10 mM Tris pH=7.8	Silicon Grids from (Nunano™)	Exponential phase O. D. ₆₀₀ ~ 0.5

Figure 5.1 a-d show *S. aureus tarO* live cells trapped in silicon holes with features similar to external mature PG observed in SH1000. Although some cells presented shape deformations (see blue arrows) the majority of the cells presented a randomly ordered mesh of fibres with different pore sizes (see Figure 5.1 c-d), similar to the external PG structure from *S. aureus* WT (see Figure 3.1 c). Figure 5.1 e-h shows *S. aureus tarO* live cells with features resembling the external nascent PG observed in *S. aureus* WT. However, the concentric rings were always found in an advance growth stage, as the rings were poorly defined with pores emerging in between.[5] This could be due to alterations in the cell cycle due to the lack of WTA. The central depression was used as indicator of nascent PG architecture (see black arrows). In one occasion, two central depressions were found opposite to each other in the same cell (see Figure 5.1 f) which has never been observed in *S. aureus* WT (see Figure 3.1 b).

Two different PG architecture were found in *tarO* live cells corresponding to external mature and nascent PG regions. The finer architecture resembled the ones from WT *S. aureus*, meaning these structures are formed by peptidoglycan. The results from this control pose another questions, why the AFM cannot visualize WTA in WT cells? From the chemical structure data (see Figure 1.5) it is clear that WTA are highly flexible elongated molecules with no cross-links between them. Therefore, it is suggested the AFM tip is not sensitive enough to visualize them and probably pushes them away when imaging samples containing WTA. [5]–[8]

5.2 Removal of LTA (*SH1000 ItaS*)

The other component of the CW are the lipo-teichoic acids (LTA), see section 1.3.1.2. [2], [9], [10] LTA are polymers chemically very similar to the WTA, located on the periplasmic space between the cell membrane and the internal CW. Another control was made studying a strain lacking LTA by targeting its biosynthesis machinery.

The biosynthesis of all different types of LTA is not completely understood. [10] However, for type I LTA corresponding to *S. aureus* it has been shown that LTA synthase (LtaS) is necessary and sufficient for the correct biosynthesis and polymerization of LTA in *S. aureus*. [11] The gene *ltaS* encodes LtaS, a polytopic membrane protein with a C-terminal domain on the outer surface of the bacterial membrane. This enzyme cleaves the glycerophosphate (Gro-P) subunit from phosphatidyl glycerol and attaches it to the glycolipid anchor diglycosyl-diacylglycerol (GI₂-DAG) which is firmly anchored to the membrane, finally LtaS polymerize LTA by adding more Gro-P at the distal end of GI₂-DAG-(Gro-P). [12] After depletion of the *ltaS* gene in *S. aureus*, the amount of phosphate-containing LTA was measured and only minimal traces were detected. The morphology of an induced *ltaS* (*iltaS*) strain in LAC background has been previously reported [9], after 3h of Isopropyl β- d-1-thiogalactopyranoside (IPTG) absence, it was imaged by TEM. The cells increased in size, they had partially thickened cell walls, occasional aberrant placement of septal division and abnormal cell aggregation. [9] As LTA is essential for cell survival and growth, a whole genome approach was used [13] to identify strains that would survive despite the absence of LTA. They found that disrupting the *gdpP* gene increased the amount of the signalling molecule named c-di-AMP. This helped the cells to survive despite the extreme cell wall stress caused by the absence of LTA. [13] Thus, in this study, instead of working with the *iltaS* mutant, we used a $\Delta ltaS$ *gdpP::kan* mutation in SH1000 background instead of the LAC background, using initially the strain provided by this group [13]. The morphology of this mutant was first assessed by chemical fixation TEM thin sections, showing two different populations: cells with normal morphology (see green arrows) and some abnormal cells similar to the *iltaS* mutant (see red arrows in *Figure 5.2 a*) previously described. [9] This unpublished TEM study was performed by a colleague researcher, *Lucia Lafage*, who generously shared her findings. The $\Delta ltaS$ mutant (SH1000 $\Delta ltaS$ *gdpP::kan*, see *section 2.1.1*) [13] grows very similar to SH1000 WT. Thus, sacculi purification was successful.

After applying all the protocols optimised for imaging purified CW in liquid (see *section 2.3.2.3.2*), the best AFM images obtained from the $\Delta ltaS$ sacculi are summarized below in *Figure 5.2*. The specific alterations to the protocol required to purify CW from this mutant and the strain characteristics are detailed in *section 2.2.1.4*).

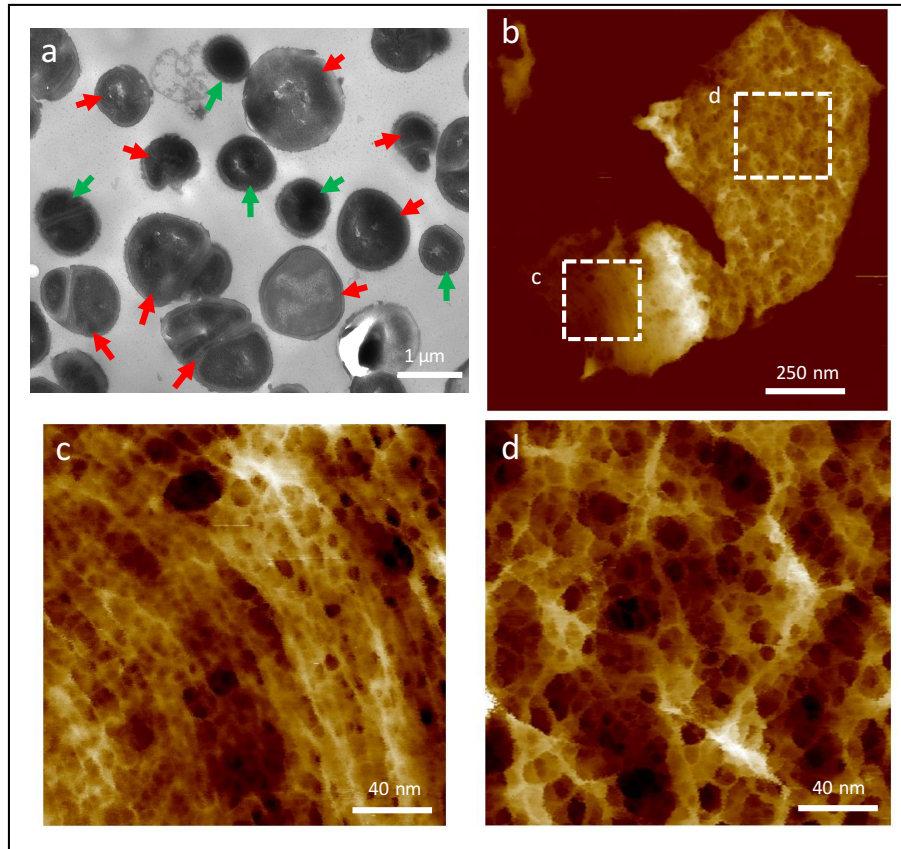


Figure 5.2 – a) Chemical fixated TEM thin section (85 nm thickness) of $\Delta ltaS$ at $OD_{600} \sim 0.6$; b) individual sacculus of $\Delta ltaS$ mutant with its external surface facing upwards; c) zoom from 'b' showing the nascent CW structure, concentric rings; d) zoom from 'b' showing a high-magnification image of the mature mesh.

The AFM images from Figure 5.2 were performed under the experimental conditions summarized in Table 5.2. The AFM type used was Bruker Dimensions Fast Scan and the AFM tip was FastScan-D. These will be consistent across the chapter and no specification will be made on the following experimental tables.

Table 5.2 – Experimental conditions used to obtain data from Figure 5.2

AFM MODE	SAMPLE TYPE	BUFFER/ ENVIRONMENT	SURFACE	SPECIFIC CONDITIONS
PEAK FORCE TAPPING	$\Delta ltaS$ Stock A Batch 8 Dilution 4	150 mM KCl + 10mM Tris pH=7.8	PLL coated MICA	Dried to be imaged the next day

Figure 5.2 b shows one individual sacculus of $\Delta ltaS$ strain. Figure 5.2 c shows a high-magnification of the nascent external CW architecture with tight concentric rings, similar to the WT (see Figure 3.11 c for comparison). Figure 5.2 d shows a high-magnification of the mature external CW architecture with a randomly disordered mesh, similar to the WT (see Figure 3.14 d for comparison). Figure 5.2 b-d are images from a sacculus fragment probably belonging to the normal morphology cell population (see green

arrows in *Figure 5.2 a*) while others had defects (see red arrows in *Figure 5.2 a*). Due to the limited amount of AFM sessions performed on this sample, no examples of the population with defects, internal surfaces or septa were found. Therefore, it cannot be discarded that these would have some differences with respect to the WT.

Despite the normal morphology from the example visualized by AFM, all the cells from this strain cannot synthesise LTA, meaning that the finer architecture observed does not correspond to LTA. In conclusion, a qualitative comparison between SH1000 WT and ΔtaS strain, as well as *tarO* (see *section 5.1*), show there is no apparent difference in the external CW organization in the absence of WTA or LTA. [5] Therefore, all our previous results (*chapter 3 and 4*) from samples containing WTA and LTA correspond solely to peptidoglycan.

5.3 Removal of SagB hydrolase (*SH1000 sagB*)

Another mutant of interest is a strain lacking the SagB hydrolase. This type of enzyme is crucial for the normal development of peptidoglycan throughout the cell cycle (see *section 1.3.3.2*). A group of four hydrolases (glucosaminidases: Atl, SagA, ScaH and SagB) are essential for normal cell growth in SH1000 background. [14] The double, triple and an inducible quadruple mutated strains of this group all show growth defects and morphological deformations visualized with super resolution microscopy. Force spectroscopy performed by AFM assessed their mechanical strength. All the strains lacking one or groups of these glucosaminidases presented an increase in CW stiffness. [14] The more significant difference was found in the absence of SagB, which also presents a substantially increase in GCL. [14], [15] This indicates that hydrolases enable normal cellular enlargement by modulating the strength of peptidoglycan. This correlates with our previous findings of the nascent material being stiffer than the older material of the cell wall. [16] The structural data produced previously by our group [7] and in this Thesis about the concentric rings evolving into randomly orientated mesh also correlates to previous findings about the importance of glucosaminidases in this structural transformation. [14], [17] Although the mechanical differences between the *sagB* mutant and WT have been studied, [14], [17] there is no literature about their molecular PG structural difference. This will be studied in this section.

5.3.1 Sacculi images of SH1000 *sagB* in liquid

Instead of studying living cells as in the previously published work, [14], [16], [17] hydrated sacculi were imaged by AFM using the wet protocol (see *section 2.3.2.3.2*). One of the main advantages of imaging sacculi is the access to the internal PG (see *chapter 4*). Therefore, a sacculi sample from the *sagB* mutant (SH1000 *sagB::kan*, see *section 2.1.1*) was prepared. The growth conditions of this mutant are specified above in *section 2.2.1.4*. The best results are summarized below in *Figure 5.3*.

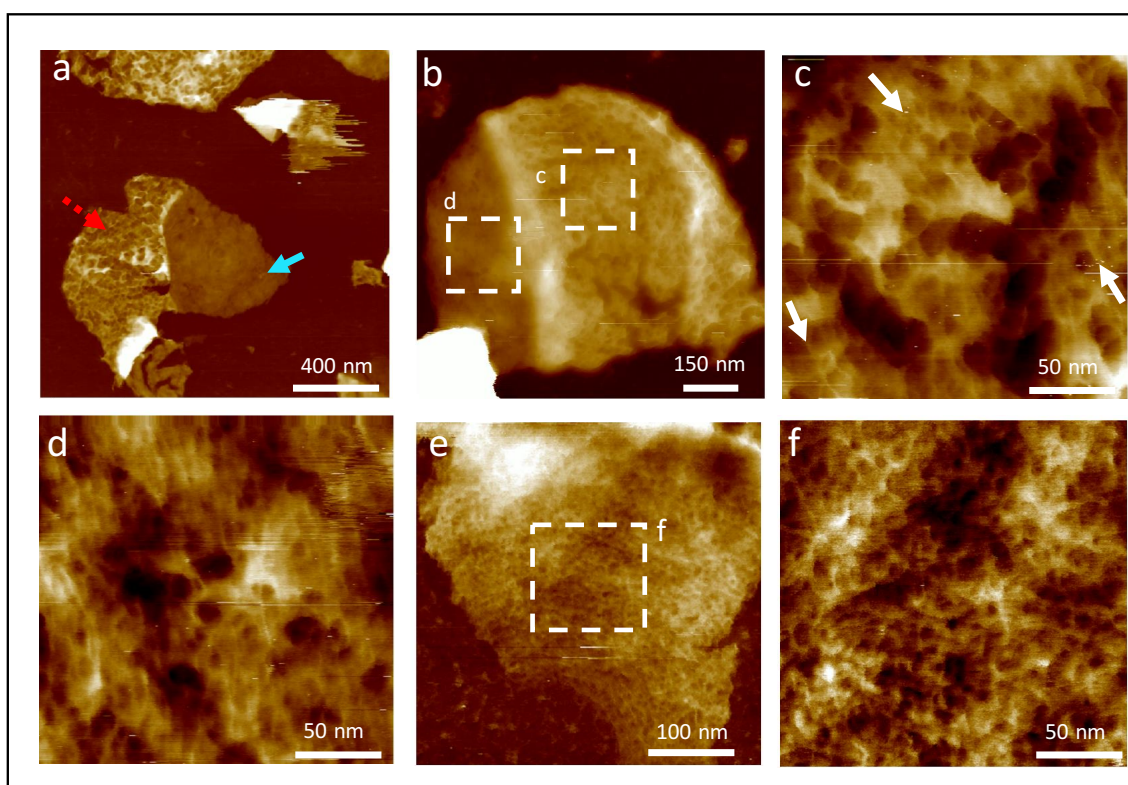


Figure 5.3 – a) sacculus fragment with external surface upwards, nascent CW (blue arrow) and mature CW (red dashed arrow); b) another sacculus fragment with external surface upwards; c) Zoom from ‘b’ of the mature CW; d) Zoom from ‘b’ of the nascent CW; e) sacculus fragment with internal surface facing upwards; f) Zoom from ‘e’.

The images from *Figure 5.3* were performed under the experimental conditions summarized in *Table 5.3*.

Table 5.3 – Experimental conditions used to obtain data from Figure 5.3, Figure 5.5 and Figure 5.6

AFM MODE	SAMPLE TYPE	BUFFER/ ENVIRONMENT	SURFACE	SPECIFIC CONDITIONS
PEAKFORCE TAPPING	<i>sagB</i> Stock A Batch 7 Dilution 4	300 mM KCl + 10mM Tris pH=7.8	Cell-Tak coated MICA	Wet preparation, never dry

Figure 5.3 shows several sacculi fragments from the *sagB* mutant. *Figure 5.3 a* shows a sacculus fragment with two main regions clearly separated by different thickness. These

two regions correspond to external nascent PG (see blue arrow) and mature PG (dashed red arrow), based on their structural features. *Figure 5.3 b* shows a similar fragment where the thickest region on the right hand side of the image corresponds to mature PG, while the thinnest region on the left hand side is more nascent PG. *Figure 5.3 c* is a zoomed image from the thicker section in *Figure 5.3 b* corresponding to the finer mature PG architecture. This architecture does not represent the most mature PG region, there are some ordered periodic features that are most likely remnants of concentric rings (see white arrows). This type of early transition from concentric rings to mesh is uncommon on WT sacculi corresponding to the same cell cycle (early exponential phase $OD_{600}=0.5-0.7$). However, the *sagB* mutant contained a higher amount of early transition PG architecture. *Figure 5.3 d* is a zoomed image from the thinner region in *Figure 5.3 b*, corresponding to nascent PG architecture. The concentric rings are not significantly different from WT nascent PG (see *Figures 3.11* and *3.12*). However, there was an increased proportion of sacculi containing nascent PG in the *sagB* mutant with respect to WT sacculi at early exponential phase, which had a mixture of mature PG, unfinished septa and nascent PG (see *Figure 4.13*). The nascent PG proportion in *sagB* mutant resembles the proportion from WT at stationary phase (see *Figure 4.13*). *Figure 5.3 e* shows a sacculus fragment with the internal PG exposed to AFM imaging. *Figure 5.3 f* shows the finer internal PG architecture of the *sagB* mutant, with no significant difference from the very tight and disordered mesh seen in WT sacculi (see *Figure 4.1* and *4.3*).

5.3.2 Pore morphology comparison between *sagB* mutant and WT

Here a quantitative analysis was performed on the mature PG architecture. Only limited data was available from internal and nascent PG and they were not further analysed quantitatively.

The semi-automated method of measuring the pore area explained in *chapter 4* (see *section 4.2.2*) was used here. The results are presented below in *Figure 5.4*.

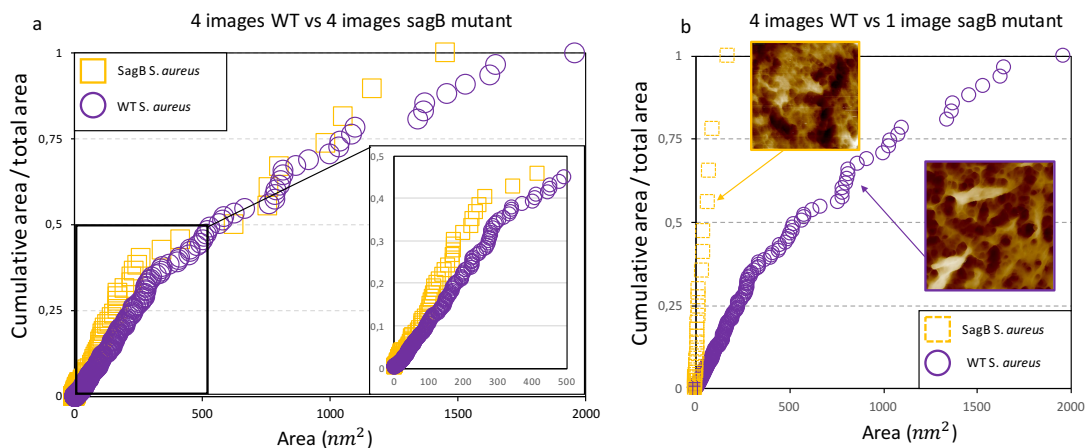


Figure 5.4 – a) Cumulative fraction of total area vs the area of individual pores of two sets of images: 4 images from WT and 4 images from *sagB* mutant, there is a zoom of the area corresponding to pores smaller than 500 nm²; b) Cumulative fraction of total area vs the area of individual pores from 4 images of WT but only one image of *sagB*.

Figure 5.4 a shows a plotting of pore area vs the cumulative fraction of the area of all pores analysed. Total pores analysed $n=292$ (see external sacculi at 50 % in Figure 4.10 and Table 4.3), from $n=4$ images of WT mature mesh (see Figure 3.14 f as example). Total pores analysed $n=118$, from $n=4$ images of *sagB* mutant mesh. No apparent difference was found between these two sets of data as they have a similar trend and the same HCFA. In contrast, another comparison was performed (see Figure 5.4 b) between the WT data set used in Figure 5.4 a and the pores from Figure 5.3 c. In this case, there is a significant difference, because this *sagB* mutant image of mesh represents an early transition stage from rings to mesh, which correlates with smaller pore area.

In conclusion, the removal of the glucosaminidase SagB affects the transition rate from concentric rings to mesh. This increases the frequency of rings per sacculi in the sample and the appearance of some early stages of rings to mesh transition which have significantly smaller pore area due to the lack of hydrolase activity.

5.3.3 Hydrogel behaviour of *sagB* mutant

Sacculi from *sagB* mutant have a non-uniform thickness (see Figure 5.3 a-b). From several images, a correlation was observed, between thickness and structure. The nascent PG regions were thinner than the mature PG regions, even from the same sacculus. The thickness of several sacculi fragments was measured following the same protocol used in chapter 3 to characterize the WT hydrogel behaviour (see section

3.5.3.3). Therefore, *sagB* sacculi was measured in both liquid and air environment. *Figure 5.5* below, shows an example of the *sagB* sacculi where the same area was imaged in both air and in liquid.

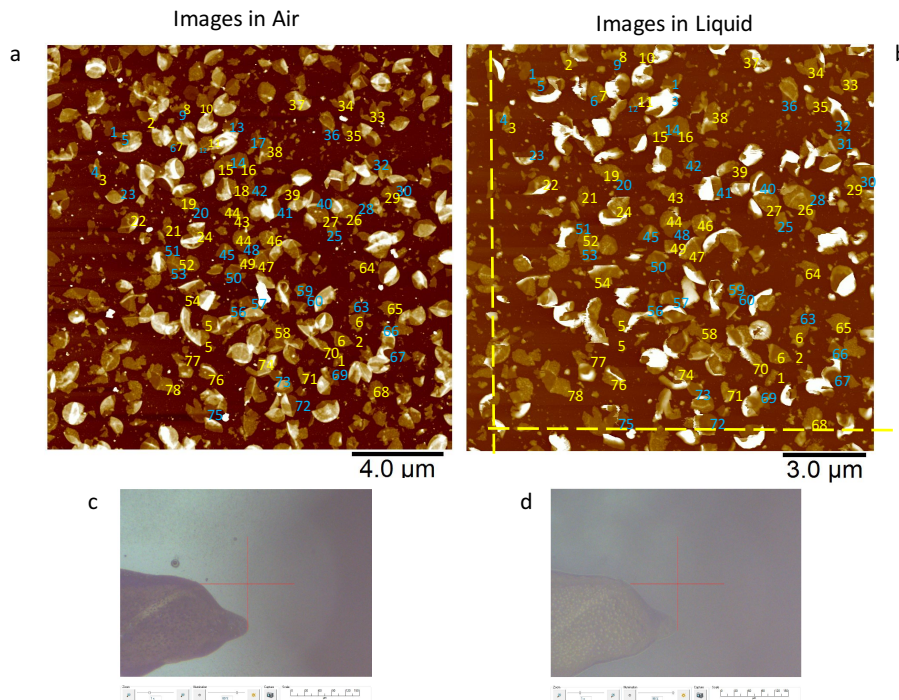


Figure 5.5 – a) sacculi from *sagB* sample imaged in air with individual sacculus marked with numbers from 1 to 78 (the blue numbers are thinner regions, the yellow numbers are higher regions); b) same area imaged in liquid; c and d) are the permanent pen marks on mica used as correlation markers on the AFM in both air and liquid

Figure 5.5 a shows *sagB* sacculi imaged in air and *Figure 5.5 b* shows the same area (marked with yellow dashed lines) as ‘a’ in liquid. Individual sacculi have been marked with numbers from 1 to 78 in both scenarios. They are divided into two groups, the thinner regions (thin *sagB*) which are marked with blue numbers; and the thicker regions (thick *sagB*) which are marked with yellow numbers. This experiment was compared with the WT measurements from *Figure 3.18*. Stock A, containing WTA, was used in both *sagB* and WT because the results will be a better representation of the native scenario. The thickness of these three sets of sacculi (WT, thin *sagB* and thick *sagB*) were measured in air and liquid using the Gwyddion software with the calculate 1D statistical functions tool (see *section 3.5.3.3* for more details). The results are shown below in *Figure 5.6*.

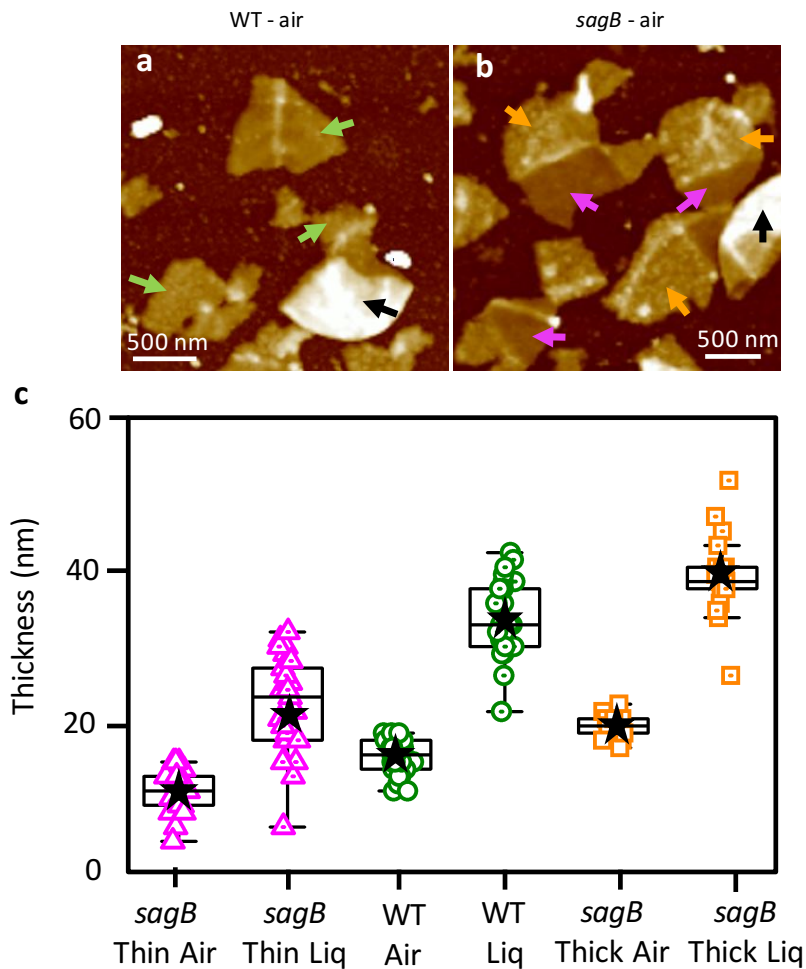


Figure 5.6 – a) Example of two groups of sacculi from WT and *sagB* sample imaged in air, both having the same data scale = 75 nm, WT single layer (green arrows), double layers (black arrows), thinner regions *sagB* (pink arrows) and higher regions *sagB* (yellow arrows); b) Thickness graph of the different samples in air and liquid (10mM Tris + 300mM KCl). The box marks the median and the 90% percentiles on the error bars, the mean values are marked with a black star.

Figures 5.6 a and b show two images in air of WT and *sagB* sacculi respectively, they both have the same colour scale (75 nm) and from the colours it can be distinguished single PG layers on WT (green arrows) which are much thinner than double layers of both samples (black arrows). There are some darker regions of *sagB* sacculi which are thinner (pink arrows) and higher (orange arrows) than the WT single PG layers. These different types of sacculi were binned separately and their thickness distributions in air and liquid are plotted in Figure 5.6 c. The WT data plotted here (green data points) are the same measurements used to plot the graph from Figure 3.18 b, PG+WTA. For all the data sets there is a significant increase in thickness in liquid (300 mM KCl + 10 mM Tris, pH = 7.8) with respect to their measurement in air, with approximately 50 % of liquid intake. The thinner regions (pink triangles) from the *sagB* mutant are significantly thinner in both air and liquid than the WT data (green circles). The thicker regions (orange

squares) from *sagB* are significantly thicker in both air and liquid than the WT data. All of these comparisons are presented in *Table 5.4* to help clarify the different values.

Table 5.4 – Mean values and their standard deviation from the data presented in Figure 5.6 c as graph

	Thickness air (mean ± s.d.) nm	Thickness Liq (mean ± s.d.) nm	% liquid uptake
<i>sagB Thin</i>	12 ± 3.0	24 ± 6.9	50 %
<i>WT control</i>	17 ± 2.1	36 ± 5.3	47 %
<i>sagB High</i>	21 ± 1.5	42 ± 5.7	50 %

The percentage of liquid uptake is very similar for all three data sets, around 50%. This probably means that this is an intrinsic biophysical property of the peptidoglycan macromolecule. Thus, despite the *sagB* mutant having different thickness, its PG hydrogel behaviour is unaffected. The two thickness populations in the *sagB* mutant is caused by an imbalance between the synthases and the hydrolases affecting the cell cycle.

In conclusion, this strain requires more time to convert the concentric rings to randomly orientated mesh, while the synthesis keeps the same rhythm as the WT. This transition seems to be directly related to the regulation of a constant CW thickness. This process, results in initially thinner cell walls that take longer to transition fully to the mature disordered mesh architecture, finishing the cycle with thicker cell walls.

5.4 Removal of non-essential synthase PBP3 (SH1000 *pbp3*)

After studying the effect of removing an hydrolase from *S. aureus*, the contrary effect was studied by removing a non-essential synthase from the PBP family, the PBP3. [18] In *S. aureus*, there are four different Penicillin Binding Proteins (PBPs) performing most of the peptidoglycan polymerisation process. PBP3 has only transpeptidase activity. Thus, when removed, the cell population still grows without any or minimum alteration to the PG composition because other PBPs carry out their transpeptidase and transglycosylate activities. [18]–[20] For more details see *section 1.3.3.1*.

The main reason a non-essential PBP like PBP3 was used for this study instead of PBPs like PBP1 or PBP2 is because these latter are essential for cell growth. Thus, only inducible mutations can be constructed, requiring IPTG to grow normally. A cell population of the *pbp3* mutant (SH1000 *pbp3::Tn*, see *section 2.1.1*) was grown at a similar OD₆₀₀ to the WT experiments: early exponential phase OD₆₀₀=0.5-0.7. Then it was

purified following the same protocol as WT with the exception of the specific growing conditions from this strain, see *section 2.2.1.4*. The PG purification from *pbp3* mutant was performed by a colleague *Dr. Joshua Sutton* and he generously shared his sample. Then, the hydrated sacculi was imaged by AFM in liquid, the best results are presented below in *Figure 5.7*.

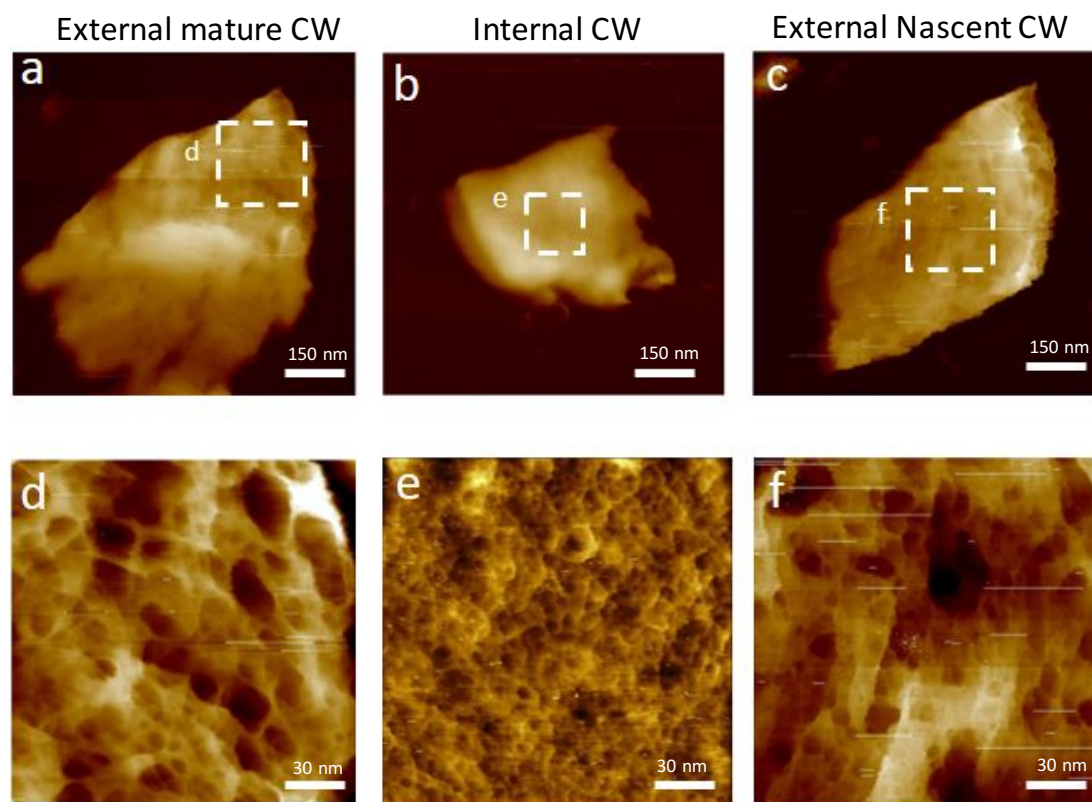


Figure 5.7 – a) Sacculus fragment of pbp3 mutant with external mature CW upwards; b) sacculus fragment of pbp3 mutant with internal CW upwards; c) sacculus fragment of pbp3 mutant with external nascent CW upwards; d-f) zooms from ‘a-c’ respectively showing the finer architecture of external and internal CW of pbp3 mutant.

The images from *Figure 5.7* were performed under the experimental conditions summarized in *Table 5.5*.

Table 5.5 – Experimental conditions used to obtain data from Figure 5.7

AFM MODE	SAMPLE TYPE	BUFFER/ ENVIRONMENT	SURFACE	SPECIFIC CONDITIONS
PEAKFORCE TAPPING	<i>pbp3</i> Stock A Batch 9 Dilution 4	150 mM KCl + 10mM Tris pH=7.8	PLL coated MICA	Dried to be imaged the next day (see 2.4.2.5)

Figure 5.7 a-c are three sacculi fragments from *pbp3* mutant showing the external mature, internal and external nascent PG surfaces respectively. *Figures 5.7 d-f* are higher magnification images from the sacculi fragments ‘a-c’ showing the fine structure of the mature external, the internal and the nascent PG respectively. There is no apparent

difference between them and the *S. aureus* WT molecular PG architecture imaged by AFM (see chapters 3 and 4). However, a quantitative corroboration of their resemblance at molecular level could not be produced due to the lack of high magnification images similar to Figure 5.7 d-f.

5.5 Removal of non-essential synthase PBP4 (SH1000 *pbp4*)

PBP4 is a non-essential synthase with a very complex role in PG biosynthesis. It is the only PBP from *S. aureus* that can be categorized as low molecular mass PBP [21] or more recently named Class C, type-5. [22] PBP4 is able to recognize the C-terminal of stem peptides (D-Ala-D-Ala), it is bifunctional with both DD-carboxypeptidase and transpeptidase activity. [21]–[24] The relevant activity for PG biosynthesis is its ability to catalyse the cross-linking between two peptide stems. This part of the PG synthesis is commonly named secondary transpeptidase. [17], [22]–[27] It has been shown that lack of PBP4 in the following strains: community acquired MRSA, hospital acquired MRSA [27] and ZO3 and 27S [26]; results in a significant decrease of highly cross-linked PG moieties. These studies were performed by HPLC measurements. A disruption of the *pbp4* gene was performed by Tn to create the *pbp4* mutant (SH1000 *pbp4::Tn*), in Prof. Simon Foster' group. This strain also shows the same trend of reduced cross-linking by HPLC measurements. One possible explanation would be that PBP4, although not being essential for cell survival, would help create additional cross-linking to glycan strands already located in the CW that would already be partially cross-linked. [22], [25], [28] This hypothesis is partially supported by the most recent liquid-state NMR study where they point out that the most probable substrate for PBP4 to catalyse is a complete muropeptide rather than an individual peptide stem chain. [29]

Previous studies have been performed on strains lacking PBP4 using AFM as the main experimental technique to test how the difference in cross-linking affects the mechanical properties of the cell wall. The first approach was pressing whole cells against the surface and measuring their response. The comparison between an *S. aureus* NCTC 8325-4 WT strain and $\Delta pbp4$ strain (NCTC 8325-4 $\Delta pbp4$) resulted in a significant reduction of the Young's modulus in the $\Delta pbp4$ strain. [30] Another study used PeakForce (QNM) technique with 1-5 nN as threshold to assess the local mechanical properties of trapped cells from CA-MRSA and HA-MRSA strains and their $\Delta pbp4$

corresponding mutants showing a concomitant decrease in the Young modulus of their CW after the mutation.[17] This last experiment together with studies in the early 2000s suggest PBP4 could be associated with glycopeptide [31] and β -lactam resistance. [25], [27], [32]

In conclusion, PBP4 is an important synthase from *S. aureus* in which the genetic implications are well established but the biochemical studies have not reached an agreement about its primary enzymatic activity and its regulation. Thus, studying a $\Delta pbp4$ strain at the fundamental level is important, especially since it has been shown that somehow it has a role on promoting resistance for several MRSA strains. However, as PBP4 only has transpeptidase activity (regarding the role of PG synthesis), it has been suggested that a synergy between PBP4 and PBP2 could be crucial.[25], [26] This is the reason, PBP4 has been recently identified as a new possible drug target. [33]

No structural studies have been published on *pbp4* mutant (SH1000 *pbp4::Tn*, see section 2.1.1), regarding architectural changes in PG. Here the same approach has been used as before (see sections 5.1 to 5.3). After imaging a sacculi sample of the *pbp4* mutant with AFM in liquid, all the results available are presented below in Figure 5.8.

The images from Figure 5.8 were performed under the same experimental conditions as the *pbp3* mutant, summarized in Table 5.5 above except the strain was *pbp4*.

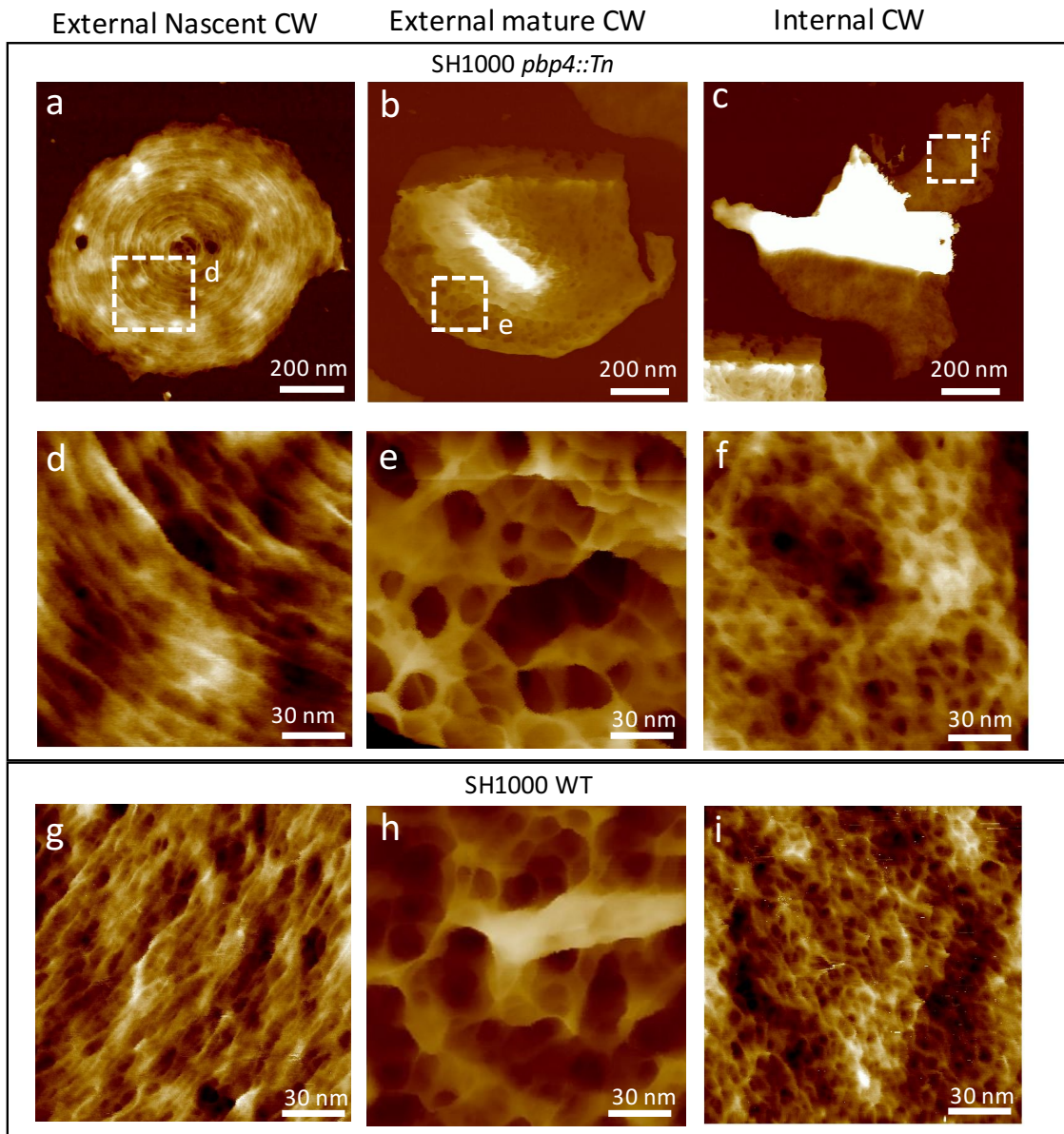


Figure 5.8– a) Sacculus fragment of *pbp4* mutant with external nascent CW upwards; b) sacculus fragment of *pbp4* mutant with external mature CW upwards; c) sacculus fragment of *pbp4* mutant with internal CW upwards; d-f) zooms from 'a-c' respectively showing the finer architecture of external and internal CW of *pbp4* mutant; g-i) Images from WT control with the same scale as images 'd-f' showing the finer architecture of external and internal CW.

Figure 5.8 a-c show three sacculi fragments from *pbp4* mutant with the external nascent, mature and internal PG respectively. Figures 5.8 d-f are zoomed images from the sacculi fragments showing the finer PG architecture from: external nascent, mature and internal respectively. There is no apparent difference between them and the *S. aureus* WT PG architecture imaged by AFM (see Figure 5.8 g-i for a direct comparison). However, in this case a quantitative corroboration of this resemblance at molecular level could not be produced, due to the lack of high magnification images similar to Figure 5.8 d-f. It was striking to be able to visualize an entire nascent region of concentric rings

without any cracks or ruptures (see *Figure 5.8 a*), which has never been imaged on a WT sample. In general, almost every sacculus fragment found contained some fraction of nascent material, similarly to the *sagB* mutant (see *section 5.3.1*). However, there was no apparent height difference in this case. However, the number of images from the *pbp4* mutant is lower than for the *sagB* mutant and WT. Therefore, it is not possible to extract any hard conclusions regarding the *pbp4* mutant CW thickness.

Additionally to the fine structure comparison, another difference was spotted, presented in more detailed below in *Figure 5.9*.

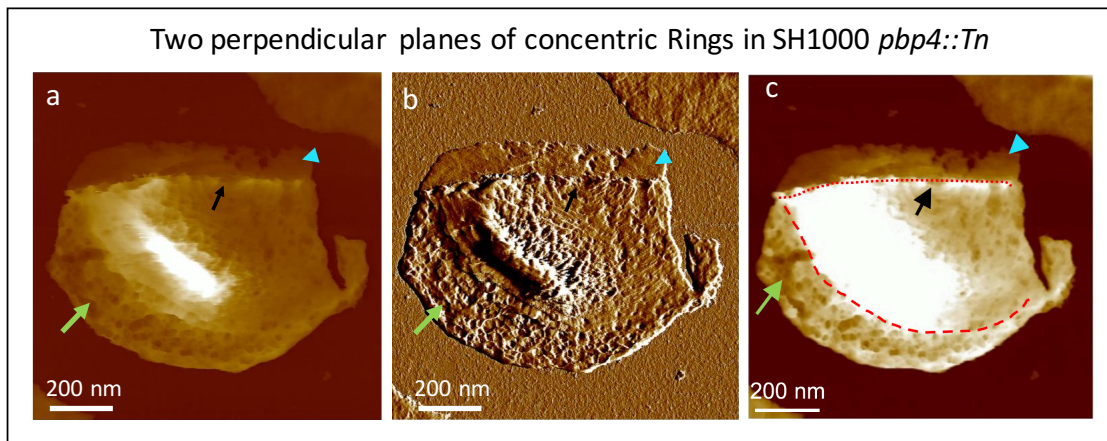


Figure 5.9 – a) same sacculus fragment as Figure 5.8b, Height channel; b) same sacculus fragment presented with the Peak Force error channel where more features are highlighted; c) same sacculus fragment as ‘a-b’ height channel with the colour scale reduced to highlight features that were otherwise obscured in ‘a’.

As mentioned above, there is no difference between the external nascent PG finer structure for WT and *pbp4* (see *Figure 5.8 d and g*), except the fraction of sacculi containing rings is higher in this sample than WT. *Figure 5.9 a-c* shows different representations of the same sacculus fragment with a small area of the mature peptidoglycan structure (green long arrow). The rest of the sacculus is covered by concentric rings. Most of them are already in the late phase of the transition to mesh (black short arrow pointing to the centre of the concentric rings). In *Figure 5.9 c* there is a manually drawn boundary with the mature structure (see red dashed line). The rest of the sacculus fragment corresponds to the newest generation of rings (blue arrow head) in *Figure 5.9 c* there is a boundary with the oldest rings (see red dotted line). It is important to highlight this is the first time two perpendicular planes of rings have been visualized at exponential phase $OD_{600} = 0.6$ in our working conditions.

Future experiments should be performed to increase the data set for this strain. If the same results are found, it could be concluded that removal of PBP4 increases the ratio of ordered concentric rings. This could mean that a complete transition from Rings to mesh would occur slower upon removal of PBP4, suggesting its secondary transpeptidase activity is necessary to create cross-linking between glycans already present on the CW. [22], [25], [26], [29] However, the increased amount of concentric rings found by the AFM images, contradicts the reduced CW stiffness previously found in $\Delta pbp4$ strains [17], [30]. From a different study on *S. aureus* SH1000 about the mechanical properties across the cell cycle, the nascent material (concentric rings) was determined to be stiffer than the mature mesh. [16] Therefore, one would expect a smaller amount of concentric rings on the *pbp4* mutant instead of the opposite.

This incongruence of results can be tackled by two approaches. One possibility is that the mechanical data of the *pbp4* mutant performed in a different background strain [17], [30], could affect the results in our SH1000 background. Therefore, repeating the mechanical measurements with our strain would be useful to resolve this issue in the future. The second and most probable explanation is that more AFM high resolution images are required to be able to have a solid quantitative comparison across the different strains.

All the data from this and the previous section show that removal of non-essential PBPs (PBP3 and 4) makes only relatively minor differences to the PG architecture. However, studying hydrated sacculi by AFM from different strains gives insight into the correlation between PG structure and the mechanistic function of specific enzymes.

5.6 Discussion

The first conclusion from this chapter is the AFM study of *S. aureus* $\Delta ltaS$ purified sacculi allow us to conclude that the topographic images obtained from the *S. aureus* WT do not correspond to LTA architecture. One could argue that WTA are being imaged rather than PG, but images of living cells stripped from their WTA show no difference (*tarO* mutant). Thus, all the previously presented AFM images of purified CW and live cells, show only the PG organization not the LTA or the WTA polymers, which are the other major components of the CW (see *sections 5.1 and 5.2*).

The second conclusion is that upon removal of one of the most important glycosaminidases in *S. aureus* (SagB) each individual PG architecture is not greatly affected: the internal mesh, the external mature mesh and the external nascent rings could be visualized in this mutant. However, the rate of fragments containing concentric rings increases with respect to the WT. A quantitative comparison of the pore area of the mature mesh results in the conclusion that removing the SagB hydrolase affects the rate at which some cells evolve from concentric rings to mesh, because some sacculi had early stages of the transition between rings to mesh with smaller pores than the regular mature mesh on the WT. The most prominent difference between this mutant and the WT was the uneven height of the CW. Two populations of height were found on the *sagB* mutant, thinner and thicker than the WT (both in air and in liquid). These two populations were often found in the same sacculi fragment, where the thinner corresponded to nascent rings and the thicker to mature mesh. When hydrated, the two regions kept their water uptake percentage (at around 50%) meaning the hydrogel properties of the PG are not affected. However, this would probably have a high impact on the stiffness of the CW as already reported. [14], [16] The difference in thickness and hence in stiffness is possibly related to the difference in glycans length, as the removal of SagB produces longer glycan strands (see *section 5.3*).

The imbalance between synthases and hydrolases was also tested by removing non-essential PBPs. The lack of PBP3 did not cause any apparent difference in architecture. The role of the PBPs must be synergistic and when a PBP is missing, the others perform its role more or less controlled. The conclusion from this and the removal of a hydrolase is that all the synthases and hydrolases are necessary for the cell to maintain a uniform CW thickness across a single cell and the entire population (see *section 5.4*). Furthermore, another non-essential PBP was removed, PBP4. Similarly to the *sagB* mutant, there was an increased in the number of sacculi containing rings. Moreover, there was a decrease in the surface area of the randomly orientated mature mesh in an individual sacculus fragment as for the first time two perpendicular regions or concentric rings corresponding to different division sites were visualized. From contrasting with previous studies, [25], [27]–[29], [31], [33] the differences found in the *pbp4* mutant could be attributed to a lack of cross-linking, meaning that in order for the cell to

completely transform from rings into mesh within one single cell cycle, it requires not only the hydrolases but also some PBPs to produce new cross-linking between existing glycan strands (see *section 5.5*).

In conclusion, this chapter shows the great potential of this experimental approach (*i.e.* AFM of sacculi in liquid). This imaging technique applied to mutant strains from genes that control the CW architecture presents a much improved method for determining the phenotype of these strains with respect to optical microscopy. In particular, subtle differences affecting only the CW architecture which probably cannot be discern with conventional phenotypic determination methods. In the future, upon further methodology improvements, this could represent a new line of research in microbiology focusing on the relationship between the function of relevant enzymes and the peptidoglycan structure they control, obtaining insights into the biological mechanisms.

5.7 References

- [1] S. Brown, J. P. Santa Maria, and S. Walker, "Wall teichoic acids of gram-positive bacteria.," *Annu. Rev. Microbiol.*, vol. 67, pp. 313–36, 2013.
- [2] J. Baddiley, "Bacterial cell walls and membranes. Discovery of the teichoic acids.," *BioEssays : news and reviews in molecular, cellular and developmental biology*. 1989.
- [3] G. Andre, M. Deghorain, P. Bron, I. Van Swam, M. Kleerebezem, P. Hols and Y. Dufrêne, "Fluorescence and atomic force microscopy imaging of wall teichoic acids in *lactobacillus plantarum*," *ACS Chem. Biol.*, vol. 6, no. 4, pp. 366–376, 2011.
- [4] M. Schlag, R. Biswas, B. Krismer, T. Kohler, S. Zoll, W. Yu, H. Schwarz, A. Peschel and F. Götz, "Role of staphylococcal wall teichoic acid in targeting the major autolysin Atl," *Mol. Microbiol.*, vol. 75, no. 4, pp. 864–873, 2010.
- [5] L. Pasquina-Lemonche, J. Burns, R. Turner, S. Kumar, R. Tank, N. Mullin, J. Wilson, B. Chakrabarti, P. Bullough, S. Foster and J. Hobbs, "The architecture of the Gram-positive bacterial cell wall," *Nature*, vol. 582, no. 7811, pp. 294–297, 2020.
- [6] R. D. Turner, N. H. Thomson, J. Kirkham, and D. Devine, "Improvement of the pore trapping method to immobilize vital coccoid bacteria for high-resolution AFM: A study of *Staphylococcus aureus*," *J. Microsc.*, 2010.
- [7] J. M. Burns, "High Resolution Atomic Force Microscopy Imaging of Living Bacterial Surfaces," University of Sheffield, 2017.
- [8] A. Touhami, M. H. Jericho, and T. J. Beveridge, "Atomic force microscopy of cell growth and division in *Staphylococcus aureus*," *J. Bacteriol.*, 2004.
- [9] A. Gründling and O. Schneewind, "Synthesis of glycerol phosphate lipoteichoic acid in *Staphylococcus aureus*," *Proc. Natl. Acad. Sci. U. S. A.*, vol. 104, no. 20, pp. 8478–8483, 2007.
- [10] M. G. Percy and A. Gründling, "Lipoteichoic Acid Synthesis and Function in Gram-Positive Bacteria," *Annu. Rev. Microbiol.*, vol. 68, no. 1, pp. 81–100, 2014.
- [11] R. M. Corrigan, I. Campeotto, T. Jegannathan, K. G. Roelofs, V. T. Lee, and A. Gründling, "Systematic identification of conserved bacterial c-di-AMP receptor proteins," *Proc. Natl. Acad. Sci. U. S. A.*, vol. 110, no. 22, pp. 9084–9089, 2013.
- [12] O. Schneewind and D. Missiakas, "Lipoteichoic acids, phosphate-containing polymers in the envelope of gram-positive bacteria," *J. Bacteriol.*, vol. 196, no. 6, pp. 1133–1142, 2014.
- [13] R. M. Corrigan, J. C. Abbott, H. Burhenne, V. Kaefer, and A. Gründling, "C-di-amp is a new second messenger in *staphylococcus aureus* with a role in controlling cell size and envelope stress," *PLoS Pathog.*, vol. 7, no. 9, 2011.

- [14] R. Wheeler, R. Turner, R. Bailey, B. Salamaga, S. Mesnage, S. Mohamad, E. Hayhurst, M. Horsburgh, J. Hobbs, and S. Foster, "Bacterial Cell Enlargement Requires Control of Cell Wall Stiffness Mediated by Peptidoglycan Hydrolases.," *MBio*, vol. 6, no. 4, p. e00660, 2015.
- [15] Y. G. Y. Chan, M. B. Frankel, D. Missiakas, and O. Schneewind, "SagB glucosaminidase is a determinant of *Staphylococcus aureus* glycan chain length, antibiotic susceptibility, and protein secretion," *J. Bacteriol.*, 2016.
- [16] R. G. Bailey, R. D. Turner, N. Mullin, N. Clarke, S. J. Foster, and J. K. Hobbs, "The interplay between cell wall mechanical properties and the cell cycle in *staphylococcus aureus*," *Biophys. J.*, 2014.
- [17] P. Loskill, P. Pereira, P. Jung, M. Bischoff, M. Herrmann, M. Pinho and K. Jacobs, "Reduction of the peptidoglycan crosslinking causes a decrease in stiffness of the *staphylococcus aureus* cell envelope," *Biophys. J.*, vol. 107, no. 5, pp. 1082–1089, 2014.
- [18] M. G. Pinho, H. De Lencastre, and A. Tomasz, "Cloning, characterization, and inactivation of the gene *pbpC*, encoding penicillin-binding protein 3 of *Staphylococcus aureus*," *J. Bacteriol.*, 2000.
- [19] D.-J. Scheffers and M. G. Pinho, "Bacterial Cell Wall Synthesis: New Insights from Localization Studies," *Microbiol. Mol. Biol. Rev.*, 2005.
- [20] D. L. Popham and K. D. Young, "Role of penicillin-binding proteins in bacterial cell morphogenesis," *Current Opinion in Microbiology*. 2003.
- [21] P. Macheboeuf, C. Contreras-Martel, V. Job, O. Dideberg, and A. Dessen, "Penicillin binding proteins: Key players in bacterial cell cycle and drug resistance processes," *FEMS Microbiol. Rev.*, vol. 30, no. 5, pp. 673–691, 2006.
- [22] E. Sauvage, F. Kerff, M. Terrak, J. A. Ayala, and P. Charlier, "The penicillin-binding proteins: Structure and role in peptidoglycan biosynthesis," *FEMS Microbiology Reviews*. 2008.
- [23] A. W. WYKE, J. B. WARD, M. V. HAYES, and N. A. C. CURTIS, "A Role *in vivo* for Penicillin-Binding Protein-4 of *Staphylococcus aureus*," *Eur. J. Biochem.*, vol. 119, no. 2, pp. 389–393, 1981.
- [24] J. L. Kozarich, J.W. ; Strominger, "A Membrane Enzyme from *Staphylococcus aureus* Penicillinase Activities * Which," *J. Biol. Chem.*, vol. 253, no. 4, pp. 1272–1279, 1978.
- [25] T. da Costa, C. de Oliveira, H. Chambers, and S. Chatterjee, "PBP4: A New Perspective on *Staphylococcus aureus* β -Lactam Resistance," *Microorganisms*, vol. 6, no. 3, p. 57, 2018.
- [26] T. Leski and A. Tomasz, "Role of Penicillin-Binding Protein 2 (PBP2) in the Antibiotic Susceptibility and Cell Wall Cross-Linking of *Staphylococcus aureus*," *J. Bacteriol.*, vol. 2, no. 5, pp. 1815–1824, 2005.
- [27] G. Memmi, S. R. Filipe, M. G. Pinho, Z. Fu, and A. Cheung, "*Staphylococcus aureus* PBP4 is essential for β -lactam resistance in community-acquired methicillin-resistant strains," *Antimicrob. Agents Chemother.*, 2008.
- [28] Y. Qiao, M. Lebar, K. Schirner, K. Schaefer, H. Tsukamoto, D. Kahne and S. Walker, "Detection of lipid-linked peptidoglycan precursors by exploiting an unexpected transpeptidase reaction," *J. Am. Chem. Soc.*, vol. 136, no. 42, pp. 14678–14681, 2014.
- [29] R. Maya-Martinez, J. Andrew, N. Alexander, C. Otten, I. Ayala, D. Vollmer, J. Gray, C. Bougault, A. Burt, C. Laguri, M. Fonvielle, M. Arthur, N. Strynadka, W. Vollmer and J. Simorre, "Recognition of peptidoglycan fragments by the transpeptidase PBP4 from *staphylococcus aureus*," *Front. Microbiol.*, vol. 10, no. JAN, pp. 1–14, 2019.
- [30] Y. Chen, W. Norde, H. C. van der Mei, and H. J. Busscher, "Bacterial cell surface deformation under external loading," *MBio*, vol. 3, no. 6, pp. 1–7, 2012.
- [31] K. Sieradzki, M. G. Pinho, and A. Tomasz, "Inactivated *pbp4* in highly glycopeptide-resistant laboratory mutants of *Staphylococcus aureus*," *J. Biol. Chem.*, vol. 274, no. 27, pp. 18942–18946, 1999.
- [32] S. Hamilton, J. Andrew, N. Alexander, J. Eun, B. Li, T. Costa, A. Severin, M. Chung and S. Aedo, "crossm High-Level Resistance of *Staphylococcus*," *Am. Soc. Microbiol.*, vol. 61, no. 6, pp. 1–10, 2017.
- [33] J. A. N. Alexander, S. S. Chatterjee, S. M. Hamilton, L. D. Eltis, H. F. Chambers, and N. C. J. Strynadka, "Structural and kinetic analyses of penicillin-binding protein 4 (PBP4)-mediated antibiotic resistance in *Staphylococcus aureus*," *J. Biol. Chem.*, vol. 293, no. 51, pp. 19854–19865, 2018.

Chapter 6 *Bacillus subtilis*

In this chapter another Gram-positive bacterial species *Bacillus subtilis* (*B. subtilis*) [1]–[4] was chosen as a *rod*-shaped model bacteria to be compared with *S. aureus* *cocci*-shaped CW architecture. Two approaches were taken to study *B. subtilis*: imaging sacculi in liquid; and imaging living cells in buffer and other environments.

6.1 *Bacillus subtilis* wild type sacculi

The Gram-positive bacteria group has a subgroup named *bacilli* with most of their species being *rod*-shape cells. [5]–[8] The most commonly studied *rod*-shape Gram-positive bacterial species is *Bacillus subtilis* (*B. subtilis*). [1]–[4], [8] Therefore, to expand the knowledge about the three-dimensional architecture of the CW in different Gram-positive organisms, *B. subtilis* was studied. The two main differences between *S. aureus* and *B. subtilis* are their shape and their pathogenesis. *B. subtilis* is a non-pathogenic soil bacteria harmless to animals or humans. However, *B. subtilis* has been one of the most studied species in the laboratory to understand fundamental questions about Gram-positive bacteria *in vitro*. Moreover, *B. subtilis* is an important organism for biotechnology applications.

When division occurs, in a *rod*-shaped bacteria there are two main machineries in place: the division or septation mechanism; and the elongation mechanism allowing the cells to achieve their desired shape and size. By contrast, *cocci*-shaped bacteria only have a septation mechanism, often called the Divisome (see *section 1.3.3.3*). Perhaps the elongation mechanism would introduce a significant change in architecture [9]. The PG chemical composition of *B. subtilis* is the following. The glycan backbone is exactly the same as *s. aureus*. The peptide stem only differs in two aminoacids (the second and the third): L-Ala, D-Glu, L-A₂pm, D-ala, D-Ala. There is no cross-bridge of Glycines, the cross-linking occurs by a direct link between the third aminoacid and the fourth of the neighbouring peptide stem (L-A₂pm – D-Ala). Finally, it has been reported that there is 56% of crosslinking in *B. subtilis* at exponential phase.

AFM could be the perfect approach to study the differences between two Gram-positive species with the shape as their main difference. More than 10 years ago, a study was

published of *B. subtilis* purified PG visualized with AFM in air environment. [1] After this study, another group used Cryo-EM as an alternative approach to decipher the CW architecture. [10] More recently, in our group, some work has been done studying *B. subtilis* external surface architecture with AFM on living cells. [11] In the rest of this chapter, more experiments were performed to try to unify the previous results and hypotheses about the three-dimensional architecture of *B. subtilis* using AFM on sacculi and living cells in different environments.

6.1.1 Atomic force microscopy images in air

Firstly, to get familiar with this organism, AFM images of *B. subtilis* were performed in air environment. On one hand, similarly to *S. aureus* (see section 3.2), the results from the previous study needed to be corroborated by repeating the working conditions as closely as possible. On the other hand, using improved AFM technologies might lead to novel structures or different interpretations of the previously identified architectures. A summary of the results from the previous study are presented below in Figure 6.1.

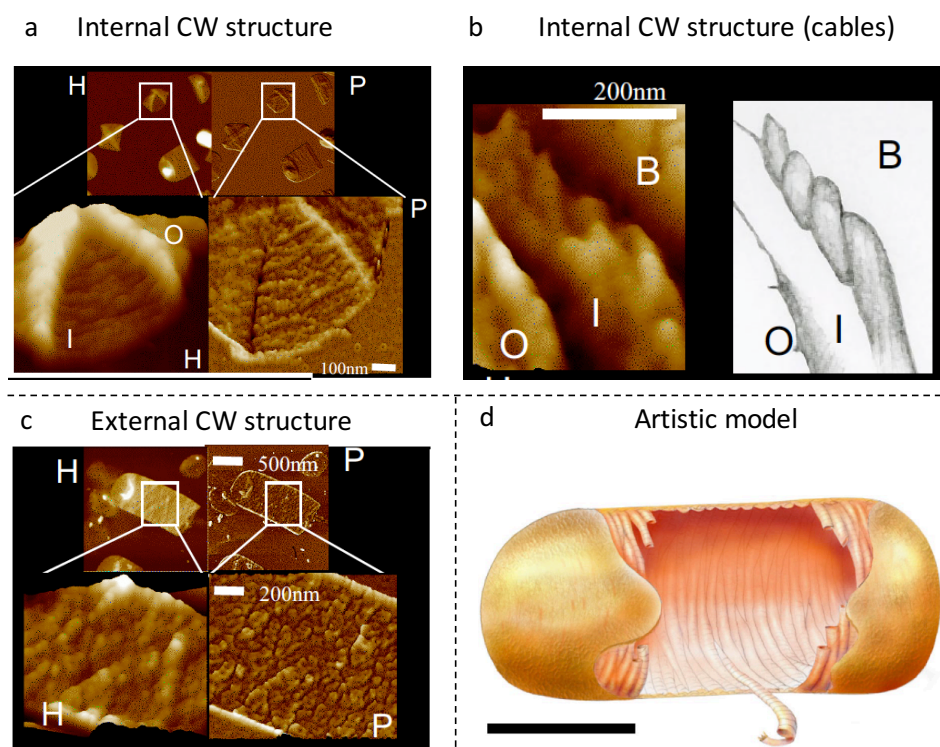


Figure 6.1 – a) *B. subtilis* sacculus fragment with the internal surface facing upwards (I) a small fraction of external structure is folded over (O), the Height (H) and Phase images (P) are presented; b) Finer structure of internal CW (I) with a folded external structure (O) and the background (B) also interpreted with a drawing on the right panel; c) External CW surface facing upwards, the height and Phase panels are presented; d) Artistic model based on results. Adapted with permission from [1]

Figure 6.1 shows two different architectures found in the cylinder of *B. subtilis*. The internal surface of the CW presented a cable like architecture with a separation pitch of approximately 50 nm. The cables aligned across the short axis of the rod (see Figure 6.1 a, b). The external surface of the CW presented a rough architecture with protrusions and dents similar to the later on called ‘knobbles’ in *S. aureus* (see Figure 6.1 c and Figure 3.3). [12] Finally, based on their data, they built a conceptual model of the *B. subtilis* CW architecture (see Figure 6.1 d).

B. subtilis 168 strain was used as a WT (see sections 2.1.1, 2.2.1.3 for more details on growing conditions). Cells were cultured in liquid media and grown up to early exponential phase ($O.D_{600}=0.5-0.6$). Then, approximately 1L of cell culture was used to purify the CW following the same method as previously shown for *S. aureus* with the exception of repeating the FastPrep cycle 15 times instead of 11 because breaking rod-shaped bacteria required more repetitions (see section 2.2.2.4). Once the stock of *B. subtilis* sacculi was obtained, the PLL coated mica protocol developed to image *S. aureus* sacculi in liquid was followed. However, instead of rehydrating the sample, it was dried with nitrogen flow and imaged under air environment (see section 2.3.2.4). The best results obtained are presented below in Figure 6.2.

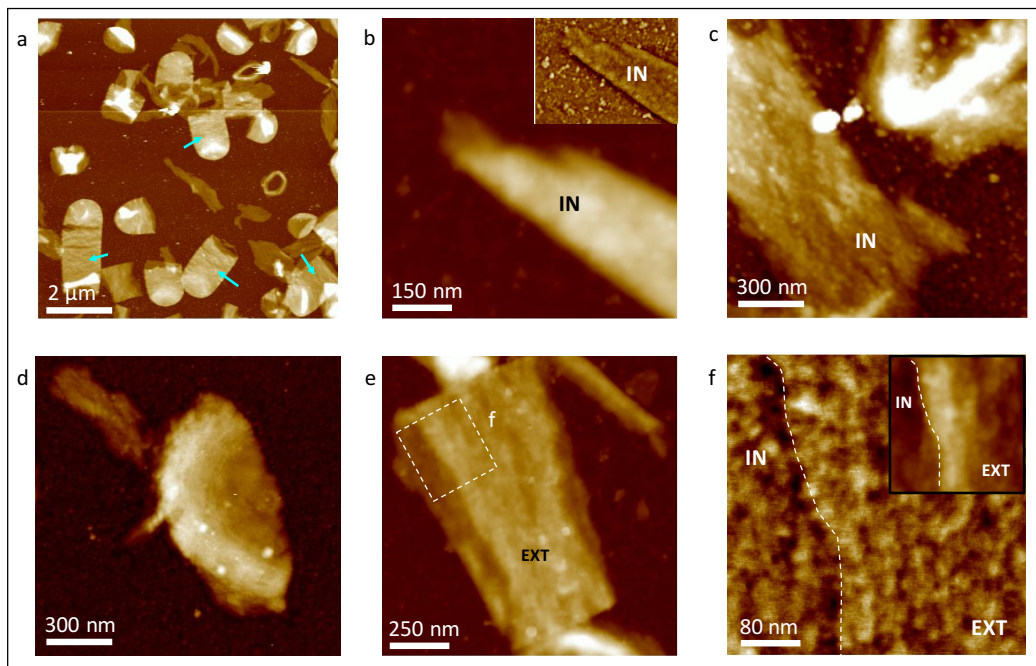


Figure 6.2 – a) Overview of *B. subtilis* sacculi sample, blue arrows show rod shaped fragments; b) Internal architecture sacculus fragment (IN), Inset: phase image of ‘b’; c) Another example of sacculus fragment with its internal CW facing upwards (IN); d) Sacculus fragment presenting a concentric rings architecture; e) Double layer sacculus fragment with most of its area showing the external surface upwards (EXT); f) Phase image zoomed from ‘e’ separating external (EXT) and internal (IN) with a dashed white line, Inset: Height image of ‘f’.

Figure 6.2 a shows an overview of a typical *B. subtilis* sacculi sample where clearly some fragments have still kept their rod-conformation (see blue arrows). Figure 6.2 b shows a fragment with the internal architecture facing upwards, its shape is similar to the sacculus from Figure 6.1 b. However, the current results show less details and the cables twisting was not possible to identify, not even on the phase image (see Figure 6.2 b, inset). Figure 6.2 c shows a bigger sacculi fragment with its internal surface facing upwards, in this case, some orientation was observed. Figure 6.2 d shows a different architecture not observed before in the previous study [1], the ‘concentric rings’ structure, probably corresponding to the newest material from the external CW surface, located in the poles. The external CW architecture (EXT) is a disordered rough structure (‘knobbles’), see Figure 6.2 e and f. Although this data has lower resolution than the previous published images, [1] it was possible to identify the different sacculi conformations (internal versus external architecture). Moreover, a novel structure was found, the concentric rings. This correlates nicely with the three different architectures identified in *S. aureus* (see Chapters 3 and 4).

6.1.2 Atomic force microscopy images in liquid

To obtain more information about the native architecture of *B. subtilis* CW the sacculi was imaged with AFM in liquid. The same samples used in air environment were re-hydrated with HPLC water and imaged using PeakForce™ Tapping.™ The best results are presented below in Figure 6.3.

The images from Figure 6.2, Figure 6.3 and Figure 6.4 were performed under the experimental conditions summarized in Table 6.1.

Table 6.1 – Experimental conditions used to obtain data from Figure 6.2 and Figure 6.3. See section 2.3.2.2.2

AFM TYPE	AFM TIP	AFM MODE	SAMPLE TYPE	BUFFER/ ENVIRONMENT	SURFACE	SPECIFIC CONDITIONS
BRUKER FAST SCAN	Tespa-V2/ Fast Scan -D	Tapping/ PeakForce Tapping	<i>B. subtilis</i> Stock A Batch 10 Dilution 5	Air / pure HPLC water	PLL coated MICA	Dried / Dried and Hydrated

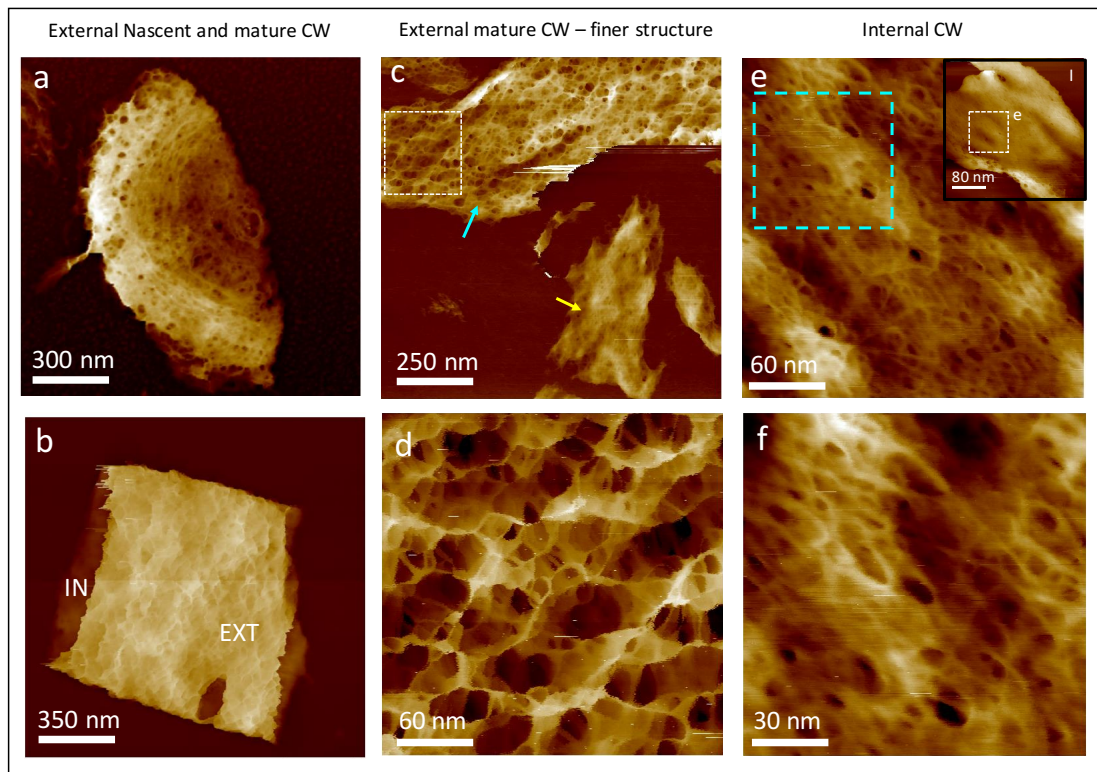


Figure 6.3 – a) Sacculus fragment with concentric rings; b) Sacculus fragment from a section of the rod cylinder body with the external CW (EXT) and the internal surface showing underneath (IN); c) Single layer of sacculus fragment with the mature external surface facing upwards (blue arrow) and sacculus with the internal surface facing upwards (yellow arrow); d) Zoom from 'c' showing a randomly orientated mesh structure; e) Finer architecture of internal surface, same scale as 'd', zoom image from Inset, white box; f) Zoom image from 'e' (blue dashed box).

Figure 6.3 a shows the same sacculus fragment as in Figure 6.2 d in liquid environment where the concentric rings are more defined. This corresponds to the nascent external CW architecture. Figure 6.3 b shows a sacculus fragment keeping partial integrity of the cylinder body, with the external surface above (EXT) and the internal surface underneath (IN). It can be appreciated that, similarly to *S. aureus*, the external surface is rougher than the internal which looks smoother at large scans ($\sim 2 \mu\text{m}$). Sacculi fragments with only a single layer attached to the surface were used to study these architectures in more detail without any displacements between the layers that could affect the interpretation of the results. Figure 6.3 c shows two sacculi fragments, one with the external surface upwards (blue arrow) and the other with the internal surface upwards (yellow arrow). The finer architecture of the external mature CW is very similar to *S. aureus*: it is a highly porous mesh where glycan strands are randomly orientated (see Figure 6.3 d). In contrast, the internal CW architecture is a much smaller mesh with oriented glycan strands along the short axis of the rod (see Figure 6.3 e and f).

All structures identified in liquid environment are the same as in *S. aureus*, except for the internal architecture. In *S. aureus*, as shown in section 4.4.3 and Figure 4.18 a-d, the internal glycan strands are randomly orientated. However, from the images shown in Figure 6.3, the glycan strands on the internal surface of *B. subtilis* seem to be orientated along the short axis. The same quantitative analysis developed in section 4.4.3 and Figure 4.17 to determine strand orientation was applied to several images of *B. subtilis* internal surface. All the available results are summarized below in Figure 6.4.

Figure 6.4 shows four molecular resolution images of the internal surface of *B. subtilis* and their corresponding orientation analysis. Figure 6.4 a is a zoom from another area of Figure 6.3 e. Figure 6.4 b(i) shows a manually drawn skeletonized version of the image from Figure 6.4 a performed with the same criteria as in section 4.4.3 Figure 6.4 b(ii) shows the proportion of automatically detected lines by the custom made MATLAB code (in green) and the lines that the program is unable to detect (in white). Figure 6.4 b(iii) shows the outcome from the program: a distribution of different orientations of the lines plotted with the Rose function. The red dashed line indicates the short axis direction according to the orientation of this sacculus fragment (see Inset from Figure 6.3 e). Figure 6.4 c to h show more examples of different sacculi fragments, all analysed in the same way as Figure 6.4 a. All the rose distribution plots show a strong correlation between the most probable orientation of the glycan strands (the biggest rose area) with the corresponding short axis for each sacculus (red or white dashed line).

The images from Figure 6.4 c to h were analysed with permission from other researchers in the group: Dr Sandip Kumar and Dr Robert Turner. This was part of a long term collaboration to produce a collaborative manuscript. [13] The fact that the results obtained by three different researchers are all in agreement, provides stronger proof that the internal glycan strands of *B. subtilis* are oriented along the short axis of the rod. This conclusion is in agreement with the cable-like structure from the previous published work, which were also oriented along the short axis of the rod. [1] Although it was not possible due to the time frame of this Thesis, a correlation experiment between dry and wet environment would be necessary in the future to correlate the cable-like structure with the ordered strands.

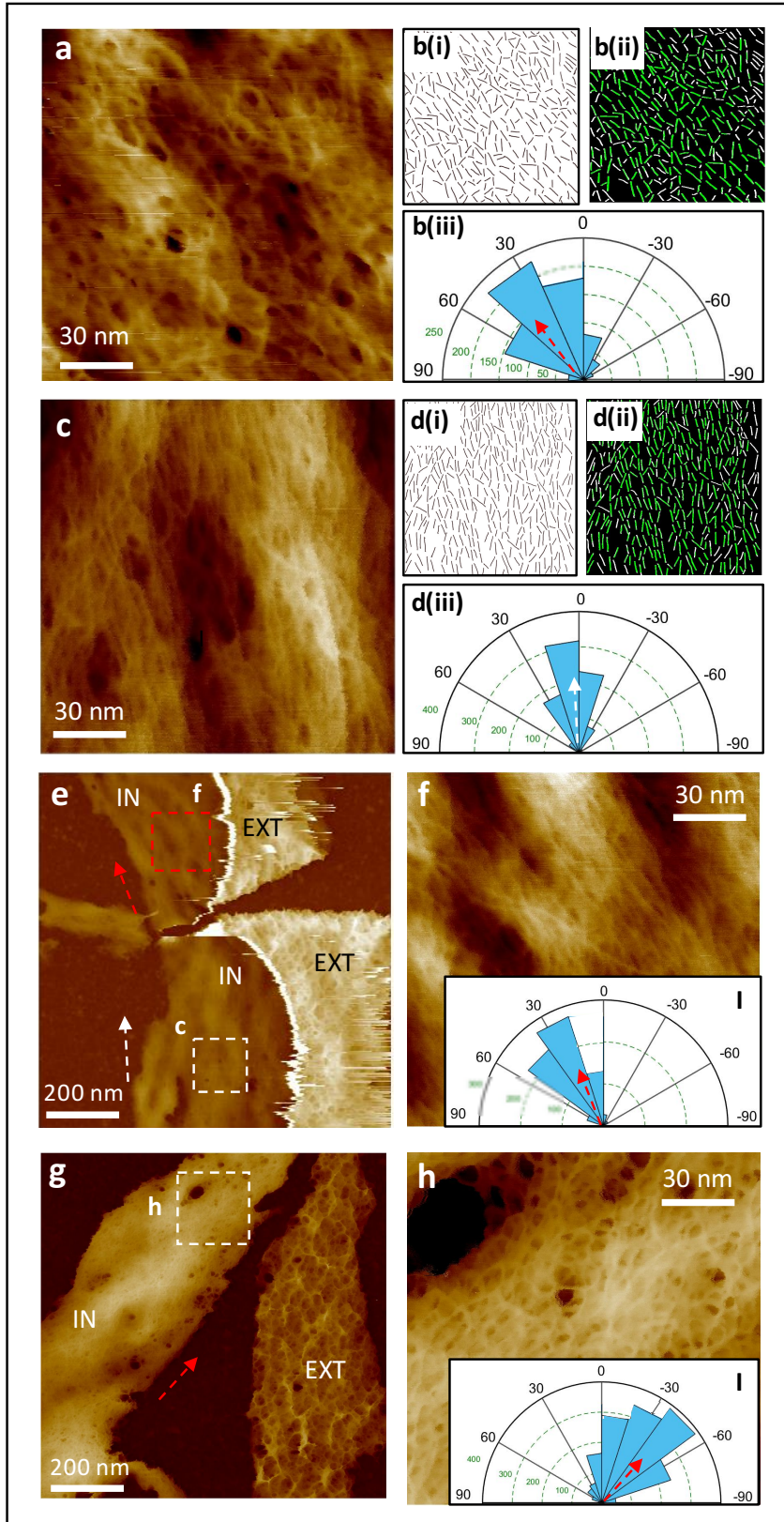


Figure 6.4 – a) Zoomed image from another region of 'Figure 6.3 e'; b) Strand orientation analysis of 'a', (i) manually drawn skeletonized version of the image, (ii) green: automatically detected lines by the custom made MATLAB code, (iii) Rose of the orientation distribution of the detected lines; c) Zoomed image from 'e' white box; d) Strand orientation analysis of 'c'; e) Two sacculi fragments with internal (IN) and external (EXT) surface showing; f) Zoomed image from 'e' red box, Inset: orientation analysis distribution; g-h) More examples.

6.1.3 The Septum

In this section the PG architecture of the septum (division plate) will be studied in different environments. In the previous work, [1] they imaged several dried septa at different stages of division, the results can be found below in *Figure 6.5*.

Figure 6.5 shows a series phase channel AFM images from different septa. They are ordered from A to H according to their stage in the cell cycle, because their aperture decreases in size. Complex structures of ridges, rings and striations were observed and described to be an important part of the division process.

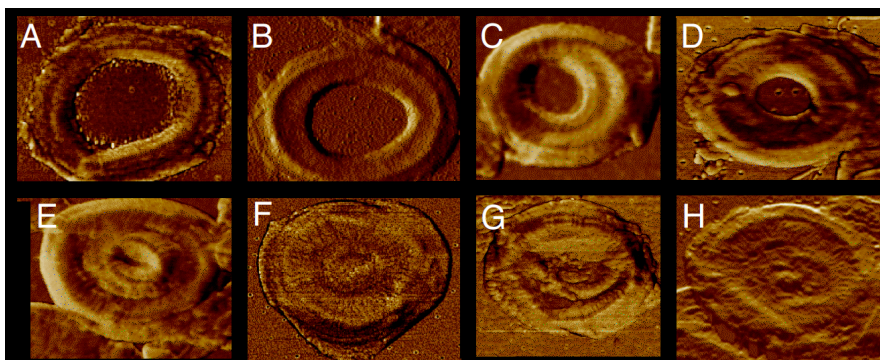


Figure 6.5 – Series of AFM phase images from B. subtilis septa. Adapted from permission [1]

6.1.3.1 Air to Liquid structural correlation

Studying the septum architecture in liquid mimics better the cellular native environment. Three septa were imaged in both liquid and dry environments to correlate the results with the previous published data. [1] See *Figure 6.6*.

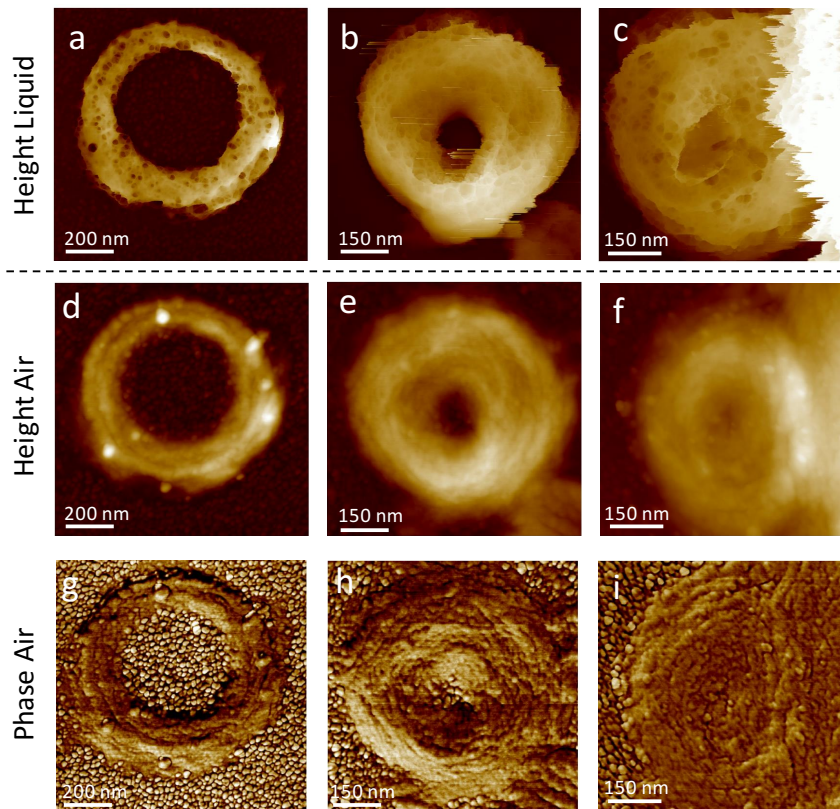


Figure 6.6 – a-c) series of septa from newest to oldest age on the cell cycle imaged in liquid; d-f) same images in air; g-i) corresponding phase images from ‘d-f’.

Figure 6.6 shows a direct liquid to air correlation from three representative septa. The liquid images (from a to c) were performed under liquid with PeakForce™ Tapping™. The PG architecture of septa in liquid resembles more the mature porous mesh than the complex ridged structure previously found. [1] The correlation with the images in air is similar to the results found in *S. aureus* (see section 3.5.3.2). The mesh when dried transforms into ‘knobbles’. Figure 6.6 d-e show some ridges and striations, but these are drying artefacts not present in the native architecture of the septa. The phase images from these same septa (see Figure 6.6 g-i) show similar features visible in the height channel in air. In contrast, the work published before [1] presented the phase channel because the height channel did not provide enough details. This makes us think that the AFM parameters such as the force exerted while imaging must be different between the two experiments causing the discrepancy in structure. The septa architecture was studied in more detailed, see Figure 6.7.

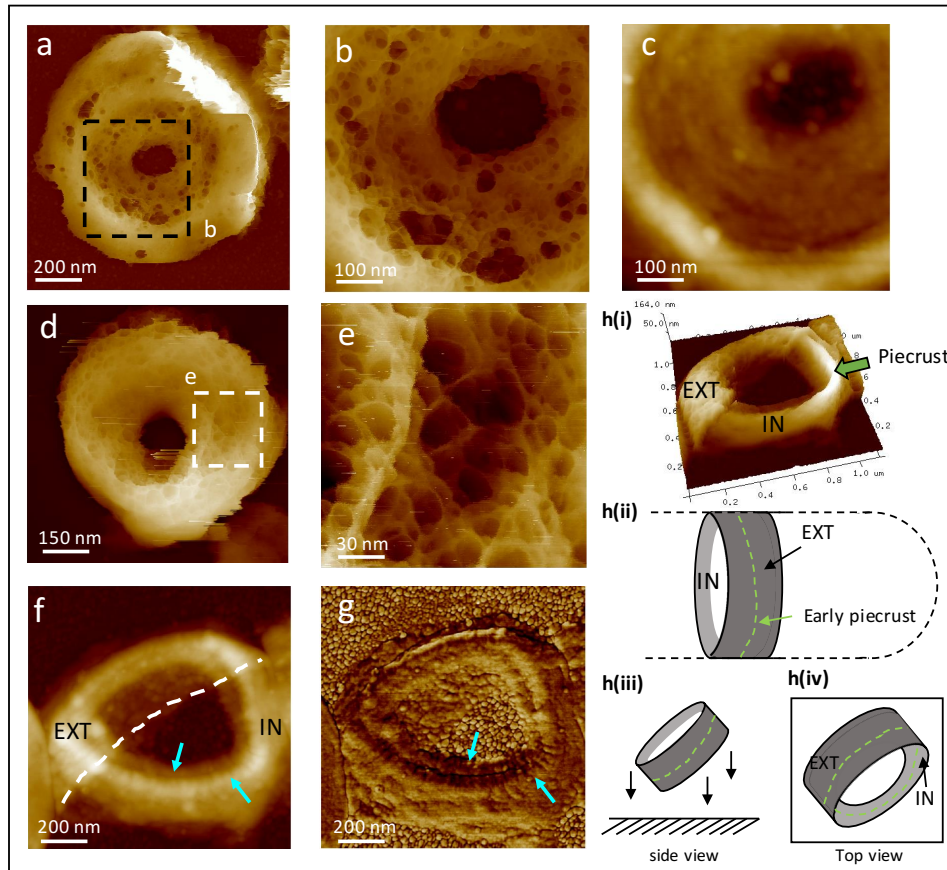


Figure 6.7 – a) Another example of semi-formed *B. subtilis* septa; b) Zoomed image from ‘a’; c) same region as ‘b’ in dry environment; d) Same septa as ‘Figure 6.6 b’; e) Zoomed image from ‘d’; f) Sacculus fragment from the cylinder rod area with the External (EXT) and internal (IN) areas marked, separated by a white dotted line; g) Phase channel from ‘f’ with the ridges highlighted (see blue arrows); h) i: three dimensional representation of ‘f’, green arrow shows the piecrust; ii-iv: schematics of one possible explanation for the conformation of this sacculi on the surface.

The images from Figure 6.6 and Figure 6.7 were performed under the same experimental conditions as Figure 6.3, detailed in Table 6.1 the parts corresponding to liquid imaging.

Figure 6.7 a and b show an incomplete septum with holes and random orientation mesh of fibres, Figure 6.7 c is the same area as Figure 6.7 b imaged in a dry environment, no ridges or other features are visualized that resembles the previous published work. [1] The visible features in the height channel are *knobbles* oriented in concentric rings. Figure 6.7 d is the same image as Figure 6.6 b and 6.7 e is a zoomed image showing a porous structure with randomly oriented glycan strands, corroborating Figure 6.7b was not an isolated case. Figure 6.7 f is a height image in air of what initially was thought to be another septum in early stages of the cell cycle like Figure 6.5 C. However, under a more careful examination of its structure and in the light of tens of other examples of sacculi fragments, it was suggested that this is a fragment of the cylinder rod area

containing a very early piecrust that has been folded with its external surface (EXT) partially over the internal (IN). *Figure 6.7 g* is the phase channel of the same fragment showing clearly some ordered pattern on the internal surface (see blue arrows) which do not appear on the EXT area. These might be created when the oriented glycan strands are under a dry environment. *Figure 6.7 h(i)* shows the three-dimensional representation of the same fragment imaged in liquid environment where it can be more clearly distinguished the external fragment folded over the internal smooth CW surface with a piecrust starting to form (see green arrow). *Figure 6.7 h(ii-iv)* is a schematic representation of what we suggest happened to this sacculi fragment, it was a part of the cylinder and then it has been placed on the surface in this exact positioning which lead to think, that both the INT and EXT were part of a septum. However, the early piecrust is not developed enough to classify this as part of the septal cycle. Moreover, the ridges and ribs from the septa published before, [1] could be caused due to high forces applied while imaging in tapping leading to the more complex architectures reported, which does not appear when hydrated or in other published work in air imaged under different parameters. [14]

In conclusion, *B. subtilis* septa have concentric rings structure that would be exposed on the external nascent CW of the two daughter cells. On the internal part of the septa the material is randomly orientated with big pores resembling the external mature surface. All the AFM images of unfinished septa show only the internal surface because the two future CWs do not split unless the septal plate is complete. This is the same phenomenon seen in *S. aureus* (see *Figures 4.11, 4.19*).

6.1.3.2 Septa pores morphology (back-filling)

Further analysis on the pores of the internal septal surface was necessary to better understand the mechanism of cell division in *B. subtilis*. Currently, there are different theories, the most widely accepted is the synthesis machinery led by the FtsZ treadmilling forming the Z-ring which creates a substrate for the PG synthesis enzymes. The Fts-Z has circular dynamics. Therefore, it has been proposed that this is the origin of the PG concentric rings architecture. [15], [16]

This is not contradictory with our results, because the concentric rings architecture has been seen in sacculi fragments, and we assume its synthesized in the external septal wall (see *Figure 4.16*). However, the CW synthesis on the internal septal wall must be regulated by another mechanism independent from the FtsZ dynamics because it does not have the concentric ring architecture. Based on the images showing a random orientated mesh with large pores (see *section 6.1.3.1*), the following was suggested: there is a synthesis machinery located at the edge of the septal plate together with another mechanism filling the pores afterwards. This has been proposed to be called *back-filling* mechanism. By analysing the area of these pores and their distance with respect to the leading edge it could elucidate more information into how this *back-filling* mechanism works.

Similarly to previous sections of this thesis, a new method of analysis was developed and optimized to obtain this specific data from all the available septa images. A combination of Fiji/Image J and MATLAB custom code was used to analyse each individual pore (the code is in *Appendix 1*). The outcome data set is composed of the area of each individual pore, the distance to the centre of the septa and the distance to the leading edge (see *Figure 6.8*).

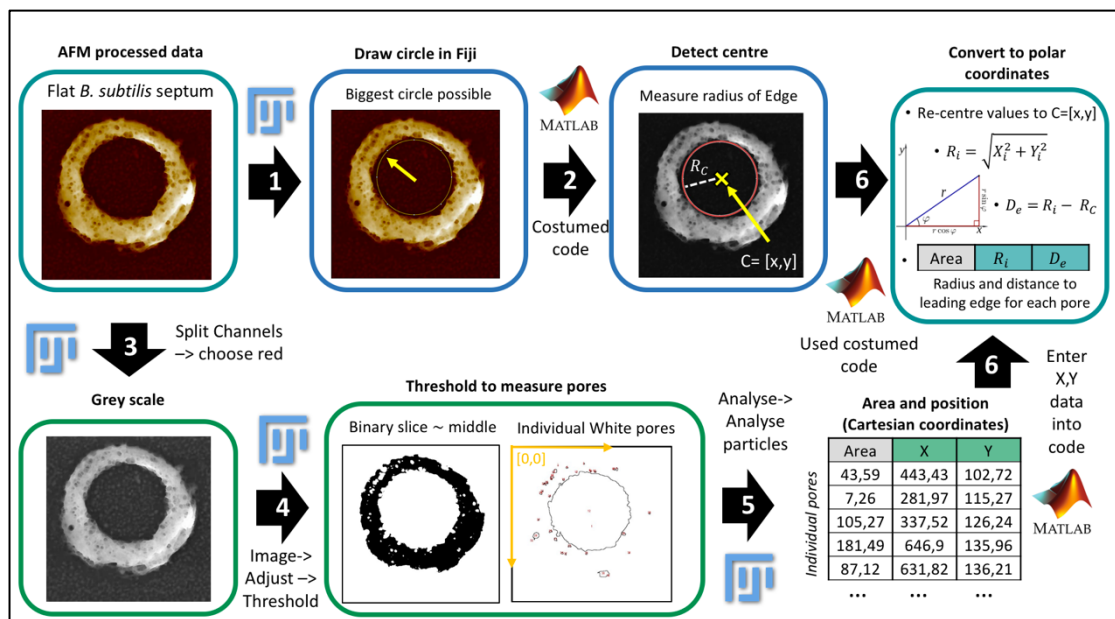


Figure 6.8 – Starting the method at the top left corner with the processed data from the AFM, Step 1: open image with Image J and draw the inner circle; Step 2: Enter the image into MATLAB code, measure Radius of the circle and its centre; Step 3: convert to Grey scale in Fiji; Step 4: threshold image; Step 5: Measure the pores in white and extract the Area and X,Y cartesian coordinates; Step 6: Enter the coordinates to the MATLAB code and return Radius and distance to edge.

Figure 6.8 shows step by step the optimized methodology to analyse the pores of the septa. Step 1 is using Fiji to draw the biggest perfect circle possible that fits the internal leading edge, the next step is to introduce this image into a custom MATLAB code that detects the centre of the circle and measure its radius. Step 3 is using Fiji to convert the AFM image into grey scale. Step 4 of the methodology is to convert the image in binary using a height threshold around the middle of the image (always trying to select the maximum number of pores possible). Step 5 is to use the 'Analyse particles' tool from Fiji which returns the area of each pore and its cartesian coordinates X and Y with respect to the centre (which is located at the left top corner of the image, see yellow arrows in step 4). The final step is to introduce the X,Y data into the program. The code recalculates each position with respect to the centre of the septum (C) while converting the values into polar coordinates to extract the radius (R_i). Finally, it calculates the distance to the leading edge (D_e) by subtracting the radius of the circle with respect to each value. The final data set obtained for each septum is the area, radius and distance to the leading edge for each individual pore.

A set of six septa images was analysed. They represent different stages of division with decreasing aperture size (see *Figure 6.9*). *Figure 6.9* shows the set of images ordered from the septum in the earliest stage of division (see *Figure 6.9 a*) to the latest (see *Figure 6.9 f*).

Images from *Figure 6.9 b-d and f* were taken in the JPK-Bio Nanowizard III and they were analysed with the JPK software by *Dr Raveen Tank*, this is the reason they have a different colour scale and flattening order. These images were included in the following analysis with her permission and this was a part of a long term collaboration to study the CW architecture of *B. subtilis* and it is part of the work in preparation. [17]

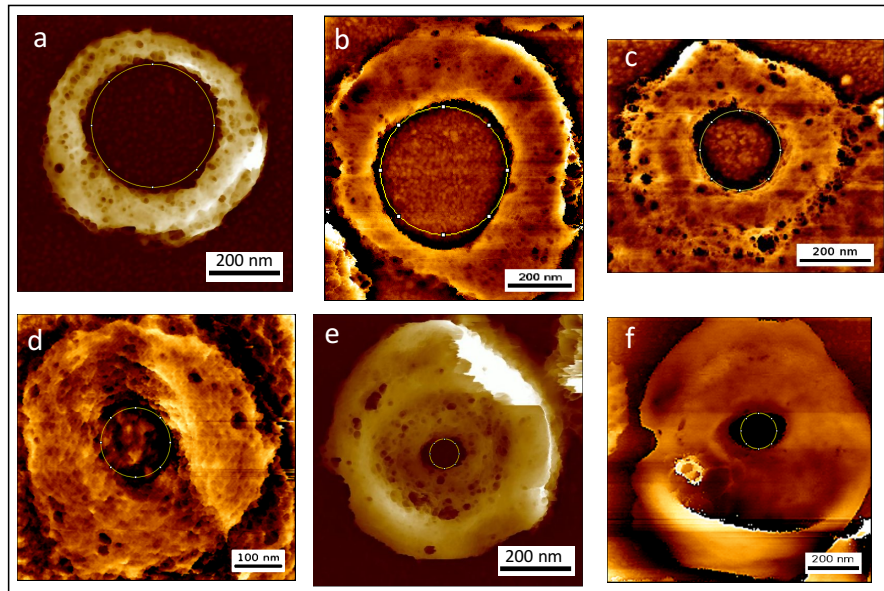


Figure 6.9 – Septa from *B. subtilis* at different stages of division. a-b) Earliest division stage; c-d) middle stage of division; e-f) late division stage; All septa have a circle drawn to determine their leading edge and centre.

The images from *Figure 6.9 a and e* were performed under the same experimental conditions as *Figure 6.3*, detailed in *Table 6.1* the parts corresponding to liquid imaging.

All the images from *Figure 6.9* were analysed following the protocol explained in *Figure 6.8*. The same process as shown in *Figure 6.9* and steps 1-2 from *Figure 6.8* was performed to measure the outer edge and the difference between the outer and the leading edge represents the septal thickness. Then the results were plotted in a two axis plot where the area of the individual pores is represented as the area of the spheres, the X axis is the radius from each pore to the centre (R_i) and the Y axis is the distance to the leading edge (D_e) summed to the septal thickness, see *Figure 6.10*.

Figure 6.10 shows the results for each septum. To interpret this graph, the spheres closer to zero in X axis represent individual pores closer to the centre of the septa on the images. The higher the spheres are in the Y axis it means they belong to a septum more advance in the cell cycle because their septal thickness is larger.

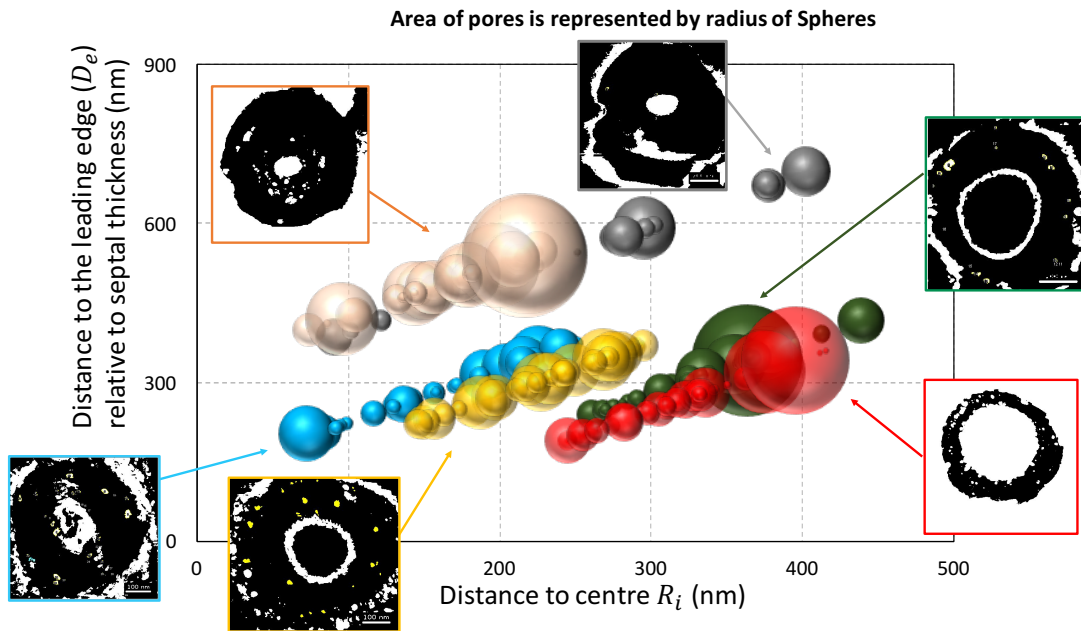


Figure 6.10– Three dimensional data set presented into a two dimensional plot (D_e versus R_i) and the size of the spheres is proportional to the area of the individual pores for each septa.

There are three differentiated groups of data. The red and green are the two septa on the early division stage (see Figure 6.9 a-b). Then, the blue and yellow data points are from the two septa at middle division stage (Figure 6.9 c-d). Finally the orange and grey data correspond to the septa at late division stage. The reason why the data is grouped like this is because the Y axis contains the distance to the leading edge from each individual pore together with the septal thickness to help visualize the data more clearly. However, X axis also helps distributing the groups of data on the x axis according to their division stage. Because in early stages all the pores are far away from the centre, while on the late division stage they cover all the range of material from one edge to the other. Contrary to what we expected, the *back-filling* mechanism does not work according to the age of the septum, because one would expect less pores to be found at bigger distances from the centre and the leading edge as the age of the septa progresses. However, from the limited data available analysed in Figure 6.10 ($n=6$ images), pores still to be filled are located randomly across the septal plate, during all division stages. Therefore, the leading edge does not govern the *back-filling* mechanism. In contrast to the FtsZ dynamics, the *back-filling* synthesis mechanism more likely acts randomly across the septa by filling different size pores that were left behind during the majority of the synthesis on the leading edge of the septa.

In conclusion, understanding how this machinery detects the position of the pores, will require the study of different strains with key mutations. Moreover, increasing the data set is necessary, because the current set of $n=6$ septa is not enough to extract strong statistical conclusions. Finally, the main difference between the septum architecture of *B. subtilis* and *S. aureus* is the size of the internal mesh, *B. subtilis* has much bigger pores than *S. aureus* septa, given that higher resolution was necessary in *S. aureus* to visualize the mesh while in *B. subtilis* at lower magnifications the pores of the mesh were visible.

6.1.4 Hydrogel behaviour

The hydrogel behaviour of the *B. subtilis* purified peptidoglycan was tested by measuring the thickness of PG single layers on air and liquid environments. The same methodology was used as in section 3.5.3.3. However, only the stock A sample was used (containing WTA). See Figure 6.11 for examples of the measurements and the results obtained for $n=19$ different sacculi.

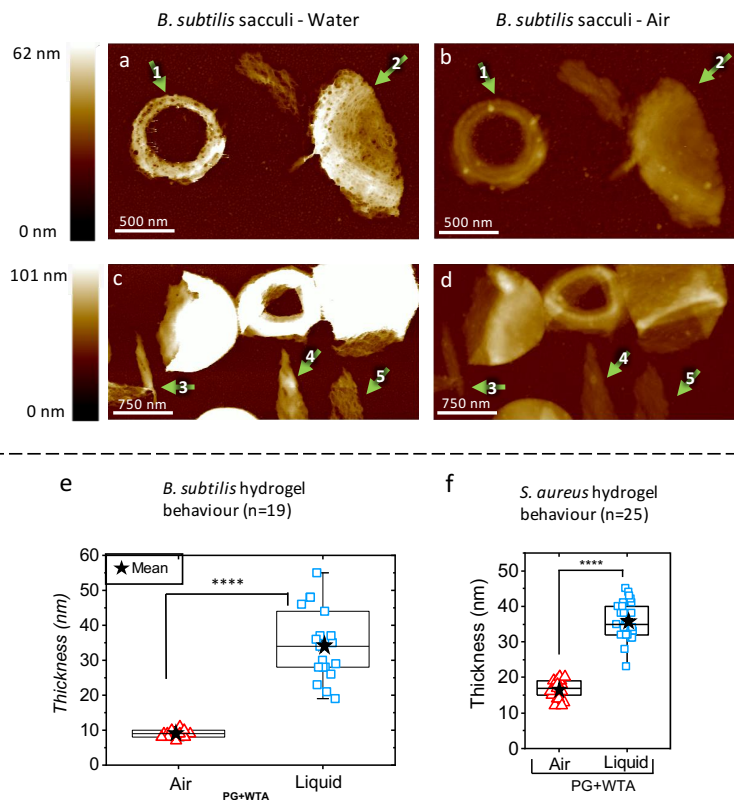


Figure 6.11 – a) Two sacculi fragments (1 and 2) imaged in liquid; b) same sacculi (1 and 2) imaged in air, at same data scale as in liquid DS = 62 nm; c) three more examples of single layer sacculi imaged in liquid (3 to 5); d) same examples (3 to 5) imaged in air and presented in the same scale as in liquid DS = 101 nm; e) Graph plotting the thickness measured of each individual sacculi ($n=19$) in air and liquid environment and their significant difference; f) *S. aureus* graph from Figure 3.18 b, PG+WTA

The images from *Figure 6.11* were performed under the same experimental conditions as *Figure 6.3*, detailed in *Table 6.1*.

Figure 6.11 shows examples of 5 different single layer sacculi marked with numbers (1-5) imaged both in air and liquid. Their thickness was measured by fitting Gaussian functions to the height distribution peaks obtained from the Gwyddion tool 'calculate 1D statistical functions' (see *section 3.5.3.3* and *Figure 3.18*). A total set of $n=19$ sacculi were measured in both environments, then plotted by groups in *Figure 6.11 e*. The mean value for the air measurements is 9 ± 1 nm (mean \pm s.d.); of thickness and for the liquid measurements is 34 ± 10 nm of thickness. The groups show a significant difference, after a two-tailed paired t test was performed with $t = 11$, $DF = 18$ and $p = 1.2 \times 10^{-9}$. The *B. subtilis* sacculi has an increase of thickness when hydrated of approximately **74%** which is bigger than in *S. aureus* with a **47%** increase. This indicates that the PG architecture of *B. subtilis* allows for bigger deformation most likely due to a lower cross-link proportion and longer GCL than *S. aureus*, as previously reported. [18]–[21]

6.2 *Bacillus subtilis* wild type living cells

After describing PG architecture of *B. subtilis* sacculi, the architecture of the CW in its native environment was further studied. *B. subtilis* living cells were imaged with AFM for the first time by a former member of our group, Dr Jonathan Burns, who obtained a small data set. [11] In this project, the same experimental protocol was followed to expand the data set of the mature external CW architecture on living *B. subtilis* cells. Moreover, the architecture of nascent CW is explored for the first time. Once the external CW architecture of healthy cells is determined, the nanometric effect on the peptidoglycan structure caused by damaging environments such as critical levels of SDS was studied.

6.2.1 External mature cell wall

First, the same protocol used before [11] was repeated to increase the data set of external mature CW images. Exponential phase cells were grown up to an $OD_{600}=0.2-0.4$, then a pellet was washed several times in the imaging buffer: 5 mM Tris pH=7.8. Then, the cell suspension was incubated for 1h onto a Cell-Tak coated mica. Finally, the excess of cells were extensively washed and the cells were imaged with AFM using small

amplitude Tapping mode [11], [22]. For more details of the sample preparation protocol see *section 2.3.3.3*. Similarly to *S. aureus* cells, the best imaging mode is soft Tapping mode which overcomes the high curvature at the edges of the bacteria. *B. subtilis* cells were directly attached to a flat surface without the need of grids because, due to their *rod*-shape, the cells have a bigger surface area than *cocci*-shaped *S. aureus* cells. The best results of *B. subtilis* external mature CW images are presented below in *Figure 6.12*.

Figure 6.12 a shows two cells in the middle of their division cycle, a fissure in the CW shows the division site (green arrow) between the two daughter cells. The majority of the surface of the daughter cells is covered by the cylindrical body (white arrows) with the oldest poles in opposite sides of the bacteria (dashed white box). This image was kindly provided by Dr Jonathan Burns and it was used for this publication. [13] *Figure 6.12 b* is an image from the new data-set showing an area close to a pole, with a rough topography. *Figure 6.12 c* is a phase channel image from another cell showing the topographic features of the CW external surface. *Figure 6.12 d* is a zoomed image from *Figure 6.12 b* and it clearly shows a porous mesh with randomly oriented fibres. The resolution was enough to visualize individual glycan strands of 1-2 nm (white arrows). Bigger fibres formed by two or three glycan strands are also visualized (blue arrows). *Figure 6.12 e* is a zoomed image from *Figure 6.12 c*, this magnification allows the visualization of bundles formed by more than three glycans together (green arrow). To verify that all the cylinder body had a mature mesh structure, a series of correlative images was taken by Dr Jonathan Burns along the same cell (see *Figure 6.12 f to j*), adapted from [11].

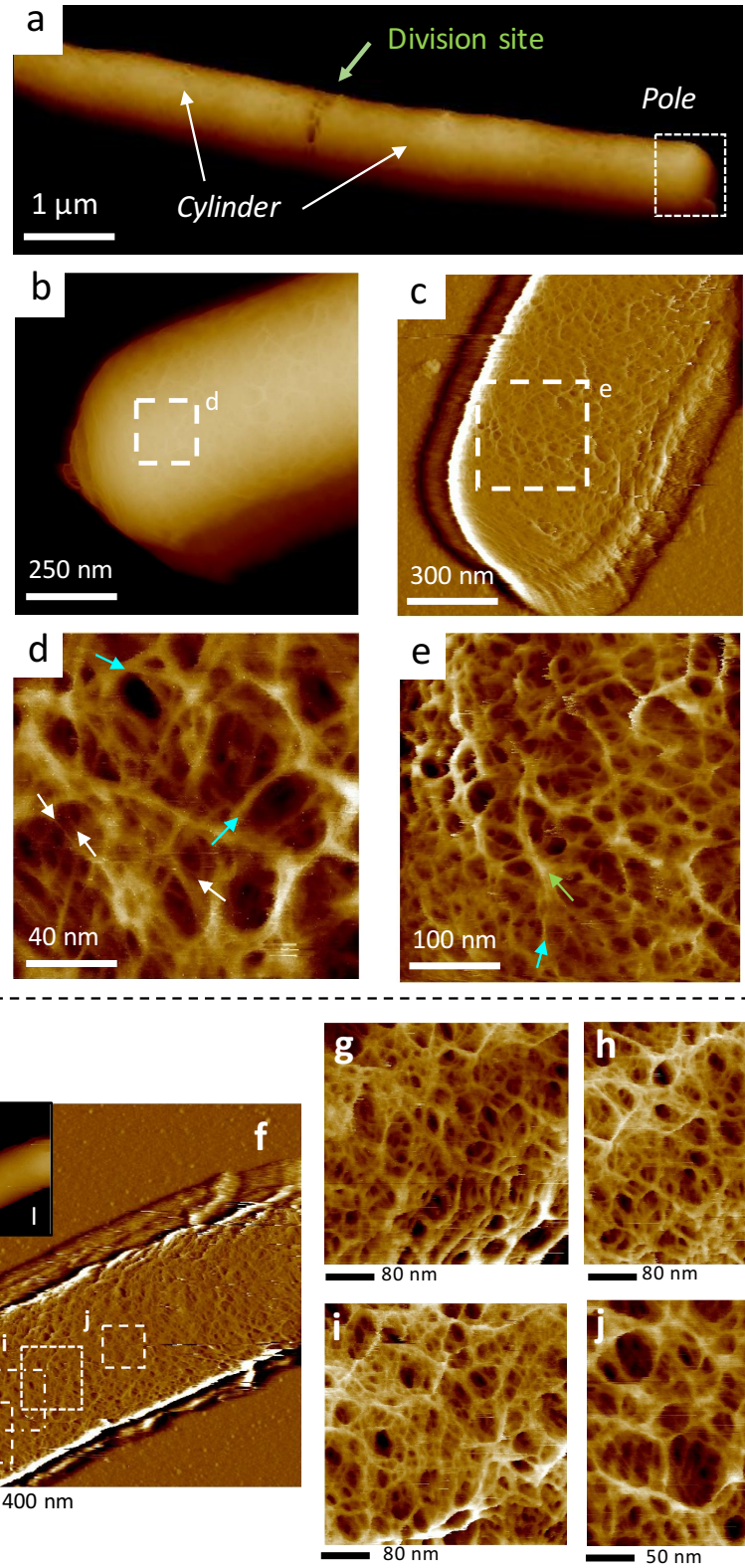


Figure 6.12 – a) Low magnification of two *B. subtilis* cells recently divided; b) Height image near the pole of exponential phase cell; c) another example of pole (phase channel); d) Zoomed image from ‘b’ showing the finer architecture of mature CW; e) Zoomed image from ‘c’ of another area of mature mesh; f) Phase image of section of cylinder of *B. subtilis* cell, Inset (l): Height channel; g-j) Zoomed image from ‘f’; Images a and f-j adapted from [11]

The images from Figure 6.12 were performed under the experimental conditions summarized in Table 6.2.

Table 6.2 – Experimental conditions used to obtain data from Figure 6.12. See section 2.3.3.3.

AFM TYPE	AFM TIP	AFM MODE	SAMPLE TYPE	BUFFER/ ENVIRONMENT	SURFACE	SPECIFIC CONDITIONS
BRUKER FAST SCAN	Fast Scan - D	Small amplitude Tapping	<i>B. subtilis</i> WT cells O.D. = 0.6	5 mM Tris at pH = 7.8	Cell-Tak coated MICA	1h incubation then rinsed

6.2.1.1 Fibre width measurements

A quantitative analysis of the different fibre widths from the external mature CW of *B. subtilis* was performed. The same approach was taken as in section 3.5.4.1 measuring the **FWHM** as explained in Figure 3.20. The best two images were used for this analysis, the same image shown in Figure 6.12 d and another image kindly provided by Dr Sandip Kumar as part of a collaboration. [13] The individual location of the fibres analysed in both images are presented below in Figure 6.13.

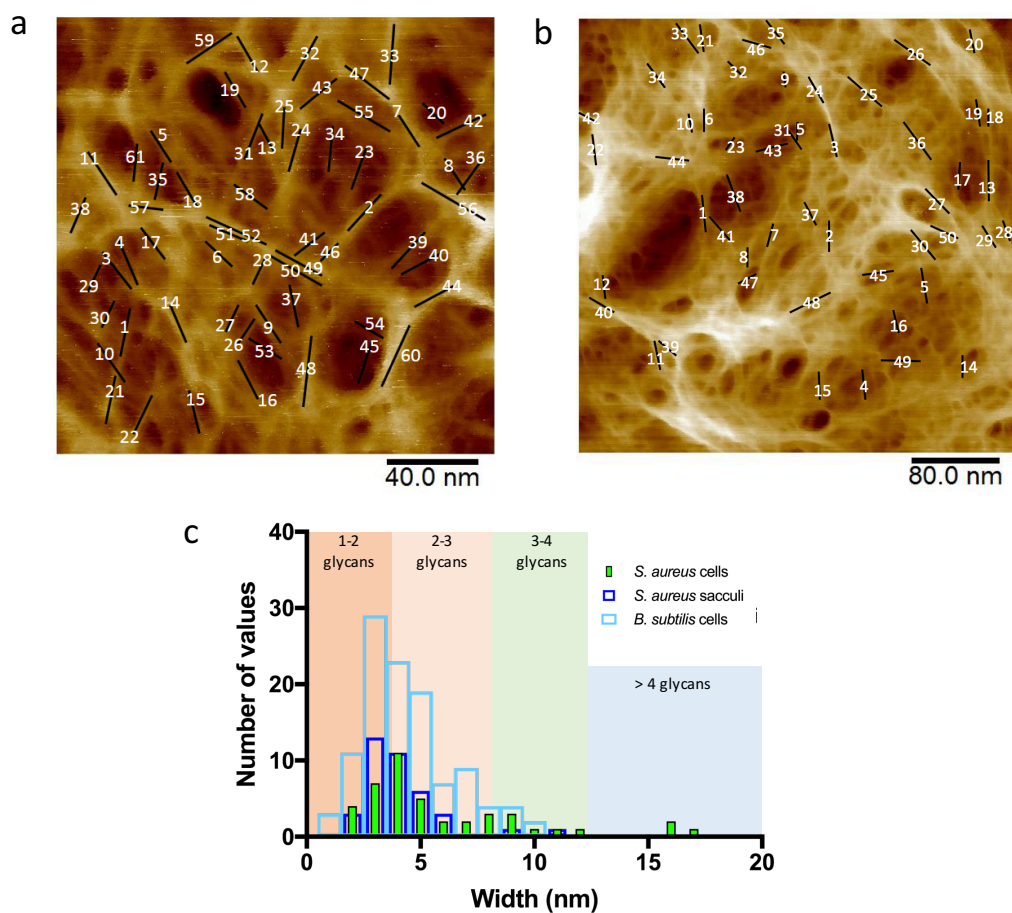


Figure 6.13 – a) Same image as Figure 6.12 d with fibres from 1-60 numbered (white numbers) and marked the position of the fibres (black lines); b) Another image with bigger magnification with fibres from 1-50 numbered and marked; c) histogram presenting all the results from *S. aureus* cells (green), sacculi (dark blue) together with *B. subtilis* cells (cyan blue).

Figure 6.13 a-b show two images of mature external CW where the fibres were numerated. For each fibre, three different profiles were taken and the FWHM was calculated. Then, a geometric mean was performed with each set of three measurements and all the means were joined together in the histogram. This non-normal distribution has a mean value with the standard deviation of 4.15 ± 1.9 nm for *B. subtilis* cells (cyan blue). The distribution is very similar to the sacculi from *S. aureus*. The maximum width found on *B. subtilis* fibres was around 10 nm, while in *S. aureus* cells it was 17 nm. This indicates that although most of the fibres species correspond to 1-2 glycan and 2-3 glycans some bundles are formed by more than three glycans together, but no species were found formed by more than four glycans. There is no statistical significant for the median values from the different samples analysed in this work, see the summarized values from Figure 3.21 and 6.13 in Table 6.3.

Table 6.3 – Fibre width median and standard deviation from three different data sets analysed in Chapter 3 and 6. Living *S. aureus* (n=43) fibres; *S. aureus* sacculi (n=38) and Living *B. subtilis* (n=111).

	Living <i>S. aureus</i> cells	<i>S. aureus</i> purified PG	Living <i>B. subtilis</i> cells
Fibre width	4.5 ± 3.8 nm	3.6 ± 1.9 nm	4.15 ± 1.9 nm

It is already known from other experiments [1], [23] that the glycan chain length (GCL) is very different for these Gram-positive species: *B. subtilis* has glycans up to 5 µm long, while *S. aureus* has much shorter glycans. Thus, our results showing a similarity in fibre width is striking. This could link to commonalities in the mechanism of synthesis and hydrolysis of these two species of bacteria, because their fibre agglomeration in the mature external surface of the CW is very similar despite their different GCL. [20], [21]

6.2.1.2 Improved quantitative characterization of pores

Another aspect of the mature external CW architecture to be analysed is the morphological characteristics of the pores. The two-dimensional sectioning analysis generating 2D and 3D depth maps developed on sections 3.5.4.2 and 3.5.4.3 were applied with the data set of *B. subtilis*. The results are summarized in Figure 6.14. Figure 6.14 a-b show the direct comparison of 2D depth maps from *B. subtilis* and *S. aureus* respectively with the following colour scale: (blue=5 nm, green=10 nm, orange= 15 nm, purple=20 nm and white=23 nm). Figure 6.14 c-d show the 3D representation of the same depth maps using the Avizo™ program, using the same colour scale used for the

2D depth maps. *Figure 6.14 e-f* show a lateral YZ section marked with a red line on *Figure 6.14 a-b*, the black areas represent the pores and the grey regions the background. It can be clearly seen that the pores from *S. aureus* are deeper, arriving up to 23 nm, while the pores from *B. subtilis* only arrive at 15 nm of maximum depth. [13]

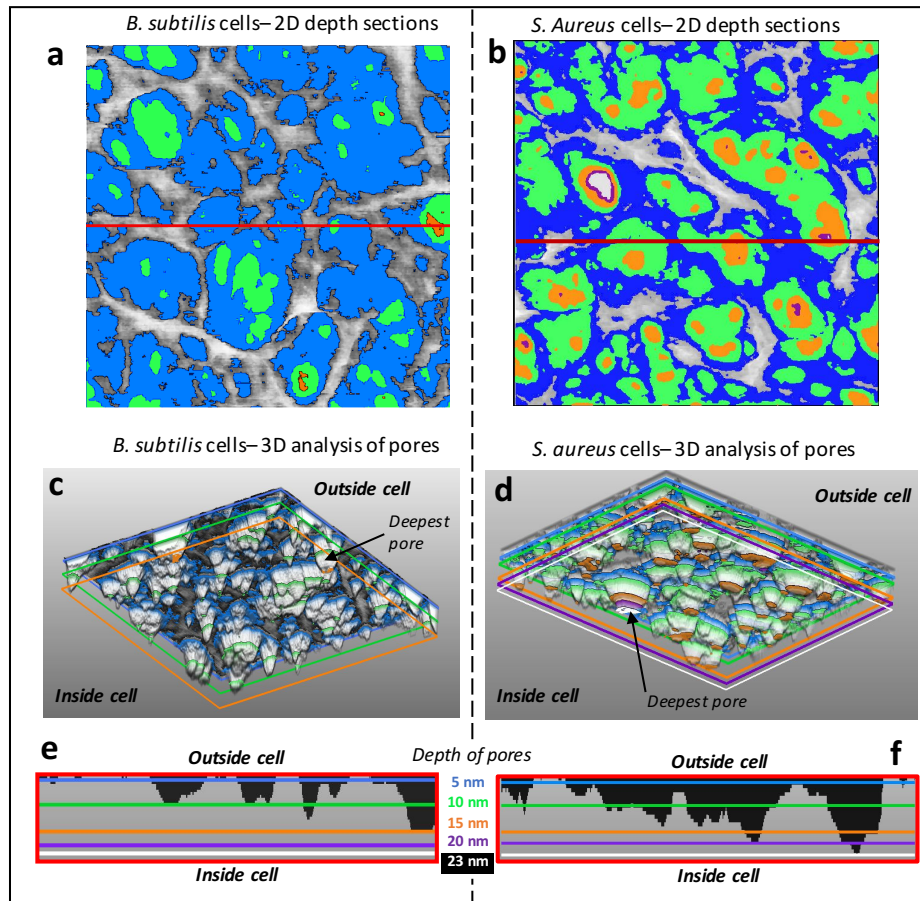


Figure 6.14– a) 2D depth sections of B. subtilis cells; b) Same analysis as ‘a’ of S. aureus cells; c-d) Corresponding 3D analysis of images ‘a-b’; e-f) lateral sections of red line from ‘a-b’.

This is not surprising, as from *Figure 6.11* the thickness of *B. subtilis* sacculi in air is only 11 nm while for *S. aureus* is 20 nm. For both, when hydrated, the sacculi increases in height 70 and 47% respectively. However, the thickness of the CW in its native state is neither of those values. The reason why the CW in the native state is different than the purified material is because of the tension caused by the turgor pressure from the internal contents of the cell. The turgor pressure must deform the CW in the Z axis altering its thickness with respect to the relaxed state that is the sacculi. From the Cryo-EM data published [24], [25] it is known that the CW thickness of living cells is 15 nm for *B. subtilis* and 25 nm for *S. aureus*. This agrees with the depth of the deepest pores for both species imaged by AFM.

Another characteristics of interest to compare with *S. aureus*, is the area of the pores. The analysis developed in *section 4.2.2* was applied to a set of images from the external surface of *B. subtilis* and no significant difference was found. The limitation of this analysis is the height threshold applied at 50% of the image. As shown in *Figure 6.14*, the two species have pores with a range of different depths. A new automated analysis was developed to study the area of the pores at different image depths, see *Figure 6.15*.

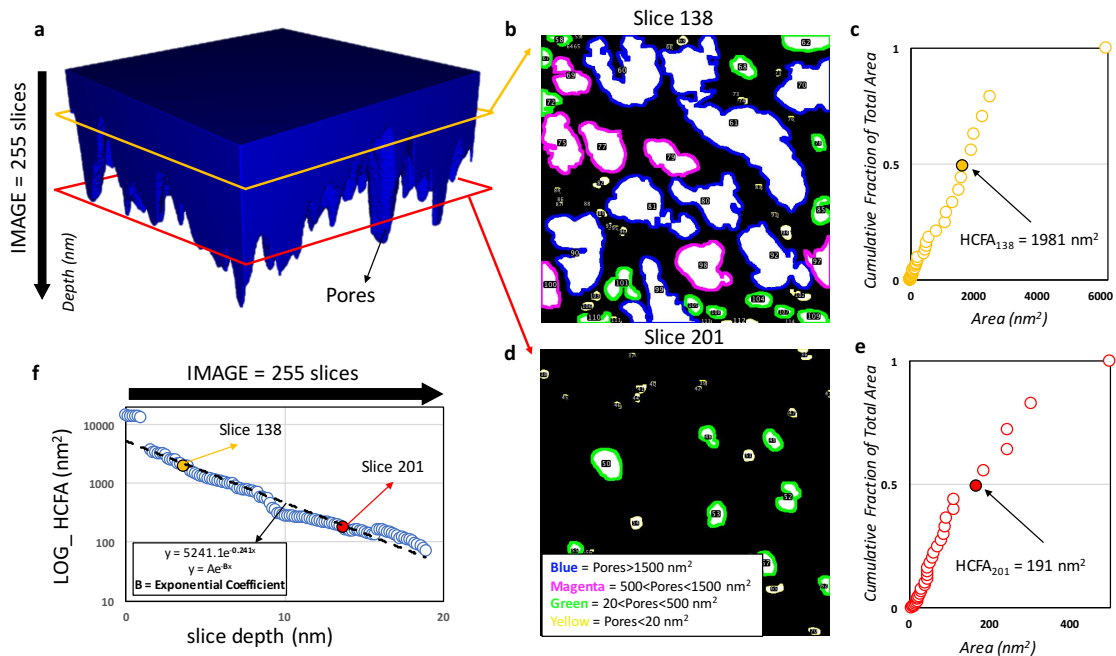


Figure 6.15 – a) Representation of what the code in Appendix 2 does, cutting the image in 255 binary slices, the three dimensional shape of the pores is in blue, the slice 138 and 201 are marked in yellow and red; b, d) Yellow and red slices from ‘a’ showing the pores in white and material in black. The pores are colour coded according to the legend in ‘d’; c, e) for each slice the program outputs the area of each pore, the cumulative fraction of total area versus the area is plotted for the yellow and red slices from ‘a’, the code also calculates the HCFA for each slice; f) All the HCFA values are plotted as a logarithm versus the slice depth, forming this exponentially decreasing HCFA curve

Instead of calculating the HCFA for one slice at a specific threshold, a new ImageJ/Fiji macro was written (see code in *Appendix 2*) which automatically divides each image in 255 binary slices (see *Figure 6.15 a*). This is the maximum number of slices Fiji can do for each image. For each slice, the macro analyses the area of the pores (white regions in *Figure 6.15 b, d*) and colour codes them by size. There are four size ranges: blue corresponds to pores bigger than 1500 nm²; magenta are pores between 500 and 1500 nm²; green are pores between 20 and 500 nm² and yellow corresponds to pores smaller than 20 nm². For each slice the HCFA is calculated (see *Figure 6.15 c, e*). Then, by plotting the logarithmic HCFA versus the slice depth a HCFA curve is obtained for each image.

These curves have a negative exponential trend from which the exponential coefficient can be obtained (see Figure 6.15 f).

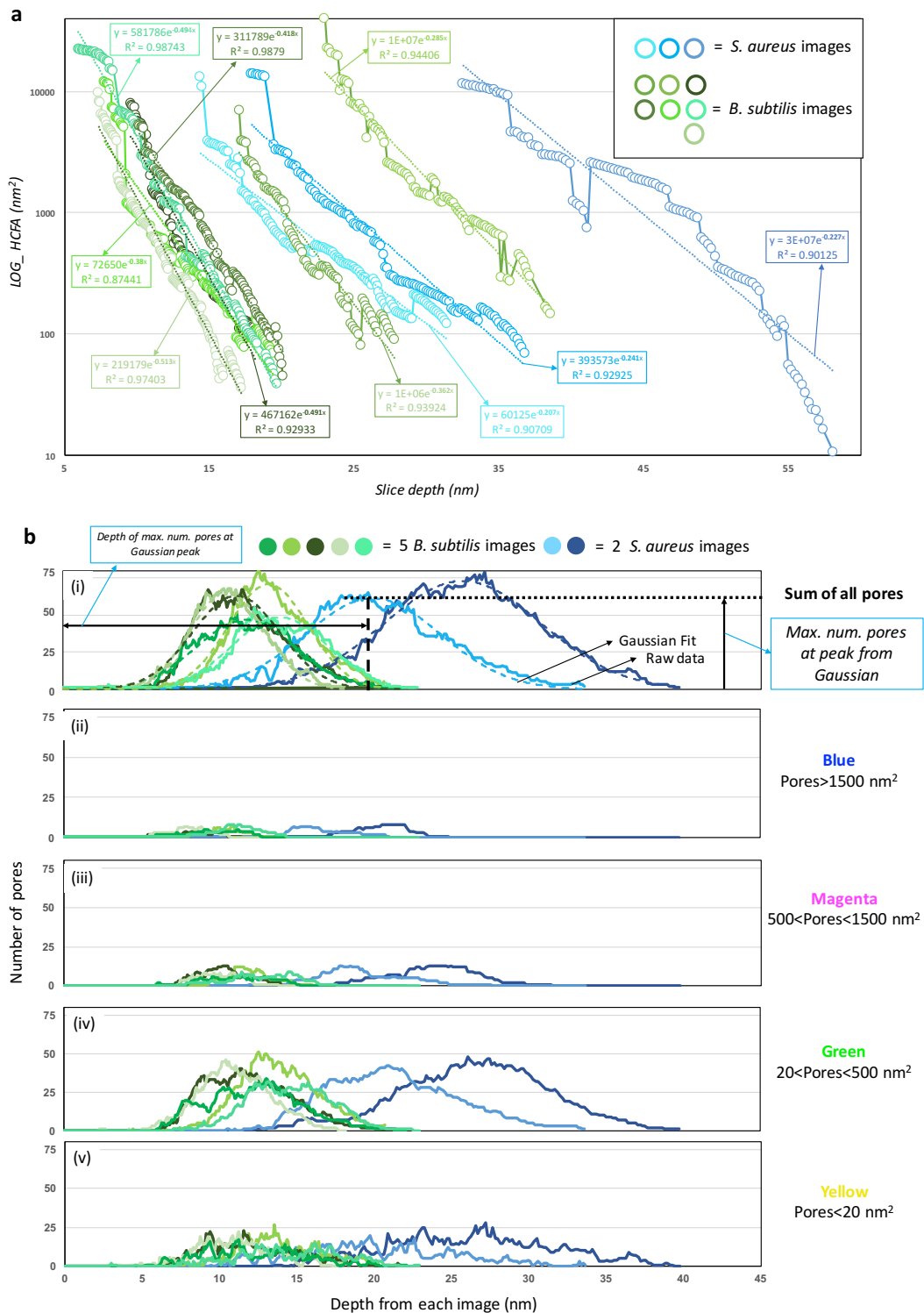


Figure 6.16 – a) Log_{10} HCFA curves for different *B. subtilis* images (the green curves) and three *S. aureus* images (blue curves), an exponential fitting and the R^2 are plotted as dotted lines for each curve; b) number of pores versus slice depth, there are five identical plots: (i) Total number of pores per each slice, where only *S. aureus* and *B. subtilis* images from the same size have been used, (ii) Blue pores, (iii) Magenta pores, (iv) Green pores and (v) Yellow pores (see all sizes in Figure)

Figure 6.16 show a direct comparison between mature external PG from *S. aureus* (n=3) and *B. subtilis* (n=7) cells. Figure 6.16 a shows the HCFA curves from individual images (*S. aureus* blue and *B. subtilis* green curves). Each curve has an exponential coefficient which indicates the rate of decreasing pore area as function of depth. The HCFA ranges for *B. subtilis* having between 143-9 nm across the image thickness, while for *S. aureus* is 127-9.2 nm. The macro also sorts the pores by size and counts them, resulting in number of pores versus depth plots (see Figure 6.16 b), only the same size images were analysed here, reducing the data set. The total number of pores plots can be fit to a gaussian curve (see Figure 6.16 b (i)). The number of pores can be split into the four size ranges (from blue to yellow) resulting in four plots (see Figure 6.16 b (ii-v)). For all the images analysed, the majority of the pores correspond to the green range, with an area between 20 and 500 nm² (see Figure 6.16 b (iv)).

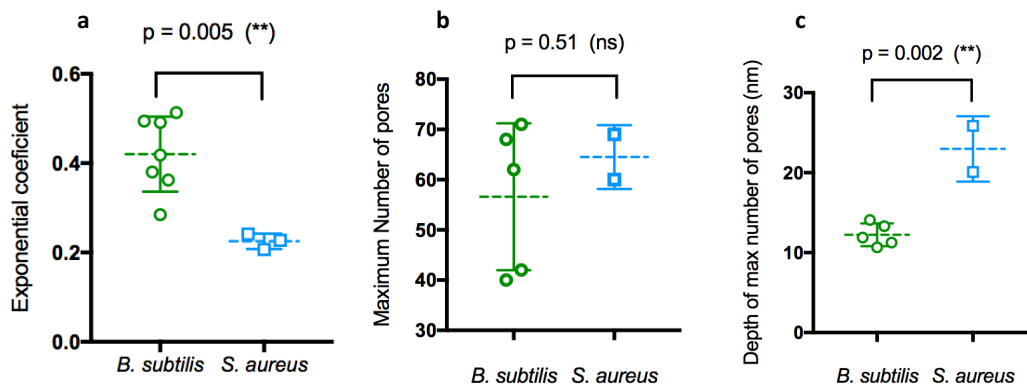


Figure 6.17 – Final comparison between *B. subtilis* and *S. aureus* for a) exponential coefficient of pore area versus depth; b) maximum number of pores; c) depth of the slice corresponding to the maximum number of pores.

All the plots extracted from the macro in Figure 6.16 contain too much information. In order to facilitate data interpretation, three crucial parameters were extracted from the plots: the exponential coefficient (from Figure 6.16 a), which is non-dependant from the image depth as corroborated with comparison between sacculi and live cells from *S. aureus* (see Appendix 3); the maximum number of pores (from the gaussian peak from the total number of pores, Figure 6.16 b (i)); and the slice depth corresponding to the maximum number of pores. Figure 6.17 summarizes these three parameters for both *B. subtilis* and *S. aureus* live cells, where each point corresponds to one image. The pores got smaller as function of slice depth, with an exponential coefficient of 0.42 for *B. subtilis* and 0.21 for *S. aureus* (see Figure 6.17 a). There was no statistical difference in the maximum number of pores for both species (Figure 6.17 b). The depth of the slice

containing the maximum number of pores was 12 nm for *B. subtilis* and 23 nm for *S. aureus*, which agrees with the depth analysis (see *Figure 6.14*). The mean HCFD from the slices containing the maximum number of pores are 34 nm for *B. subtilis* and 29 nm for *S. aureus*. This together with the HCFA ranges from *Figure 6.16 a* leads to conclude that *B. subtilis* has bigger but less deep pores than *S. aureus*.

6.2.2 External nascent cell wall

As mentioned above, the second objective of studying *B. subtilis* cells was to determine the architecture of the external nascent CW. It has been challenging to obtain this information due to this structure being located exclusively at the end of the poles of recently divided cells. There were unsuccessful efforts of imaging *B. subtilis* cells vertically, where the poles would be fully exposed to AFM imaging [11]. Therefore, a compromise was achieved by attaching *B. subtilis* cells to a flat surface, where the poles would only be partially exposed to AFM imaging.

The sample was prepared with the same methodology used to image external mature CW from living cells, see *section 2.3.3.3* for more details. See *Figure 6.18* for the initial results from this experiment, where the focus was on the poles.

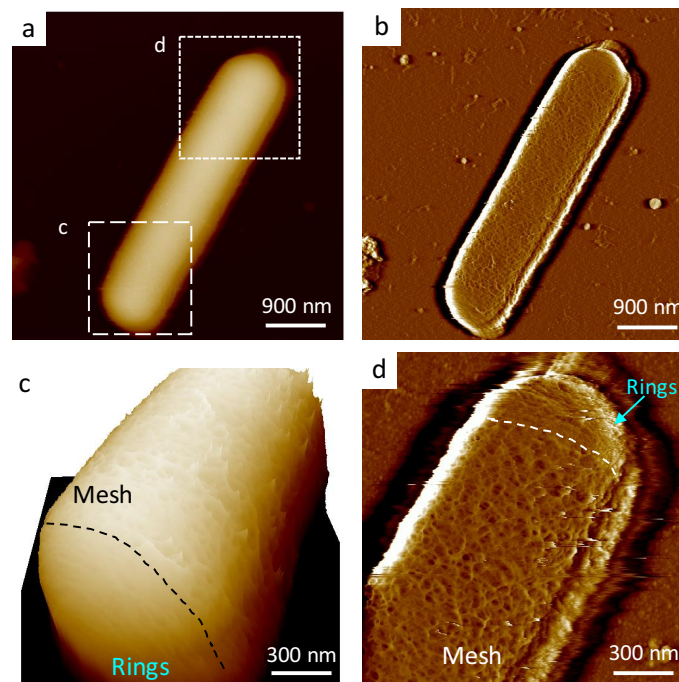


Figure 6.18 – a) Height image of a single *B. subtilis* cell attached to the surface; b) Phase channel from ‘a’; c) Bottom pole zoomed from ‘a’ see big dashed white box, two regions are distinguished on the 3D representation of the image: Mesh and Rings separated by a dashed black line; d) Top pole zoomed image from ‘a’ small dashed white box, Mesh and Rings separated by a dashed white line

Figure 6.18 a-b show height and phase images respectively of one single *B. subtilis* cell at low magnification. Figure 6.18 c shows the three dimensional height image with higher magnification of the bottom pole. There are two distinct regions separated by a black dashed line: the partial pole region with a smooth surface (i.e. concentric rings); and the rest of the cylinder of the cell with a rough architecture (i.e. mesh). Figure 6.18 d shows the phase image of the top pole from Figure 6.18 a with the two distinct regions separated by a white dashed line. To confirm that the nascent external material has concentric rings structure, higher magnification images were required, see Figure 6.19. The images from Figure 6.18 and Figure 6.19 were performed under the same experimental conditions as Figure 6.12, detailed in Table 6.2.

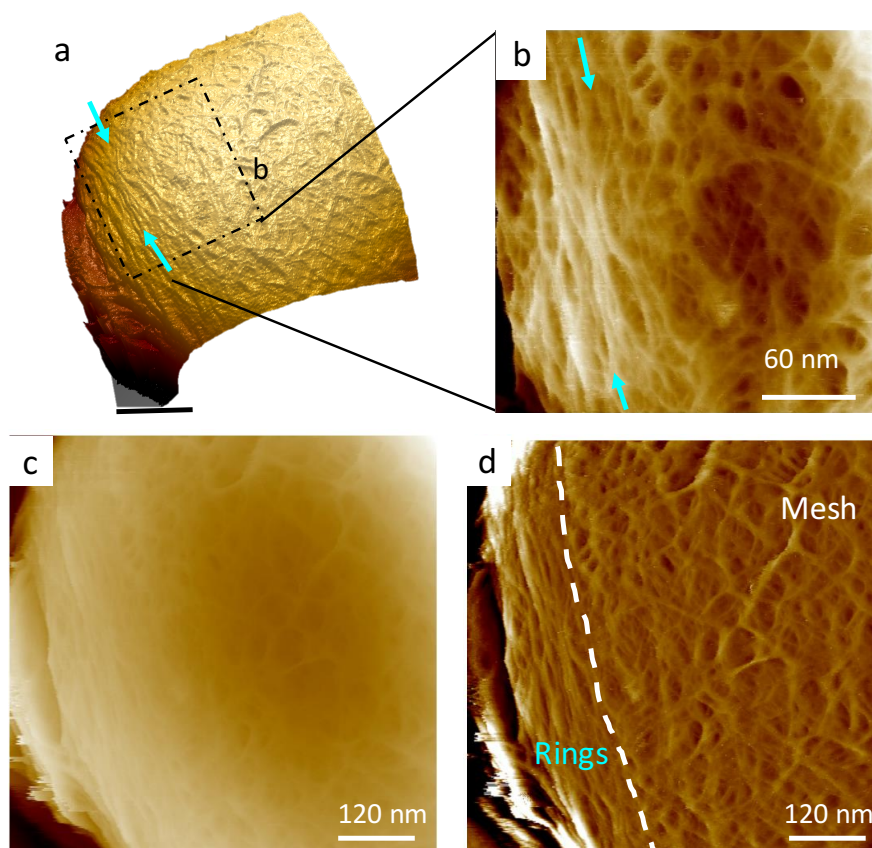


Figure 6.19 – a) Three-dimensional representation with mixed effect of the end of a pole; b) Zoomed image from ‘a’ where clearly the concentric rings are marked with blue arrows; c) Same image as ‘a’ from the height channel; d) same image as ‘c’ high-passed filtered where the region of Rings and Mesh is separated by white dotted line.

Figure 6.19 a shows the end of a pole with a three dimensional representation with mixed effect and lighting at the appropriate angle to highlight the edges of the concentric rings (blue arrows). Figure 6.19 b is a zoomed image from Figure 6.19 a showing different glycan orientation between the partial nascent pole on the left of the image with ordered parallel glycans (blue arrows) and the rest of the mature CW surface

with randomly orientated glycans. *Figure 6.19 d* is the same image as *Figure 6.19 a* but it has been high-passed filtered, where all the features are better highlighted, a manually drawn white dashed line separates the concentric rings area and the mature mesh area. To corroborate the rings are not an artefact from any of the image representations, see the raw data in *Figure 6.19 c*

In conclusion, the nascent external CW surface from *B. subtilis* shows concentric rings architecture, strikingly similar to *S. aureus*. It was previously thought, these two organisms would have completely different CW architectures, but robust data is showing the opposite.

6.2.3 SDS treatment of *Bacillus subtilis*

A set of experiments were designed to try to answer the following question: how does the PG organization of a living bacteria get altered if the turgor pressure of the bacteria is affected?

The chosen treatment was sodium dodecyl sulphate (SDS). It is well known that certain levels of SDS kill bacteria, this is why it is widely used as bacterial disinfectant. [26]

6.2.3.1 Killing dynamics of SDS at population level

Firstly, the effect of SDS was tested on a liquid culture of *B. subtilis*. *Figure 6.20* summarizes some of the steps during the performance of this experiment and the results from the OD₆₀₀ measurements. The first step is to grow a *B. subtilis* liquid cell culture overnight for 15 h. The next morning, the overnight was inoculated into fresh media with an initial OD₆₀₀=0.05 and grown up to OD₆₀₀~0.55 on 8 falcon tubes under constant shaking at 37 °C. This was considered time-point 0h and OD measurements and plates were taken (see *Figure 6.20 a* and *c*). Then the treatment of SDS was introduced at progressively decreasing percentages from 5% to 0.01% to tubes 2-8, with 1 being a control with no treatment. After 1h OD measurements and plates were made (see *Figure 6.20 d*). After 2h of treatment only OD measurements were made (see *Figure 6.20 b*). With these three time-points: 0h, 1h and 2h; an OD killing curve was produced for each sample (1-8), see the normalized plot in *Figure 6.20 e*. In parallel, to this experiment, from the same 8 tubes, 1 ml was extracted at time-point 0h from each tube and kept at room temperature without shaking for 1 h. Then, 5, 1, 0.1 and 0.01% SDS

concentrations were added to the 1 ml tubes. Next, 200 μ l of cell suspension were added to a glass coverslip (see *Figure 6.20 f*) and after 2h the total volume of sample was recovered from the glass coverslip and plated (see *section 2.2.1.7*).

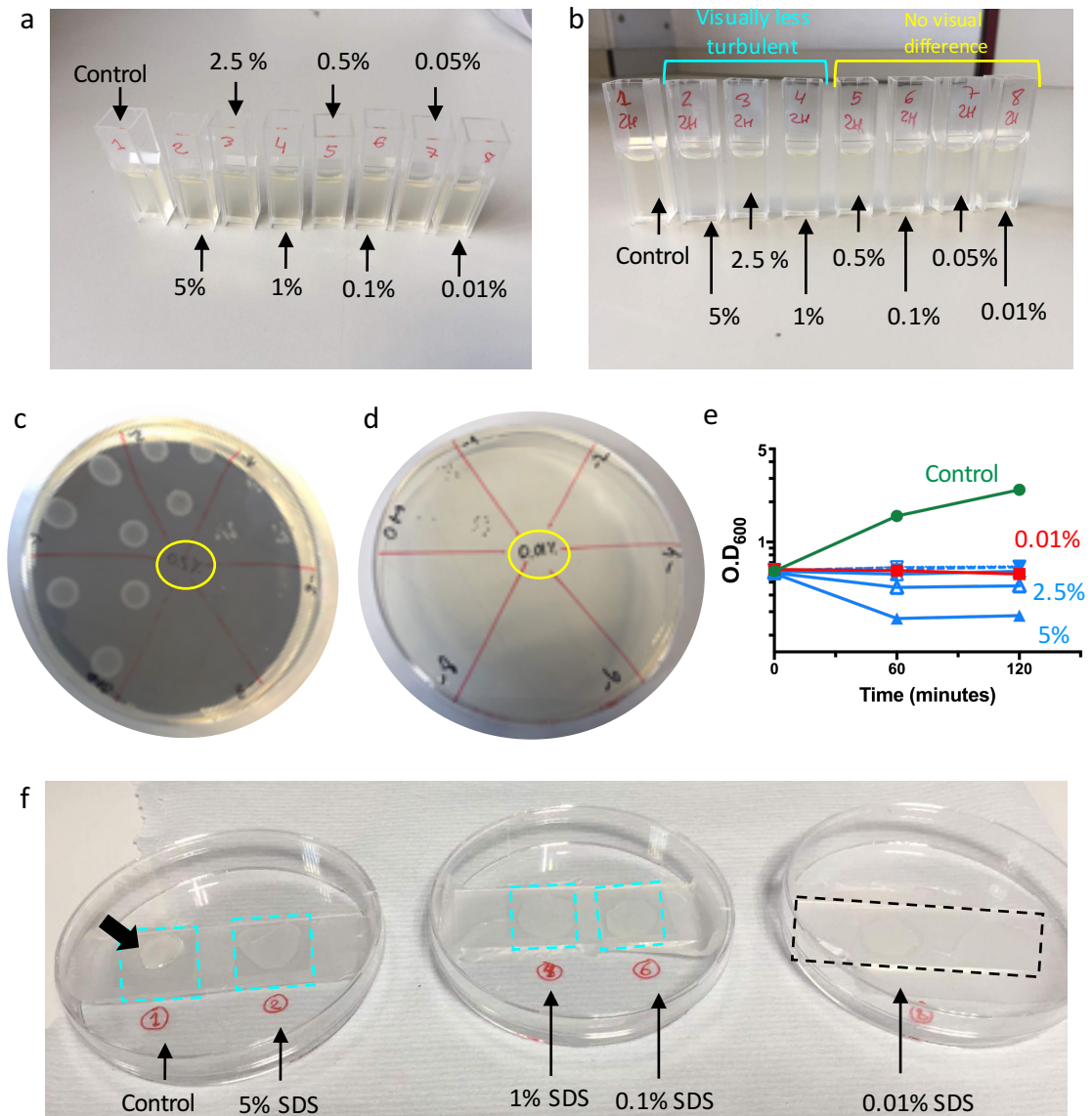


Figure 6.20 – a) OD cuvettes to measure the initial OD at time 0h before the SDS addition, different percentages will be added as indicated in the photograph; b) same samples after 2h of SDS treatment on a Falcon 50 ml tube; c) Initial plate at time 0h to measure the CFUs in this case from sample 5 (0.5% SDS); d) Example of plate from sample 8 (0.01% SDS after 1h of SDS treatment on the tube; e) logarithmic OD₆₀₀ graph from all the samples after 1h and 2h of SDS treatment in the tube; f) Droplets of five different samples 1, 2, 3, 6 and 8 on high-precision glass slides.

The SDS killing experiment was performed on glass coverslips at RT and without any rotation to try to replicate the conditions under the AFM when living cells are being imaged. In the first environment, the cell culture is grown up to exponential phase, then SDS was introduced and the cells were put back to their growing environment: 37^o and 250 rpm shaking. However, on an AFM set-up, the cells are grown at the appropriate OD

and then they are removed from that environment and all the rest of operations are performed at RT without any shaking. By comparing the same treatment in these two different environments the minimum concentration of SDS needed to kill the cells under AFM can be found.

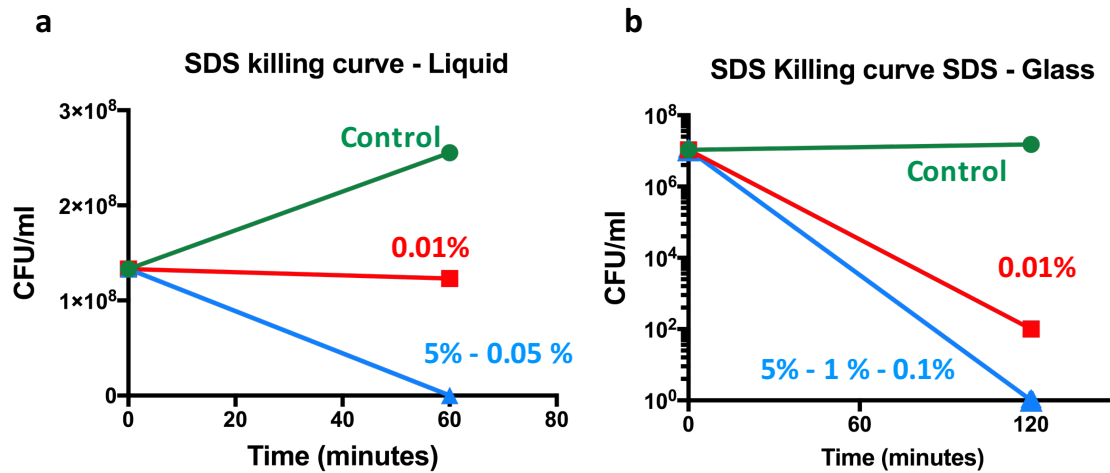


Figure 6.21 – a) Killing curves from the cell culture inside the Falcon tubes at 37 °C and 250 rpm shaking; b) Killing curves from the cell solution incubated in the glass coverslip for 1h during the SDS treatment, RT and 0 g.

Figure 6.21 a shows the killing curve performed in the first environment: plates were made after 1h of different concentrations of SDS. The percentages 5-0.05% (in blue) show complete killing after 1h. However, with 0.01% of SDS the cells are in stasis. Figure 6.21 b shows the killing curved performed in the second environment: after 2h of SDS treatment and incubated on the glass slide. The same trend is appreciated, for 5, 1 and 0.1% of SDS all the cells are killed after 2h but for 0.01% still some cells remain. However, for the control, there is significantly less growth after 2h of being in the environment mimicking the AFM than 1h in the favorable environment. This shows, that experiments performed in controlled laboratory conditions cannot be completely translated to the AFM environment for experiments involving dynamics, because the growing of the cells will be completely different. The conclusion from the SDS treatment is that any percentage above 0.1% should completely kill the cells in 1 to 2 h, even if they are incubated on a surface without motion and at RT.

6.2.3.2 Dynamics of 2.5% SDS under Atomic force microscopy

The chosen percentage to perform the AFM experiment was 2.5% of SDS to ensure killing of all the cells when a random location is picked. For this experiment, a few cells

were imaged at high resolution before and after the SDS was added. The best results were obtained by performing rectangular images covering the majority of the cylinder body of one cell. The chosen imaging mode was PeakForce Tapping which provided more stability over time than Tapping. The best results are summarized in *Figure 6.22*.

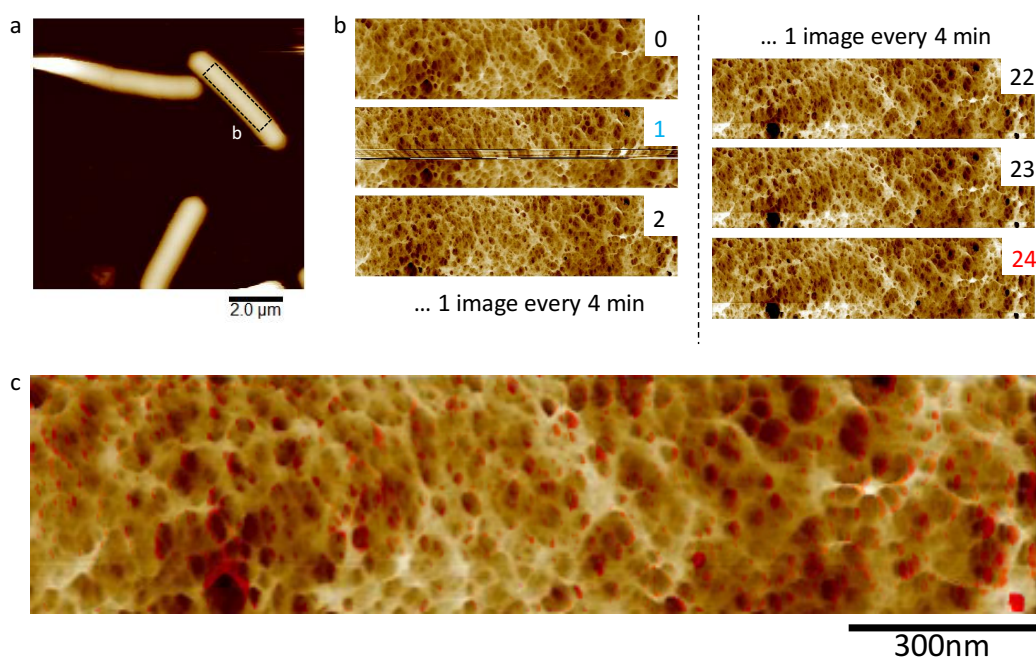


Figure 6.22 – a) Overview of the region before adding SDS; b) Zoom images from top right cell in ‘a’, images every 4 min, 0 is before the addition of SDS, 1 is during the addition of SDS, 24 is after 1h and 30 min of addition of SDS; c) Overlapping images 0 and 24, the red spots are regions of image 0 which are different from 24, which is shown in normal colour scale.

The images from *Figure 6.22* before the addition of SDS were performed under the same experimental conditions as *Figure 6.12*, detailed in *Table 6.2*. See section 2.2.3.3.1.

Figure 6.22 b shows a series of images on the same cell before (0) and after (1-24) the addition of 2.5% of SDS. This series of frames can be put together and played as a movie, what can be observed is an initial expansion of the material between frames 0 and 2. Then, there is a contraction and the material returns approximately to its original position. There are permanent slight changes, highlighted in *Figure 6.22 c* where frames 0 and 24 (1 hour and 30 minutes) have been overlapped together, the red areas are differences between the images.

In order to further explore these small variations after the addition of 2.5% SDS, a high resolution image was taken before and after this treatment on another cell which was not imaged continuously. See a direct comparison in *Figure 6.23* below.

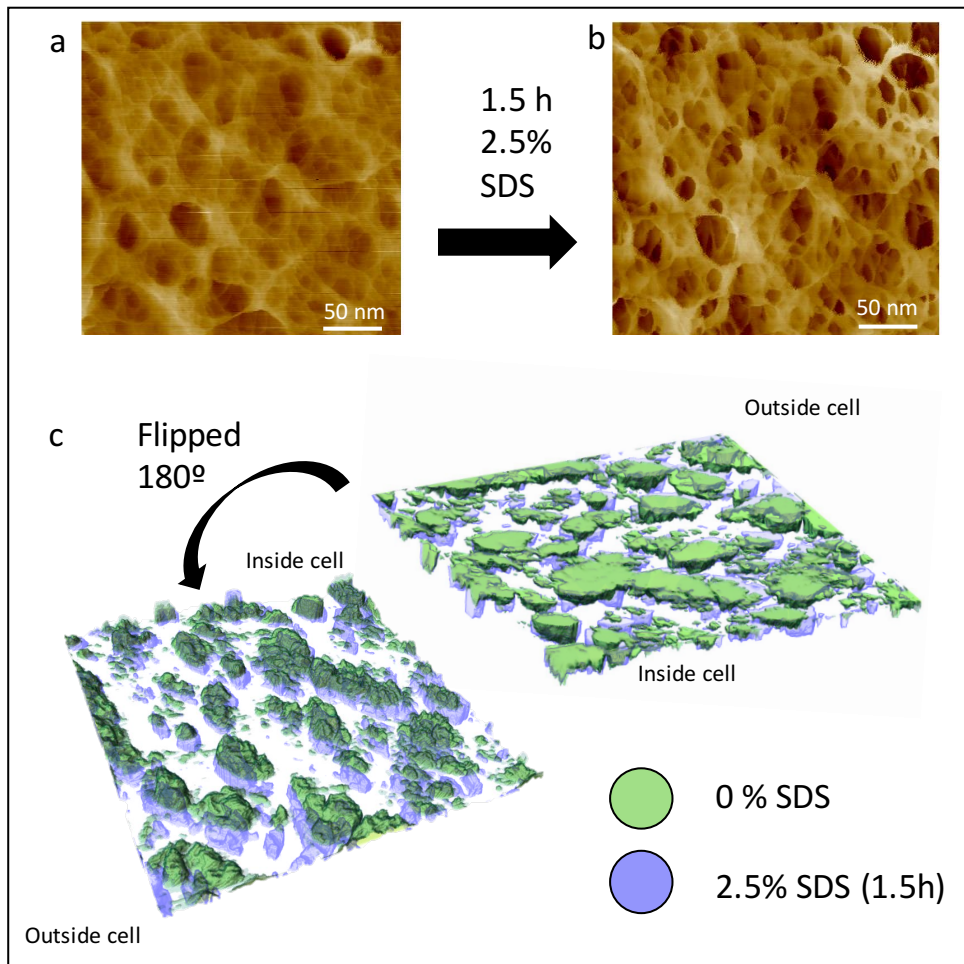


Figure 6.23 – a) High resolution image of a mature mesh region of *B. subtilis* cells before the addition of SDS (0%); b) Same region as 'a' after 1h and 30 min of 2.5% SDS treatment; c) Three-dimensional representation of both images where the pores have been highlighted in green for 'a' and blue for 'b', then they are overlapped.

Figure 6.23 shows the direct comparison of the same area of mesh before (see Figure 6.23 a) and after the addition of 2.5% SDS for a period of 90 min (see Figure 6.23 b). The post-treatment image has two main differences: it is less fussy (maybe because the WTA or the proteins have been affected); and it resembles more the mesh from the purified PG (see Figure 6.3 d) than the living cells (see Figure 6.12). The dimensions of the mesh pores was quantified using the bearing analysis tool on Nanoscope Analysis™ and measuring at 54% of the image, the ratio between the volume of the pores and the area was measured using: $C=V/A$; where V represents the Volume of the pores and A their area. The value of C was measured for the untreated and treated images with the following results: $C_{0\%SDS}=3.76$; $C_{2.5\%SDS}=4.62$. This means the dimensions of the pores have increased ~20% after treatment (n=1 cell). This dimension difference can be visually appreciated when a three-dimensional representation of the pores was

produced for both images and overlapped, see *Figure 6.23 c*. The green shows the pores from *Figure 6.23 a* and the blue areas are the pores from *Figure 6.23 b*.

According to the literature, [26]-[27] SDS treatment disrupts the cytoplasmic membrane and assuming it also alters their turgor pressure. The hypothesis is that the stress caused by the turgor pressure changes, alters the volume of the pores on the CW observed by AFM. However, much more prominent changes were expected due to the high effectivity of this treatment in liquid cell culture (see *Figure 6.21*).

6.2.3.3 Dynamics of 5% SDS under Atomic force microscopy

To corroborate this theory, a second experiment was produced doubling the amount of SDS by adding 5% of SDS instead of 2.5%. If the physical changes to the CW are directly related to the stress cause by the SDS treatment, increasing the concentration to 5% could cause more prominent deformations in the same time-frame. Here, different cells were imaged before adding SDS and the same cells were imaged after a certain time passed. No consecutive frames were taken to avoid altering the cells with the AFM tip. The best results are summarized below in *Figure 6.24*.

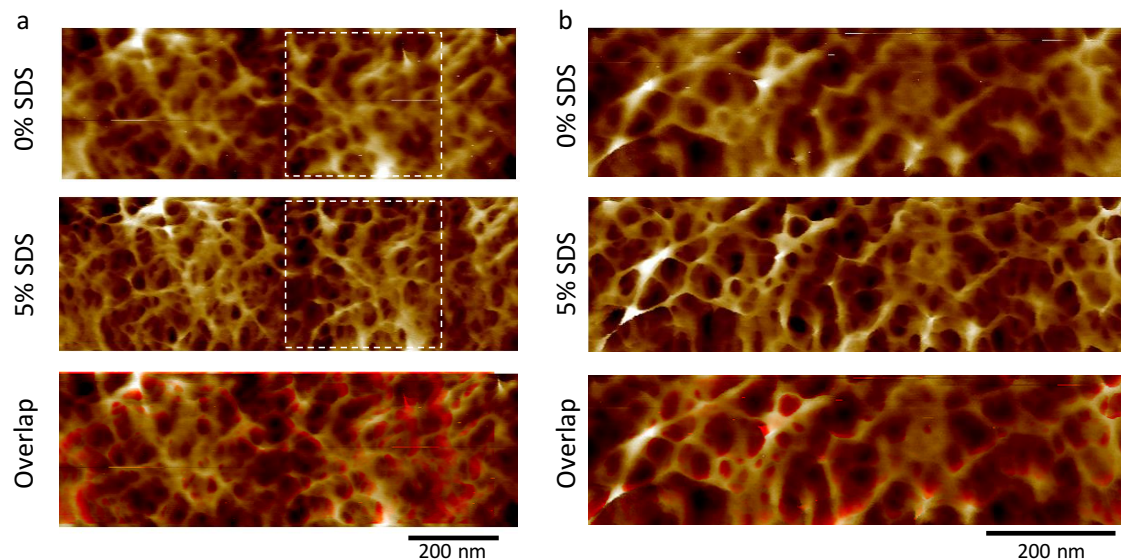


Figure 6.24– a) Top: High-resolution before adding SDS of middle region of B. subtilis cell, Middle: same area after 1.5h of 5% SDS treatment, Bottom: Overlap of the two previous images, the red spots are differences between them. White dashed box: volume measurements; b) Top: High-resolution of another B. subtilis cell before adding SDS, Middle: Same area after 1.5h of 5% SDS treatment, Bottom: Overlap of the two previous images, the red spots are differences between them.

The images from *Figure 6.24* before the addition of SDS were performed under the same experimental conditions as *Figure 6.12*, detailed in *Table 6.2*.

Figure 6.24 a shows the direct comparison of the PG architecture of one living *B. subtilis* cell before and after the treatment of 5% SDS for 1.5h. The overlap shows the final position in a normal colour scale and the initial position in red. It can be appreciated that there is higher amount of red pixels in this image in comparison to *Figure 6.22 c* where the cell was treated with 2.5% SDS. *Figure 6.24 b* shows another example in a different cell, the bottom image shows the overlap between the initial architecture (in red) and the same position after 1.5h of 5% SDS treatment (in normal colour scale). Moreover, measurements of volume and area were performed in a zoomed image from *Figure 6.24 a* (see white dashed square). The constant C was calculated using the same methodology as *Figure 6.23*. The results are: $C_{0\%SDS}=1.9$; $C_{2.5\%SDS}=2.6$. This means the dimensions of the pores have increased ~25% after treatment of 5% SDS for (n=1 cell).

Figure 6.24 only shows two examples, but a total of 5 different cells were studied. What can be inferred from the high-resolution overlaps is that the CW has features that seem to be further apart than the initial position. Contrary to what it was expected, the cells get inflated after the treatment. This would mean an increase in the total cell volume due to this inflation. Then, to corroborate this, the dimension of the entire bacteria cells were measured. The images used to compare the dimensions of the bacteria are shown in *Figure 6.25*.

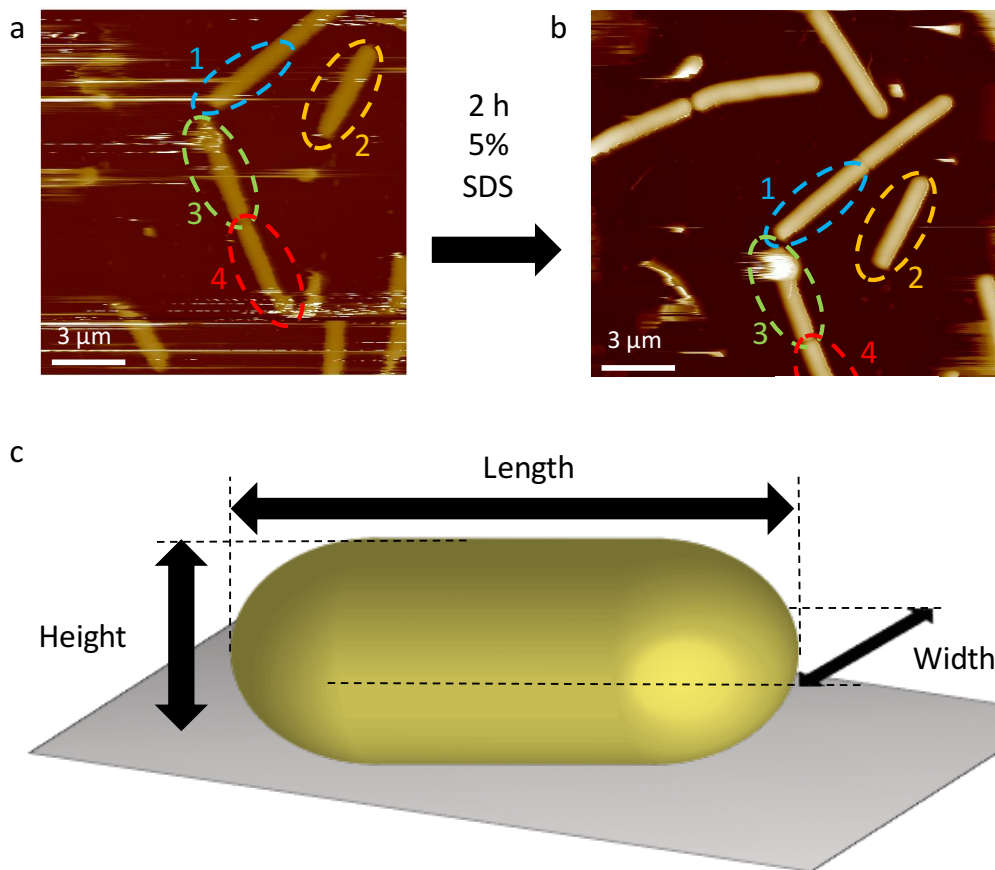


Figure 6.25– a) overview of the system before the addition of SDS; b) Same region slightly shifted after 2h of 5% SDS treatment; c) Representation of the three magnitudes measured for the four cells marked in ‘a-b’ with 1-4.

Figure 6.25 a shows the location of the four cells used in this comparison before the treatment. Figure 6.25 b shows the same four cells (1-4) after 2h of 5% SDS treatment. The overall AFM tracking after the treatment was better than initially as it can be visualized in Figure 6.25 b where there are fewer spikes and lines than in Figure 6.25 a. Figure 6.25 c is just a schematic representation of the three magnitudes chosen to test if the cell shape was altered: length, height and width. After measuring the three magnitudes for the four cells the results are summarized in Table 6.4 below.

Table 6.4 – Three magnitudes of four different cells before and after 2h treatment with 5% SDS.

	Height (nm)		Width (nm)		Length (μm)	
	0% SDS	5% SDS	0% SDS	5% SDS	0% SDS	5% SDS
Cell 1	810	920	861	807	4.9	5.05
Cell 2	812	897	838	815	4.3	4.6
Cell 3	810	893	768	703	4.5	4.38
Cell 4	802	914	745	833	-	-

From the results in *Table 6.4* it can be concluded that all four cells increase in height by approximately 10%. All cells except cell 4 decrease in width by a 6%. Cells 1 and 2 also increase in length by 5% but cell 3 decreases by 2.7%. The length measurement of Cell 4 was not possible due to this cell being out the area imaged after the treatment. This information, in addition to the deformations on the finer architecture would indicate a slight swelling of most of the cells. However, due to the problematic AFM tracking of the overview image before the treatment (see *Figure 6.25 a*) and the reduced data set (n=4 cells), the measurements presented in *Table 6.4* are not robust and the differences found could be due to the AFM artefacts.

To conclude, the killing assays at population level would indicate a radical change in morphology of the cells after 1h treatment with 2.5% and 5% SDS respect to the control. However, this has not been translated on the AFM experiments. This could be because of two reasons. Either the conditions on the AFM are different and the cells are not dying within the time-frame studied. Otherwise, it could be that even when the cells are dead and the membrane is disrupted by the SDS the CW maintains the overall structure. Or the cells could be dead when attached to the surface of the AFM before adding SDS. More data and different experiments would be required to distinguish which of these two explanation is true.

6.3 *Bacillus subtilis* mutants

In previous *sections 6.1 and 6.2*, the WT *B. subtilis* 168 strain [3] (see *section 2.1.1*) has been extensively studied in different forms: as purified sacculi in dry and liquid environment; as healthy living cells and SDS treated cells. Here, other strains are studied in order to better understand some of the PG synthesis mechanism of *B. subtilis*.

6.3.1 The MreB filaments

The MreB is a protein that self-assembles into curved filaments which have a crucial role in the PG synthesis and shape definition of *B. subtilis* cells. A mutant lacking this protein has been chosen for this study to correlate a major cell shape change with its molecular PG organization. This mutant has been extensively studied in the literature mostly by super resolution fluorescence and internal reflection fluorescence microscopy (TIRFM).

[9], [28], [29] However, no data has been obtained using high-resolution AFM visualizing directly its PG architecture.

6.3.1.1 The role of MreB complex in cell morphology

Rod-shaped bacteria have a slightly different synthesis machinery than *cocci*-shaped species. The commonly named elongasome is a group of enzymes called Rod complex which includes the proteins: MreB, MreC, MreD (encoded by the *mreBCD* operon) and RodZ, together with the glycosyltransferase/transpeptidase enzyme pair RodA/PBP2. The Rod complex was identified because using single-particle tracking with super-resolution imaging it was shown that the motion of all these proteins is coupled with each other and the loss of any of the components stops the motion of the others. [9]

The Rod complex has been shown to be crucial for determination of the cell shape of *B. subtilis* by performing PG synthesis at the appropriate orientation. These proteins (or their homologs) have been shown to be conserved across different rod-shaped organisms and be absent in *cocci* species. The most important component of this complex is the MreB protein which forms filaments following the cytoplasmic membrane curvature and serve as a coordinating scaffold for the rest of the complex to perform their function as PG synthesis in a circumferential motion around the cylindrical axis of the cell.

MreB filaments sense the regions with the highest lipid membrane curvature. In the case of *rod*-shaped cells, the highest curvature corresponds to the short circumferential axis. Then, the MreB filaments move circularly along the short axis of the cells constraining the localization of the PG synthesis machinery (RodA/PBP2). [9], [28] Next, the new cell wall is inserted with a circumferential orientation at the internal surface of the CW (corroborated with our AFM images in the previous sections of this chapter). The lack of MreB filaments causes the PG synthesis machinery to not have any preferential location and the *rod*-shape is lost and the bacteria acquires spheroid shape. Many experiments have been performed to confirm this model. For example, correlating the loss of shape of the bacteria with the lack of directed movement of the PG synthase enzyme PBP2a (see *Figure 6.26 a*). Where a spheroid shaped *mreBCD* mutant was used to track PBP2a (see immobile proteins in red), when the *mreBCD* gene was activated by increasing

Xylose concentration, the PBP2a showed movement (see trajectories in green) and the cells regained their rod-shape.

Conversely, another group of PBPs named aPBPs, such as the PBP1, do not have a directed movement and their activity is independent of the Rod complex. Many experiments were performed trying to understand the relationship between these two PG synthesis machineries (see Figure 6.26 b). The conclusion was that in order for a rod-shaped bacteria to maintain its shape, a perfect balance between the activities of the two complexes was required. The Rod complex synthesises oriented glycans along the short axis of the cell providing higher strength to the CW against the uneven stress caused by the turgor pressure. Simultaneously, the aPBPs are necessary to synthesise randomly ordered glycans all over the cell. When there is a slight unbalance between the two PG synthesis machineries, the cell gets thinner or wider instead of maintaining the right proportions (see Figure 6.26 c). [29]

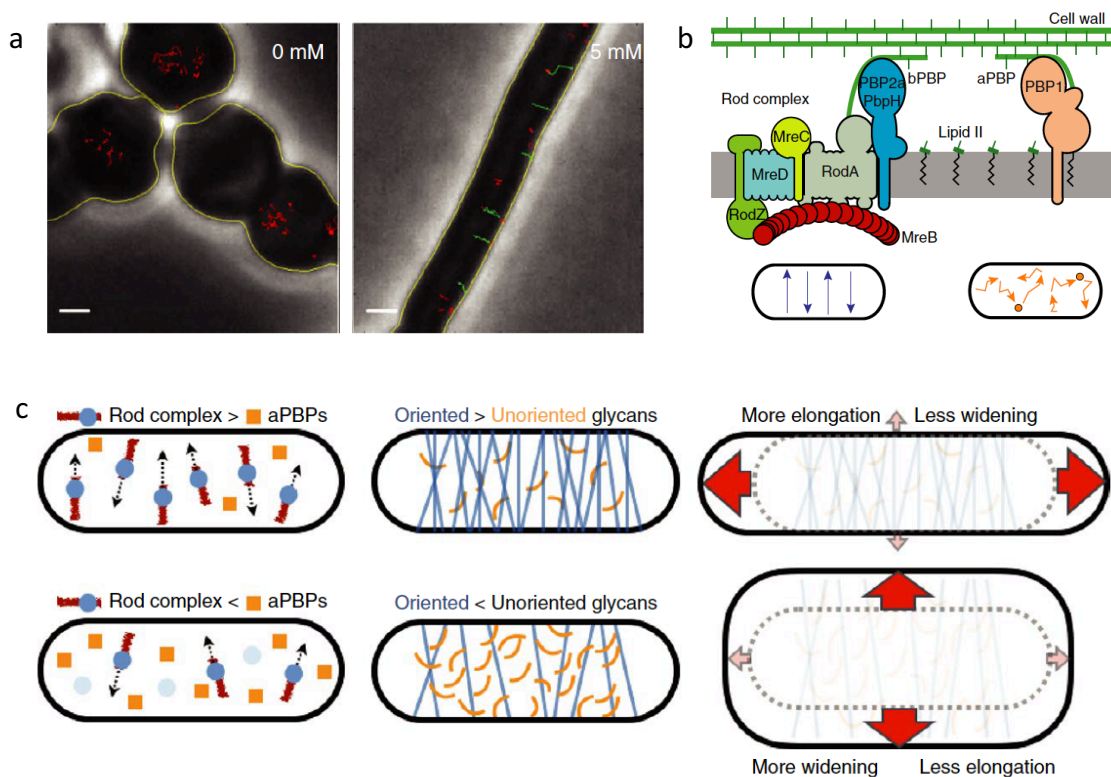


Figure 6.26 – a) Experiment showing an *mreBCD* mutant on the left losing its rod-shape and the same mutant with the gene activated on the right recovering its rod-shape; b) schematics of two different PG synthesis complexes; c) Model explaining the unbalance activity of both complexes resulting in thinner or wider cells. Adapted with permission from [29].

Here, only the lack of MreB filaments from the Rod complex will be studied using a strain lacking the three MreB paralogs that *B. subtilis* contains in its genome: MreB, Mbl and

MreBH. These three proteins have been shown to co-polymerize into mixed filaments *in vitro* and also they always colocalize *in vivo*. This means that in order to fully remove the ability to create MreB filaments, all three genes have to be altered. Although a similar mutant (affecting the mreBCD operon) has been studied in the literature, [9], [28], [29] most of the experiments were focused on localizing and tracking the movements of PBPs and other proteins. Others, performed labelling experiments using fluorescence D-amino-acids (FDAAs) which cross-linked to newly incorporated PG. Here later, the resolution was not enough to resolve any ordered structure of the newly incorporated glycans either for the mutant nor the controls. Thus, there is a gap in the literature of a direct study of PG architecture of this type of strain.

The AFM methods developed in all the previous chapters were applied to understand the PG architecture from a mutant without ability to create MreB filaments. If the data provides solid conclusion this could complete the literature gap and complement all the proposed models.

6.3.1.2 Molecular structure of strain lacking MreB (Δ mreB strain)

The triple mutant Δ mreB Δ mbl Δ mrBH in a *rsgI::spec* background (Δ mreB strain) was purified and the PG sacculi were imaged with AFM in liquid following the same methodologies presented in *chapters 3-5* and in the previous sections of this chapter. See *sections 2.2.1* and *2.2.1.5* for growing conditions of this mutant. The best images are presented in *Figure 6.27*.

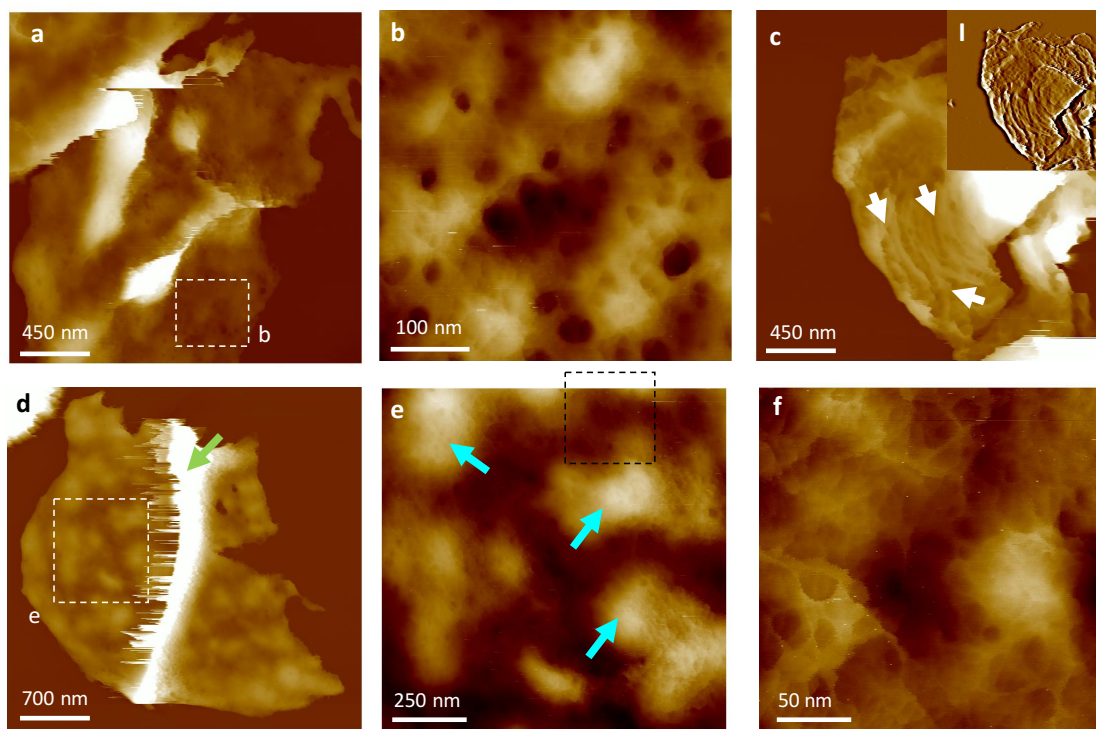


Figure 6.27– a) fragment of $\Delta mreB$ mutant sacculi with unknown surface; b) zoomed from ‘a’; c) Another fragment with a section with reminiscence of rings (see white arrows); d) This fragment is probably the internal surface, because there is the characteristic piecrust in the middle (see green arrow); e) zoomed image from ‘d’; f) zoomed image from ‘e’.

The AFM images from Figure 6.27 were performed using the experimental conditions summarized below in Table 6.5.

Table 6.5– Experimental conditions that images from Figure 6.27 were taken with.

AFM TYPE	AFM TIP	AFM MODE	SAMPLE TYPE	BUFFER/ ENVIRONMENT	SURFACE	SPECIFIC CONDITIONS
BRUKER FAST SCAN	Fast Scan - D	PeakForce Tapping	$\Delta mreB$ strain Stock A Batch 11 Dilution 4	150 mM KCl + 10mM Tris pH=7.8	PLL coated MICA	Dried to be imaged the next day

Figure 6.27 shows three different architectures of PG found on the *B. subtilis* $\Delta mreB$ strain. Figure 6.27 a shows a sacculi fragment with a rather smooth surface, initially thought to be the internal surface. Figure 6.27 b is a zoomed image from Figure 6.27 a showing a smooth PG surface with small holes randomly distributed. This architecture has never been observed before. Therefore, it is unknown which part of the cell it is. Figure 6.27 c shows another fragment with a section displaying concentric rings (see white arrows). This presumably corresponds to the external surface, as the WT also display rings on the external and not on the internal surface. Figure 6.27 d shows

another fragment with a very prominent piecrust in the middle (see green arrow). From the results in chapter 4, this probably corresponds to the internal surface of the CW. *Figure 6.27 e-f* are consecutive magnifications from *Figure 6.27 d*, showing a randomly orientated mesh of glycan strands. Moreover, another distinctive feature was found, the big patches across this surface (see blue arrows), not seen in the WT.

In conclusion, the results from [9], [28], [29] regarding *rod*-shape lost of this strain could be corroborated with the AFM results of *Figure 6.27* as no *rod*-shaped sacculi fragments were found. The $\Delta mreB$ strain resembles more a *cocci*-shaped species like *S. aureus*. The finer architecture of the internal surface is completely different from *B. subtilis* WT, the strands are not orientated and instead of a smooth continuous surface it has patches of denser material. The external architecture could not be clearly determined, as no mature mesh was found. There is a novel architecture that still is unknown to what side of the CW it corresponds and presumably the concentric rings do correspond to the external surface. To have a complete picture of the three-dimensional CW architecture of the $\Delta mreB$ strain it would be necessary in the future to obtain images from living cells to clearly identify the external CW architecture and complement our current findings.

6.3.2 The *rsgI* mutant (background strain for $\Delta mreB$)

As mentioned in the previous section, the $\Delta mreB$ strain used in this study was not constructed on the 168 WT background. It was constructed on another background, the 168 $\Delta rsgI$ background ($\Delta rsgI$ strain). This is a mutation that affects heat-inducible transcription process,[30] it should not affect the CW structure and therefore the PG phenotype should be the same as the WT. However, the $\Delta rsgI$ strain was imaged by AFM as a control for the previous results of the $\Delta mreB$ strain. The best images are summarized in *Figure 6.28*.

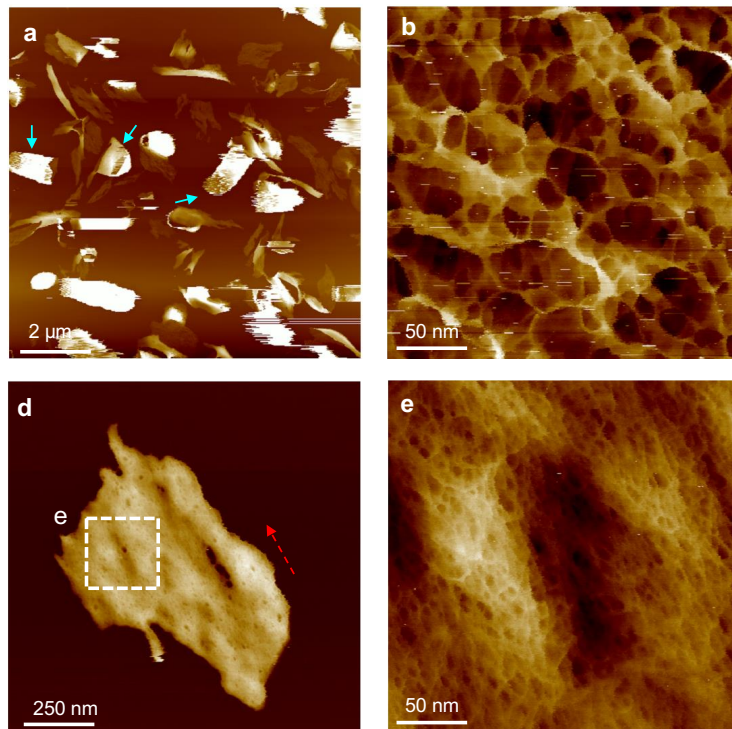


Figure 6.28 – a) Overview of the *rsgI* sacculi sample in liquid, with rod fragments (see blue arrows); b) Finer architecture of external mature mesh; d) fragment showing the internal surface upwards; e) zoomed image from 'd'.

Figure 6.28 shows two different architecture of the $\Delta rsgI$ strain, the internal and the mature external surfaces. Figure 6.28 a shows an overview of the sample, where several fragments display rod-shape (see blue arrows). Figure 6.28 b shows a high magnification from another fragment of sacculi, the finer mature external structure is clearly the same as the mature mesh from the WT. Figure 6.28 d-e show the best images obtained from the internal surface showing glycan strands orientated along the short axis (see red dashed arrow) of the cylinder in the same way as the WT. Experimental conditions are the same as in Table 6.5.

6.3.3 Internal strand orientation is shape dependant

Quantitative analyses were performed to compare the WT, the $\Delta rsgI$ and $\Delta mreB$ strains. The internal PG surface was the relevant part of the CW to be studied as the Rod complex localizes close to the membrane. The glycan orientation analysis developed and explained in chapter 4 see section 4.4.3 and Figure 4.17 was used here and the results are summarized below in Figure 6.29.

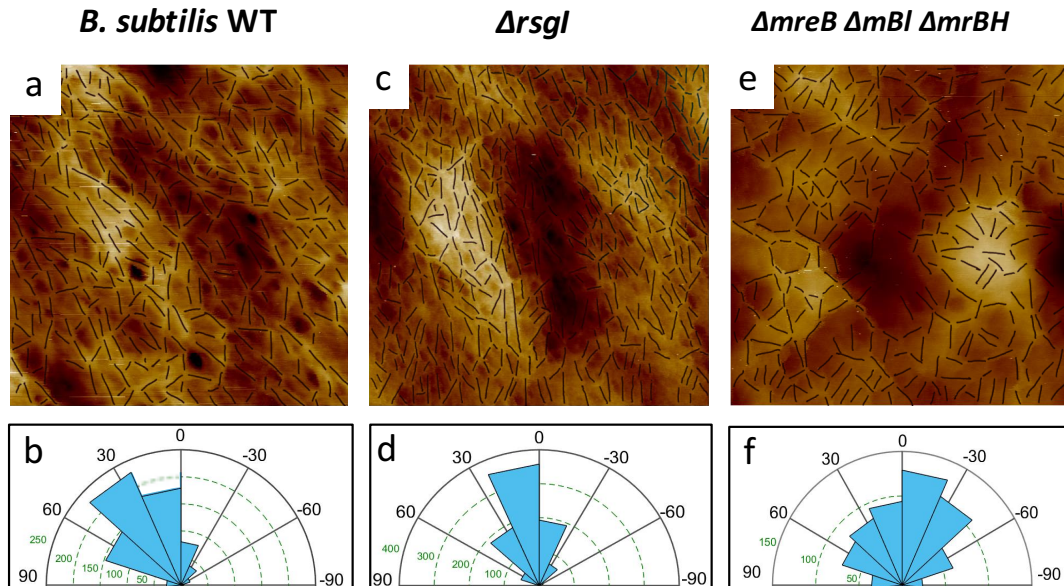


Figure 6.29 – a) Internal septal wall of *B. subtilis* WT image with the manual drawing overlapped; b) resultant rose plot of angles from 'a'; c) Internal septal wall of *B. subtilis* $\Delta rsgI$ strain with the manual drawing overlapped; d) resultant rose plot of angles from 'c'; e) Internal septal wall of *B. subtilis* $\Delta mreB$ strain with the manual drawing overlapped; f) resultant rose plot of angles from 'e'.

Figure 6.29 shows a clear similarity between the internal septal wall of the *B. subtilis* WT and the internal surface of the $\Delta rsgI$ strain. Their rose plots have a major angle of predominant orientation (Figure 6.29 b and d) and other glycans have an orientation of $\pm 30^\circ$ from the predominant angle. This shows that the control has the same internal architecture as the WT. When the main components of the Rod complex are affected: on the $\Delta mreB$ strain, instead of having a predominant orientation there are glycans in all possible angles (see Figure 6.29 e). The rose plot although having an angle corresponding to the majority of glycans (between 0 and -30°), the neighbouring angles correspond to similar amount of glycans, see Figure 6.29 f. Moreover, there are glycans with angles in all the directions between 90° and -90° (which does not happen in an ordered structure like the WT or the $\Delta rsgI$ strain).

This quantitative analysis shows that the internal PG architecture becomes randomly orientated when the three *B. subtilis* MreB paralogs (MreB, Mbl and MreBH) from the Rod complex are affected. Thus, although the PG synthesis machinery still works, without the proper guide from the Rod complex it cannot synthesise the appropriate PG architecture to produce *B. subtilis* rod-shaped cells. The rose plot from the $\Delta mreB$ strain (see Figure 6.29 f) has much more similarity to the internal surface of *S. aureus* which is also randomly orientated (see Figure 4.18 d) than the internal surface of *B. subtilis* WT.

To conclude, the finer PG architecture, especially the orientation of the glycan strands, plays an important role in determining the shape of bacteria. This also applies to *rod*-shaped Gram-negative bacteria (*E. coli*) as it has been recently shown by a former member of our group. [31] This opens new opportunities to combine the high-resolution AFM and the quantitative tools developed in this work with fundamental microbiology studies to understand the role of specific enzymes. Ultimately, finding a robust connection and relation between the known CW molecular pathways and their effect on the architecture and function of the CW.

6.4 Discussion

This chapter has been focused on studying the Gram-positive species: *B. subtilis*. Similarly to *S. aureus*, two main samples were used: purified PG and living cells.

In *section 6.1*, the *B. subtilis* sacculi was studied in different environments. Three different architectures were identified: the internal ordered tight mesh, the external nascent rings and mature mesh. In comparison to *S. aureus*, the external surface of both species has the same structure. However, the internal surface has similarities and differences. They both have a much more tight mesh on the internal surface than the external mesh. However, the orientation of the glycan strands depends on the shape of the bacteria. The *rod*-shaped *B. subtilis* has glycan strands oriented along the short axis; in the *cocci*-shaped organism (*S. aureus*) the glycans are randomly orientated because the stress caused by the turgor pressure is uniform. The sacculi sample allowed also the study of the septum architecture. In contrast with *S. aureus*, *B. subtilis* has a much more porous septa with different pore sizes across the thickness of the septa. The suggested model based on quantitative analysis is the following: there is a synthesis machinery located at the edge of the septal plate together with the *back-filling* mechanism in filling the big pores afterwards (see *section 6.1.3.2*). Finally, the thickness of single layers of CW (PG containing WTA) were measured in air and liquid environment. The measurement in air with 9 ± 1 nm was significantly smaller than *S. aureus* with 17 ± 2 nm. The measurement in liquid with 34 ± 10 nm had no statistical difference than *S. aureus* with 36 ± 5.3 nm. However, the liquid uptake was higher in *B. subtilis* with 74% and *S. aureus* with 47%, meaning that their hydrogel properties are slightly different despite their similarities in PG architecture.

In *section 6.2*, the *B. subtilis* living cells were studied in different environments. In a buffer environment, the mature external surface was found to be randomly orientated fibrous mesh located along the cylinder and occasionally in mature poles as well.[13] Some differences were found between the two species after performing quantitative analysis. The pores on the mesh are deeper in *S. aureus* than in *B. subtilis*, which agrees with the difference in thickness, TEM data measured the thickness of the CW from *B. subtilis* cells as being 15 nm. [32] A completely automatic method of analysis to measure the pores across the image thickness was improved from *section 4.2.2*, instead of calculating the HCFA for one slice, a program (see code in *Appendix 2*) was written to automatically slice each image in 255 binary slices obtaining HCFA values and number of pores (see *section 6.2.1.2*). The size of the pores was slightly different, the mean HCFD from the slices containing the maximum number of pores are 34 nm for *B. subtilis* and 29 nm for *S. aureus*. The depth of the slice containing the maximum number of pores was 12 nm for *B. subtilis* and 23 nm for *S. aureus*. However, there was no statistical difference in the maximum number of pores or the fibre width between the two species. Regarding the nascent external surface of *B. subtilis* living cells consist of concentric rings located at the poles. All of these results would explain a common model for Gram-positive bacteria which presumably would apply to other bacteria aside from *S. aureus* and *B. subtilis*.

Figure 6.30 shows the proposed model of the PG architecture for *S. aureus* and *B. subtilis* that was extracted from this study and the previous work performed in our group. [13] By joining data from four different types of samples: *S. aureus* [11] and *B. subtilis* living cells ([11] and this study); *S. aureus* and *B. subtilis* purified hydrated PG (this study and data from [13], [17] taken by other researchers). This model highlights the commonalities and differences, attributable to the shape, between the two species. The model was only based on the data obtained from the WT strains SH1000 and 168, highlighting the PG structure of healthy cells. AFM images can be obtained on other samples: WT strains with treatments like SDS or antibiotics (see *Chapter 7*); other strains with mutations affecting the CW (see *Chapter 5*).

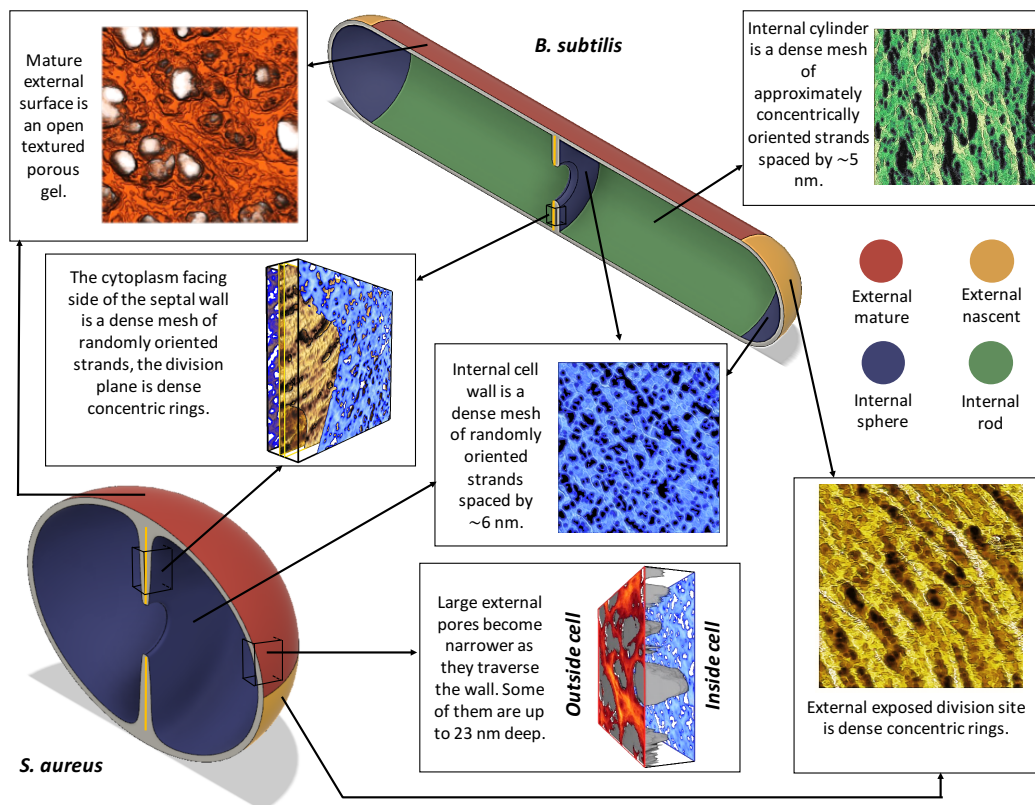


Figure 6.30 – Molecular PG architecture model for *S. aureus* and *B. subtilis* based on high resolution AFM images.

The resultant molecular architecture of these cell samples can be compared to the healthy WT strains shown here in Figure 6.30.

In section 6.2.3, *B. subtilis* living cells were given an SDS treatment to understand the relationship between the internal turgor pressure of the cell and the PG architecture. Firstly, population killing assays were performed in two different environments: the conventional microbiology growing conditions; other conditions mimicking an AFM experiment. There was a significant difference in growth between these two environments. This shows a gap in the literature about the different behaviour of challenged cells in suspension or attached to a surface. When the AFM dynamic experiment was performed, some structural differences were found between the cells before and after SDS treatment. However, from the killing assays, more radical changes in the PG architecture were expected due to a perturbation of the turgor pressure.

Finally, in section 6.3, the hydrated sacculi of $\Delta mreB$ strain was studied. This gave us a mechanistic insight into the PG biosynthesis machinery and shape-definition enzymes of *B. subtilis*. When removing $\Delta mreB \Delta mbl \Delta mrBH$ from a strain, this triple mutant produced cells without rod-shape and the internal PG contained glycan strands

randomly orientated instead of ordered as in the WT. As shown in *Figure 6.30*, our model states that the only main difference between the two targeted species is the glycan strands orientation on the internal CW surface depending on their overall shape. The AFM quantitative results show the MreB is a key component of the Rod complex which is necessary to maintain the *rod*-shape of the bacteria. The $\Delta mreB$ strain internal surface has randomly orientated glycan strands resembling the internal CW of *cocci*-shaped cells. These results complement our model, *B. subtilis* and *S. aureus* have the same CW architecture when the difference in shape is removed. The study of *B. subtilis* has added structural information; and correlation between the PG molecular organization and mechanistic function of specific enzymes. In the future, this could represent a new branch of research regarding the function-structure relationship of different proteins and enzymes in microbiology.

To conclude, now that the three-dimensional architecture of Peptidoglycan has been solved for Gram-positive bacterial species, the effect of CW antibiotics can be studied at molecular level (see *chapter 7*). This will increase our understanding of the interaction between the CW and antibiotics and will bring us one step closer to defeat the AMR crisis.

6.5 References

- [1] E. J. Hayhurst, L. Kailas, J. K. Hobbs, and S. J. Foster, "Cell wall peptidoglycan architecture in *Bacillus subtilis*," *Proc. Natl. Acad. Sci.*, vol. 105, no. 38, pp. 14603–14608, 2008.
- [2] R. M. Martinez, "Bacillus subtilis," in *Brenner's Encyclopedia of Genetics: Second Edition*, 2013.
- [3] T. J. Smith, S. A. Blackman, and S. J. Foster, "Peptidoglycan hydrolases of *Bacillus subtilis* 168," *Microb. Drug Resist.*, 1996.
- [4] T. J. Smith, S. A. Blackman, and S. J. Foster, "Autolysins of *Bacillus subtilis*: Multiple enzymes with multiple functions," *Microbiology*. 2000.
- [5] W. F. Doolittle, "Bacterial evolution.," *Can. J. Microbiol.*, vol. 34, no. 4, pp. 547–551, 1988.
- [6] R. S. Gupta, "Evolutionary relationships among photosynthetic bacteria," *Photosynth. Res.*, vol. 76, no. 1–3, pp. 173–183, 2003.
- [7] R. S. Gupta, "What are archaeobacteria: life's third domain or monoderm prokaryotes related," *Molecular Microbiology*, vol. 29, no. 3. p. 695, 1998.
- [8] J. L. Slonczewski and J. w. Foster, *Microbiology and evolving science*, Third, Int. Canada: W.W.Norton & Company, Inc., 2014.
- [9] E. C. Garner, R. Bernard, W. Wang, X. Zhuang, D. Z. Rudner, and T. Mitchison, "Coupled, circumferential motions of the cell wall synthesis machinery and MreB filaments in *B. subtilis*," *Science (80-.)*, 2011.
- [10] M. Beeby, J. C. Gumbart, B. Roux, and G. J. Jensen, "Architecture and assembly of the Gram-positive cell wall," *Mol. Microbiol.*, 2013.
- [11] J. M. Burns, "High Resolution Atomic Force Microscopy Imaging of Living Bacterial Surfaces," University of Sheffield, 2017.
- [12] R. D. Turner, E. C. Ratcliffe, R. Wheeler, R. Golestanian, J. K. Hobbs, and S. J. Foster,

- “Peptidoglycan architecture can specify division planes in *Staphylococcus aureus*,” *Nat. Commun.*, 2010.
- [13] L. Pasquina-Lemonche, J. Burns, R. Turner, S. Kumar, R. Tank, N. Mullin, J. Wilson, B. Chakrabarti, P. Bullough, S. Foster and J. Hobbs, “The architecture of the Gram-positive bacterial cell wall,” *Nature*, vol. 582, no. 7811, pp. 294–297, 2020.
- [14] K. Li, X. Yuan, H. Sun, L. Zhao, R. Tang, Z. Chen, Q. Qin, X. Chen, Y. Zhang and H. Su, “Atomic force microscopy of side wall and septa peptidoglycan from *Bacillus subtilis* reveals an architectural remodeling during growth,” *Front. Microbiol.*, vol. 9, no. MAR, pp. 1–6, 2018.
- [15] A. Bisson-Filho, Y. Hsu, G. Squyres, E. Kuru, F. Wu, C. Jukes, Y. Sun, C. Dekker, S. Holden, M. Van Nieuwenhze, Y. Brun and E. Garner, “Treadmilling by FtsZ filaments drives peptidoglycan synthesis and bacterial cell division,” *Science (80-.)*, 2017.
- [16] D. W. Adams and J. Errington, “Bacterial cell division: Assembly, maintenance and disassembly of the Z ring,” *Nat. Rev. Microbiol.*, vol. 7, no. 9, pp. 642–653, 2009.
- [17] R. Tank, V. Lund, R. Turner, S. Kumar, L. Pasquina-Lemonche, N. Mullin, S. Foster and J. Hobbs., “STORM-force and the study of *B. subtilis*,” *Nat. Commun.*, vol. In prepara, 2020.
- [18] I. G. Boneca, Z. H. Huang, D. A. Gage, and A. Tomasz, “Characterization of *Staphylococcus aureus* cell wall glycan strands, evidence for a new β -N-acetylglucosaminidase activity,” *J. Biol. Chem.*, 2000.
- [19] W. Vollmer and S. J. Seligman, “Architecture of peptidoglycan: more data and more models,” *Trends Microbiol.*, vol. 18, no. 2, pp. 59–66, 2010.
- [20] S. J. Kim, J. Chang, and M. Singh, “Peptidoglycan architecture of Gram-positive bacteria by solid-state NMR,” *Biochimica et Biophysica Acta - Biomembranes*. 2015.
- [21] R. Wheeler, S. Mesnage, I. G. Boneca, J. K. Hobbs, and S. J. Foster, “Super-resolution microscopy reveals cell wall dynamics and peptidoglycan architecture in ovococcal bacteria,” *Mol. Microbiol.*, vol. 82, no. 5, pp. 1096–1109, 2011.
- [22] S. Kumar, M. Cartron, N. Mullin, P. Qian, G. Leggett, C. Hunter and J. Hobbs, “Direct Imaging of Protein Organization in an Intact Bacterial Organelle Using High-Resolution Atomic Force Microscopy,” *ACS Nano*, vol. 1, p. acsnano.6b05647, 2016.
- [23] S. M. Desmarais, M. A. De Pedro, F. Cava, and K. C. Huang, “Peptidoglycan at its peaks: How chromatographic analyses can reveal bacterial cell wall structure and assembly,” *Mol. Microbiol.*, vol. 89, no. 1, pp. 1–13, 2013.
- [24] V. R. F. Matias and T. J. Beveridge, “Cryo-electron microscopy reveals native polymeric cell wall structure in *Bacillus subtilis* 168 and the existence of a periplasmic space,” *Mol. Microbiol.*, vol. 56, no. 1, pp. 240–251, 2005.
- [25] V. R. F. Matias and T. J. Beveridge, “Native cell wall organization shown by cryo-electron microscopy confirms the existence of a periplasmic space in *Staphylococcus aureus*,” *J. Bacteriol.*, vol. 188, no. 3, pp. 1011–1021, 2006.
- [26] L. De León and L. Moujir, “Activity and mechanism of the action of zylasterone against *Bacillus subtilis*,” *Journal of Applied Microbiology*, vol. 104, no. 5. pp. 1266–1274, 2008.
- [27] E. Rojas, G. Billings, P. Odermatt, G. Auer, L. Zhu and A. Miguel, F. Chang, D. Weibel, J. Theriot and K. Huang, “The outer membrane is an essential load-bearing element in Gram-negative bacteria,” *Nature*. 2018.
- [28] S. Hussain, C. Wivagg, P. Szwedziak, F. Wong, K. Schaefer, T. Izoré, L. Renner, M. Holmes, Y. Sun, A. Bisson-Filho, S. Walker, A. Amir, J. Löwe and E. Garner, “MreB filaments align along greatest principal membrane curvature to orient cell wall synthesis,” *Elife*, 2018.
- [29] M. Dion, M. Kapoor, Y. Sun, S. Wilson, J. Ryan, A. Vigouroux, S. van Teeffelen, R. Oldenbourg and E. Garner, “*Bacillus subtilis* cell diameter is determined by the opposing actions of two distinct cell wall synthetic systems,” *Nat. Microbiol.*, 2019.
- [30] K. Asai, T. Ootsuji, K. Obata, T. Matsumoto, Y. Fujita, and Y. Sadaie, “Regulatory role of RsgI in sigI expression in *Bacillus subtilis*,” *Microbiology*, 2007.
- [31] R. D. Turner, S. Mesnage, J. K. Hobbs, and S. J. Foster, “Molecular imaging of glycan chains couples cell-wall polysaccharide architecture to bacterial cell morphology,” *Nat. Commun.*, 2018.
- [32] V. R. F. Matias and T. J. Beveridge, “Lipoteichoic acid is a major component of the *Bacillus subtilis* periplasm,” *J. Bacteriol.*, 2008.

Chapter 7 Antibiotic effect on *Staphylococcus aureus*

After decades of clinical use of β -lactams such as Penicillin and Methicillin, and glycopeptides such as Vancomycin, their killing mechanism is still unknown. Despite its crucial importance in society, there is not a clear understanding of why bacteria die after the introduction of antibiotics, the bulk of the state-of-the-art antibiotic research is focusing primarily on understanding the mechanisms of resistance and trying to develop new antibiotics. However, we think it is also important to fill the literature gap about what happens after the antibiotic targets are blocked. How exactly is the CW affected and how does it lead to cell death? This is the reason a long-term collaboration with Professor Simon Foster's group started with the objective of investigate the effect of antibiotics at a cellular and population level, proposing an improved model of cell death. In order to achieve this, it was necessary to combine conventional microbiology assays, super resolution fluorescence microscopy and other biophysical techniques with high resolution AFM.

In this chapter the antibiotic effect of two different compounds, Methicillin and Vancomycin, will be tested at molecular level on *S. aureus* WT sacculi. The techniques developed in the previous chapters are implemented here. Molecular resolution AFM together with quantitative image analysis will provide more insights into the structural changes the CW undergoes after antibiotic treatment eventually leading to cell death.

7.1 Methicillin versus Vancomycin

These two antibiotics have the similarity that both target the CW or its synthesis mechanism. This is a very common target for several antibiotic classes because this biomolecule and its enzymatic machinery are not present in mammalian cells, allowing a very specific recognition of bacterial infections inside a host organism. Methicillin and Vancomycin belong to two different classes of antibiotics: β -lactam and glycopeptides respectively.

7.1.1 β -lactam antibiotics

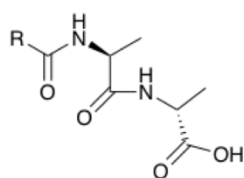
This class of antibiotics was the first ever discovered. The natural product Penicillin, produced by the mould *Penicillium chrysogenum*, was discovered by Alexander

Flemming in 1928. [1] It was used clinically for the first time in 1930 when Cecil Paine and his team used some doses in local patients in Sheffield. Later in 1940 Cecil and Howard Florey published wider studies about Penicillin effectivity in mice and humans. Due to the narrow range of action of penicillin against different pathogens, other derivatives were discovered since 1961, which are now known as the β -lactam class. [2]

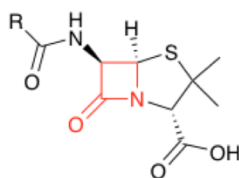
Different groups of antibiotic target different parts of the CW biochemical pathway: cytoplasmic, lipid linked or cell surface and assembly. This latter is where β -lactam antibiotics are focused. They are cell-wall synthesis inhibitors by covalently binding to PBPs and inhibiting their transpeptidation activity.

The PBPs are the main PG synthases that catalyse the polymerisation of the new PG material between the membrane and the CW. As previously explained, *S. aureus* has four different PBPs: PBP1, PBP2, PBP3 and PBP4 (see section 1.3.3.1). Only PBP 2 has both transglycosylation and transpeptidation activity; PBP 1 and 3 have only transpeptidation activity and PBP 4 is bifunctional with both DD-carboxypeptidase and transpeptidase activity. [3]–[6] All β -lactam antibiotics share the same chemical moiety: the β -lactam ring. [2], [7] This ring mimics the D-Ala-D-Ala terminus from the PG peptide side chains (see Figure 7.1). As the PBPs have an active binding site that recognizes the D-Ala-D-Ala dipeptide, when the β -lactam antibiotic is placed close to the PBPs, it acylates the serine hydroxyl group in the active site forming a covalent bond blocking their function as transpeptidases. [8]

D-Ala-D-Ala PG Terminus



Penicillin General structure



Methicillin structure

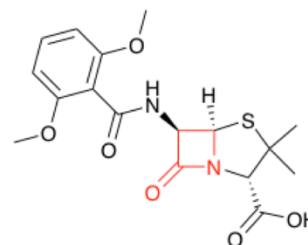


Figure 7.1 – Chemical structure from left to right of: D-Ala-D-Ala terminus in the PG peptide stem; Penicillin general structure where different radical groups gives different types of Penicillin; finally a derivate on the right, Methicillin.

This class is bactericidal, meaning a bacterial population is ultimately killed after treatment. Other antibiotics are bacteriostatic, slowing the growth rate. As β -lactams

target the PG synthesis and most of the synthesis in *S. aureus* occurs during cell division, they primarily kill cells during the division process. It is not clear what is the effect of these antibiotics on stationary cells, thus in this chapter, all experiments involving β -lactam antibiotic will be performed in exponential phase, to ensure cell death.

7.1.1.1 Methicillin

Methicillin is a semi-synthetic water soluble compound derived from the natural product Penicillin. Their chemical structures are very similar, maintaining the β -lactam ring (see *Figure 7.1*). It was the first antibiotic used to treat *S. aureus* infections and hence it was also known as Staphcillin. However, after extensive use of this antibiotic in clinical settings, the sensitive strains of *S. aureus* (MSSA) quickly evolved Methicillin resistance, creating MRSA strains. [9] The clinical use of Methicillin has been highly reduced. [10] However, this is a good β -lactam antibiotic model, precisely because understanding its mechanism of action could help combat antimicrobial resistance.

7.1.2 Glycopeptide antibiotics

Glycopeptides were first discovered in 1956. They are a different class of antibiotics targeting the final assembly steps of the PG synthesis pathway by binding to the D-Ala-D-Ala terminus of lipid II precursor, forming a non-covalent complex. Although PBPs would function in a cell treated with glycopeptides, they do not have a substrate to use in the polymerisation, affecting both transpeptidation and transglycosylation. [11], [12]

7.1.2.1 Vancomycin

The first identified Glycopeptide ever discovered was Vancomycin in 1956 by Eli Lilly. [13] It was also a natural product, produced by the soil organism *Amycolatopsis orientalis*. It was first used to treat Penicillin-resistant *S. aureus*. However, soon it was considered a last resource antibiotic and its commercialization was limited to avoid the emergence of resistant strains. Despite these efforts, in 2002 some clinical episodes of infections caused by Vancomycin Resistant *Staphylococcus aureus* (VRSA) were detected. The chemical structure of Vancomycin is very different from the β -lactam class. It is bigger and more complex (see *Figure 7.2*), there is less understanding on the link between Vancomycin and its target, but it is hypothesized that its size play an

important role acting like a physical barrier for other enzymes to interact with the substrate lipid II. Vancomycin has also been shown to attach to the D-Ala-D-Ala residues of the uncross-linked peptide stem of the CW. For this reason, it is a very common fluorescence dye of fixed bacteria for labelling the CW. [14]

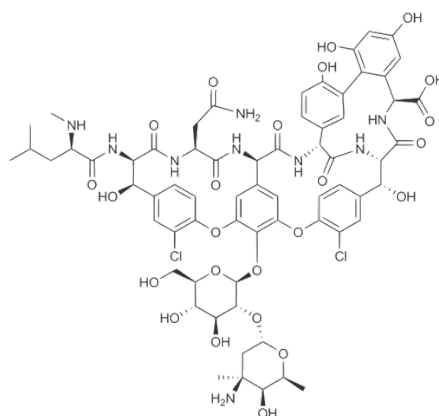


Figure 7.2 – Vancomycin chemical structure

7.1.3 Methicillin and Vancomycin effect at population level

The results from this section were produced by a fellow researcher: Dr Milena L Von Und Zur Muhlen. [15] However, the results are presented and summarized here because they are closely linked to the AFM experiments (explained below from *section 7.2* onwards).

7.1.3.1 Growing and killing assays

The limited literature about the understanding of the effect of antibiotics and determination of a molecular pathway leading to cell death was largely published in the late 90s. The techniques used vary between measuring killing using optical density (turbidity of cell culture) and counting the amount of survival cells (by using CFU counting). Other studies focused on micrographs from cryo-EM, leading to the first proposed model of the penicillin death pathway. This model claimed the cell undergoes its first cell cycle as normal and death occurs by cytoplasm leaking when it attempts to divide on the second cycle. [16] More recently, in the late 2010s other groups have focused on gene depletion mutants to study the influence of individual enzymes/proteins on the antibiotic molecular pathway. Some of these studies led to contradicting theories to those previously proposed, one of the them says the cause of

death are the presence of Reactive Oxygen Species (ROS) leading to fatal damage of the genetic material.[17] Regarding glycopeptides, most of the studies were focused on tolerance and resistance instead of understanding the molecular pathway leading to cell death.

All of these competing models create a confusing background. So, the work carried on in our groups started by performing killing assays to determine the killing dynamics in a population of *S. aureus* SH1000, without assuming any of the previous theories correct.

The minimum inhibition concentration (MIC) of Methicillin required to kill *S. aureus* under *in vitro* conditions was measured by serial dilution. The MIC against *S. aureus* SH1000 was found to be 4 μ g/mL. All experiments involving Methicillin presented in this Chapter were conducted with a concentration of 10 times the MIC to oversaturate the system and ensure that eventually the cell population would be killed (*i.e.* 40 μ g/mL). The same experiment was performed for Vancomycin with the MIC being 4 μ g/mL as well. [15]

An *S. aureus* overnight cell culture was resuspended and allowed to grow up to O.D₆₀₀=0.2-0.3. Then, a 10xMIC concentration of Methicillin (40 μ g/mL) and Vancomycin (40 μ g/mL) were added to different cultures. These types of experiments are based on studies performed in the 60s.[18]–[20] Every 30 min for the first 2 h, 1ml of the sample was rinsed and plated into fresh Agar. Then, between the 2nd h and the 6th h a sample was taken only every hour. These plates were grown overnight and the CFU were counted the next day. For analysing the Vancomycin treated culture samples were taken every hour from 0-6 h. The resulting graphs are presented in *Figure 7.3* to be directly compared.

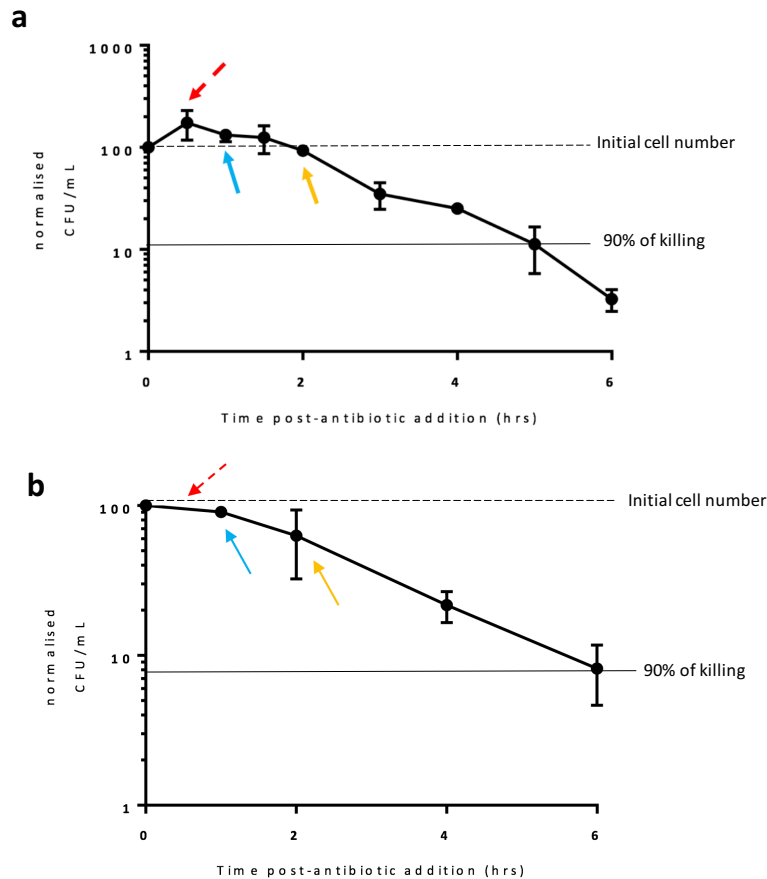


Figure 7.3 – a) Effect of 40µg/mL Methicillin on *S. aureus* SH1000, CFU/ml were counted at each time-point. The data was normalised by setting the first time point to 100%. The experiment was done in triplicates; b) Effect of 40µg/mL Vancomycin on *S. aureus* SH1000, CFU/ml were counted at each time-point. The data was normalised by setting the first time point to 100%. The experiment was done in triplicates. Adapted with permission from [15]

Figure 7.3 a shows the plot of all the CFU/ml extracted from the cell culture after the treatment of Methicillin. After the first 30min of antibiotic treatment, there is an increase in cell population (see dashed red arrow). However, after 1h of antibiotic treatment, the cells start to die (see blue arrow). Then, after 2h, the cells have returned to the initial cell number (yellow arrow, black dashed line). The 90% of the killing was reached after 5h of treatment (see black line). Figure 7.3 b shows the plot of all the CFU/ml extracted from the cell culture after the treatment of Vancomycin. There is a gradual killing that is slower in the first hour and then has a constant rate from 2h to 6h. In contrast to Methicillin, by 2 h (yellow arrow) the cell number is below the initial cell number, meaning Vancomycin kills faster for the first 2 h. However, the 90% of the killing was reached after 6 h of treatment, instead of 5 h like Methicillin.

It was decided that the initial phase of the killing process (between 0 and 2h) would be the focus of this investigation to understand how the cells are dying. Four samples were

chosen for each antibiotic (see *Table 7.1*) and these were used to perform both fluorescence and AFM experiments.

Table 7.1 – Nomenclature of samples at different time points after 10xMIC Methicillin and Vancomycin treatment

<i>Type of Antibiotic</i>	<i>Sample name</i>	<i>Time after Antibiotic addition</i>
<i>Methicillin</i>	WT M0	0 min (Control)
	WT M30	30 min
	WT M60	60 min
	WT M120	120 min
<i>Vancomycin</i>	WT V0	0 min (Control)
	WT V30	30 min
	WT V60	60 min
	WT V120	120 min

7.1.3.2 Cell volume variability

Once the killing dynamics of Methicillin and Vancomycin were studied, the next logical step was to interrogate the morphology of the cells across the selected time-points.

Structural illumination microscopy (SIM) was chosen due to its high-yield and its capacity to obtain images with lateral resolution half of the diffraction limit (100-130 nm), being able to discern several dye molecules attached to the cell wall. The chosen dye for this experiment was Alexa Fluor 555 *N*-hydroxysuccinimide (NHS) ester. This ester functionality is reactive towards D-Ala-D-Ala such as the ones found at the end termini of the side chains of PG. [21]

The cells were fixed with 16 % (w/v) of paraformaldehyde after the time points shown in *Table 7.1*. Then, they were incubated with 0.5 mg/ml of NHS ester for 30 min. Finally, the samples were washed and imaged using SIM. The cell volume was measured using a reported analysis method [22] primarily using Fiji software.[23] The resultant images and analysis are summarized in *Figure 7.4*.

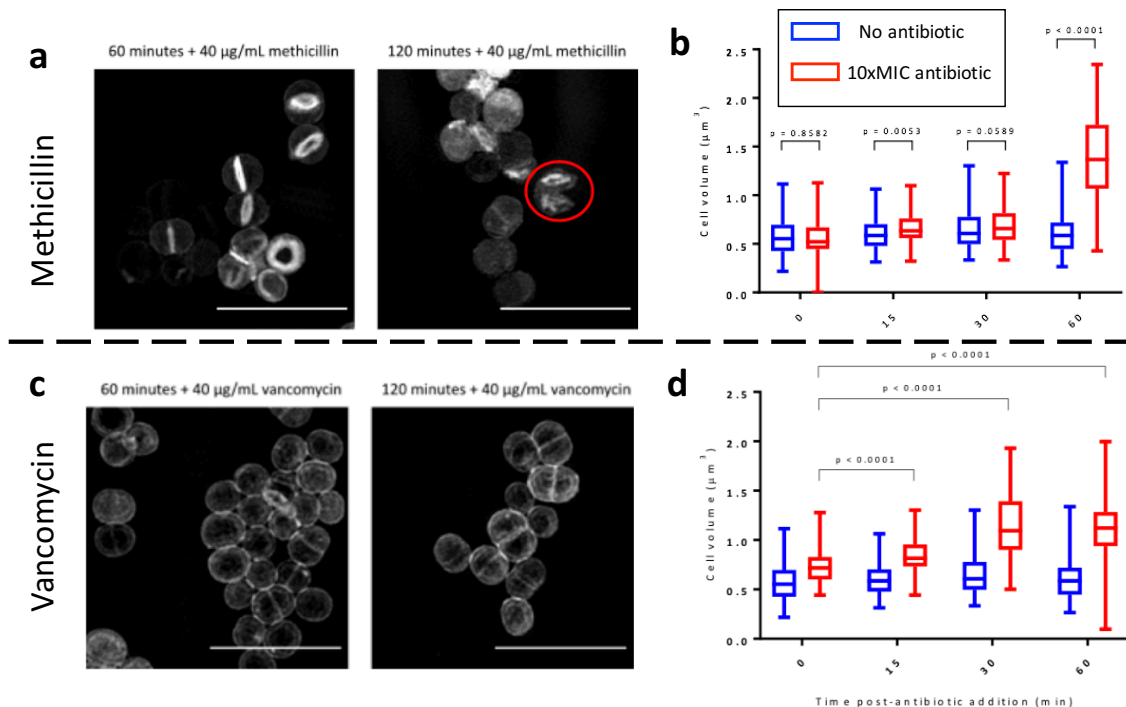


Figure 7.4 – a) SIM images of *S. aureus* treated with 10xMIC Methicillin for 60 and 120 min (WT, scale bars = 5 µm; b) The volume of multiple cells was measured from the SIM images (n=100 each time point). c) SIM images of *S. aureus* and treated with 10xMIC Vancomycin for 60 and 120 min, scale bars = 5 µm; b) The volume of multiple cells was measured from the SIM images (n=100 each time point). The measurement was performed with Fiji. Figure adapted with permission from [15]

Figure 7.4 a shows SIM images of areas containing several cells. From the morphology, it was identified that after 60 min of Methicillin treatment the cells were deformed. After 120 min cells were highly deformed and even some remnants of dead cells were visualized (i.e. sacculi, see red circle in Figure 7.4 a). Figure 7.4 b shows a graph of the cell volume measured from several images similar to Figure 7.4 a. No significant increase of cell volume was found in the first 30 min of treatment. However, the cell volume increased significantly (twice as the control) after 60 min of Methicillin treatment. No measurements were performed after 60 min, because most of the cells were already dead, not allowing relevant volume measurements. Figure 7.4 c shows SIM images of areas containing several cells after 60 and 120 min of Vancomycin treatment. In contrast to Methicillin, no significant change was identified in the morphology of the cells. Figure 7.4 d shows a graph of the cell volume measured from several images like in Figure 7.4 c. There is a significant increase after 15 min of Vancomycin treatment and even bigger difference was found after 60 min. The maximum volume increase was 1.5 times the control after 30 min of treatment. No measurements were performed after 60 min either as a comparison between antibiotics was required.

The significant increase in cell volume was bigger and occurred earlier for Vancomycin treatment in comparison to Methicillin treatment. However, fewer morphological changes were visible in the SIM images.

The significant increase in cell volume was hypothesized to be due to imbalance between peptidoglycan synthesis and hydrolysis. Because, as shown previously,[24] synthesis and hydrolysis are required for maintaining a normal cell morphology (see *Chapter 5*) and a constant cell volume.

7.1.3.3 Di-peptide and ^{14}C -GlcNAc incorporation

The amount of synthesis occurring in a cell before and after addition of antibiotics was quantified by two methods: measuring the Fluorescent D-amino-acid (FDDA, *i.e.* di-peptide) and ^{14}C -GlcNAc incorporation. These methods determine the level of transpeptidase and trans-glycosylase activity respectively. The first method measures the fluorescence intensity of D-amino-acids; which the cell incorporates into new peptide side chains on the PG structure of the CW. The second method is based on introducing a radioactive sugar (^{14}C -GlcNAc) [25] which the cell introduces into the new glycan strand being added to the CW; then the radiation levels are quantified in dose per minute (DPM) per each CFU.

The results of these two quantifications for both antibiotics are presented below in *Figure 7.5*.

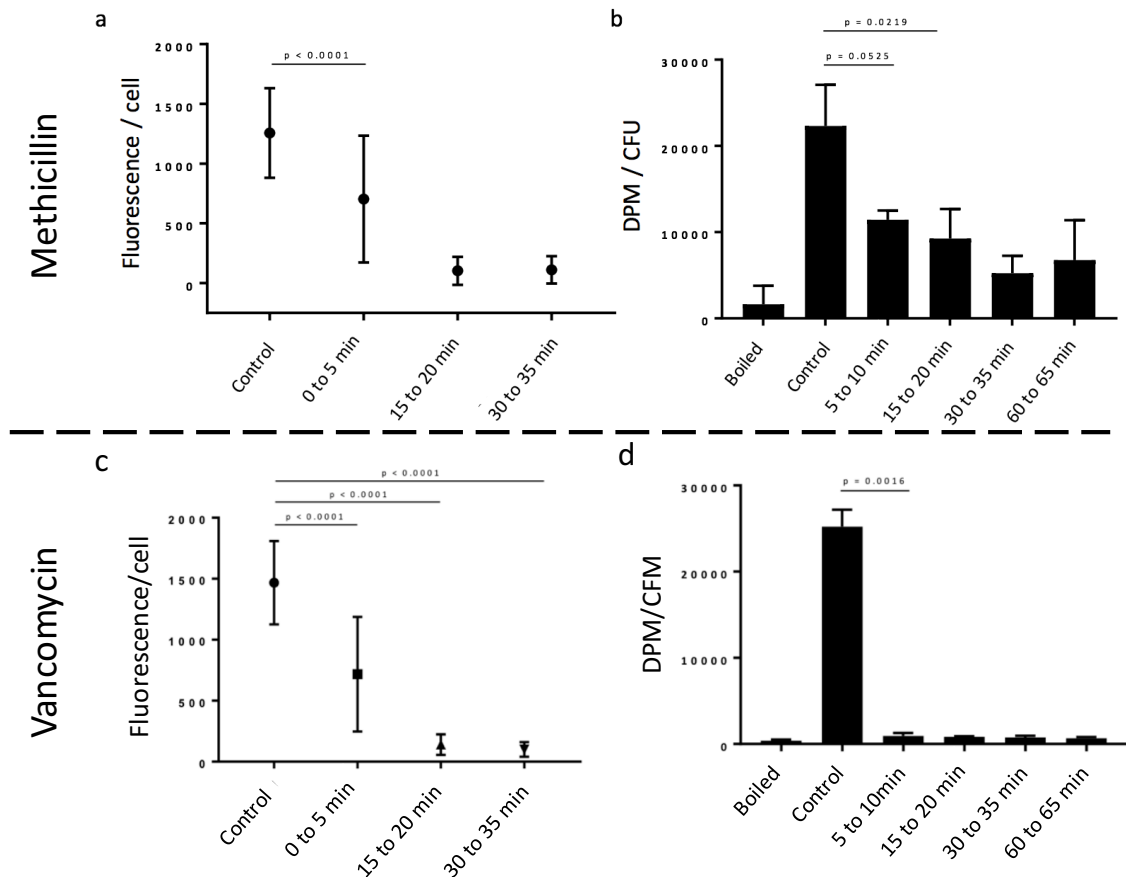


Figure 7.5 – a) Quantification of di-peptide incorporation in *S. aureus* after 10xMIC Methicillin treatment; b) Quantification of ¹⁴C-GlcNAc incorporation in *S. aureus* after 10xMIC Methicillin treatment; c) Quantification of di-peptide incorporation in *S. aureus* after 10xMIC Vancomycin treatment; d) Quantification of ¹⁴C-GlcNAc incorporation in *S. aureus* after 10xMIC Vancomycin treatment. All graphs have the p value specified between some of the time-points. Adapted with permission from [15]

Figure 7.5 a shows the di-peptide incorporation with significant decrease of the transpeptidase activity on the first 5 min of Methicillin treatment and only residual incorporation is present after 15 min. Figure 7.5 b shows the ¹⁴C-GlcNAc incorporation with significant decrease of the trans-glycosylase activity after 15 min of Methicillin treatment. However, after 60 min there is still 30% of the DPM/CFU from the control. Figure 7.5 c shows significant decrease of the transpeptidase activity on the first 5 min of Vancomycin treatment and only baseline levels were observed after 15 min. These results are very similar to Methicillin (see Figure 7.5 a). Figure 7.5 d shows a significant decrease in the first 5 min of treatment and the rest of the time points show baseline levels. This is very different to the Methicillin treatment in which after 60 min there was still 30 % of the DPM/CFU from the control (see Figure 7.5 b). The almost immediate decrease of trans-glycosylation and transpeptidation activity after Vancomycin

treatment agrees with previous published work that looked at the effect of 25 µg/mL on *S. aureus* cells and found an 80% decrease on CW incorporation. [18]–[20]

During methicillin treatment there is an addition of ¹⁴C-GlcNAc while the di-peptide is no longer incorporating. This incongruity could have different explanations. The ¹⁴C-GlcNAc could be added to lipid II, meaning the cell would be accumulating PG precursors without building new PG. Alternatively, it could be due to the presence of other transglycosylases which could still be active: PBP2, Sgt, MgtA, FtsW and RodA. However, it is very unlikely that glycan chains could be incorporated into the CW without being crosslinked. A third explanation is that ¹⁴C-GlcNAc is added to the linkage unit of WTA, the synthesis of which could initially be unaffected by Methicillin. The fact that FDAA (di-peptide) incorporation almost stops immediately after 30 min of treatment contradicts other theories about the cell dying after the first cell cycle was complete. This was also corroborated with two coloured fluorescence to investigate the fate of new material incorporated 5 min before the antibiotic was added (results not shown here).[15] The conclusion from this experiment is that the cells seem to be stuck in the first cell cycle when the antibiotic is added.

All of these data presented in this section strongly suggest that lack of incorporation of new PG while unperturbed hydrolysis weakens the CW ultimately leads to cell death.

This was common for both antibiotics, indicating some similarities in the killing mechanism. Contrary to other theories, it has been shown through the SIM images that generalised lysis is not the cause of death in *S. aureus* after Methicillin or Vancomycin treatment. Thus, subtle changes in PG architecture are expected to lead to cytoplasm leakage and ultimately to cell death. These structural changes cannot be assessed with the techniques presented in this section. Atomic Force Microscopy was chosen to discern the structural nanometric changes caused by Methicillin and Vancomycin.

7.2 *Staphylococcus aureus* sacculi treated with Methicillin

To assess the effect of Methicillin by AFM and complement the results at population level (*section 7.1.3*), the sample preparation needed to be as similar as possible. The use of living cells was not a viable option because the growing conditions under the AFM would be rather different than the well-controlled *in vitro* environment usually used (as

already experienced in the SDS experiment, see *section 6.2.3*). Thus, cells were grown *in vitro* with the same conditions as the killing curve experiment (see *Figure 7.3*), then the antibiotic was added. After certain treatment time-points, the cells were purified, avoiding any fixing steps. Alternatively, the centrifugation and boiling steps from the original protocol [26], [27] were inverted, in order to boil the cells right after removing them from the culture (see more details in *sections 2.2.2.3, 2.2.2.5*).

Thus, using the time points obtained from the killing curves (see *Table 7.1*) three types of sacculi were prepared from the same cell culture after adding the antibiotic, finally a control was prepared at the same time in a different flask (see *Figure 7.6*).

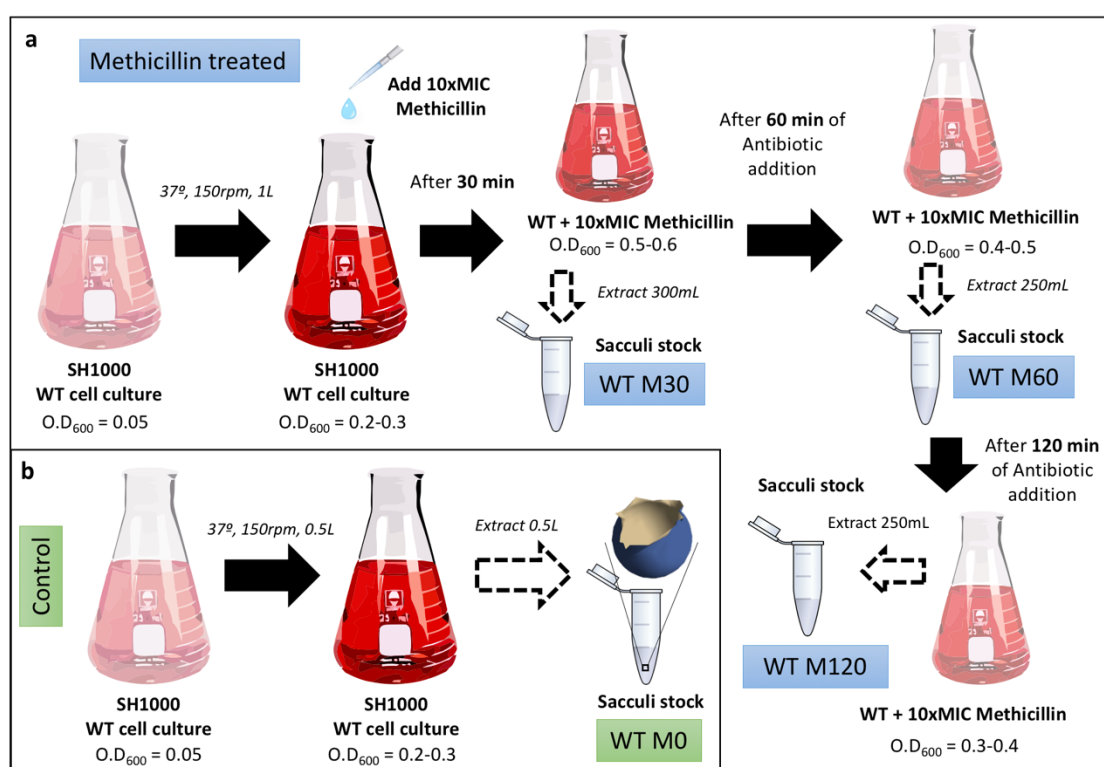


Figure 7.6 – a) Schematics of sacculi preparation step by step. Three different sacculi were prepared from this 1L pot: WT M30, WT M60, WT M120; b) Control sacculi (WT M0) extracted at the same $O.D_{600}$ as when the antibiotic was introduced in the treated cell culture. Vancomycin samples were prepared following the same protocol

Figure 7.6 shows the four different samples extracted from this experiment: WT M0, WT M30, WT M60 and WT M120 (see *Table 7.1*). They are the exact same time-points as the highlighted ones on the killing curve (see *Figure 7.3*) and the SIM images (see *Figure 7.4*). Thus, direct comparison between AFM data and these previous experiments would be possible. The same protocol (see 2.2.2.5) was followed for Vancomycin using the same time-points to be able to compare directly the molecular effect of both antibiotics.

7.2.1 Methicillin effect in sacculi after 30 min treatment

Four samples were prepared according to the previous sections: WT M0, WT M30, WT M60 and WT M120. The sample WT M0 was imaged and no apparent differences were found with other batches of healthy *S. aureus* sacculi imaged previously. Thus, from now on, all the rest of the samples presented in this chapter will be compared to the results already obtained from non-treated samples of *S. aureus* sacculi presented in *chapter 3* and *4*. Sample WT M30 was imaged, the best images can be found in *Figure 7.7*.

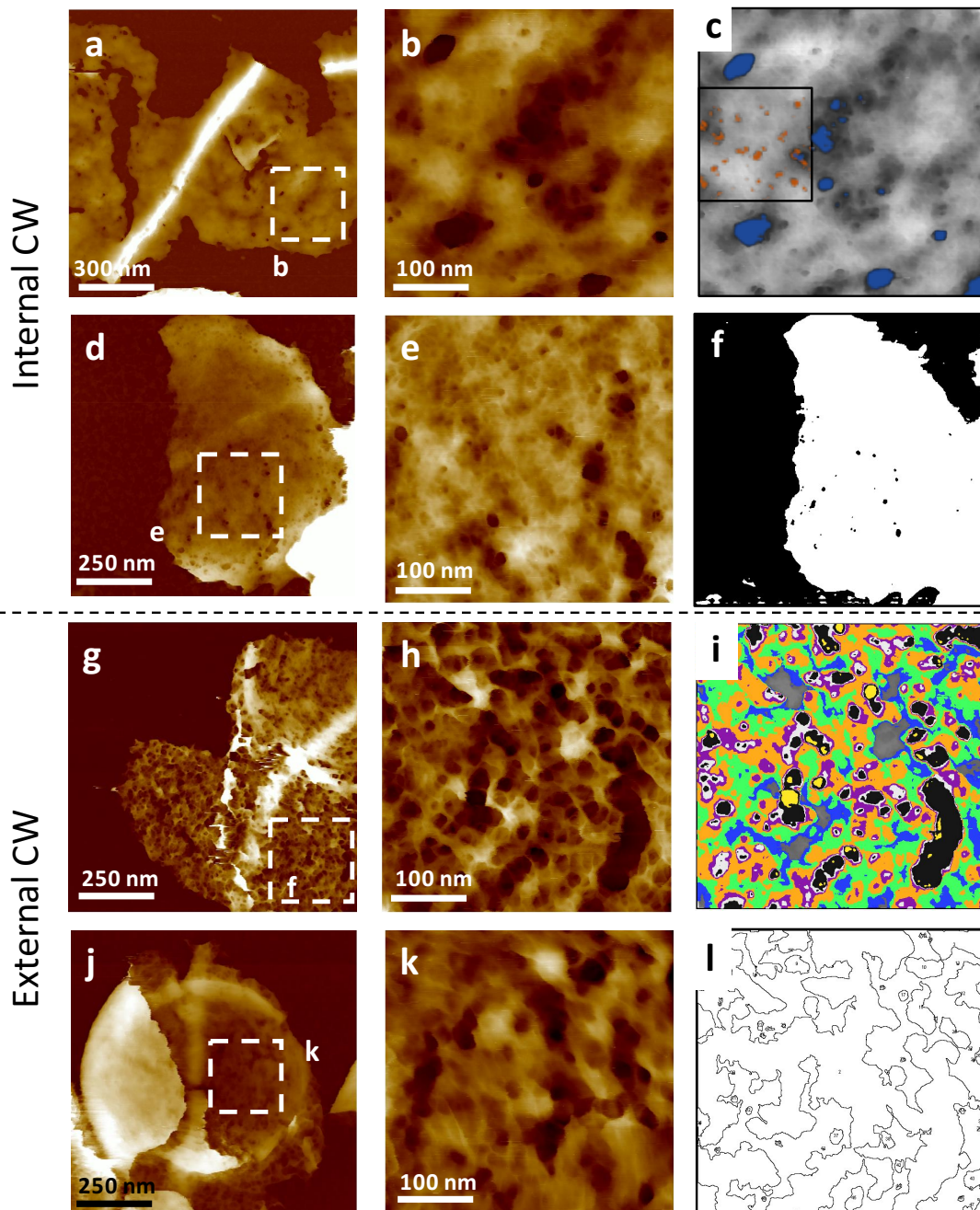


Figure 7.7 – WT M30. a) sacculus fragment corresponding to the internal surface because there is a piecrust in the middle of the fragment with aspect ratio < 1 ; b) zoomed image from 'a'; c) Image 'b' in grey scale with two

superimposed analyses featuring the perforating holes (blue) the internal mesh (orange); d-f) another example of internal surface; g-i) Mature external surface; j-l) Nascent external surface, rings already transitioning to mesh.

The images from Figure 7.7 were obtained under the experimental conditions summarized in Table 7.2.

Table 7.2 – Experimental conditions used to obtain data from Figure 7.7. See 2.3.2.2.2.

AFM TIP	AFM MODE	SAMPLE TYPE	ENVIRONMENT	SURFACE	SPECIFIC CONDITIONS
FAST SCAN - D	PeakForce Tapping	WT M30 Stock A Batch 6 Dilution 5	150 mM KCl + 10mM Tris pH=7.8	PLL coated MICA	Dried to be imaged 3 months later (no tip sonicated)

Figure 7.7 shows two groups of images, a-f corresponding to the internal CW and g-l to the external CW; Figure 7.7 j,k correspond to concentric rings. As sacculi containing rings were rarely found in WT M30, no further analysis was performed on them. There are some scars on the internal CW. After observing many sacculi with these types of scars such as Figure 7.7 a-e a new analysis approach was designed to characterize them. The method is summarized in Figure 7.8.

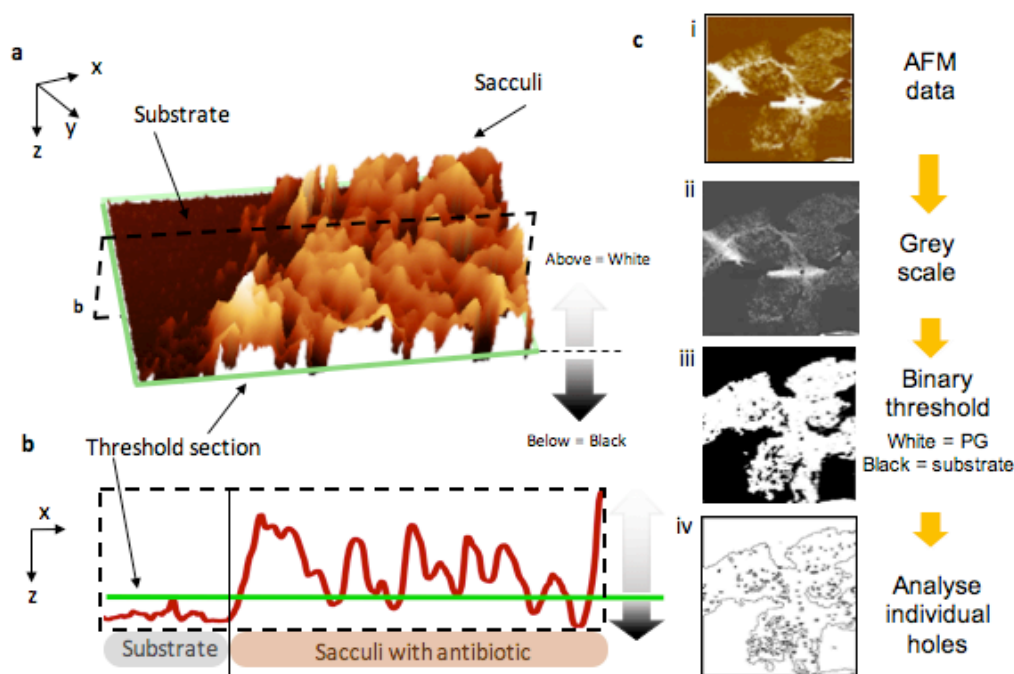


Figure 7.8 – a) schematics of the three dimensional space occupied by the sacculi with respect to the substrate and the position where the threshold touches the sacculi (green square); b) same as 'a' but lateral view, where for a healthy sacculi it is clear the threshold would divide between the sacculi material above and the substrate below; c) summary of all the steps required to perform this analysis. Software used Fiji [23].

Two different types of images were analysed: 1) low-magnification images with entire sacculi like Figure 7.7 a, d; 2) high-magnification images like Figure 7.7 b, e. Low-

magnification images are ideal to assess if the scars perforate the total thickness of the sacculi because there is flat substrate as reference (see *Figure 7.8 a*). First, the AFM image is converted into grey scale with Fiji [23] (*Figure 7.8 c (ii)*) and then a threshold is applied. The position of this threshold is crucial for this analysis, it needs to be right above the features on the substrate (see green line in the lateral profile *Figure 7.8 b*). The data points above the threshold correspond to PG material from the sacculi (colour white), regions below the threshold correspond to the substrate or scars (*i.e.* holes) entirely perforating the sacculi (colour black). The binary image clearly highlights the holes due to antibiotic treatment (see black holes in *Figure 7.8 c (iii)*). Then, the holes can be analysed with the *analyse particles* tool in Fiji (see *Figure 7.8 c (iv)*). The number of holes and their size was analysed for all samples and summarized in *Figure 7.23*. A representative example was chosen for WT M30 which was shown in *Figure 7.7 f*.

The high-magnification images containing the finer architecture of the internal PG were analysed in a similar manner to that shown in *Figure 7.8*. However the threshold was applied at the bottom 20th slice (each image has 255 slices once converted to grey scale, see *section 6.2.1.2*). The black regions were considered to be perforating holes despite not having the reference substrate, but they were not included in the previous data set extracted from the low-magnification images. These holes were overlapped with the grey scale image (see blue regions on *Figure 7.7 c*). It was evident, that most of the non-perforating pores were not included in this analysis. Therefore, image crops were performed in the PG areas between the holes, containing the non-perforating pores (*i.e.* internal mesh), see orange regions in *Figure 7.7 c*. Then, a threshold was made at 50 % of the image depth following the semi-automated analysis presented in *section 4.2.1.2*. Both types of data: holes and internal mesh were measured using the *analyse particles* tool in Fiji and their cumulative fraction of total area was plotted together with the internal mesh of healthy sacculi (see *Figure 4.10 a*). A data set of n=3 images similar to *Figure 7.7 c* was used to produce the graph from *Figure 7.9* below.

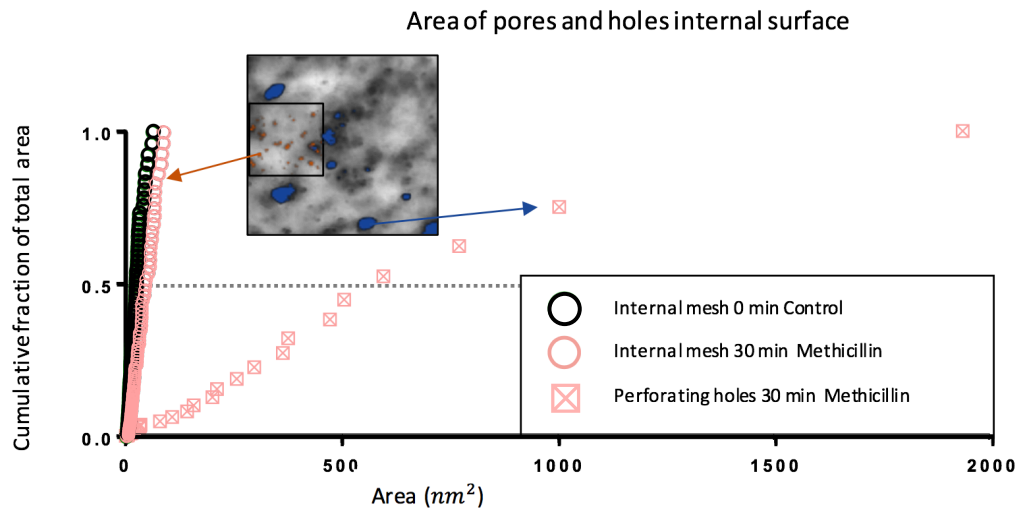


Figure 7.9 – Plot presenting individual values of pore area measured from internal surface images treated with $10\times\text{MIC}$ Methicillin for 30 min (pale pink) and comparing the results to the control of untreated cells (black).

Figure 7.9 shows three different sets of data: the control black circles, which corresponds to the internal mesh presented previously in Figure 4.10 a with $\text{HCFA}_{\text{Diameter}} (\text{HCFD}) = 6.4 \text{ nm}$ (see section 4.2.2 for more details); the internal mesh like the pores highlighted in orange in the example image (pink circles), with a $\text{HCFD}_{\text{pores}} = 7.3 \text{ nm}$ and the third data set corresponds to the perforating holes (squared crosses, highlighted in blue in the example image) having a $\text{HCFD}_{\text{holes}} = 26.5 \text{ nm}$. This value clearly exceeds the theoretical calculation of critical pore diameter $8\text{-}12 \text{ nm}$ as the limit which would lead to cell membrane bursting. No significant difference was found between the internal mesh of healthy sacculi and WT M30.

Regarding the external surface of the CW, the two-dimensional sectioning (*i.e.* depth maps) explained in section 3.5.4.2 was applied. Figure 7.7 i is the depth map (colour depths from top of the image: blue = 5 nm, green = 10 nm, orange = 15 nm, purple = 20 nm, white = 23 nm, black = 25 nm and yellow = 30 nm) of Figure 7.7 h. The orange slice at 15 nm of depth is presented in Figure 7.7 l. The depth maps are useful to visually compare different data sets. However, to answer the question: is the porous three-dimensional architecture being affected by the antibiotic regarding the size, depth and number of the pores?; the automated analysis on 255 slices of the images developed in section 6.2.1.2 (see Figure 6.15) was applied to external mesh images similar to Figure 7.7 h. The HCFA curves and the number of pores graphs like Figure 6.16 were obtained for WT M0, $n=6$ images and WT M30, $n=4$ images (see Figure 7.10).

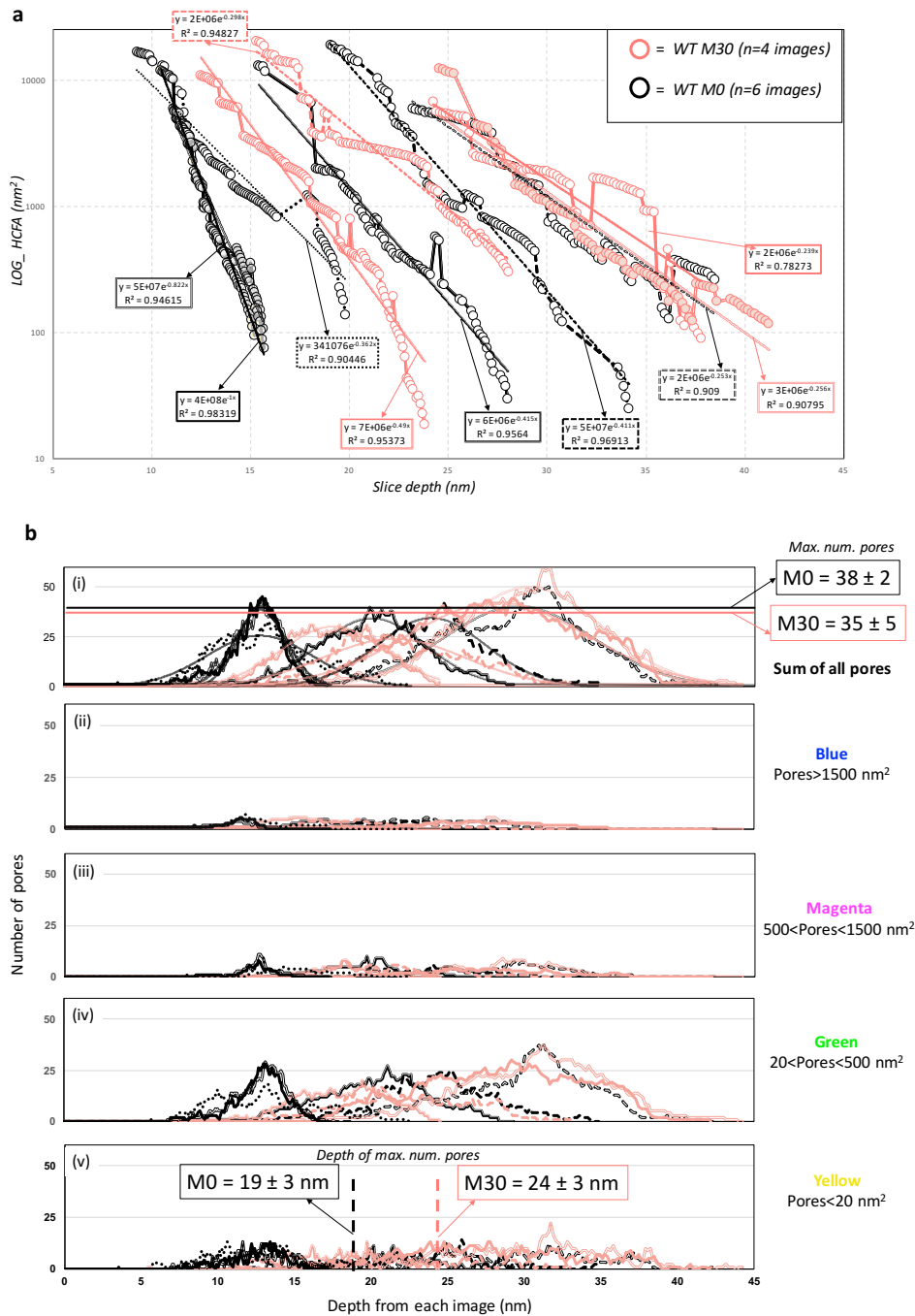


Figure 7.10 – a) HCFA curves for different WT M30 images (the pink curves) and M0 images (black curves), an exponential fit and the R² are plotted as dotted lines for each curve; b) number of pores versus slice depth, there are five identical plots: (i) Total number of pores for each slice, images from the same size have been used, (ii) Blue pores, (iii) Magenta pores, (iv) Green pores and (v) Yellow pores (see all sizes in Figure 6.15 and Appendix 2)

Figure 7.10 a shows the HCFA curves from individual images (*S. aureus* WT M0 black and WT M30 pink curves). The trend of the curves and the ranges of HCFA values are very similar for both data sets. A comprehensive comparison between the exponential coefficients for all the different antibiotic samples is summarized at the end of the chapter in Figure 7.22. Figure 7.10 b shows all the number of pores per depth graphs obtained from the classification of different pore sizes. These graphs were produced for

all antibiotic, but from now on only the total number of pores and the green group will be presented because there was no difference with respect to the control for the yellow, magenta and blue groups. Two parameters were extracted from these plots: the maximum number of pores (from the gaussian peak, *Figure 7.10 b(i)*); and the slice depth corresponding to the maximum number of pores *Figure 7.10 b(v)*). These two parameters were calculated for all the different antibiotic samples and they are summarized at the end of the chapter in *Figure 7.22*.

7.2.2 Methicillin effect in sacculi after 60 min treatment

Sample WT M60 was prepared and imaged in the same way as *section 7.2.1*, the summary of the best images are shown in *Figure 7.11*.

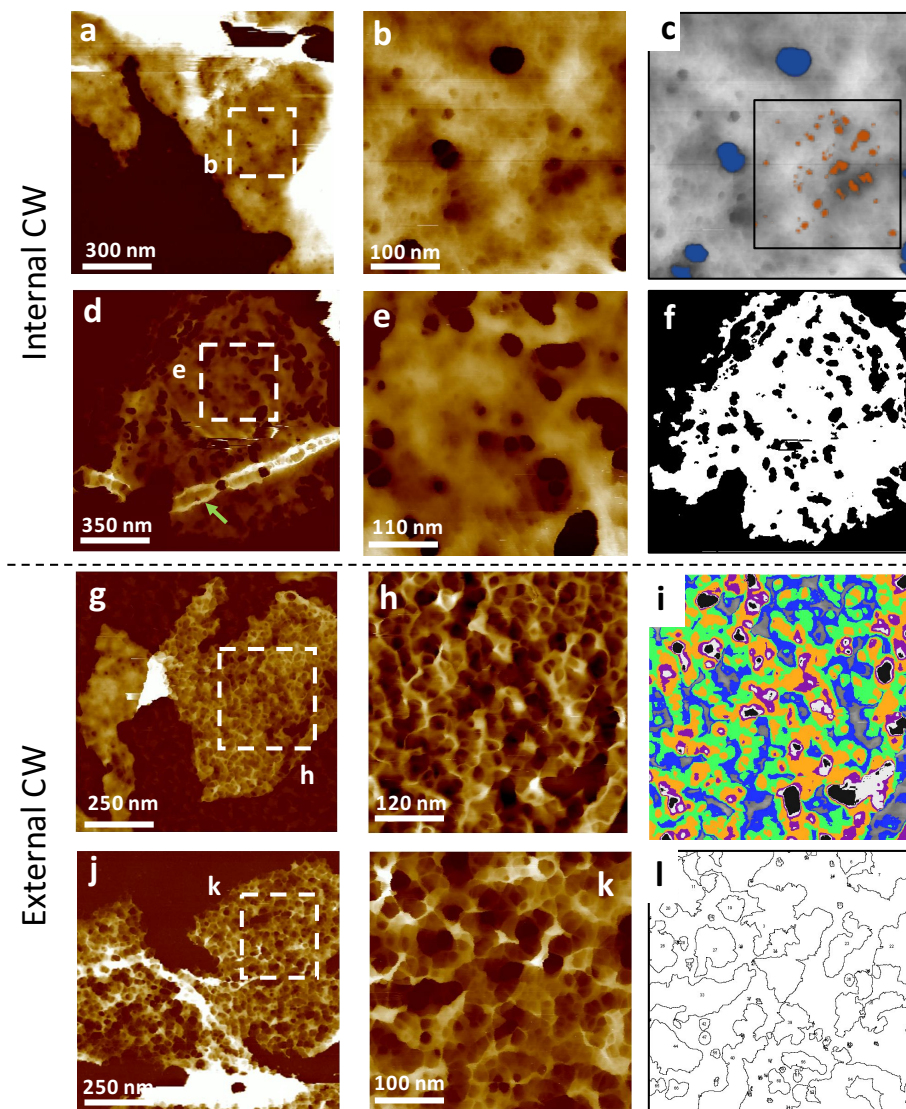


Figure 7.11 – WT M60. a) example of sacculus fragment with internal structure upwards; b) zoomed image from ‘a’; c) Image ‘b’ in grey scale with two superimposed analysis featuring the perforating holes (blue) the internal mesh

(orange); d) sacculus fragment corresponding to the internal surface because there is a piecrust in the middle of the fragment with aspect ratio < 1 (green arrow); e) zoomed image from 'd'; f) Analysis of the perforating holes, binary image representing black = the substrate; white = sacculi material above; e-h) Mature external surface; i) pore depth map from image 'h'; j-k) another example of mature external surface; l) two dimensional sectioning at 15 nm depth from image 'k'.

The images from *Figure 7.11* were obtained under the experimental conditions summarized in *Table 7.2*. The samples WT M30 and WT M60 were prepared from the same batch and the same day, as explained in *Figure 7.6*. *Figure 7.11* presents the same organization and structure as *Figure 7.7*, *a-f* corresponding to the internal CW and *g-l* to the external CW. The analysis of the internal structure is shown in *Figure 7.12 a* performed with the same methodology as *Figure 7.9*. The binary transformation explained in *Figure 7.8* was applied to image *Figure 7.11 d* resulting in *Figure 7.11 f*, where big perforating holes cover the entire sacculi. The depth map of *Figure 7.11 i* represents different depths which are colour coded in the same way as *Figure 7.7 i*. Another example of external mesh is shown in *Figure 7.11 k* and *Figure 7.11 l* represent an individual slice at 15 nm of depth. The same quantitative analysis on the external CW from *Figure 7.10* was performed for WT M60 and it is summarized in *Figure 7.12 b, c*.

A data set of WT M60 n=3 internal CW images similar to *Figure 7.11 c* was used to produce the graph from *Figure 7.12 a* below. A data set of WT M60 n=4 external CW images similar to *Figure 7.11 h and k* were used to produce graphs from *Figure 7.12 b-c*. The main difference between the WT M60 internal mesh pores (red circles) and the WT M30 internal mesh from *Figure 7.9* is a slightly different trend with respect to the control. All the **HCFD values** are summarized in *Table 7.4* and *Figure 7.21* and the conclusion will be extracted from the comparison between all the antibiotic samples. Regarding the external pore size analysis in *Figure 7.12 b*, the HCFA curves follow similar trends as WT M0 except for sudden increases in pore size in two of the images (see green arrows), the exponential fit of these curves was poorer with $R^2 \sim 0.8$, but these changes in individual slices do not affect the overall analysis (see exponential coefficient values in *Figure 7.22*). The number of pores and depth analysis in *Figure 7.12 c* show no difference with respect to WT M0 or WT M30 except for one image having 3-5 pores in the bottom slice instead of 1 like the rest of the images analysed. This could be attributed to green pores that are perforating holes, see inset and the overlap with

performing analysis in Figure 7.12 c (ii). This small difference in the graph, does not affect the parameters extracted from this analysis, summarized as well in Figure 7.22.

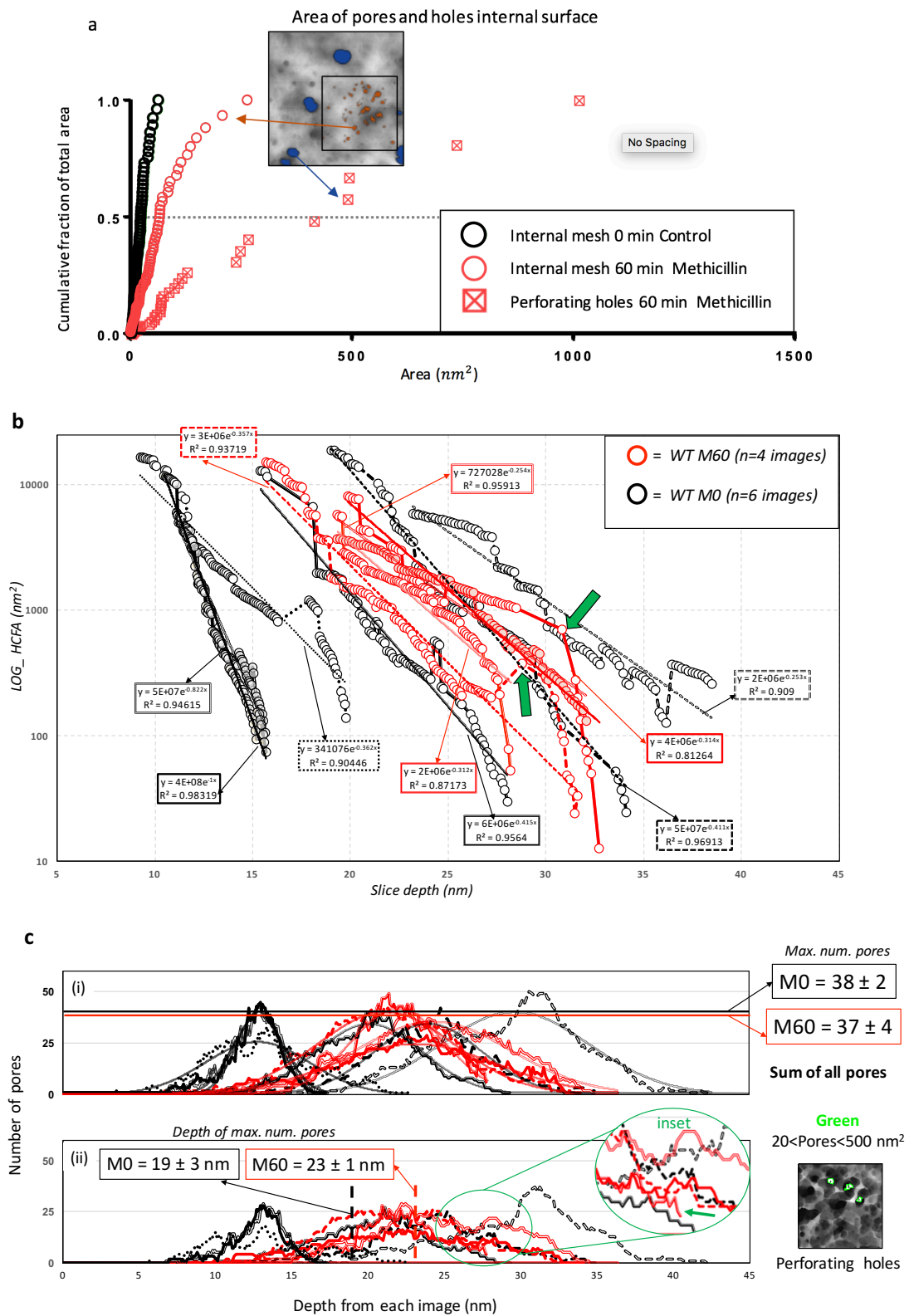


Figure 7.10 – a) Plot presenting individual values of pore area measured from internal surface images treated with 10xMIC Methicillin during 60 min (red) and the control, M0 (black). b) HCFA curves for different WT M60 images (the red curves) and M0 images (black curves), an exponential fitting and the R^2 are plotted as dotted lines for each

curve, green arrows indicate local anomalies; c) number of pores versus slice depth, there are two identical plots: (i) Total number of pores for each slice and ii) pores between 20 and 500 nm² (Figure 6.15 and Appendix 2)

7.2.3 Methicillin effect in sacculi after 120 min treatment

Sample WT M120 was prepared and imaged in the same way as section 7.2.1, the summary of the best images are shown in Figure 7.13.

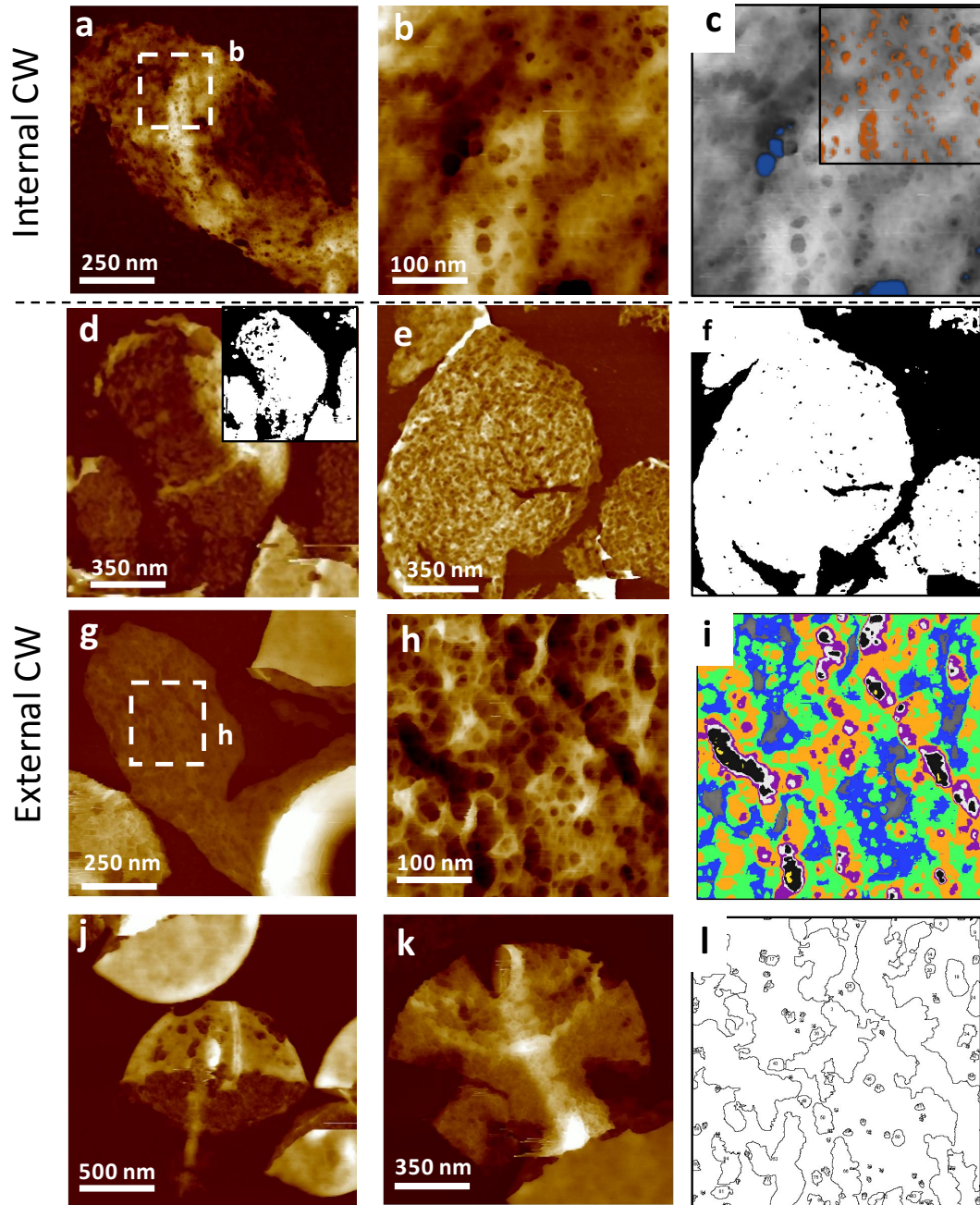


Figure 7.13 - WT M120. a) example of sacculus fragment with internal structure upwards; b) zoomed image from 'a'; c) Image 'b' in grey scale with two superimposed analyses featuring the perforating holes (blue) the internal mesh (orange); d) sacculus fragment corresponding to the external surface, Inset: perforation analysis; e) another example of flat external structure; f) Analysis of the perforating holes, binary image representing black = the substrate; white = sacculi material above; g-h) Mature external surface at high resolution; i) pore depth map from image 'h'; j-k) examples of entire sacculi suggesting these cells lysed; l) section at 15 nm depth from image 'h'.

The images from *Figure 7.13* were obtained under the experimental conditions summarized in *Table 7.2*. The sample WT M120 was also prepared from batch 6 as explained in *Figure 7.6*. *Figure 7.13* presents the same organization and structure as *Figure 7.7*, *a-f* corresponding to the internal CW and *g-l* to the external CW. The binary transformation was applied to image *Figure 7.13 d-e* resulting in *Figure 7.13 d, inset* and *Figure 7.13 f*, where the big perforating holes observed in WT M60 are not found in here, smaller perforations cover the sacculi. The depth map of *Figure 7.13 i* represents different pore depths from *Figure 7.13 h*. Two examples of partially whole sacculi showing both the external and internal PG surfaces are displayed in *Figure 7.13 j-k*. These broken sacculi are similar to the ones found in the SIM images at the same time-point (see *Figure 7.4*), which indicates that by 2 h some of these cells were already dead when the sacculi were purified.

A data set of WT M120 n=2 internal CW images similar to *Figure 7.13 c* was used to produce the graph from *Figure 7.14 a* below. A data set of WT M120 n=3 external CW images similar to *Figure 7.13 h* were used to produce graphs from *Figure 7.14 b-c*.

Figure 7.14 a and *Figure 7.12 a* are almost identical, so no need to comment on any special characteristics of WT M120 regarding internal PG analysis. Regarding the external pore size analysis in *Figure 7.14 b*, the HCFA curves follow similar trends as WT M0 except for one curve that shows much smaller pores at the end (see green arrow), the exponential fit of these curves was better than for WT M60 $R^2 \sim 0.9$. The number of pores and depth analysis in *Figure 7.14 c* show no difference with respect to WT M0, WT M30 or WT M60 and the parameter values extracted from these curves will be explained and summarized together with the rest of the samples in *Figure 7.22*.

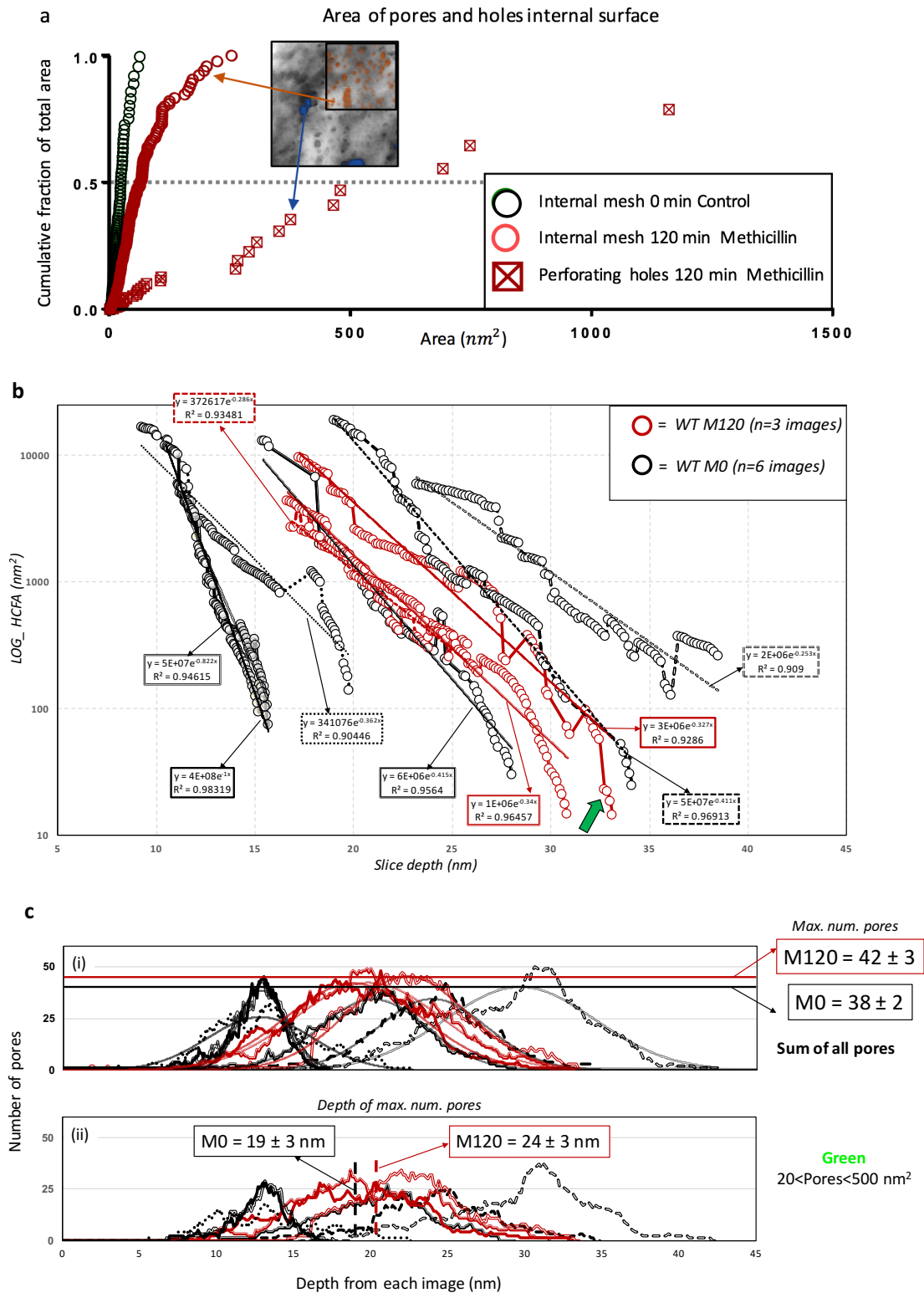


Figure 7.14 – a) Plot presenting individual values of pore area measured from internal surface images treated with 10xMIC Methicillin during 120 min (dark red) and the control, M0 (black). b) HCFA curves for different WT M120 images (dark red curves) and M0 images (black curves), an exponential fit and the R^2 are plotted as dotted lines for each curve, green arrows indicate local anomalies; c) number of pores versus slice depth, there are two identical plots: (i) Total number of pores per each slice and (ii) pores between 20 and 500 nm^2 (Figure 6.15 and Appendix 2)

7.3 *Staphylococcus aureus* sacculi treated with Vancomycin

To study the nanometric effect of Vancomycin on *S. aureus*, the experiments were performed following the same methodology and image analysis as in *section 7.2*. The control sample, WT V0 was imaged and no significant differences were found with WT M0. Thus, the same control data set was used as in *section 7.2*.

7.3.1 Vancomycin effect in sacculi after 30 min treatment

The first time-point of 30 min treatment (WT V30) was prepared and imaged under the AFM, all the data available is presented in *Figure 7.15*.

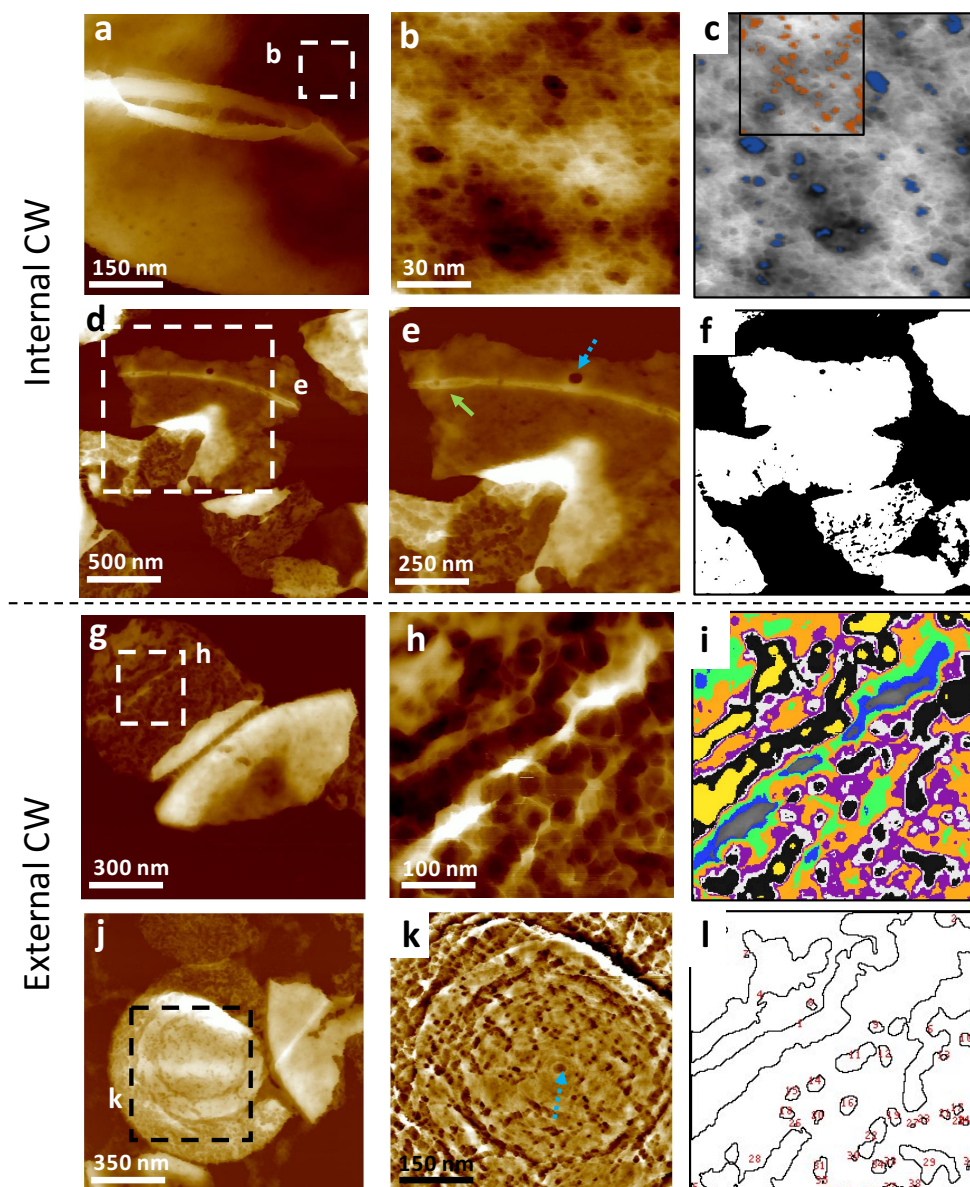


Figure 7.15 - WT V30. a) example of sacculus fragment with internal structure upwards; b) zoomed image from 'a'; c) Image 'b' in grey scale with two superimposed analyses featuring the perforating holes (blue) the internal mesh (orange); d) sacculus fragment corresponding to the internal surface; e) zoomed image from 'd', there is a piecrust in

the middle of the fragment with aspect ratio < 1 (green arrow) and surprisingly there is an aperture or cavity (dashed blue arrow) similar to an incomplete-septum ; f) Analysis of the perforating holes, binary image representing black = the substrate; white = sacculi material above; g-h) Mature external surface; i) pore depth map from image 'h'; j-k) another example of mature external surface showing rings with the centre of the concentrating rings still visible (dashed blue arrow; l) section at 15 nm depth from image 'h'.

The images from *Figure 7.15* were obtained under the experimental conditions summarized in *Table 7.3*.

Table 7.3 – Experimental conditions used to obtain data from Figure 7.15. See 2.3.2.2.2.

AFM TIP	AFM MODE	SAMPLE TYPE	ENVIRONMENT	SURFACE	SPECIFIC CONDITIONS
FAST SCAN -D	PeakForce Tapping	WT V30 Stock A Batch 7 Dilution 5	150 mM KCl + 10mM Tris pH=7.8	PLL coated MICA	Dried to be imaged 1 month later

Figure 7.15 presents the same organization and structure as *Figure 7.7*. There is a distinctive feature worth mentioning visualized for the first time: a piecrust (green arrow) located next to an unfinished septum aperture (see dashed blue arrow in *Figure 7.15 e*). This will be further explored if the same feature appears in other samples. The depth map of *Figure 7.15 i* has more 30 nm pores (yellow) than any other sample analysed so far. *Figure 7.15 j-k* are images of mature concentric rings in an advanced stage of the cell cycle with the central depression still distinguishable (see blue arrows). For WT V30 n=1 internal CW image (*Figure 7.15 c*) was the only available image used to produce the graph from *Figure 7.16 a* below. A data set of WT V30 n=2 external CW images similar to *Figure 7.15 h* were used to produce graphs from *Figure 7.16 b-c*.

Figure 7.16 a shows for the first time that the WT V30 perforating holes (blue square crosses) have similar size and trend as the WT V30 internal mesh with respect to the control. Regarding the external pore size analysis in *Figure 7.16 b*, there are no specific characteristics worth mentioning. The number of pores and depth analysis in *Figure 7.16 c* show no difference with respect to the control or the Methicillin samples. The parameter values extracted from *Figure 7.16* will be explained and summarized together with the rest of the samples in *Figure 7.22*.

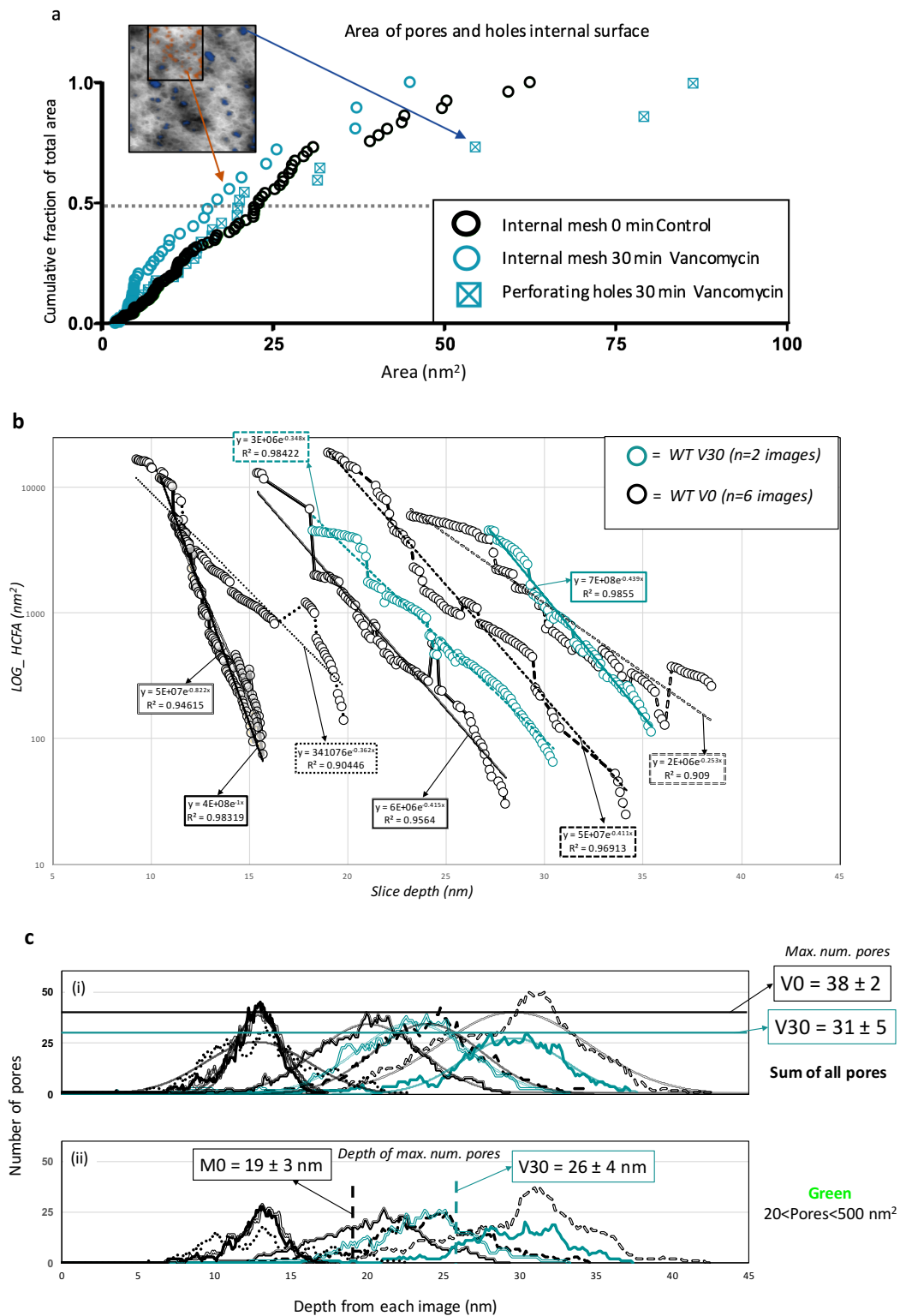


Figure 7.16 – a) Plot presenting individual values of pore area measured from internal surface images treated with 10xMIC Vancomycin during 30 min (turquoise) and the control, M0 (black). b) HCFA curves for different WT V30 images (turquoise curves) and M0 images (black curves), an exponential fitting and the R^2 are plotted as dotted lines for each curve; c) number of pores versus slice depth, there are two identical plots: (i) Total number of pores for each slice and (ii) pores between 20 and 500 nm² (Figure 6.15 and Appendix 2)

7.3.2 Vancomycin effect in sacculi after 60 min treatment

Sample WT V60 was prepared and imaged in the same way as *section 7.3.1*, the summary of the best images are shown in *Figure 7.17*.

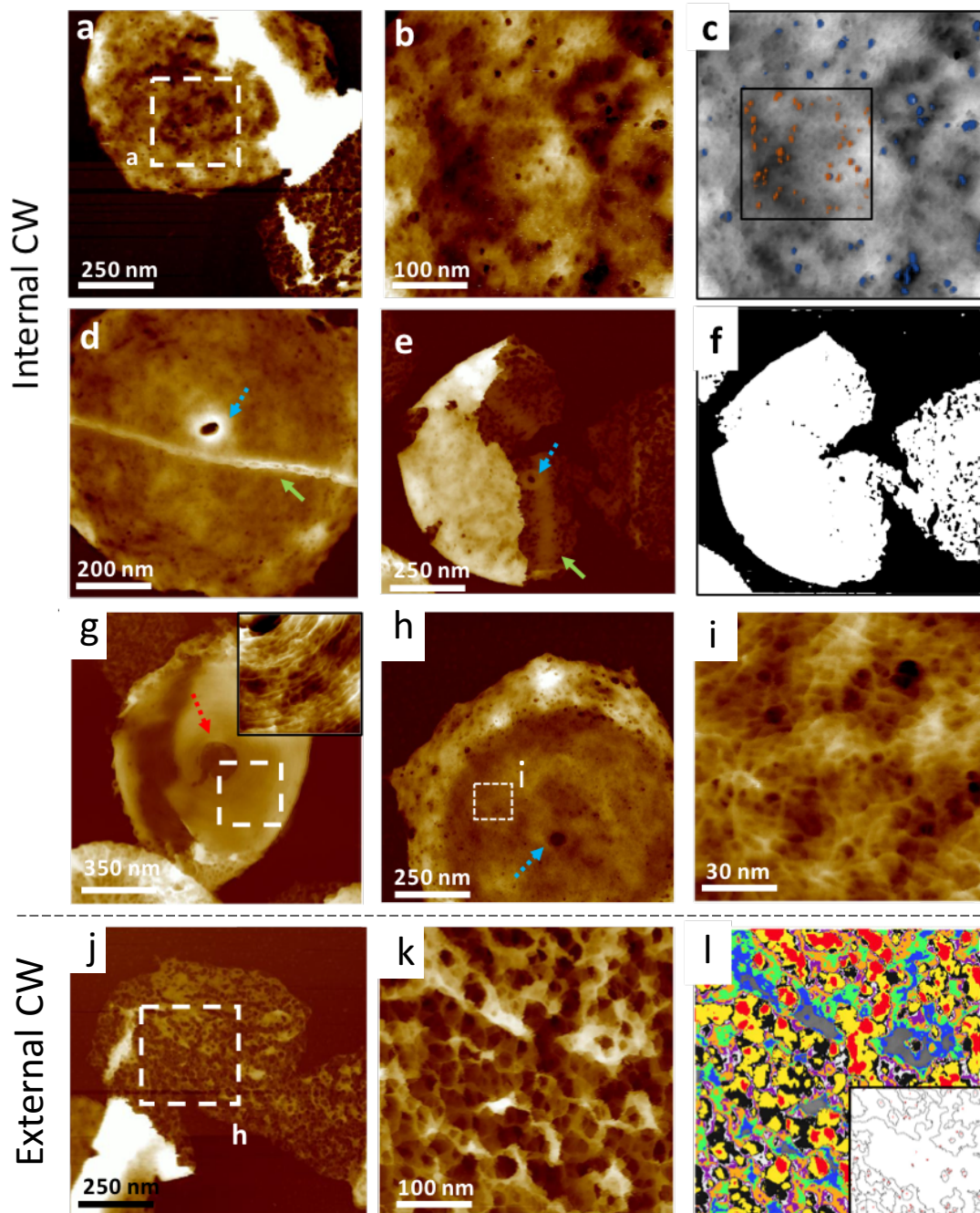


Figure 7.17 - WT V60. a) example of sacculus fragment with internal structure upwards; b) zoomed image from 'a'; c) Image 'b' in grey scale with two superimposed analyses featuring the perforating holes (blue) the internal mesh (orange); d) another sacculus fragment corresponding to the internal surface; e) sacculus fragment with the internal surface on top of the external surface where there is a piecrust in the middle of the fragment with aspect ratio > 1 (green arrow) and surprisingly there is an aperture or cavity (dashed blue arrow) similar to an incomplete-septum ; f) Analysis of the perforating holes from image 'e', binary image representing black = the substrate; white = sacculi material above; g) sacculus showing the internal surface with the external side of an unfinished septal plate laying on top, see cavity (dashed red arrow), with concentric rings structure (Inset); h) internal surface of unfinished septal

plate with cavity (dashed blue arrow); i) zoomed image from 'h'. j) mature external surface; k) zoom from 'j'; l) pore depth map from image 'k', binary image of 15 nm depth (Inset)

The images from *Figure 7.17* were obtained under the experimental conditions summarized in *Table 7.3* above, WT V60 was also from Batch 7.

Figure 7.17 a-i correspond to the internal CW and *j-l* to the external CW. The piecrust next to the aperture feature was visualized in this sample as well, *Figure 7.17 d,e* are two examples (see piecrust: green and aperture: dashed blue arrows). Another feature not found in the control was the presence of unfinished-septal plate with the concentric rings facing upwards (see *Figure 7.17 g* and inset). There were also unfinished septa with the internal smooth mesh structure facing upwards (see *Figure 7.17 h-i*). The depth map of *Figure 7.17 l* has an additional colour: red, corresponding to pores 35 nm deep.

For WT V60 $n=2$ internal CW images (like *Figure 7.17 c*) were used to produce the graph from *Figure 7.18 a* below. A data set of WT V60 $n=2$ external CW images similar to *Figure 7.17 k* were used to produce graphs from *Figure 7.18 b-c*.

Figure 7.16 a is almost identical to *Figure 7.9* from WT M30, which could indicate some similarities between the two antibiotics. Regarding the external pore size analysis in *Figure 7.18 b*, one of the HCFA curves from WT V60 follows similar trends as WT M0, but the other HCFA curve has an area with almost no reduction of the pore size (see green arrows), the exponential fit of this curves was poorer with $R^2 \sim 0.8$, but these changes, in the top slices of the image, do not affect the overall analysis (see exponential coefficient values in *Figure 7.22*). The number of pores and depth analysis in *Figure 7.18 c* show no difference with respect to the control or the Methicillin samples. However, the image with an HCFA that looks normal presents a significantly higher number of pores than the control or the other image. The parameter values extracted from *Figure 7.18* will be explain and summarized together with the rest of the samples in *Figure 7.22*.

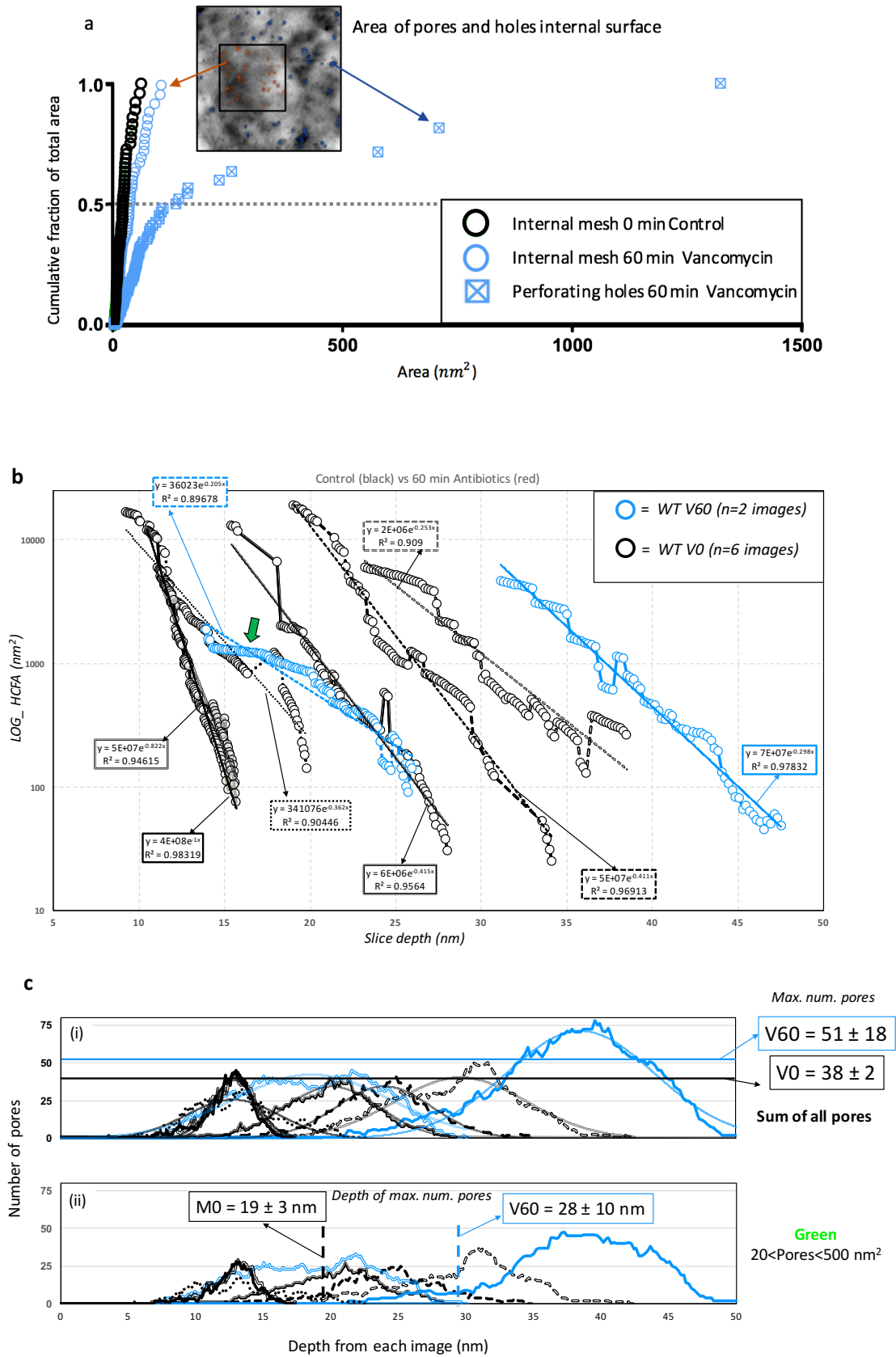


Figure 7.18 – a) Plot presenting individual values of pore area measured from internal surface images treated with 10xMIC Vancomycin during 60 min (light blue) and the control, M0 (black). b) HCFA curves for different WT V60 images (light blue curves) and M0 images (black curves), an exponential fitting and the R^2 are plotted as dotted lines for each curve, green arrow indicates local anomaly; c) number of pores versus slice depth, there are two identical plots: (i) Total number of pores per each slice (ii) pores between 20 and 500 nm^2 (Figure 6.15, Appendix 2)

7.3.3 Vancomycin effect in sacculi after 120 min treatment

Sample WT V120 was prepared and imaged in the same way as *section 7.3.1*, the summary of the best images are shown in *Figure 7.19*.

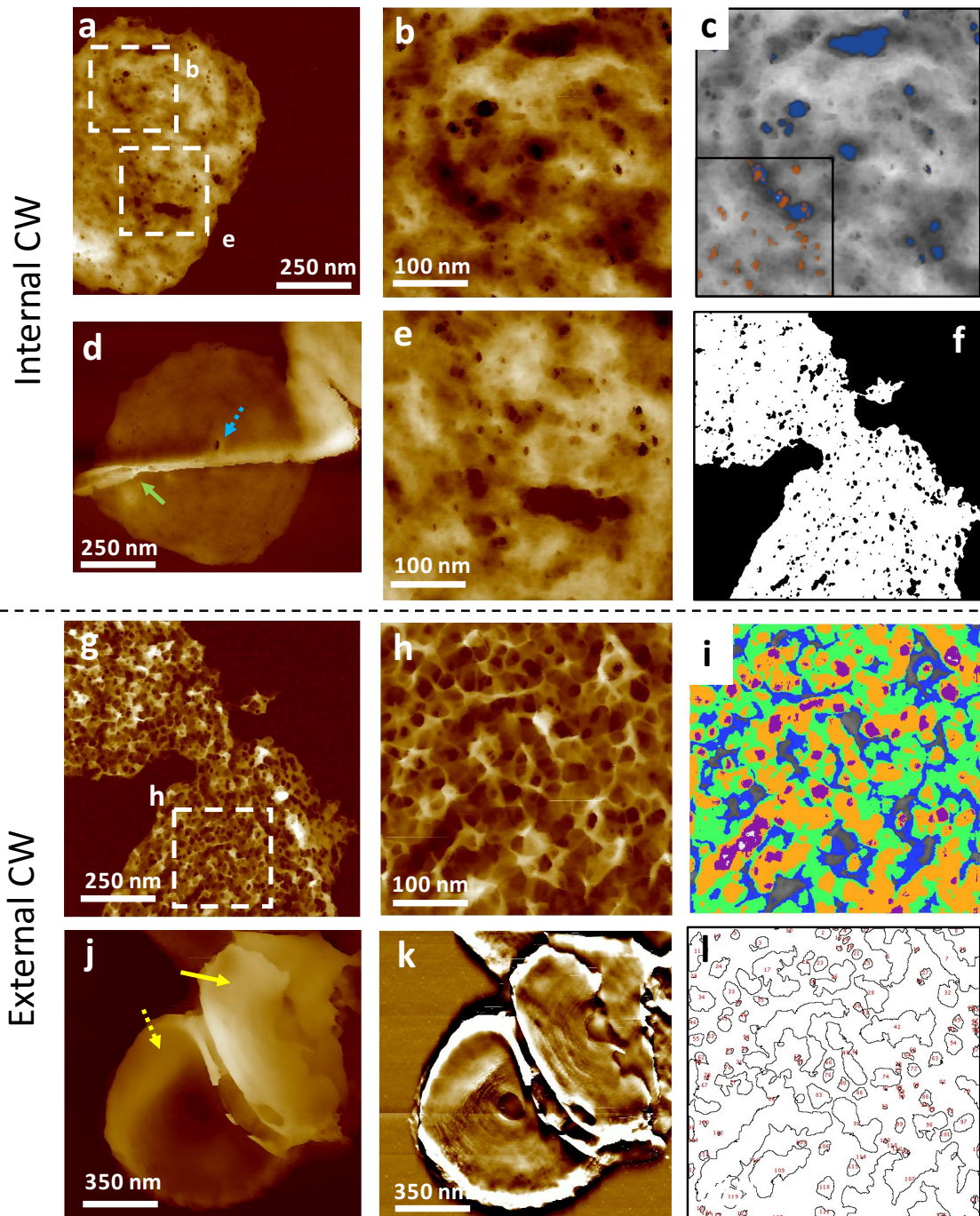


Figure 7.19 - WT V120. a) example of sacculus fragment with internal structure upwards; b) zoomed image from 'a'; c) Image 'b' in grey scale with two superimposed analyses featuring the perforating holes (blue) the internal mesh (orange); d) another sacculus fragment corresponding to the internal surface where there is a piecrust in the middle of the fragment with aspect ratio < 1 (green arrow) and a cavity (dashed blue arrow) similar to an incomplete-septum; e) another example of high resolution internal structure, zoomed image from 'a'; f) Analysis of the perforating holes from image 'g'; g-h) Mature external surface; i) pore depth map from image 'h'; j) sacculus showing two external sides of an unfinished septal plate (dashed and normal yellow arrows); k) Peak Force error channel of 'j'; l) section at 15 nm depth from image 'h'.

The images from *Figure 7.19* were obtained under the experimental conditions summarized in *Table 7.3* above, WT V120 was also from Batch 7 (see *section 2.1.8*).

Figure 7.19 presents the same organization and structure as *Figure 7.15*. The piecrust next to the aperture feature was visualized in this sample as well, *Figure 7.19 d*, confirming this feature appears in all Vancomycin treated samples. If this feature was observed on a healthy cell, the explanation would be that before the septal aperture is complete, the next piecrust is being synthesized. However, for Vancomycin treated cells, the Di-peptide and ¹⁴C-GlcNAc incorporation experiments (see *Figure 7.5 c-d*) showed a complete lack of PG incorporation after 5 min of treatment. Therefore, there is two possible explanations: after the septa is complete and the next piecrust starts to form, the hydrolysis occurs at the central depression first because it is more vulnerable; or the cell has a recycling mechanism to use PG components from the rest of the CW. Then, the cell recycles the stored PG components and builds a premature piecrust next to an unfinished septa after to reinforce the CW because its normal biosynthesis is affected by the antibiotic. More experiments are required to fully understand this phenomenon. Regarding the unfinished septa showing concentric rings, it also appeared in this sample with both sides of the septal plate still attached to each other (see yellow arrows in *Figure 7.19 j-k*). This corroborates our model from the septa presented in *chapter 4* (see *Figure 4.21*), where we suggested the external septal wall from both daughter cells are opposed to one another. In a healthy sacculi sample these two surfaces rarely separate before finishing septation, but the Vancomycin treated samples repeatedly showed this feature, another indication of hydrolase activity during lack of synthesis.

For WT V120 n=2 internal CW images (like *Figure 7.19 c*) were used to produce the graph from *Figure 7.20 a*. A data set of WT V120 n=4 external CW images similar to *Figure 7.19 h* were used to produce graphs from *Figure 7.20 b-c*.

Figure 7.20 a and *Figure 7.18 a* are almost identical, so no further comments are required. Regarding the external pore size analysis in *Figure 7.20 b*, one of the HCFA curves from WT V120 has deeper pores than the rest of the curves, *Figure 7.20 c* shows another curve having a significant increase in number of pores (see green arrows). The parameter values extracted from *Figure 7.18* will be explain and summarized together with the rest of the samples in *Figure 7.22*.

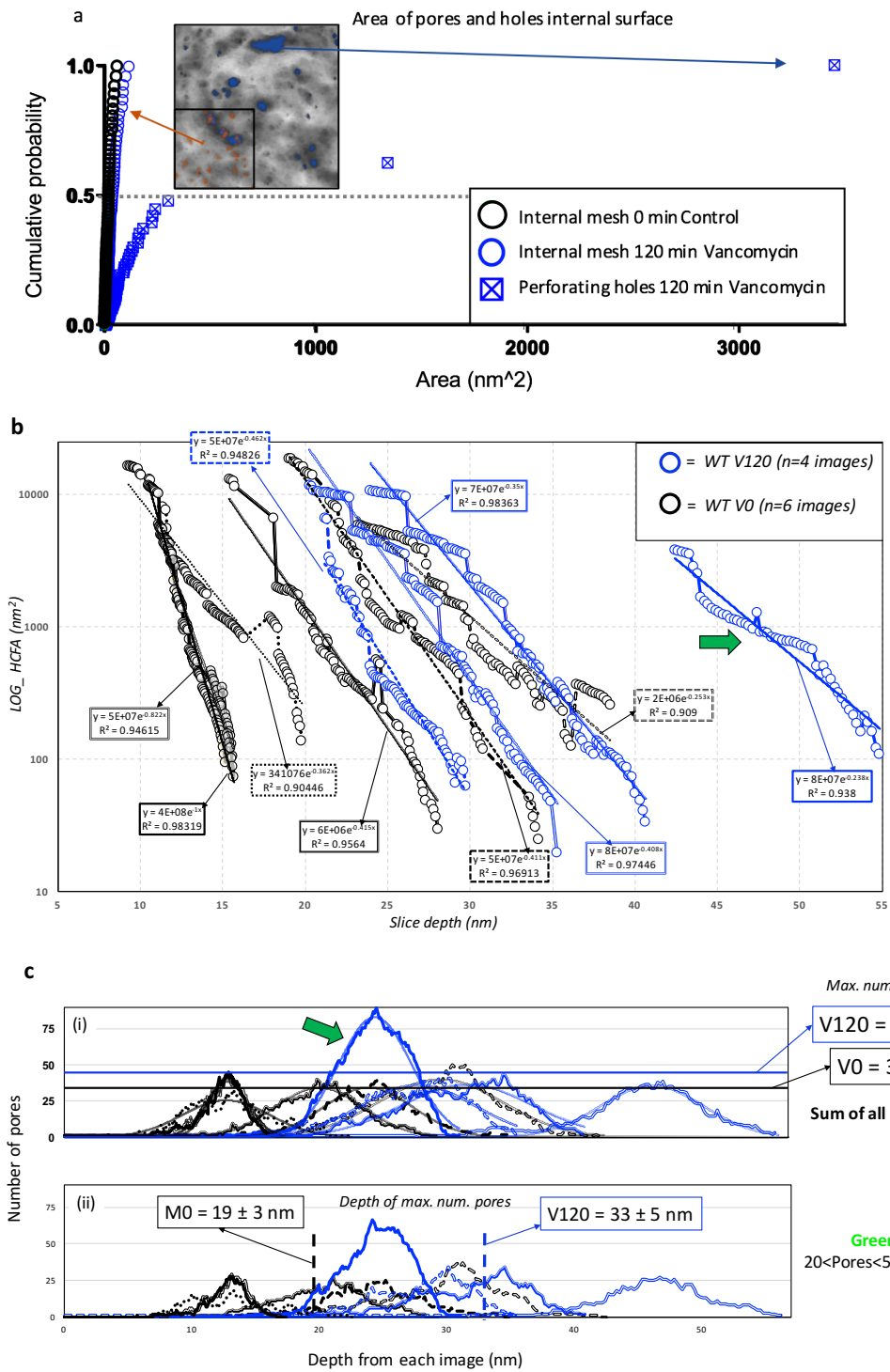


Figure 7.20 – a) Plot presenting individual values of pore area measured from internal surface images treated with 10xMIC Vancomycin during 120 min (dark blue) and the control, M0 (black). b) HCFE curves for different WT V120 images (dark blue curves) and M0 images (black curves), an exponential fitting and the R² are plotted as dotted lines for each curve, green arrows indicate local anomalies; c) number of pores versus slice depth, there are two identical plots: (i) Total number of pores per each slice (ii) pores between 20 and 500 nm² (Figure 6.15, Appendix 2)

7.4 Quantitative comparison between healthy and Methicillin/Vancomycin treated cells

Firstly, the three dimensional architecture of PG under Methicillin and Vancomycin treatment was quantified using the cumulative fraction representation and the HCFA curves (see *Chapters 4 and 6*). From the internal surface, HCFD values from the perforating holes and internal mesh were calculated. From the external surface, HCFD values from the slice with the maximum number of pores for each image was calculated and the mean value \pm s.d. is plotted below. *Figure 7.21* summarizes the AFM images of the internal surface and a graph with the HCFD values for each sample.

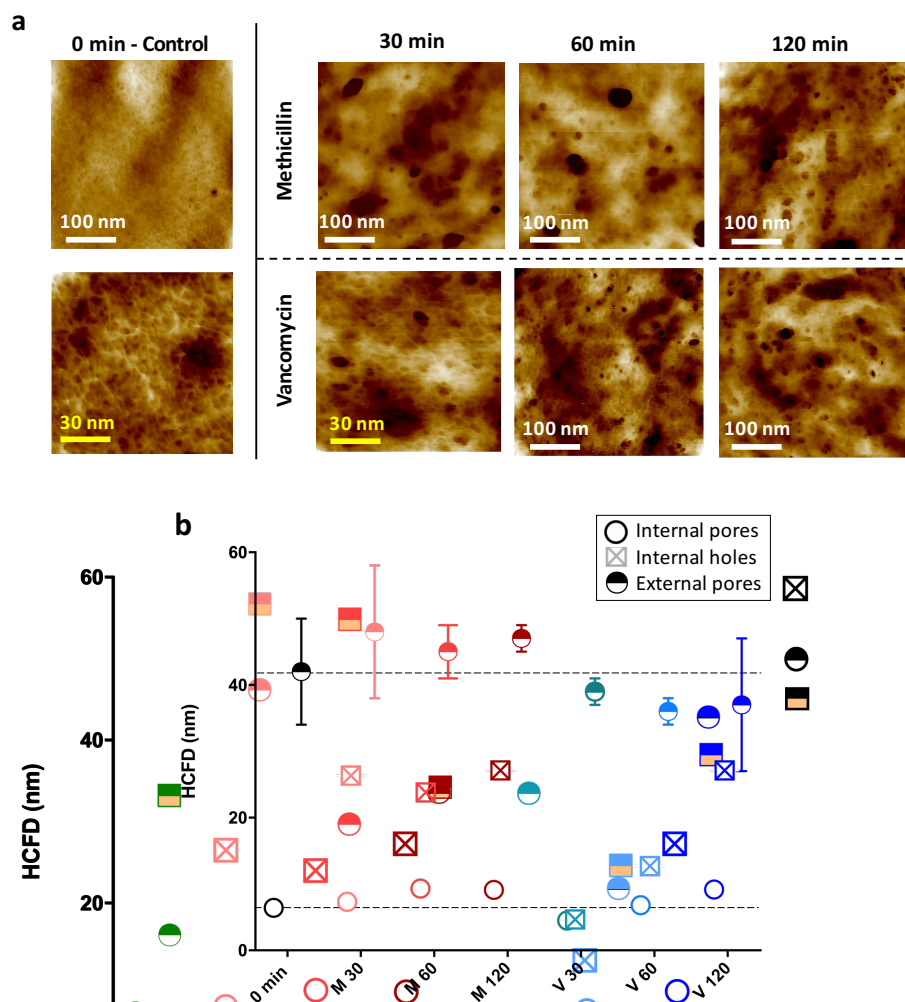


Figure 7.21 – a) Internal structure images for all samples; b) graph built with all the HCFD data previously described. The internal pores and holes do not have error bars because the data from different images were merged together in order to have enough points to calculate the HCFA (see for example 7.20a) and then calculate the HCFD.

Figure 7.21 a shows the best images from the internal surface of *S. aureus* sacculi for each sample, allowing a direct visual comparison (V30 is the only available example, compare with control with the same scale, yellow scale bars). The qualitative conclusion

is that all the antibiotic treated samples present scars and deformations compared to the much more smooth and uniform surface of the control. *Figure 7.21 b* shows three data sets of HCFD for each sample: internal and external pores which constitute the PG fibrous mesh and the internal perforating holes which are only present in antibiotic treated samples. All the samples treated with antibiotics (except WT V30) present perforating holes much bigger than the internal pores but smaller than the external pores. Both, the internal and external pores of the antibiotic treated samples do not visually vary from the 0 min control (see data in close proximity to black dashed lines).

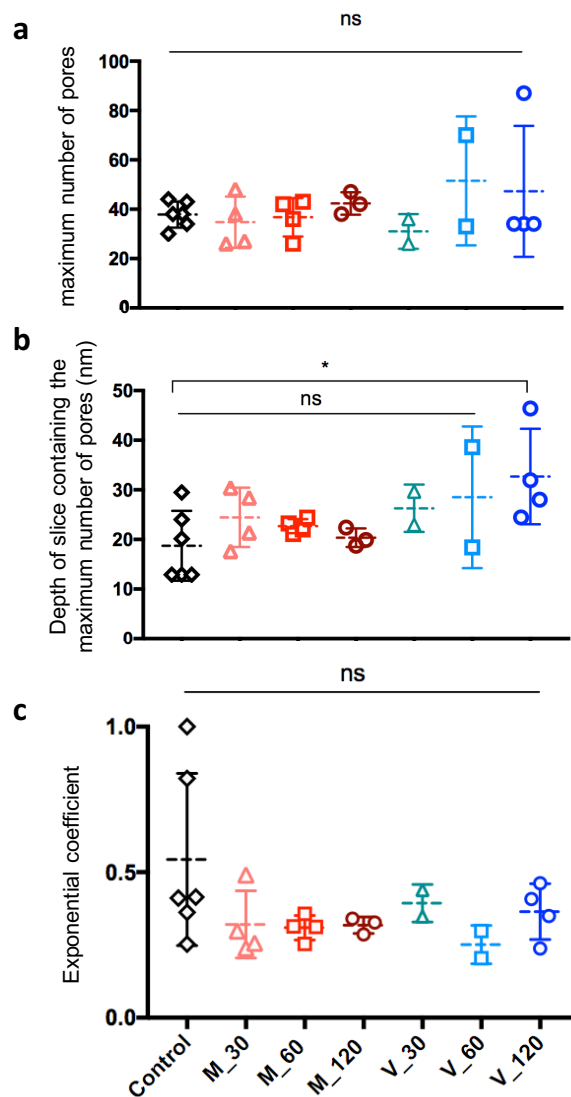


Figure 7.22 – a) Maximum number of pores per each sample; b) depth of the slice containing the maximum number of pores per each sample; c) exponential coefficient from the HCFA curves

Secondly, from the analysis of the external images using the automated program (see *Appendix 2*) three main parameters were extracted: the maximum number of pores; the

depth from the slice containing the maximum number of pores and the exponential coefficient from the HCFA curves fitting. For each sample, the slight differences from this analysis have already been commented before. Here, we compare the overall PG mesh properties. The exponential coefficient indicates the shape of the pores across the CW thickness: higher values correspond to cone-shaped pores with bigger area on the top of the CW to smaller at the bottom; smaller values correspond to cylinder-shaped pores. After performing t tests with Welch's correction (it does not assume similar SD for different groups), no significant difference was found between the control and the antibiotic samples for the maximum number of pores or the exponential coefficient (see *Figure 7.22 a, c*). However, a significant difference ($p < 0.02$) was found between the control and WT V120 in the depth of the pores (see *Figure 7.22 b*). This difference in depth was primarily due to one outlier image, therefore to corroborate this result a bigger data set is required. The results from *Figure 7.22* and *Figure 7.21* show that the bulk of the PG architecture is not altered by these antibiotics with the exception of the perforating holes (which could be the cause of death).

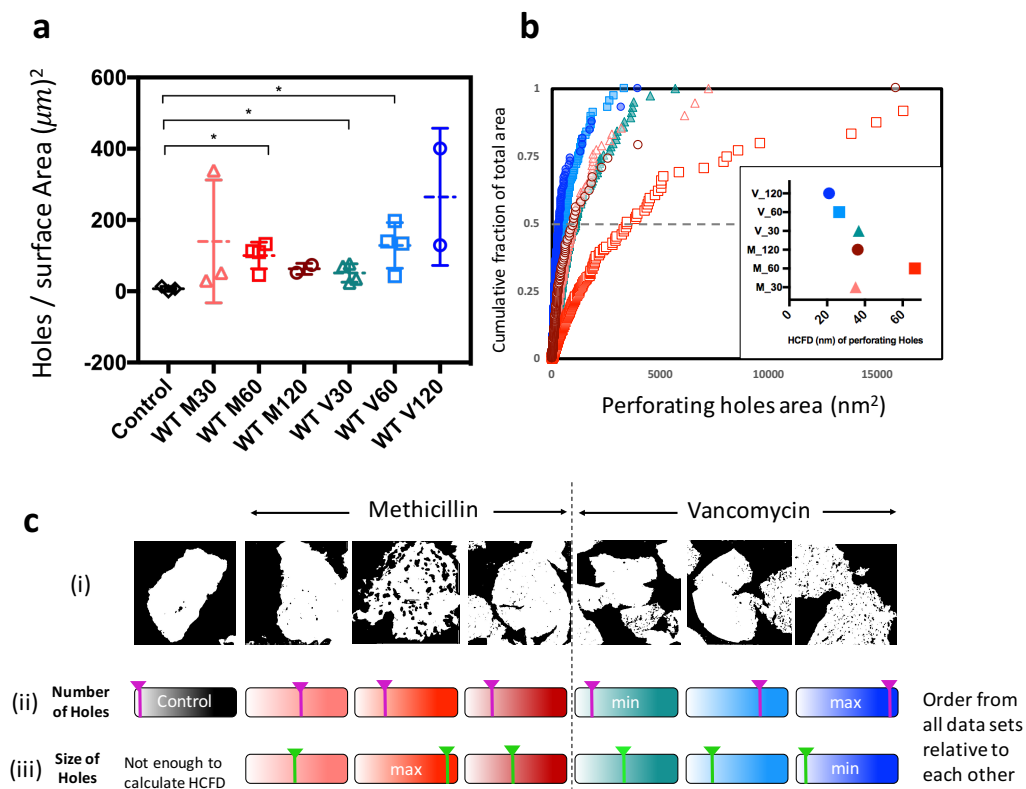


Figure 7.23 – a) Number of perforating holes per surface area; b) cumulative fraction of total area of perforating holes, inset: HCFA from each curve; c) Visual summary from 'a-b' (i) binary images from left to right: Control, M30, M60, M120, V30, V60, V120; (ii) The pink cursor is placed in each sample relative to each other showing the number

of holes, the left of each band is 0 and the right is the maximum number of holes (see the sample V30 with the minimum number of holes after the Control and V120 with the maximum); (iii) same representation where the green cursor indicates the HCFD of the holes with V120 having the smallest holes and M60 the biggest.

The perforating holes are the common feature amongst all the antibiotic treated samples and the main difference with the control images. Therefore, they were analysed in more detail. Following the method explained in *Figure 7.8* for all the samples, the perforating holes were characterized for several low-magnification images. *Figure 7.23 a* shows the number of holes per surface area (μm^2) where each point represents an image. After performing Welch's t tests a small significant difference ($p < 0.02$) was found between the control and the samples: M60, V30 and V60. *Figure 7.23 b* shows the hole area plotted against the cumulative fraction of total area, where each curve represents the individual holes joined from all the images analysed. The inset shows the HCFD for each sample. The maximum HCFD value corresponds to M60. *Figure 7.23 c* summarizes the main conclusion from this analyses: Methicillin treatment causes bigger perforating holes than Vancomycin, but there is a smaller number of them. This can also be qualitatively appreciated from the binary images (see *Figure 7.23 c (i)*, black = holes, white = PG, (ii-iii) showing a visual comparison from the groups relative to each other).

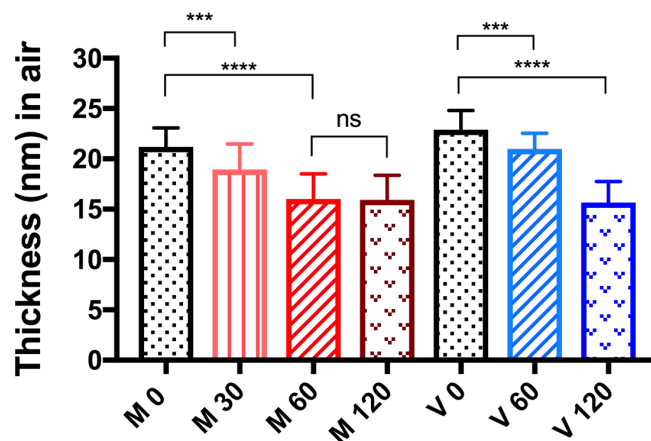


Figure 7.24 – Thickness of sacculi fragments in air for M0, M30, M60, M120, V0, V60 and V120. The significant difference analysis had p values from left to right: $p_{M0-M30} = 4.18 \cdot 10^{-4}$, $p_{M0-M60} = 6.81 \cdot 10^{-12}$, $p_{M60-M120} = 0.903$, $p_{V0-V60} = 3.73 \cdot 10^{-4}$, $p_{V0-V120} = 8.48 \cdot 10^{-14}$; $n=20$ sacculi for each group.

Finally, the last characteristics of sacculi to be quantified was their thickness. As shown in *Chapter 3* and in the literature [27] a typical sacculi thickness in air, for a healthy sacculus, is around 19-23 nm. The sacculi thickness was measured in air, following the methodology described in *section 3.5.3.3*, for all the samples (except V30 due to lack of data). At least $n=20$ individual sacculi were measured for each sample. *Figure 7.24*

summarize the mean values (error bars represent *s.d.*). The control samples M0 and V0 were measured separately because slight variations in thickness have been observed before for different batches. The Methicillin treated cells are significantly thinner after 30 and 60 min of treatment. However, there is no statistical difference between 60 and 120 min of treatment (unpaired *t* tests were performed with *p* values: $p_{M0-M30} = 4.18 \cdot 10^{-4}$; $p_{M0-M60} = 6.81 \cdot 10^{-12}$; $p_{M60-M120} = 0.903$). The Vancomycin treated cells get significantly thinner after 60 and 120 min of treatment (*p* values: $p_{V0-V60} = 3.73 \cdot 10^{-4}$; $p_{V0-V120} = 8.48 \cdot 10^{-14}$). Looking at all the data, no cells were found thinner than a **limiting thickness (~16 nm)**. Methicillin reaches this limit after 60 min of treatment whereas Vancomycin needs at least 120 min to reach it.

The most relevant numerical results presented above in *Figures 7.21-24* are also tabulated below in *Table 7.4*.

Table 7.4 – Results from quantitative analysis performed on AFM images of all samples studied in this chapter.

Data Type	HCFD Internal pores (nm)	HCFD Internal perforating holes (nm)	HCFD external pores (nm)	Amount of holes/ μm^2 sacculi	HCFD of Holes entire sacculi (nm)	Maximum number of pores	Depth of max. num. of pores (nm)	Air height (nm)
M0	6.4	-----	42±8	7±3	----	38±2	19±3	21±0.4
M30	7.3	26.5	48±10	140±120	35	35±5	24±3	19±0.5
M60	9.3	24	45±4	101±38	66	37±4	23±1	16±0.5
M120	9.1	27.3	47±2	63±15	36	42±3	24±3	16±0.5
V30	4.5	5.0	39±2	52±26	37	31±5	26±4	-----
V60	6.8	13.2	36±2	128±64	26	51±18	28±10	21±0.3
V120	9.15	27.3	38±10	265±192	21	47±13	33±5	16±0.5

Despite having very limited data sets of AFM images for all the antibiotic treated samples (specially for WT V30, where only one successful AFM session was achieved) quantitative results have been achieved. However, the conclusion extracted from the AFM data have to be corroborated by acquiring larger data sets in the future.

7.5 Model of action of cell wall antibiotics

For the first time, some insight has been shed into the molecular structural changes induced by two different classes of antibiotics both targeting the CW.

Joining multidisciplinary experimental techniques such as fluorescence microscopy, population *in vitro* essays and Atomic Force Microscopy the molecular pathway leading

to cell death has been proposed for both antibiotics. We propose a model where they both have some commonalities and some differences. The main hypothesis from this model is the following: both antibiotics stop PG synthesis without stopping the PG hydrolysis. The unbalanced cell cannot control the action of the hydrolases which continue their normal reorganization of the peptidoglycan. However, unlike a healthy cell, a cell treated with CW antibiotics cannot produce new peptidoglycan material to be added to the right place to compensate the effect of hydrolases. Then, the CW gets weaker because of two main events: perforating holes larger than the critical size limit (> 12 nm) appear due to a nucleation process driven by the hydrolases; the total thickness of the CW decreases until achieving a critical thickness of 16 nm (in air). Finally the combination of these two events causes the CW to be too weak to support the turgor and the cell dies by plasmolysis. In this model, general lysis is not necessary for the killing to happen (*Figure 7.4*), instead several local leaks appear throughout the cell.

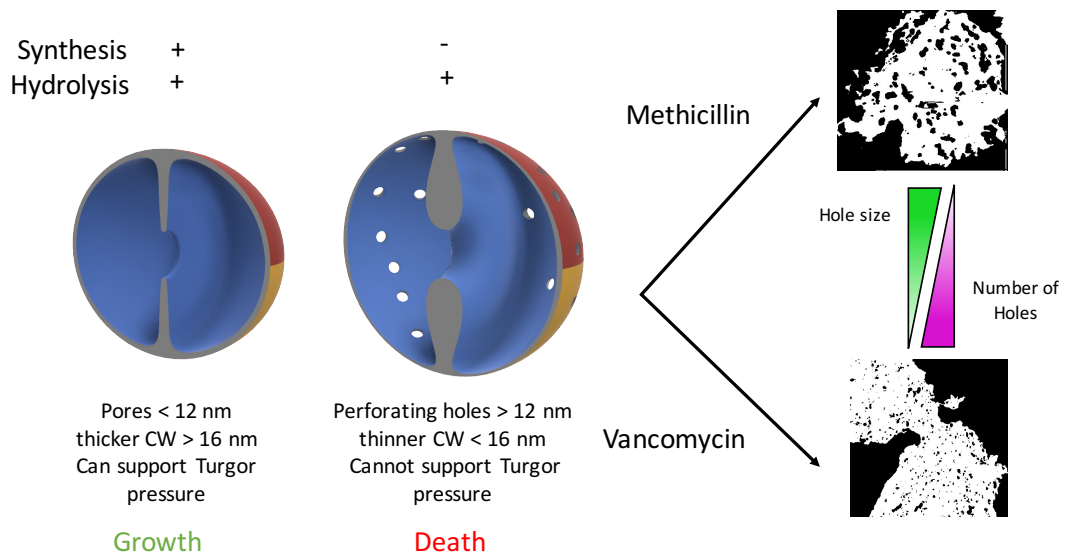


Figure 7.25 – Model of death mechanism caused by antibiotics targeting the CW synthesis pathway; on the right two arrows point to subtle differences between two different antibiotics: Methicillin and Vancomycin

From the AFM experiments some differences between both antibiotics were detected: Methicillin creates bigger holes than Vancomycin (see green triangle in *Figure 7.25*). Vancomycin produces smaller perforating holes but they are deeper and there is a higher number of them (see pink triangle in *Figure 7.25*). From the thickness decrease, it can be inferred that Methicillin might be acting at a faster rate than Vancomycin to ultimately induce similar structural changes. Both antibiotics ultimately lead to cell

death by the common mechanism explained above. However, these subtle differences influence the killing dynamics as reported [15] (see *Figure 7.3*).

This model was based on experiments at population level [15] together with AFM experiments at molecular and cellular level. The first step to build this model was to gather a deep understanding of the healthy *S. aureus* CW architecture and its evolution throughout the cell cycle. Experiments at cellular and atomic level with healthy *S. aureus* were performed extensively in the past. [28]–[34] This thesis summarizes the experiments at molecular level using high resolution AFM in healthy *S. aureus* (see *Chapters 3-4*). Moreover, the use of mutants such as *sagB*, *pbp3* and *pbp4* helped us identify the importance of a perfect balance between synthesis and hydrolysis (see *Chapter 5*).

7.6 Discussion

This chapter has been focused on studying the molecular effect of CW antibiotics on *S. aureus* using high resolution AFM imaging in liquid as the main experimental tool.

In *section 7.1.1.1* and *7.1.2.1* the main characteristics and chemical structure of Methicillin and Vancomycin have been explained according to current literature. These two antibiotics correspond to two different classes but target the CW biosynthesis from different angles. Methicillin blocks the transpeptidase activity from PBPs, while Vancomycin binds to the precursor lipid II and the D-Ala-D-Ala terminus from uncross-linked peptide chains from the existing PG structure. Then, in *section 7.1.3* the differences and commonalities between these two antibiotics and their effect at cell population level was assessed via conventional microbiology essays and super resolution fluorescence microscopy (SIM). This work was carried out by a fellow researcher: Dr Milena L Von Und Zur Muhlen. [15] The first conclusion extracted from her work is the slightly different killing dynamics from the two antibiotics (see *Figure 7.3*). Then, by assessing the morphology changes, it was concluded that general lysis was not required for cell death. However, a significant increase in cell volume was observed on the first 60 min of treatment for both antibiotics (see *Figure 7.4*). Next, the incorporation of new PG material was measured by di-peptide labelling and radioactive ^{14}C -GlcNAc finding a striking difference between the two antibiotics: Methicillin has

residual glycan incorporation for the first 30 min while Vancomycin has no residual incorporation after 5 min of treatment. An hypothesis about the mode of action of these two antibiotics was formed: the prolonged PG hydrolysis activity coupled with a lack of PG synthesis causes fractures in the CW that lead to cell death.

To corroborate this hypothesis, the study of the CW at molecular level was necessary, using AFM. Thus, in *section 7.2*, the effect of Methicillin on *S. aureus* sacculi was studied. Three samples were prepared at different time-points after treatment: 30, 60 and 120 min (M30, M60 and M120). All samples shared a common feature: scars that when analysed were determined to be perforating holes through the CW thickness. A new routine of analysis was developed (see *Figure 7.8*) where binary images could be used to clearly identify and measure these holes (see *Figure 7.9*). Then, the external mesh was analysed following the novel automatic method developed to compare *B. subtilis* to *S. aureus* CW architectures (see *section 6.2.1.2*). If very similar structures from two healthy Gram-positive species could be clearly distinguish with the three parameters obtained from this method (see *Figure 6.17*), a comparison between non-treated *S. aureus* and Methicillin treated *S. aureus* will result in insightful information (see *Figures 7.10,12 and 14*) . All the samples were compared in *Figure 7.22*, concluding that no significant difference was found in the shape, depth or number of pores between the control and the Methicillin treated samples. The only significant difference was the presence of perforating pores in the internal surface of all three samples. These internal holes are much bigger than the established critical size (8-12 nm, see *section 4.3*), while the rest of the PG three-dimensional architecture is not altered. To conclude, these perforating holes are most likely the cause of death by Methicillin and they are probably caused by a nucleation process. Once a pore has become a hole, the probability of further hydrolysis is higher around that area, making the hole bigger rather than randomly hydrolyse the rest of the CW.

In *section 7.3*, the effect of Vancomycin on *S. aureus* sacculi was studied. Three samples were prepared at different time-points after treatment: 30, 60 and 120 min (V30, V60 and V120). The same approach was taken as in *section 7.2* to analyse the images and obtain quantitative results. The same conclusion can be extracted regarding the external mesh: no significant changes were observable on the bulk of PG material aside from the

perforating holes (which were bigger than the critical size for V60 and V120). From a qualitative observation of the images, two new morphological features were observed for the first time. A nascent piecrust perpendicular to an unfinished septal aperture (see *Figure 7.17*). The most probably explanation for this feature is that hydrolysis occurs at the central depression first because the recent synthesised aperture is most vulnerable. The second feature was the unfinished septa with the concentric rings (*i.e.* external septal wall) facing upwards, in some occasions two daughter cells were observed with their external septal walls facing each other, corroborating the septa model (see *Figure 4.19*). This could be visualized because the hydrolyses separate the cells while they still have an unfinished septa. This is probably another mechanism of cell death upon CW antibiotic treatment.

On one hand, the similarities between the two antibiotics are exposed as follows. Both antibiotics start their killing dynamics after one hour of treatment (see *Figure 7.3*). The cells treated with both antibiotics ultimately increase their volume (see *Figure 7.4*) while their CW gets thinner than a limit thickness of 16 nm (see *Figure 7.24* and *Table 7.4*). The molecular effect of both antibiotics are perforating holes without any major changes to the rest of the CW. The perforating holes are bigger than the limit size (8-12 nm) for which it was theoretically calculated that the internal lipid membrane of the cell would be able to bend and burst out of the cell due to turgor pressure assuming the turgor pressure remains constant during this process. Then, the proposed model for cell death when there is no synthesis while hydrolysis is still active (upon CW antibiotics) was that through these perforating holes, the membrane would burst and the cytoplasm would leak, killing the cell without the need for general lysis (see *Figure 7.25*).

On the other hand, a inconsistency between the results shown from all these experiments and the biochemical differences between the two classes of antibiotics is the difference in hole size. According to the literature (see *section 7.1*), Methicillin only inhibits the transpeptidase activity while Vancomycin inhibits both, the transglycosylation and transpeptidase activity. This might bring us to think that perforating holes would be bigger under Vancomycin effect. However, the experimental results have shown the opposite (see *Figure 7.23* and *Table 7.4*). One hypothetical explanation is that the Vancomycin molecule also attaches itself to the side chains of the cell wall

while Methicillin only targets the PBPs. It might be that Vancomycin being physically present in the CW makes it difficult for the hydrolases breaking certain links and for this reason the holes cannot be as big as in Methicillin. From the thickness decrease, it can be inferred that Methicillin might be acting at a faster rate than Vancomycin to ultimately induce similar structural changes. However, this contradicts the killing curves (see *Figure 7.3*) and the di-peptide and ^{14}C -GlcNAc incorporation experiments (see *Figure 7.5*) which conclude that Vancomycin kills faster than Methicillin for the first 2h but Methicillin ultimately kills more bacteria than Vancomycin in 5h. These results do not necessarily contradict each other because they measure different things. On a killing curve, the ability of survivor cells to reproduce again once the antibiotic has been removed from the media is measured. By contrast, the AFM experiments were performed on purified sacculi which includes two cell populations: the survivors and the dying cells. Therefore, new experiments should be designed in the future that fills the gap between the current results: for example by looking at earlier time-points between 0 and 30 min of treatment or by sorting the two cell populations using flow cytometry prior to the AFM study.

All of these conclusions were extracted bearing in mind the limited amount of AFM data available for some of the samples discussed in this chapter. Although it has been shown that this experimental set-up provides very detailed information at molecular scale, there is less statistical significance than other high-throughput techniques, because of the limited number of images. In the future, this is something that needs to be addressed.

To conclude, for the first time a biological pathway has been proposed after joining multidisciplinary experimental techniques such as fluorescence microscopy, population assays and Atomic Force Microscopy. Methicillin and Vancomycin have some commonalities and some differences. However, the main cause of cell death are the hydrolases. The glucosaminidases have been shown to be key for cell viability [24] but there are a total of 21 hydrolases in *S. aureus*; an unknown combination of hydrolases could be crucial for this process to happen. The next step in the future would be to explore different hydrolases mutants such as SagB or AtL using the same approach

presented here or even with improved methods. This will further increase our knowledge of the cell death mechanism proposed here.

7.7 References

- [1] M. Letek, "Alexander Fleming, The Discoverer of the Antibiotic Effects of Penicillin," *Front. Young Minds*, 2020.
- [2] M. J. Macielag, K. Bush, and M. J. Macielag, "New b-lactam antibiotics and b-lactamase inhibitors," *Expert Opinion on Therapeutic Patents*, vol. 20, no. 10. pp. 1277–1293, 2010.
- [3] P. Macheboeuf, C. Contreras-Martel, V. Job, O. Dideberg, and A. Dessen, "Penicillin binding proteins: Key players in bacterial cell cycle and drug resistance processes," *FEMS Microbiol. Rev.*, vol. 30, no. 5, pp. 673–691, 2006.
- [4] E. Sauvage, F. Kerff, M. Terrak, J. A. Ayala, and P. Charlier, "The penicillin-binding proteins: Structure and role in peptidoglycan biosynthesis," *FEMS Microbiology Reviews*. 2008.
- [5] A. W. WYKE, J. B. WARD, M. V. HAYES, and N. A. C. CURTIS, "A Role *in vivo* for Penicillin-Binding Protein-4 of *Staphylococcus aureus*," *Eur. J. Biochem.*, vol. 119, no. 2, pp. 389–393, 1981.
- [6] J. L. Kozarich, J.W. ; Strominger, "A Membrane Enzyme from *Staphylococcus aureus* Penicillinase Activities * Which," *J. Biol. Chem.*, vol. 253, no. 4, pp. 1272–1279, 1978.
- [7] Y. Kuroda, M. Okuhara, T. Goto, M. Kohsaka, H. Aoki, and H. Imanaka, "FR-900130, a novel amino acid antibiotic II. isolation and structure elucidation of the acetyl derivative of FR-900130," *J. Antibiot. (Tokyo).*, 1980.
- [8] E. Sauvage, A. Powell, J. Heilemann, H. Josephine, P. Charlier, C. Davies and R. Pratt, "Crystal Structures of Complexes of Bacterial β -Peptidases with Peptidoglycan-Mimetic Ligands: The Substrate Specificity Puzzle," *J. Mol. Biol.*, 2008.
- [9] K. Poole, "Resistance to b-lactam antibiotics," *Cellular and molecular life sciences : CMLS.*, vol. 61, no. 17. Basel :, pp. 2200–2223, 2004.
- [10] E. Y. Furuya and F. D. Lowy, "Antimicrobial-resistant bacteria in the community setting," *Nat. Rev. Microbiol.*, vol. 4, no. 1, pp. 36–45, 2006.
- [11] J. Williams, R. Derek Marshall, H. van Halbeek, and J. F. G. Vliegthart, "Structural analysis of the carbohydrate moieties of human tamm-horsfall glycoprotein," *Carbohydr. Res.*, 1984.
- [12] H. R. Perkins, "Composition of Bacterial Cell Walls in Relation to Antibiotic Action," *Adv. Pharmacol.*, 1970.
- [13] D. Mullins, A. Kuznik, F. Shaya, N. Obeidat, A. Levine, L. Liu and W. Wong, "Cost-effectiveness analysis of linezolid compared with vancomycin for the treatment of nosocomial pneumonia caused by methicillin-resistant *Staphylococcus aureus*," *Clin. Ther.*, 2006.
- [14] S. Matsuoka, G. J. Patti, J. Schaefer, S. J. Kim, and G. J. Patti, "Vancomycin derivative with damaged D-Ala-D-Ala binding cleft binds to cross-linked peptidoglycan in the cell wall of *Staphylococcus aureus*," *Biochemistry.*, vol. 47, no. 12. Washington, DC :, pp. 3822–3831, 2008.
- [15] M. L. V. U. Zur Muhlen, "Life and Death: Cell Wall Antibiotic killing of *Staphylococcus aureus*," University of Sheffield, 2019.
- [16] P. Giesbrecht, T. Kersten, H. Maidhof, and J. Wecke, "Staphylococcal cell wall: morphogenesis and fatal variations in the presence of penicillin.," *Microbiol. Mol. Biol. Rev.*, 1998.
- [17] X. Zhao and K. Drlica, "Reactive oxygen species and the bacterial response to lethal stress," *Current Opinion in Microbiology*. 2014.
- [18] F. J. Marshall, "Erratum: Structure studies on vancomycin (Journal of medicinal chemistry (1965) 8 (18)).," *Journal of Medicinal Chemistry*. 1965.
- [19] G. K. Best and N. N. Durham, "Vancomycin adsorption to *Bacillus subtilis* cell walls," *Arch. Biochem. Biophys.*, 1965.
- [20] Y. Hirai, "Review and prospect of vancomycin," *Japanese Journal of Clinical Pharmacology and Therapeutics*. 2012.
- [21] I. Gunsolus, D. Hu, C. Mihai, S. Lohse, C. Lee, M. Torelli, R. Hamers, C. Murhpy, G. Orr and C. Haynes, "Facile method to stain the bacterial cell surface for super-resolution fluorescence microscopy," *Analyst*, 2014.
- [22] X. Zhou, D. Halladin, E. Rojas, E. Koslover, T. Lee, K. Huang and J. Theriot, "Mechanical crack propagation drives millisecond daughter cell separation in *Staphylococcus aureus*," *Science*,

- 2015.
- [23] J. Schindelin, I. Arganda-Carreras, E. Frise, V. Kaynig, M. Longair, T. Pietzsch, S. Preibisch, C. Rueden, S. Saalfeld, B. Schmid, J. Tinevez, D. White, V. Hartenstein, K. Eliceiri, P. Tomancak and A. Cardona, "Fiji: an open-source platform for biological-image analysis.," *Nat. Methods*, vol. 9, no. 7, pp. 676–82, 2012.
- [24] R. Wheeler, R. Turner, R. Bailey, B. Salamaga, S. Mesnage, S. Mohamad, E. Hayhurst, M. Horsburgh, J. Hobbs, and S. Foster, "Bacterial cell enlargement requires control of cell wall stiffness mediated by peptidoglycan hydrolases," *MBio*, 2015.
- [25] M. D. F. S. Barbosa, G. Yang, J. Fang, M. G. Kurilla, and D. L. Pompliano, "Development of a whole-cell assay for peptidoglycan biosynthesis inhibitors," *Antimicrob. Agents Chemother.*, 2002.
- [26] J. M. Walker, *Cell Wall Homeostasis*. 2016.
- [27] R. D. Turner, E. C. Ratcliffe, R. Wheeler, R. Golestanian, J. K. Hobbs, and S. J. Foster, "Peptidoglycan architecture can specify division planes in *Staphylococcus aureus*," *Nat. Commun.*, vol. 1, no. 3, p. 26, 2010.
- [28] D. C. Yang, K. M. Blair, and N. R. Salama, "Staying in Shape: the Impact of Cell Shape on Bacterial Survival in Diverse Environments," *Microbiol. Mol. Biol. Rev.*, 2016.
- [29] S. Taheri-Araghi, S. Bradde, J. Sauls, N. Hill, P. Levin, J. Paulsson, M. Vergassola and S. Jun, "Cell-size control and homeostasis in bacteria," *Curr. Biol.*, 2015.
- [30] S. J. Kim, J. Chang, and M. Singh, "Peptidoglycan architecture of Gram-positive bacteria by solid-state NMR," *Biochimica et Biophysica Acta - Biomembranes*. 2015.
- [31] S. M. Desmarais, M. A. De Pedro, F. Cava, and K. C. Huang, "Peptidoglycan at its peaks: How chromatographic analyses can reveal bacterial cell wall structure and assembly," *Mol. Microbiol.*, vol. 89, no. 1, pp. 1–13, 2013.
- [32] S. Meroueh, K. Bencze, D. Hsek, M. Lee, J. Fisher, T. Stemmler and S. Mobashery, "Three-dimensional structure of the bacterial cell wall peptidoglycan," *Proc. Natl. Acad. Sci. U. S. A.*, 2006.
- [33] B. A. Dmitriev, F. V. Toukach, O. Holst, E. T. Rietschel, and S. Ehlers, "Tertiary structure of *Staphylococcus aureus* cell wall murein," *J. Bacteriol.*, vol. 186, no. 21, pp. 7141–7148, 2004.
- [34] I. G. Boneca, Z. H. Huang, D. A. Gage, and A. Tomasz, "Characterization of *Staphylococcus aureus* cell wall glycan strands, evidence for a new β -N-acetylglucosaminidase activity," *J. Biol. Chem.*, 2000.

Chapter 8 Conclusions and future work

In this thesis, Atomic Force microscopy was used to decipher the PG 3D architecture in different bacterial strains and environments. AFM is the only microscopy technique that can directly image both live and dead cells in liquid environment with resolution on the order of a few nm. Armed with optimised methodology and quantitative analysis, the question of how CW antibiotics disrupt the PG and kill the cell was answered. Here are the main conclusions and future work extracted from the five experimental chapters in this thesis.

In *Chapter 3* the external peptidoglycan structure has been characterized for both hydrated purified PG and living cells. In order to perform a comprehensive comparison between these samples, a method was optimized for the first time to image hydrated *S. aureus* sacculi with lateral resolution of 1-3 nm, comparable to the previously obtained images of living cells. The PG 3D architecture from the external surface was conserved in hydrated sacculi, despite losing the tension caused by the internal turgor pressure.

The nascent external CW consists on a set of concentric rings orientated along the current division plane and perpendicular to the most recent division plane. Imaging this surface in flat sacculi fragments was less challenging than on the highly curved surface from living cells. Therefore, the finer structure of the rings was achieved with a higher throughput. The main feature being concentric glycan strands. Upon more detailed inspection, approximately 4 nm periodic protrusions were observed either along the glycan strands or between them. We suggested that these periodic protrusions represent the location of peptide side chains with a helical organisation, previously predicted with indirect techniques such as NMR and HPLC. Therefore, AFM has achieved for the first time a direct visualization of the peptidoglycan chemical architecture.

The mature external CW consists of a random fibrous mesh for both hydrated sacculi and living cells. This three-dimensional material is composed of peptidoglycan fibres from different widths and bundling degree which creates pores between them across the CW thickness. It was suggested that these pores must have a crucial role in the permeability function of the CW, allowing nutrients and other molecules to pass through its external barrier. Controversially, they pose hard constraints for other CW

components such as extracellular proteins and their interaction with the environment. Several quantitative analysis techniques were developed to obtain meaningful information from the pore dimensions. First, a novel transformation of the AFM images into a binary image stack was developed using a software combination composed of Gwyddion, ImageJ/FIJI and Avizo™. This approach highlights specific information from the image (*e.g.* pores) and provides 2D analysis through the thickness of the image, obtaining 3D information such as the depth of the pores. The Avizo™ software allows visualization in 3D of an AFM image converted into a 30 binary slice stack. The external mature CW images from living cells and hydrated sacculi were compared using these methodologies, with the sacculi having deeper pores than living cells. This means that peptidoglycan is a flexible material which can rearrange its bulk structure without changing its chemical composition depending on the environment and tension conditions. The discovery that the mature external CW has a fibrous mesh architecture in hydrated sacculi contrasts with the ‘knobbles’ structure found in the past when studying dried sacculi. A correlation experiment was performed to show the ‘knobbles’ appeared when the mature mesh was dried and disappeared upon hydration. During this analysis on different environments, a significant increase in thickness was found in hydrated sacculi. This was observed in both samples (with and without WTA). Therefore, this hydrogel behaviour is an intrinsic property of the peptidoglycan material. This change in structure and thickness was shown to be a reversible transition, portraying the high flexibility of this biomolecule.

One of the main advantages of studying hydrated sacculi is the access to the internal CW surface, which has never been described before. In *Chapter 4*, the optimized methodologies from *Chapter 3* were used to describe the internal peptidoglycan architecture of *S. aureus* with molecular resolution, visualizing individual glycan chains.

The internal peptidoglycan surface for the majority of the cell can be described as a smooth tight layer of material, when observed under low resolution. However, with a routinely achieved resolution of 1-2 nm the finer structure is better described as a disordered fibrous mesh forming two dimensional pores, visibly smaller than the pores from the external mature CW. The pore size was measured using the two-dimensional binary slice at a certain image depth. The non-normal distributions of pore size for both

data sets could not be compared with traditional statistical methods. Instead, a significant visual comparison was performed when the cumulative fraction of total area was plotted against the area of each pore. The pores from the internal surface were significantly smaller than the pores from the external surface. The half of the cumulative fraction of the total diameter (HCFD) represents the most probable pore size a particle randomly landing on the cell surface would find. These values were $HCFD_{\text{internal}} = 6.4$ nm and $HCFD_{\text{external}} = 23$ nm, which were much higher than expected. The next question raised from these results, how can the cell fulfil its role maintaining turgor pressure with the CW being such a porous material? To answer this, the critical pore size from which the cell membrane would irreversibly bulge through was theoretically calculated using the Helfrich-Canham theory of elastic deformation energy. Some assumptions were required given the lack of experimental data (*e.g.* membrane bending modulus, shape of bulge). Considering a turgor pressure of 20 bar, the critical pore diameter ranges between 8-12 nm. This implies that the pores from the internal PG surface are just small enough that membrane rigidity is able to maintain cell turgor. More accurate calculations could be possible if some of these assumptions were substituted by experimental values, which are not currently available but could be in the future.

The second main advantage of working with hydrated sacculi is the access to the septal plate at different stages of cell division to study its molecular architecture. The septal plate has two distinct regions of interest. The internal septal wall which is closer to the cytoplasmic membrane, surprisingly has a randomly oriented tight mesh architecture, similar to the internal PG surface from the rest of the cell. By contrast, the external septal wall that gets exposed to the exterior right after division has a concentric rings architecture, even before the splitting happens. A novel quantitative analysis of strand orientation was designed to characterize the internal septal wall PG architecture and compare it to the nascent external surface, resulting in disordered and ordered respectively. This novel level of resolution achievable by AFM together with the capacity to explore the internal surface of the CW using hydrated sacculi, will allow further studies on cell division.

In *Chapter 5*, *S. aureus* WT and other mutant strains were compared. The first mutants to be explored were strains lacking other components of the CW: LTA and WTA. *S.*

aureus Δ ltaS *gppgD::kan* purified sacculi allowed us to conclude that the topographic images obtained from the *S. aureus* WT do not correspond to LTA architecture. Similarly, images of living cells stripped from their WTA show no difference (Δ tarO mutant). Thus, these mutants serve as a control to corroborate that live cell images and sacculi containing WTA did not include artefacts from Teichoic acids. The second mutant lacked one of the most important glucosaminidases in *S. aureus*, SagB. From hydrated sacculi images, all the previously described PG architectures are still present in this strain: the internal mesh, the external mature mesh and the external nascent rings. However, the rate of fragments containing concentric rings increases respect the WT. Removing the SagB hydrolase affects the rate of evolution from concentric rings to mesh. The fragments at early stages of this transition had smaller pores on the external mesh than WT. There was a striking discovery of two populations of CW thickness for the *sagB* strain, thinner and thicker than the WT; often found in the same sacculi fragment. The thinner regions corresponded to nascent rings and the thicker to mature mesh. When hydrated, the two regions kept their water uptake percentage unaffected (at around 50 %). However, the difference in thickness and the higher rate of concentric rings has a high impact in CW mechanical properties as previously reported.

The imbalance between synthases and hydrolases was also tested by removing non-essential PBPs. The lack of PBP3 did not cause any apparent difference in architecture but the available data set was limited and it should be expanded before any conclusions are made. Furthermore, another non-essential PBP was removed, PBP4. Similarly to the *sagB* strain, there was an increase number of sacculi with concentric rings architecture. Moreover, there was a decrease in the surface area of the randomly orientated mature mesh in an individual sacculus fragment as for the first time two perpendicular regions of concentric rings corresponding to different division events were visualized. From contrasting with previous studies the differences found in the *pbp4* strain could be attributed to a lack of cross-linking, meaning that in order for the cell to completely transform rings into mesh within one single cell cycle, it requires not only the hydrolases but also some PBPs to produce new cross-linking between existing glycan strands. To conclude, the role of the PBPs must be synergistic and when a PBP is missing, the others perform its role in a less controlled manner. The perfect homeostasis between

hydrolases and synthases is necessary for the cell to maintain a uniform CW thickness and produce the proper PG architecture for cell viability. This first link between PG architecture and function of specific enzymes opens the path to a new subfield in microbiology which could be further explored in the future.

After studying *S. aureus* PG architecture in depth under different environments, in *Chapter 6* another Gram-positive species, the rod-shaped *B. subtilis* was studied to interrogate the relationship between PG architecture and bacterial shape.

First, sacculi were studied in different environments. In comparison to *S. aureus*, the external surface for both species has the same structure (mature mesh and concentric rings). However, the internal surface of *B. subtilis* despite being also a tight mesh, has glycan strands oriented along the short axis. In contrast to the *cocci*-shaped organism *S. aureus*, where the glycan strands are randomly orientated. The main conclusion from this, is that depending on the shape of the bacteria the stress caused by the turgor pressure is symmetrical or asymmetrical, causing the internal glycan strands to orient accordingly. This was corroborated by imaging a mutant strain lacking MreB, which is a key component of the Rod complex necessary to maintain the *rod*-shape of the bacteria. The internal PG architecture of the $\Delta mreB$ strain has randomly orientated glycan strands resembling the internal CW of *cocci*-shaped cells. Sacculi fragments were used to measure the thickness in air and liquid environment. The liquid uptake was higher in *B. subtilis* with 74 % compared to *S. aureus* with 47 %, meaning that their hydrogel properties are slightly different besides their similarities in PG structure. Another focus of the study was the septum architecture. In contrast with *S. aureus*, *B. subtilis* has a much more porous septa with different pore sizes across the thickness of the septal plate. The suggested model based on quantitative analysis is the following: there is a synthesis machinery located at the edge of the septal plate together with the *back-filling* mechanism plastering the big pores afterwards. These results shed some light into the division dynamics and septal plate formation for *B. subtilis*, which is currently still the object of controversy in the literature.

Secondly, *B. subtilis* live cells were studied in different environments. In buffer, the mature external surface was found to be randomly orientated fibrous mesh located along the cylinder and occasionally in mature poles. Some subtle differences were found

between the two species after performing a completely automatic method of analysis. This method was improved from *Chapter 4*, instead of calculating the HCFA for one slice, a program was written to automatically slice each image into 255 binary slices obtaining HCFA values and number of pores for each slice. The size of the pores was slightly different, the mean HCFD from the slices containing the maximum number of pores is 34 nm for *B. subtilis* and 29 nm for *S. aureus*. The depth of the slice containing the maximum number of pores was 12 nm for *B. subtilis* and 23 nm for *S. aureus*. These results agree with the difference in thickness, measured both with AFM and TEM. However, there was no statistical difference in the maximum number of pores or the fibre width between the two species. Regarding the nascent external surface of *B. subtilis* living cells consist of concentric rings located on the poles. All of these results would explain a common model for Gram-positive bacteria which presumably would apply to other bacteria with similar shape aside to *S. aureus* and *B. subtilis*.

After studying healthy samples, *B. subtilis* live cells were given an SDS treatment to understand the relationship between the internal turgor pressure of the cell and the PG architecture. Firstly, population killing assays were performed. There was a significant difference in growth between the conventional microbiology growing conditions and other conditions mimicking an AFM experiment, highlighting a gap in the literature about the different behaviour of challenged cells in suspension or other environments. Then, an AFM dynamic experiment was performed, where living cells attached to a surface were imaged with high resolution before and after the SDS treatment. Assuming SDS perturbs the turgor pressure, radical structural changes on the PG architecture were expected. However, only subtle changes in structure and cell shape dimensions were detected. This questions the dogma that SDS affects the turgor pressure, this property should be directly measured to extract solid conclusions from this type of experiments. Moreover, methodology improvements should be made to ensure AFM dynamic experiments are controlled and reproducible.

The final experimental chapter (*Chapter 7*) investigates the effect of CW antibiotics on *S. aureus* sacculi. The molecular effect from both antibiotics on sacculi was studied at different time-points: 30, 60 and 120 min. The automatic method developed in *Chapter 6* to study the external mesh was used. The conclusion was reached that non-significant

difference was found in the size, depth or number of pores between the control and the Methicillin or Vancomycin treated samples. This means the bulk of PG material is not affected by these antibiotics. All challenged sacculi shared a common feature: perforating holes through the CW thickness. A new routine of analysis was developed where binary images separating the substrate and the material above could be used to identify and measure these holes. From internal PG images, these perforating holes were measured to be much bigger than the theoretical critical size 8-12 nm calculated in *Chapter 4*. To conclude, these perforating holes, probably caused by a nucleation process, are the cause of death by Methicillin and Vancomycin.

The main difference between the two antibiotics is the perforating holes size. Despite Methicillin inhibiting only the transpeptidase activity while Vancomycin inhibits both the transglycosylation and transpeptidase activity, the holes upon Methicillin treatment are bigger than Vancomycin. One possible explanation is that Vancomycin being physically attached to the CW makes it difficult for the hydrolases breaking certain links and for this reason the holes cannot be as big as in Methicillin. The thickness was measured in air for all the samples showing a decrease over time until reaching a limit thickness of 16 nm. Methicillin treated cells reached the limit thickness after 1 h of treatment, while Vancomycin treated cells, required 2 h. From these results it can be inferred that Methicillin might act faster than Vancomycin to ultimately induce similar structural changes. However, from the killing curves and incorporation experiments it was concluded that Vancomycin kills faster than Methicillin for the first 2 h but Methicillin ultimately kills more bacteria than Vancomycin in 5 h. These results do not necessarily contradict each other because they measure different things. On a killing curve, the ability of survivor cells to reproduce again once the antibiotic has been removed from the media is measured. By contrast, the AFM experiments were performed on purified sacculi which includes two cell populations: the survivors and the dying cells. Therefore, new experiments should be designed in the future that fill the gap between the current results. Although there are some small differences between antibiotics, a model for cell death after CW antibiotic treatment was proposed. Due to lack of synthesis while hydrolysis is still active, localized perforating holes appear

throughout the CW surface; the membrane burst through the holes and there is multiple cytoplasm leaking points, killing the cells without the need of generalise lysis.

For the first time a biological explanation for how the cells die upon CW antibiotic treatment has been proposed after joining multidisciplinary experimental techniques such as fluorescence microscopy, population essays and Atomic Force Microscopy. Methicillin and Vancomycin have some commonalities and some differences. However, the main cause of cell death are the hydrolyses. The glucosaminidases have been shown to be key for cell viability but there are a total of 21 hydrolases in *S. aureus*; an unknown combination of hydrolases could be crucial for this process to happen. The next step in the future would be to explore different hydrolases mutants such as ScaH or AtL using the same approach presented here together with improved methods.

To conclude, this Thesis has pushed the limits of high resolution on living organisms and purified peptidoglycan. However, the low throughput of some of these challenging experiments such as the periodicity along the glycan strands or comparison with some of the mutant strains does not allow for solid biological conclusions to be extracted yet. Improving the techniques and gathering more data are key to building a solid framework. In the future, this could represent a new branch of research regarding the relationship between the peptidoglycan architecture and its complex function. The last experimental chapter from this thesis has given an answer to the question: what mechanism causes death upon cell wall antibiotic treatment to bacterial cells. This was unanswered for more than 80 years, since the commercialization of Penicillin. Although, the effectivity of current antibiotics can be proven and quantified, the underlying question of why the cells die after disrupting the PG biosynthesis machinery was never answered until now. The unbalance between the disrupted biosynthesis together with working hydrolysis, creates perforating holes from the PG internal layer which are bigger than the critical size. Then, the turgor pressure cannot be contained and leakage of multiple locations caused by the hydrolases leads to cell death. This new knowledge will allow us to design better antibiotics in the future, revealing possible new antibiotic targets or novel approaches that cause a similar effect to the cell wall inducing death. It is only armed with these new tools that human society will be able to defeat the rapidly approaching antimicrobial resistance crisis.

Appendix 1 – MATLAB code for *Bacillus subtilis* septa pores

The code can be found in this provisional link (pre-viva):

<https://figshare.com/s/4a5e6bd42248fd76ab68>

The public link is the following DOI (not activated before viva):

10.15131/shef.data.12780809

The documents containing information from Appendix 1 are the following: Appendix_1_code.m which is the executable MATLAB code; the code in text form can be found in the first section of All_codes.docx.

Appendix 2– FIJI code for mature mesh pores

The code can be found in this provisional link (pre-viva):

<https://figshare.com/s/4a5e6bd42248fd76ab68>

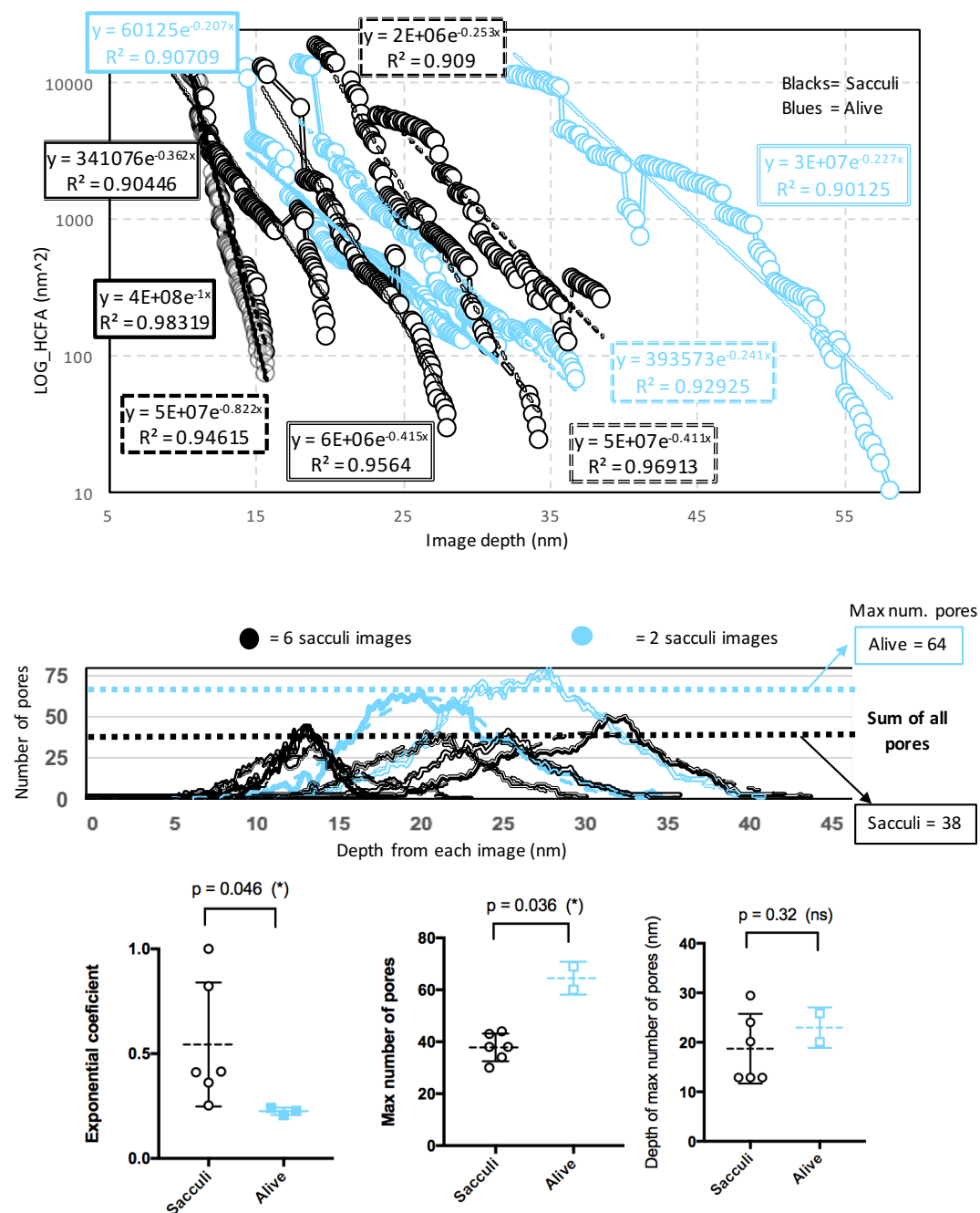
The public link is the following DOI (not activated before viva):

10.15131/shef.data.12780809

The documents containing information from Appendix 2 are the following: Appendix_2_code_1.ijm and Appendix_2_code_2.ijm which are the executable FIJI macros; the codes in text form can be found in the second section of All_codes.docx.

Appendix 3 – Comparison between *S. aureus* sacculi and live cells

Results from comparing 6 sacculi images (black data) and three live cells images (blue data) from *S. aureus*. The logarithmic HCFA curves are plotted on the top panel. The middle graph shows the total number of pores per slice for each image and the bottom three graphs present three parameters: exponential coefficient of the HCFA curves, maximum number of pores and the depth of the slice containing the maximum number of pores. The first two present statistical difference after performing a t test with Welch's correction. The sacculi data is the same used as a control for all the different samples in Chapter 7. The live cells data is the same as presented for *S. aureus* in Figure 6.16 and 6.17. In this case, the differences between images do not depend on image depth as most of the images had comparable Z range numbers.



Abbreviations list

2D = two dimensions
3D = three dimensions
AFM = Atomic Force Microscope
AMR = Antimicrobial resistance
ASP = amplitude set-point value
B. subtilis = *Bacillus subtilis*
CFU = colony forming unit
CW = Cell Wall
Cryo-EM=cryogenic electron microscopy
Cryo-TEM=cryogenic transmission electron microscopy
D-Ala = D-Alanine
dH₂O = deionized water
D-iso Gln = D-Isoglutamine
DLVO = Derjaguin, Landau, Verwey, Overbeek
DNA = Deoxyribonucleic acid
DPM = Dose per minute
DU = Disaccharide forming unit
E. coli = *Escherichia coli*
EDL = Electric double layer
EM = Electron microscopy
FWHM = Full Width at Half Maximum
 F_{el} = Double-layer forces
 F_{vdW} = van der Waals forces
GCL = Glycan Chain Length
gdpP = GGDEF domain protein containing Phosphodiesterase
GI2-DAG = glycolipid anchor diglycosyl-diacylglycerol
GlcNAc = N-acetyl-glucosamine
Gly = Glycine
Gro-P = glycerophosphate
HCFA = half of the cumulative fraction of the total area
HCFD = half of the cumulative fraction of the total diameter
HF = Hydrofluoric acid
HPLC=High Pressure Liquid Chromatography
IC-AFM = Intermittent contact or Tapping™ mode
IPTG = Isopropyl β- d-1-thiogalactopyranoside
K = Spring constant
KCl = Potassium chloride
kDa = kilo Daltons
KOH= Potassium hydroxide
L-Lys = L-Lysine
LAC = (find what LAC background means).
LTA = Lipo teichoic acids
ltaS = Lipo Teichoic acids Synthetase gene
mM = milli molar
mg= milligrams
ml=mili liters
MRSA= Methicillin Resistant *Staphylococcus aureus*
MSSA= Methicillin Sensitive *Staphylococcus aureus*
MurNAc = N-acetyl-muramic acid

NAG = *N*-acetyl-glucosamin
 NAM = *N*-acetyl-muramic acid
 NMR=Nuclear Magnetic Resonance
 nm= nanometre
 nN = nano Newtons
 OD₆₀₀ = Optical Density at 600 nm wavelenght
 PBPs = Penicillin Binding Proteins
 PFM = Pulse force mode
 PG = Peptidoglycan
 PG-bridges = cross-linking pentaglycine bridges
 PG-unit = Peptidoglycan forming unit
 PLL = Poly-L-lysine
 Pbp3 = Penicillin Binding Protein 3 gene
 Pbp4 = Penicillin Binding Protein 4 gene
 PeakForce = PeakForce Tapping mode
 Piezo = Piezoelectric
 PtP = Peak to Peak
 REDOR = solid-state NMR
 RT = Room Temperature
 Rbo-P = Ribitol-phosphate
S. aureus = *Staphylococcus aureus*
 s.d. = standard deviation
 SDS= Sodium dodecyl sulphate
 SEM = scanning electron microscopy
 SIM = structural illumination microscopy
 SPM = Scanning probe microscopy
 STM = Scanning tunnelling microscopy
 STORM = stochastic optical reconstruction microscopy
 Sacculi = Purified Cell wall
 Stock A= sacculi containing WTA
 Stock B= sacculi without WTA, only PG
 TA = Teichoic acids
 tarO = teichoic acid ribose gene
 TEM=transmission electron microscopy
 TGase = transglycosylase
 TPase = transpeptidase
 UDP = Uridine diphosphate
 Und-P = undecaprenyl phosphate
 VRSA= Vancomycin Resistant *Staphylococcus aureus*
 WT = Wild type
 WT M120 = wild type treated with Methicillin for 120 minutes
 WT M30 = wild type treated with Methicillin for 30 minutes
 WT M60 = wild type treated with Methicillin for 60 minutes
 WT V120 = wild type treated with Vancomycin for 120 minutes
 WT V30 = wild type treated with Vancomycin for 30 minutes
 WT V60 = wild type treated with Vancomycin for 60 minutes
 WTA = Wall teichoic acids

Å = Angstrom
 μl = microliters
 μm = micrometre